



HAL
open science

Two-dimensional electron gas oxide heterostructures for microelectronic in extreme environments

Hicham Zaid

► **To cite this version:**

Hicham Zaid. Two-dimensional electron gas oxide heterostructures for microelectronic in extreme environments. Materials Science [cond-mat.mtrl-sci]. Université Paris sciences et lettres, 2016. English. NNT : 2016PSLEM050 . tel-01651077

HAL Id: tel-01651077

<https://pastel.hal.science/tel-01651077>

Submitted on 28 Nov 2017

HAL is a multi-disciplinary open access archive for the deposit and dissemination of scientific research documents, whether they are published or not. The documents may come from teaching and research institutions in France or abroad, or from public or private research centers.

L'archive ouverte pluridisciplinaire **HAL**, est destinée au dépôt et à la diffusion de documents scientifiques de niveau recherche, publiés ou non, émanant des établissements d'enseignement et de recherche français ou étrangers, des laboratoires publics ou privés.

THÈSE DE DOCTORAT

de l'Université de recherche Paris Sciences et Lettres
PSL Research University

Préparée à MINES ParisTech

**Two-dimensional electron gas oxide heterostructures
for microelectronic in extreme environments**

**Hétérostructures d'oxydes à gaz d'électrons
bidimensionnels pour microélectronique
en environnements extrêmes**

Ecole doctorale n°432

Sciences des Métiers de l'Ingénieur

Spécialité :
Sciences et Génie des Matériaux

COMPOSITION DU JURY :

M. Alexander DEMKOV
University of Texas at Austin (USA)
Président du jury

M. Jean-Luc MAURICE
CNRS - Ecole Polytechnique
Rapporteur

M. Ian VICKRIDGE
CNRS – Université Pierre et Marie Curie
Rapporteur

M. Denis JALABERT
CEA - Université Grenoble Alpes
Membre du jury

M. Michael WALLS
CNRS – Université Paris Sud
Membre du jury

M. Alp SEHIRLIOGLU
Case Western Reserve University (USA)
Membre du jury

Mme. Marie-Hélène BERGER
MINES ParisTech
Membre du jury

Soutenue par **Hicham ZAID**
le 09 décembre 2016

Dirigée par **Marie-Hélène BERGER**



This thesis is dedicated to my grand-mother, my parents and my brothers.

**“Theory is when you know all and nothing works.
Practice is when all works and nobody knows why.
In this case we have put together theory and practice: nothing works... and nobody knows why!”**

Attributed to Albert Einstein

Acknowledgments

L'accomplissement d'une thèse est rarement un travail individuel, et particulièrement dans ce cas présent. Cette expérience a été profondément enrichie par les nombreuses personnes qui y ont contribué directement ou non, et le succès de ce travail leur est dû en grande partie. Je souhaite ainsi témoigner ma gratitude envers l'ensemble des personnes qui m'ont apporté leur soutien et ont fait de ce projet une belle aventure humaine et scientifique.

First I would like to warmly thank all the members of jury for accepting to analyze our works and their benevolence. I am highly honored by the presence of each member. I would like to start by the president of the jury, Professor **Alexander A. Demkov** from the University of Texas at Austin. I am deeply grateful to you for coming from so far away to attend my defense. I also thank Sir **Ian Vickridge** and **Jean-Luc Maurice** for reviewing my thesis, and for their relevant, benevolent and constructive comments.

La grande majorité de ma thèse s'est déroulée au Centre des Matériaux (Mines ParisTech) sous la direction de **Marie-Hélène Berger**. Je tiens à lui témoigner mon incommensurable reconnaissance pour toutes ces années passées ensemble et pour la confiance qu'elle a placée en moi. Ces quatre dernières années furent les plus enrichissantes et les plus réjouissantes grâce à toi (j'ai failli écrire vous !). Tu as rendu cette expérience à la fois scientifiquement et humainement passionnante. Tu as fait de chaque matin un plaisir pour moi de me lever (bon ça dépendait quand même de l'heure), ton sourire quotidien a fait de chaque jour un enchantement. Tu es une des plus belles rencontres que j'ai faites jusqu'à présent. Finalement je vais faire une liste (sinon je risque d'entendre « Le problème c'est que tu fais des phrases trop longues »), non exhaustive, de l'ensemble des qualités qui font de toi LA meilleure responsable que quiconque rêverait d'avoir : Ta culture scientifique qui m'a appris et orienté bien des fois lorsque je m'égarais, ton humilité, ta gentillesse, ta générosité, ta bienveillance, ta disponibilité malgré des journées toujours très chargées, ton humour, ton ouverture d'esprit, ton altruisme, ton honnêteté, ta fiabilité, ton intégrité, ta patience. J'ai appris énormément à tes côtés autant d'un point de vue scientifique qu'humain. La qualité de ce travail n'aurait jamais été possible sans toi. Pour tout ce que tu as fait durant ces années, pour ce que tu es toi, MERCI !

Je tiens également à prendre du temps pour remercier l'ensemble des collaborateurs qui ont contribué à rendre cette thèse meilleure. Dans l'ordre chronologique des personnes que j'ai rencontré, **Mike Walls** était le premier à m'avoir accueilli chaleureusement au sein du Laboratoire de Physique des Solides de l'Université Paris-Sud. Ces années de collaboration ont été un réel plaisir et ont considérablement enrichi cette thèse. Malgré des lames MET pas toujours bien préparées, tu as toujours essayé de tirer le maximum de résultats possible, quitte à rester tard. Nos visites à Orsay ont toujours été réjouissantes grâce à ta gentillesse et ton humour. J'ai été très heureux d'avoir pu travailler avec toi. Je remercie aussi les personnes de ton laboratoire qui sont souvent descendues

nous voir et nous ont apporté de précieux conseils, notamment **Laura, Katia March, Mathieu Kociak** et **Marcel Tencé**.

Ensuite, je voudrais témoigner de ma profonde reconnaissance à **Pascal Berger** du CEA à Saclay. Nos nuits passées au Laboratoire Pierre Süe, lors des manips RBS, ont toujours été animées par la bonne humeur et la convivialité, notamment grâce à vos valeurs humaines. D'ailleurs je garderai un souvenir impérissable de ce concert privé auquel j'ai eu droit. Votre disponibilité et vos explications toujours très claires m'ont facilité énormément la compréhension des principes de fonctionnement des techniques de spectroscopies nucléaires. J'aimerais également remercier **Sylvie Poissonnet** du CEA à Saclay pour nous avoir permis d'avancer considérablement dans la préparation des lames MET en nous préparant des échantillons par FIB.

Dans un troisième temps, je tiens à souligner mon immense gratitude envers **Denis Jalabert** du CEA à Grenoble. Sans ces travaux autour du MEIS, il m'aurait été difficile d'apporter une quelconque avancé dans ce domaine. Si j'ai pu développer une compréhension aussi précise autour de cette technique, c'est indéniablement dû à vos explications extrêmement claires et votre pédagogie. Vos qualités humaines ont fait de mes voyages à Grenoble de vrais beaux moments de partage. J'aimerais également remercier **François Pierre** et **Philippe Charrault** pour leur aide lors des manips et leur sympathie.

Then I want to thank particularly all the members of the international consortium that permitted to achieve a complete study of this topic. This thesis was built in the context of an international consortium between Case Western Reserve University, NASA Glenn Research Center and Mines ParisTech, and was supported by Air Force Office of Scientific Research (AFOSR) Grant FA 9550-12-1-0441. The success of this collaboration mainly owes to Pr. **Alp Sehrioglu** from CWRU, the Principal Investigator of this group of research, who managed the project with humility and generosity. I am deeply grateful to you for all you have done during my thesis. Your kindness, your wise advices, your cleverness, your altruism, and your benevolence contributed to make this thesis greater, I really appreciated to work with you. You warmly welcomed me during four months in Cleveland in spring 2014, and took care of me in order to help me to improve my understanding of the project. Our conversations about any topics were always rewarding and I learnt a lot by your side. I also would like to thank Pr. **Walter Lambrecht** (CWRU) and Pr. **Xuan Gao** (CWRU) for their huge help that permitted to go further in the understanding of the behavior of the LAO/STO heterostructures, in the field of modeling and electrical measurements respectively. The help that you provided was clearly mentioned as one of the strengths of this thesis. Among the student, I would like to particularly thank **Richard Akrobetu** for all what he has done. You provided me so many samples, you answered all my questions even if you were overwhelmed by your own work, you picked me up every morning to go to NASA and drove me back. We have shared so many things, and for all of that thank you my friend. I am also very grateful to **Jon Mackey**, from NASA Glenn Research Center, who is one of the kindest people I have ever met. You invited for every occasion you had even when we did not know well each other, and particularly you brought me to an event that I would have never thought to attend: the truck pulling. You introduced me to everyone at NASA and you helped to find all the people I needed to achieve my works. You really made my stay greater! Finally I want to thank all the people I met at NASA and at CWRU who considerably contributed make my stay enjoyable: **Fred Dynys** for your warm welcoming, **Philander** for our great discussions, **Jelani** for your kindness and your suitcase, **Ben** for taking care of me when I needed, **AmirAli** for teaching me the American way

to drive, **Danqi Wang** for your TEM expertise at Case, **Anita** for your help in using TEM and PIPS device at NASA, **Elahe** for her help in preparing TEM cuts by FIB, **Shyam** for driving me everywhere I needed, your open mind and your beautiful Godfather's song performance.

All these achievements would not have been possible without the help of one of the greatest man I have ever met, Dr. **Ali Sayir**. You have always supported me whereas I was nobody, you welcomed me with open arms each time we met, your kindness, your daily smile and your sense of humor made my stay at Washington highly gratifying. I do not have enough vocabulary to say how much grateful I am for all you have done during these years. I hope that I could realize a work meeting your expectations. It was a huge privilege to know you. And I really do mean all of it. I hope I will be able to meet you again.

I also would like to acknowledge all the people I met during my thesis through meetings and conferences. First my gratitude goes to the great scientist I met at the AFOSR Program Review taking place each year in Washington, your company enriched me both scientifically and humanly: **Suneel Kodambaka** (UCLA), **Laura Silvestroni** (CNR – ISTECE), **Diletta Sciti** (CNR – ISTECE), **Andreï Voevodin** (AFRL), **Hitomi Yamaguchi Greenslet** (U. Florida). I insist to thank **Lena F. Kourkoutis** (Cornell U.) who gave me constructive and benevolent advices on EELS interpretations during the MRS Spring Meeting in 2014 at San Francisco, **Salome L. Aguero Molina** (ORNL) who helped me by sharing her own way to prepare TEM samples, **Felix Gunkel** (RWTH Aachen U.) for interesting discussions at EMRS Fall Meeting 2015 in Warsaw and sharing his work on strontium vacancies. I also extend my warmest thanks to **Florencio Sánchez** (ICMAB - CSIC), **Gertjan Koster** (U. Twente), **Josée Kleibeuker** (U. Cambridge), and **Valentin CRACIUN** (INFLPR) who honored me by attributing me the Best Student Presentation Award of our Symposium at the EMRS Fall Meeting 2015.

Enfin je voudrais remercier l'ensemble des personnes avec qui j'ai partagé mes quatre années de thèse au Centre des Matériaux – Mines ParisTech. Tout d'abord, j'aimerais commencer par les permanents du laboratoire, et notamment Monsieur **Yves Bienvenu**. Je tiens à vous remercier pour ces merveilleux moments passés en votre compagnie. Nos multiples conversations sur tout un tas de sujets comme Tintin, le zoo (où vous me pensiez y être quotidiennement), José San Martin, le général De Gaulle, les épiluchures de riches, les fruits et fromages qui permettent de développer une quantité certaine d'anticorps, et bien évidemment le plus important de tous, l'ASNL, m'ont considérablement enrichi. Votre humour sans pareil, votre immense culture et votre gentillesse m'ont appris ce que c'est d'être un homme de valeurs. Je souhaite également remercier Monsieur **André Pineau**, qui fait la renommée de notre laboratoire. Vous avez contribué à combler mes nombreuses lacunes culturelles (maintenant je connais la date de la mort de Louis XIV), et à égayer mes pauses café. Merci à **Ziradjoudine Akber** pour sa disponibilité, sa serviabilité, sa générosité, et sa communication souvent transparente. Ta bonhomie quotidienne et ta gentillesse à toute épreuve ont rendu ces années plus joyeuses. Merci à **Kaïs Ammar** pour toutes ces années de soutien. Tu as toujours cru en moi. Ta bonne humeur légendaire, ta joie de vivre et ton optimisme naturel ont considérablement rendu ces années plus douces. Je t'ai dérangé à des heures souvent extrêmement matinales et tu ne m'en as jamais tenu rigueur. Par contre, tu m'as toujours témoigné de la chaleur humaine, tu m'as accueilli à bras ouvert et rendu un nombre incalculable de services lorsque j'en avais besoin. Bien que tu restes et resteras mon (plus très) jeune apprenti FIFA, je voudrais profiter de ces lignes pour te témoigner sans ironie mon amitié et te souhaiter tout le bonheur du monde pour le futur. Merci à **Farida Azzouz** qui a toujours eu une oreille attentive, et pour nos chaleureux

moments passés à la cafèt. Ta bienveillance, ton soutien et ton sourire m'ont été très précieux durant ces années au CdM. J'aimerais également remercier **Sarojinee Lorgambal Bonneville**. Tes nombreux messages d'amours ont ensoleillé mes journées. Tu prenais les devant pour savoir si je ne manquais de rien. Je tiens à t'exprimer ma profonde gratitude pour tout ce que tu as fait. Merci à **Gérard Brabant**, aussi connu comme étant la Source. Tu as toujours fait preuve d'altruisme, tu m'as aidé à résoudre de nombreux problèmes tout au long de ces années. Bien que les discussions dérivaiement souvent, j'ai énormément apprécié les moments en ta compagnie (et visiblement je ne suis pas seul dans ce cas, quand je vois ton fan club...). Tu es quelqu'un de profondément gentil et serviable, le Centre a beaucoup de chance de te compter parmi les siens. Merci à **Anthony Chesnaud** pour ces moments conviviaux passés ensemble. Je ne suis pas sûr que la pharmacie de Villabé fait des cartes de fidélité, donc j'espère que tu prendras soin de toi. Merci à **Régis Clément**, notre footballeur national, pour sa bonhomie et sa gentillesse. Merci à **Claudine Devemy** pour son sourire quotidien, j'espère que je saurais un jour d'où viennent ces petites étoiles. Merci à **Jérôme Crépin**, Monsieur le directeur du CdM. Vous m'avez toujours soutenu et cru en moi. Vous avez toujours été bienveillant à mon égard. J'ai beaucoup apprécié nos conversations faites d'humour et d'autodérision. Merci à **Cécilie Duhamel**, aussi connu comme étant le Cerveau de la bande. Ton impertinence et ta répartie ont animé nos midis. Malgré que j'ai du mal à l'écrire, je suis bien obligé de rétablir la vérité, ces instants passés en ta compagnie ont été très sympas et chaleureux. Même si tu as passé l'âge d'avoir un doudou, et que tu vis au siècle précédant le précédant, et que le cubis de villageoise est dangereux pour la santé, je tiens à te témoigner ma gratitude pour tous ces agréables moments passés au Centre. Je voudrais aussi remercier **Anne Laurent** (ou Honey) qui nous a quitté pour de nouvelles aventures. Ce fut toujours un plaisir de te croiser fortuitement, ou non, dans les couloirs du labo. Même si tu es parti, tu ne m'as pas oublié...et moi non plus. Merci à **Yazid Madi** (ou Monsieur Mazid) pour cette bonté d'âme dont il a fait preuve durant toutes ces années. Tu m'as toujours accueilli avec un sourire radieux et une bienveillance qui te font honneur. Je tiens à souligner ma profonde gratitude à **Abdenour Meddour** (ou Joe) qui a incontestablement rendu meilleur mon séjour au CdM. Tu m'as nourri le corps et l'esprit. Tu m'as ouvert ta porte. Je savais qu'en cas de besoin tu serais toujours là pour moi. Je ne pense pas pouvoir retranscrire avec des mots à quel point je suis reconnaissant pour tout ce que tu as fait, donc tout simplement MERCI. Je souhaite également remercier **Lyn-Thy Mingault**, aussi connu sous le nom de Unlucky luke (car tu tires moins vite que ton ombre). Ce fut toujours un plaisir de te croiser dans les couloirs et de partager ces petits moments en ta compagnie. Merci à **Djamel Missoum-Benziane** (ou Wikipédia). Tu nous en as raconté des histoires, sur toi, ta famille, sur Chlef, sur l'Algérie, sur la cuisine, sur les deux Guerres Mondiales, sur les ordinateurs, sur le langage informatique, sur ta passion pour le foot, sur ton goût prononcé pour la mode, sur les moins cent vingt-six milles, sur les moteurs de voitures, sur celui qui a inventé les moteurs de voitures, sur la famille de celui qui a inventé les moteurs de voitures. Merci pour ces nombreuses pauses café passées ensemble à refaire unilatéralement le monde. Merci pour m'avoir sauvé la mise quand j'étais aux USA. Merci pour ton amitié sans faille durant toutes ces années. Je te souhaite un bonheur sans fin, surtout avec ton mini toi qui arrive. Je remercie aussi **Franck N'Guyen**, l'homme qui court presque nu dehors en hiver. Nos discussions sur la science et son éthique, sur son essor et son importance, m'ont apporté une certaine relativité sur notre discipline et une sérénité sur notre condition. Merci à **Catherine Rouil** (ou Cat la loubarde) qui nous accueille chaque matin avec le sourire. Merci à **Mohamed Sennour** (ou sa Majesté Messire) pour son humour, son ouverture d'esprit, sa gentillesse, son indulgence vis-à-vis du TEM. Tu étais mon voisin de bureau, et tous les matins pendant toutes ces années tu me saluais avec un sourire

radieux. Merci également à **Cédric Toussaint**, pour sa gentillesse et son flegme. Ton humour bien particulier a systématiquement égayé nos rencontres. Je souhaiterais terminer ce paragraphe par remercier l'ensemble des permanents que j'ai côtoyé et qui m'ont témoigné de la sympathie pendant ces quatre années : **Odile Adam** pour son aide et son sourire, **Yann Auriac** pour sa rigueur autour de notre sécurité, **François Borit** pour son authenticité et sa sincérité, **René Cluzet** pour ses incitations à lui rendre visite, **Stéphanie Dang** pour son état d'esprit, **Nicole De Dave** pour son franc-parler, **Antoine Debray** pour son humour, **Françoise Di Rienzo** pour son courage, **Sandrine Fontaine** pour nos discussions autour d'un café, **Samuel Forest** pour ses remarques bienveillantes, **Anne-Françoise Gourgues** pour son dynamisme et son soutien, **Jean-Yves Herry** pour sa gentillesse et pour avoir toujours su garder sa porte ouverte lorsqu'un problème se présentait, **Véronique Matos** pour son aide concernant la partie administrative, **Christophe Meurin** pour sa comparaison avec l'Abbé Pierre (« mais jeune ») et ses qualités humaines, **Brigitte Raviart** pour la tendresse que laissait transparaître sa timidité, **Konaly Sar** pour sa bonne humeur, **Mickael Siry** pour m'avoir évité bien des ennuis informatiques et nous avoir fait partager ses connaissances sur le côté obscur, **Alain Thorel** pour ses conseils avisés, **Jean-Christophe Teissedre** pour sa bonne humeur quotidienne et toujours prêt à échanger, **Karine Viellevigne** pour sa gentillesse, **Vladislav Yastrebov** pour sa poignée de main énergique et **Maria** qui passait chaque matin avec sourire et politesse dans mon champ de bataille.

Ces années passées au CdM n'auraient pas été aussi agréables sans la présence des nombreux Post-Doc et doctorants qui ont fréquenté ses couloirs. Je voudrais donc en profiter pour les remercier chaleureusement. Je vais commencer par les anciens, et la mafia thaïlandaise. Kop Khun Krap à **Pongsak Nimdum**, **Ekkarin Phongphinitana**, et surtout **Baramee Patamaprohm** et **Arruck Tragangoon**. Vous m'avez toujours témoigné votre amitié avec tendresse et chaleur. Vous m'avez appris le kit de survie de la langue thaïlandaise, vous m'avez ouvert l'esprit sur bien des domaines, on a bien ri pendant ces années. Je souhaite vous dire que votre amitié m'honore. เช่นเดียวกับระยะเวลาที่เผยให้เห็นน้ำที่ดีเวลาที่แสดงให้เห็นว่าเป็นคนดี (Source google translate, la maison décline toute responsabilité en cas de fautes). Je voudrais également remercier **Adrien Lebrun** pour ce qu'il est. Tu m'as aidé à résoudre des problèmes de programmation auxquels je ne comprenais rien, tu m'as invité à partager des maquereaux au fin fond des contrées perdues, tu m'as aidé à déménager alors que je n'avais rien pour. Tu es d'une générosité rare, tu donnes sans attendre quoi que ce soit en retour. Tu es une personne profondément bien, comme rarement j'ai eu l'occasion d'en rencontrer. Merci à **Raphael Maestracci** (ou Nigbout) pour nos franches rigolades dans les couloirs du CdM. J'aimerais remercier **Myriam Gharbi** et sa famille. Tu as toujours fait preuve de générosité, de bonté d'âme et de bienveillance. Nous avons partagé de merveilleux moments à Evry, Corbeil ou autour de barbecue le dimanche. Tu m'as accueilli chez toi avec tes enfants et ton mari, avec Mohamed passionné des (para para) parasaurolophus, et Eya toujours joyeuse. Je te souhaite à toi ainsi qu'à ta petite famille un avenir radieux vers de nouveaux horizons. I want to warmly thank **Martin Horak**, můj mladý námořník, můj myška v šuplíku, můj mala verveka na drakovi. These years spent by your side were incredibly (neuvěřitelný) enjoyable. Your sense of humor, your kindness, your open-mind, your spirit, your own way to build french sentences, made hugely better my days at the CdM. Therefore, I would like to thank you for who you are. You are one of the most incredible man I have ever met. I hope we will keep in touch. Je souhaite remercier **Francesco Delloro** pour nos moments passés à la cafèt. Nos discussions autour des voyages en bateau, de l'Italie, de la cuisine, et des nombreux autres sujets sur lesquels nous avons débattu pendant toutes ces années m'ont enrichi humainement. J'ai beaucoup apprécié ta compagnie. Parmi

les derniers arrivés, je voudrais remercier **Juan-Manuel Garcia** (el señor de la Vega) pour son amitié et sa bonne humeur. Merci à **Olivier Ponte-Felgueiras** pour son soutien et son humour hors du commun. Tes traits d'esprit m'ont toujours fait rire, et faisait transparaître ta bonté de cœur. Merci à **André-Pierre Abellard** pour m'avoir délivré presque tous les soirs, et pour sa gentillesse sans pareille. Merci à **Kévin Ardon** (le grimpeur de l'extrême) pour sa générosité sans limite, et son amitié. Merci à **Rudy Michel** (mein klein weichheit) pour son calme, sa douceur et son sens de l'humour. Merci à **Clémentine Fellah** (ou bichette) d'avoir partagé avec moi Marie-Hélène. Si tu es la couchoutte, c'est qu'il doit bien y avoir une raison. Merci à **Mariam Trabelsi** pour son sourire quotidien qui illumina mes journées. Je tiens à te remercier pour la générosité et la gentillesse dont tu as fait preuve durant cette dernière année. Merci à l'ensemble des anciens et des nouveaux du Centre avec qui j'ai passé d'excellents moments : **Mamadou Mbacke, Mouhcine Kahziz, Judith Wollbrett-Blitz, Georges Kamgaing, Mehand Tebib, Quentin Blochet, Rim Ben Toumi, Victor DeRancourt, Harry Pommier, Guillaume Burgaud, Isabelle Turque, David Masson, Amal Chebbi, et Pierre-Emmanuel Léger.**

Je voudrais remercier ceux qui m'ont accompagné tous les jours comme **Michel** (qui nous a sorti du pétrin à bien des moments), **Georges**, le grand **Jacques, Nino, Hans, Jalal, Illiass**, et tous les autres qui ne m'en voudront pas si je les oublie. Et enfin je voudrais finir ce paragraphe consacré au CdM par exprimer ma gratitude envers les nombreuses personnes qui ont partagé mon bureau et ont rendu plus joyeuses et conviviales nos journées: **Mona BenAchour, Nada Bousselmi, Anaïs, Francesco, Di Li, Tang Shi, Xhang Yang** et les petites dernières **Wijdene Guediche et Sarah Saanouni.**

Je tiens à remercier tout particulièrement **Battal Tuzun**, professeur de mathématique au collège Henri Wallon à Ivry-sur-seine, pour sa contribution au succès de mon doctorat. Ta rigueur, ton hospitalité, ta bonhomie, ta créativité ont rendu ces années formidables. Merci à mes amis de Nancy, de Paris et d'ailleurs.

Je souhaite terminer cette partie par le plus important, la famille. Aussi je remercie infiniment tous les membres de ma famille de France et du Maroc pour leur soutien indéfectible. Tout d'abord ma Mima hbiba qui n'a pas cessé de m'apporter amour et tendresse depuis toujours. Je remercie mes parents qui m'ont toujours poussé dans mes études, ont cru en moi et apporter réconfort. Sans vous je ne serais là où je suis actuellement. Merci à mes frères pour leur joie de vivre, et leur droiture qui en font des exemples pour leur génération. Comme j'ai rarement le courage de vous le dire, je vous l'écris : Je vous AIME ! J'ai une pensée émue pour mes trois grands-parents qui n'ont pu assister à cette réussite, et qui aurait été fiers.

En relisant cette partie, je me rends compte de l'immense chance et privilège que j'ai eu à évoluer dans un environnement aussi riche scientifiquement et humainement.

Merci à toutes et tous pour ces belles années.



Hicham Zaïd

Docteur | Sciences et Génie des Matériaux

Abstract

Novel behavior at the interface between two insulating polar/non polar perovskites has been recently discovered. The polarization discontinuity at $\text{LaAlO}_3/\text{SrTiO}_3$ drives the formation of quasi two dimensional electron gas. Both the local mechanism and quantification of such behavior remain unclear due to interplay of structural, chemical and electronic factors. Several mechanisms have been proposed, such as the polar catastrophe, structural distortions, oxygen vacancies, cationic intermixing at the interface and film non-stoichiometry. In the frame of an international project conductive and insulating heterostructures have been synthesized by Pulsed-Laser Deposition. In this thesis, we have developed a comprehensive approach to investigate the origin of the charge carriers. The interfaces have been systematically analyzed by combining high resolution imaging (STEM-HAADF) to atomic resolved electron (EELS) and ion (MEIS) spectroscopies. The observed and quantified parameters have been related to the electrical properties of the interfaces measured in the consortium. Buckling of the atomic layers, intermixing and electron transfer reduce the polar divergence. This rules out the polar catastrophe scenario. The formation of donor defects at the film surface is favored above a critical film thickness. Electrons are transferred to interface in the STO conduction band. A competing compensation mechanism of the positive interfacial charge by negatively charged strontium vacancies has been demonstrated that generates an in-plane compression of the STO, unfavorable for a strict 2D confinement of the charges. Varying the process parameters such as growth duration, oxygen partial pressure, temperature, and plume stoichiometry, shifts the equilibrium of the different mechanisms highlighted. This thesis emphasizes the complex relations between the process and the properties through the defects distribution around these singular interfaces.

Résumé

De nombreuses propriétés étonnantes ont été récemment découvertes à l'interface de deux perovskites isolantes l'une polaire l'autre non polaire. La discontinuité de charge à l'interface $\text{LaAlO}_3/\text{SrTiO}_3$ engendre un gaz d'électron quasi-bidimensionnel qui confère un caractère métallique à cette interface. Les mécanismes locaux et la quantification des propriétés ne font pas consensus car l'interdépendance de facteurs structuraux, chimiques et électroniques complexifie la résolution du problème posé. Une catastrophe polaire, des distorsions structurales, des lacunes d'oxygène, une interdiffusion cationique et une non-stœchiométrie du film ont été séparément avancées pour expliquer cette conduction. Dans le cadre d'un programme international, nous avons reçu des hétéro-interfaces conductrices et isolantes élaborées par ablation laser pulsé (PLD). L'origine des porteurs de charge a été recherchée par une approche globale liant procédé, structure et propriétés électriques (mesurées dans le consortium). Nous avons systématiquement analysé les interfaces en combinant imagerie à haute résolution (STEM-HAADF) et spectroscopies électroniques (EELS) et ioniques (MEIS). Une non planéité des couches atomiques, une interdiffusion cationique et un transfert d'électrons permettent de réduire la divergence de potentiel, la catastrophe polaire n'a donc pas lieu. La formation de défauts donneurs à la surface du film devient favorable au-delà d'une épaisseur critique. Les électrons sont transférés à l'interface dans la bande de conduction du STO. Nous avons mis en évidence un mécanisme de compensation concurrentiel de la charge interfaciale par des lacunes de strontium chargées négativement, qui mettent le substrat en compression plane et s'opposent au confinement 2D électrons. La variation des paramètres procédés, tels que la durée du dépôt, la pression partielle en oxygène, la température et la stœchiométrie de la plume déplace l'équilibre des différents mécanismes mis en évidence. Ce travail démontre la relation complexe liant procédé, propriétés électriques et distribution des défauts autour de ces interfaces singulières.

Table of content

Introduction	2
Bibliography.....	4
Chapter I	
LAO/STO hetero-interfaces: State-of-the-art	6
I.1 Perovskite	6
I.2 SrTiO ₃	8
I.3 LaAlO ₃	11
I.4 LaAlO ₃ /SrTiO ₃ Heterostructure.....	12
I.4.1 Two-dimensional electron gas with high mobility	12
I.4.2 Superconductivity.....	13
I.4.3 Magnetism.....	14
I.4.4 Substrate termination	15
I.4.5 Critical thickness.....	17
I.4.6 Applications	18
I.5 Origins 2DEG.....	19
I.5.1 Polar Catastrophe.....	20
I.5.1.1 The pristine model.....	20
I.5.1.2 Chemical modification of the film surface	21
I.5.1.3 Experimental evidence of the polar catastrophe model.....	22
I.5.1.4 Electron reconstruction below the critical thickness	22
I.5.1.5 Other incoherency of the polar catastrophe model	23
I.5.2 Oxygen vacancies	23
I.5.2.1 The process as a source of oxygen vacancies in STO	24
I.5.2.2 Oxygen vacancies and electrical conduction.....	24
I.5.3 Intermixing	26
I.5.4 Structural Distortions	29
I.5.4.1 Effect of strain in perovskites.....	29

1.5.4.2	Effect of epitaxial strain.....	30
1.5.4.3	Strain induced rotation and distortion of oxygen octahedra.....	31
1.5.4.4	Elongation of the TiO ₆ octahedra and Jahn-Teller effect	32
1.5.4.5	Buckling of AO and BO ₂ layers	33
1.5.5	Film stoichiometry.....	35
1.5.5.1	Film stoichiometry and PLD process parameters.....	35
1.5.5.2	Film stoichiometry and lattice parameters	35
1.5.5.3	Film stoichiometry and hetero-interface conductivity.....	36
1.6	Summary.....	39
	Bibliography.....	40
	Résumé - Chapitre I	49

Chapter II

Experimental methods	54
II.1 Pulsed Laser Deposition (PLD).....	54
II.1.1 Substrate Preparation	54
II.1.2 PLD Process.....	55
II.1.2.1 Plasma mechanisms	57
II.1.2.2 Growth monitoring by RHEED	57
II.2 Film growth.....	60
II.3 PLD growth conditions	61
II.3.1 Laser Fluence	61
II.3.1.1 Film stoichiometry.....	62
II.3.1.2 Film structure	62
II.3.1.3 Electrical properties.....	63
II.3.2 Plasma plume	64
II.3.2.1 Target-to-substrate distance	64
II.3.2.2 Plume Angle.....	64
II.3.3 Oxygen pressure	65
II.3.3.1 Film stoichiometry.....	65
II.3.3.2 Film growth.....	66
II.3.3.3 Intrinsic defects	66
II.3.3.4 Conduction extension.....	67
II.3.3.5 Cationic exchanges	67

II.3.3.6	Cationic defects	67
II.3.4	Temperature.....	68
II.3.4.1	Film growth.....	68
II.3.4.2	Lattice structure	68
II.3.4.3	Electrical properties.....	68
II.3.5	PLD growth relative to this thesis.....	69
II.4	Transmission Electron Microscopy (TEM)	72
II.4.1	Sample preparation for TEM investigations.....	72
II.4.1.1	Mechanical Polishing.....	72
II.4.1.1.1	Tripod polishing.....	72
II.4.1.1.2	Ion-milling.....	73
II.4.1.1.3	Difficulties faced during tripod/ion thinning.....	73
II.4.1.2	Focused Ion Beam (FIB)	74
II.4.2	TEM-STEM imaging.....	75
II.4.3	Electron Energy Loss Spectroscopy (EELS)	77
II.4.3.1	Ti valence	77
II.4.3.1.1	Multivariate Analysis.....	78
II.4.3.1.2	Linear combinations of EELS reference spectra.....	79
II.4.3.2	Oxygen vacancies	80
II.5	Nuclear Spectroscopies	82
II.5.1	Fundamentals of physics of ion-solid interactions.....	82
II.5.1.1	Kinematic factor	82
II.5.1.2	Electronic / Nuclear Stopping power	83
II.5.1.3	Scattering cross section.....	84
II.5.2	Rutherford Backscattered Spectroscopy (RBS)	86
II.5.3	Medium Energy Ion Scattering (MEIS)	89
II.5.3.1	Random mode	92
II.5.3.2	Channeling mode.....	94
II.5.3.3	Blocking mode	95
II.5.3.4	Buckling profiles	97
II.6	Electrical measurements	99
II.7	Summary.....	101
	Bibliography.....	102
	Résumé - Chapitre II	107

Chapter III

Origin(s) of the q-2DEG at the LAO/STO hetero-interface	112
III.1 Film growth.....	112
III.2 Polar catastrophe	114
III.2.1 Critical thickness.....	114
III.2.2 Ti valence.....	115
III.3 Oxygen vacancies	118
III.4 Intermixing	119
III.4.1 A-site cations intermixing.....	120
III.4.2 A-site versus B-site cations intermixing	121
III.5 Structural distortions.....	124
III.5.1 Strain profiles	125
III.5.2 Buckling profiles	129
III.5.3 Origins of the strain and buckling.....	130
III.5.3.1 Deformation induced by Ti^{3+}	130
III.5.3.2 Compensation of the polar field by dipole formation: Ti off-centering.....	130
III.5.3.3 Compensation of the polar field by dipole formation: buckling of A-O and/or B-O layers.....	131
III.5.3.4 Formation of Strontium vacancies in the substrate and their impact on deformation.....	132
III.5.3.5 Distribution of the strontium vacancies in the 3 u.c. and 5 u.c. sample	134
III.6 Discussion	135
Bibliography.....	138
Résumé - Chapitre III	143

Chapter IV

Dependence of the $LaAlO_3/SrTiO_3$ electrical properties to growth conditions	148
IV.1 Film thickness effect.....	149
IV.1.1 Electrical Measurements	149
IV.1.2 Ti^{3+} Contribution	150
IV.1.3 Oxygen vacancies	152
IV.1.4 Intermixing	153
IV.1.5 Thickness effect: Discussion	154

IV.2	Effect of Oxygen Partial Pressure during film growth	156
IV.2.1	Film growth.....	156
IV.2.2	Electrical Measurements.....	157
IV.2.3	Ti ³⁺ Contribution	158
IV.2.4	Oxygen vacancies	159
IV.2.5	Intermixing	160
IV.2.5.1	EELS investigations	160
IV.2.5.2	MEIS investigations.....	161
IV.2.6	Structural distortions.....	162
IV.2.6.1	Strain Profiles	162
IV.2.6.2	Buckling profiles	165
IV.2.6.3	Ferroelectric-like distortions	165
IV.2.7	Oxygen Partial Pressure effect: Discussion	166
IV.3	Deposition angle effect	167
IV.3.1	Film growth.....	167
IV.3.2	Ti ³⁺ Contribution	170
IV.3.3	Oxygen vacancies	172
IV.3.4	Intermixing	172
IV.3.5	Structural distortions.....	173
IV.3.6	Deposition Angle: Discussion	175
IV.4	Temperature effect	176
IV.4.1	Film growth.....	176
IV.4.2	Ti ³⁺ Contribution	177
IV.4.3	Oxygen vacancies	178
IV.4.4	Intermixing	179
IV.4.5	Structural distortions.....	180
IV.4.6	Temperature effect: Discussion	181
IV.5	Discussion	182
	Bibliography.....	183
	Résumé - Chapitre IV	186
	<u>Conclusion & Outlook</u>	190

Glossary

2DEG	Two-Dimensional Electron Gas
AFM	Atomic Force Microscope
ALD	Atomic Layer Deposition
CVD	Chemical Vapor Deposition
DFT	Density Functional Theory
EELS	Electron Energy Loss Spectroscopy
ELNES	Energy-Loss Near-Edge Structure
FIB	Focused Ion Beam
FWHM	Full Width at Half Maximum
HAADF	High-Angle Annular Dark-Field
ICA	Independent Component Analysis
LAO	Lanthanum aluminate – LaAlO_3
MBE	Molecular Beam Epitaxy
MEIS	Medium-Energy Ion Scattering
MOSFET	Metal-Oxide-Semiconductor Field-Effect Transistor
MS	Magnetron Sputtering
MVA	Multivariate Analysis Method
PCA	Principal Component Analysis
PIPS	Precision Ion Polishing System
PLD	Pulsed Laser Deposition
p_{O_2}	Oxygen partial pressure
q-2DEG	Quasi Two-Dimensional Electron Gas
RBS	Rutherford Backscattering Spectroscopy
RF	Radio Frequency
RHEED	Reflection High Energy Electron Diffraction
SAED	Selected Area Electron Diffraction
SEM	Scanning Electron Microscopy
STEM	Scanning Transmission Electron Microscopy
STO	Strontium titanate – SrTiO_3
TEA	Toroidal Electrostatic Analyzer
TEM	Transmission Electron Microscopy
u.c.	unit cell
USTEM	Ultra Scanning Transmission Electron Microscopy
V''_{Sr}	Strontium vacancies
V''_{O}	Oxygen vacancies



Introduction

The field of electronics is widely and constantly subjected to innovations. In the middle of the XXth century, the Nobel Prize in Physics was attributed to Bardeen, Brattain and Shockley for their discoveries of the transistor effect. The electrical current became controllable and the world of electronics has been overwhelmed by devices based on semiconductor technology. Then, in 1973, this prize was awarded to Giaever and Esaki for their experimental researches on the tunneling phenomena in semiconductors. In 2000, Kilby was rewarded by the Nobel Prize in Physics for inventing the integrated circuits which is essential for most of technologies around us. This distinction was shared with Kroemer and Alferov for their works on semiconductors. This class of materials allowed huge progresses in the electronic industry, and the modernity of its devices. It is still under intensive researches, testified by the Nobel Prize received in 2009 by Boyle and Smith, to improve their performances. In this context, oxide materials rise up to be good candidates, notably to overcome the issues linked with the extreme environments. Great interest has been focused on these materials, they exhibit an interplay between their properties and so leading to multifunctional devices. The strength of these materials is based on the ability to control their behavior by manipulating intrinsic and/or extrinsic parameters (such as their structure, chemistry, temperature, pressure, electric field, magnetic field, etc.) due to the electronic correlations, which are particularly relevant in the transition metal oxides. Electrons of such oxides display strong interactions with electrons of neighboring atoms giving rise to new functionalities such as superconductivity, large magnetoresistance, (anti-)ferroelectricity, magnetism, (anti-)ferromagnetism, piezoelectricity, metal-insulator transitions etc. In this context, new materials were created artificially by combining various oxides involving the emergence of interfaces where new phenomena occur. The properties exhibited by heterostructures can be totally different from the bulk properties of each component. Recent advances in thin-film deposition and characterization techniques made possible the experimental realization of such oxide heterostructures. The ability to control the growth of thin films, at atomic level, has contributed to the great interest developed toward these materials. Furthermore as the crystal lattice sizes are close to each other, it broadens the possibility of combinations between oxides materials, promising new functionalities and devices concepts. The scientific researches about the physics of mechanisms occurring at the interface of oxides materials increased over and over, and allowed to tune the heterostructures properties. For example, the combination of two antiferromagnetic insulators, LaFeO₃ and LaCrO₃, results in a ferromagnetic heterostructure, or the

$\text{SrZrO}_3/\text{SrTiO}_3$ superlattice which is ferroelectric whereas none of its components shows ferroelectricity. The common point between the above materials is that they are made from crystalline structure of perovskite, ABO_3 . The keen interest developed around this class of oxides is mainly due to the wide types of A and B cations usable, giving rise to an almost infinite possibility of combinations, and so of physical phenomena and properties. Maybe one of the most fascinating examples is the metal-insulator transition between two insulators. In 2004, Ohtomo and Hwang [1] demonstrated that at the interface of two bulk insulators, LaAlO_3 and SrTiO_3 , a conductive layer occurred, depicted as 2D electron gas (2DEG). This sub-nanometer thick conducting channel opens up the possibility of a new step in the miniaturization of electronic devices, pushed forward by new technological needs. Since then, many research groups have focused their energy on the explanations of the origins of this surprising conduction. This first observation of a metallic sheet formation was attributed to a decrease in valence of Ti cations located in the first unit cell of SrTiO_3 through a mechanism called “polar catastrophe”, and proposed by Ohtomo and Hwang [1]. Nevertheless this model was clearly undermined by many groups, and the mechanisms of charge transfer and transport in this system are still not clearly established despite of all the experimental results already existing. Other structural and chemical changes have been revealed near the interface, including the expansion of SrTiO_3 cells and polar distortions, cation intermixing, oxygen vacancies and lanthanum deficiency in the film. The specific roles of these phenomena in the interfacial conduction are yet not fully understood. Indeed, in the literature, one main factor is constantly varying, the process and above all its growth conditions. The atomic structures of the $\text{LaAlO}_3/\text{SrTiO}_3$ heterostructures are not strictly identical. This can lead to major differences in the properties of this strongly correlated electron system, and must be kept in mind when reviewing the various mechanisms developed from the interpretation of diverging experimental data. Therefore, a better control of the relation between process and properties is needed to clarify the influence of each mechanism on the 2DEG at the interface of the heterostructure. The main aim of this thesis is to investigate the mechanisms responsible for the conductivity at the $\text{LaAlO}_3/\text{SrTiO}_3$ hetero-interface by studying the structure as fundamental link between process and properties.

Our work was included in an international research project gathering Case Western Reserve University (CWRU) and Ecole des Mines de Paris, called « Quantitative identification of electro-physical properties of oxide based hetero-interfaces at extreme environment ». We could rely on dynamic collaboration putting together the different fields required in such a topic, from the elaboration to the characterization. The $\text{LaAlO}_3/\text{SrTiO}_3$ heterostructures were synthesized at the NASA Glenn Research Laboratory by Richard Akrobetu and Pr. Alp Sehirlioglu from the Departments of Materials Science and Engineering of CWRU. The electrical measurements were carried out in the Departments of Physics of CWRU by Nicholas Goble and Pr. Xuan Gao. The modeling part was achieved in the same department by Ittipon Fongkaew and Pr. Walter Lambrecht.

The manuscript is divided into four chapters. The first chapter contextualizes the thesis subject. We provide a description of the $\text{LaAlO}_3/\text{SrTiO}_3$ heterostructures by presenting the crystalline and electronic structures of perovskites and bulks LaAlO_3 and SrTiO_3 , their properties, and their applications. An overview of the state-of-art of the different mechanisms believed to be at the origins of the conductivity at the $\text{LaAlO}_3/\text{SrTiO}_3$ hetero-interface will be presented in order to gather and clarify all the results brought by the researchers during the past decade. Chapter two exposes the experimental methods used to process and characterize the $\text{LaAlO}_3/\text{SrTiO}_3$ systems during my PhD work. The process and the influence of its various parameters on the heterostructures behavior

Introduction

will be discussed, as well as the samples preparation and the experimental techniques used to obtain the results exhibited in the next chapters. Chapter three discriminates the origins of the interfacial conductivity by analyzing two samples differing from each other by their electrical properties. Chapter four discusses the influence of the growth parameters on the structural and electronic properties of the $\text{LaAlO}_3/\text{SrTiO}_3$ heterostructures.

Bibliography

- [1] A. Ohtomo and H. Y. Hwang, "A high-mobility electron gas at the $\text{LaAlO}_3/\text{SrTiO}_3$ heterointerface," *Nature* **427**, 423–426 (2004).

Chapter I

LAO/STO hetero-interfaces: State-of-the-art

This chapter introduces the subject of $\text{LaAlO}_3/\text{SrTiO}_3$ heterostructures and the formation of a *quasi*-two-dimensional electron gas at their interface. To set the context of this work, we will first make a rapid presentation of the family of perovskite, the structure and properties of the strontium titanate and the lanthanum aluminate. Then, we will focus on the coupling of LaAlO_3 and SrTiO_3 by describing the specific properties of the heterostructure, in particular the insulator/metal transition. We will finish by a presentation of each of the mechanisms proposed in the literature to explain this intriguing conducting behavior.

I.1 Perovskite

The first mineral named perovskite was the calcium titanate (CaTiO_3) discovered in 1839 by the German mineralogist G. Rose in the Ural Mountains, who named the crystal after the Russian mineralogist Lev A. Perovski. By extension the word perovskite refer to materials with the same type of structure as CaTiO_3 . Their general formula is ABX_3 , where A and B stand for a wide range of metal cations, with A cations having a larger size than B one, and X represents most often O^{2-} but can also be chosen amongst halogen elements. The crystal structure of a ABO_3 perovskite (Figure I.1) consists of infinite chains of corner sharing BO_6 octahedra in the three directions where A cations fill the cuboctahedral site which occupy every hole created by eight BO_6 octahedra (Figure I.1c). Ideally, this crystal adopts a centrosymmetric cubic structure (space group of $\text{Pm}\bar{3}\text{m}$), where the centers of the cubic faces are occupied by O anions, A cations (12-fold coordination) are located at the corners of the cube, the center of the cube being occupied by a B cation (6-fold coordination) (Figure I.1a). As we will see later, perovskites crystallize as a layered sequence of AO and BO_2 .

The electronic structure and the size of the cations are determinant to understand the perovskite behavior. The richness of this class of materials lies in the combinations allowed for A and B,

broadening the diversity of physical and chemical behaviors, such as electrical insulating, metallic, superconducting, magnetic, piezoelectric etc.

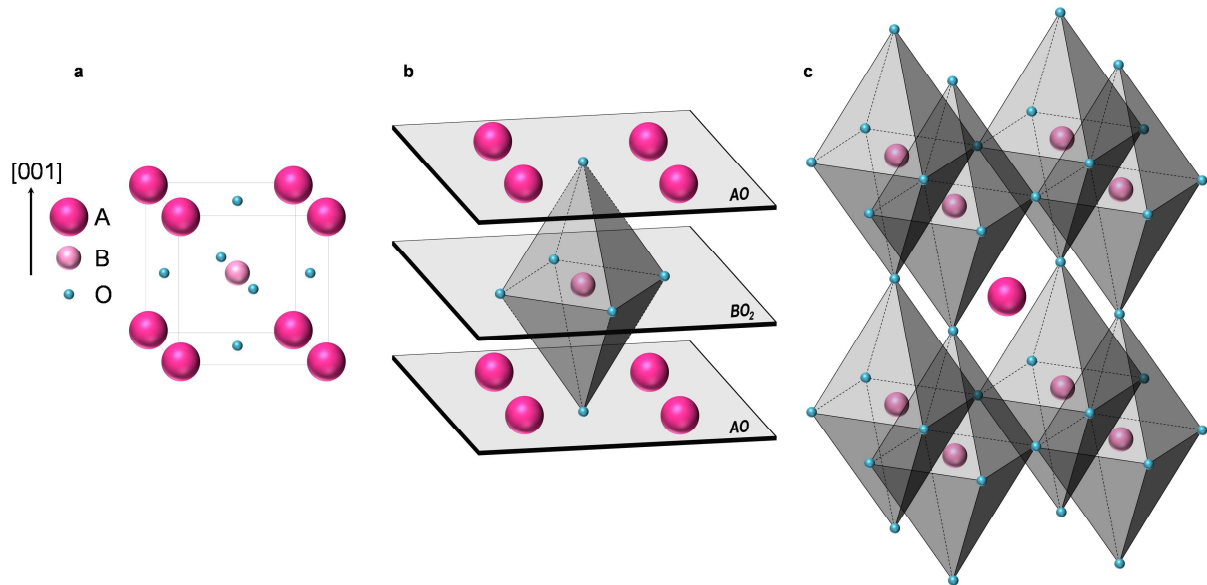


Figure I.1 | Schematic drawing of a perovskite structure ABO_3 . **a**, Cubic unit cell with A cations at its corners, B cations in its center and O anions at the center of each faces. **b**, Perovskite structure viewed as a stacking of alternating AO and BO_2 layers. **c**, Perovskite structure viewed with successive octahedra. A cations occupy the hole created by the O octahedra. The spheres sizes the perovskite atoms are not related to atomic radii. The oxygen octahedral were elongated to visualize clearly the structure.

Most of the perovskite structures do not have an ideal cubic unit cell. The compounds are submitted to crystallographic distortions giving rise to a perovskite polymorphism. The shape and the stability of the lattice are linked to diverse factors, such as the relative ionic radii of cations, their valence, or Jahn-Teller effects as it will be explained later. The first study about these distortions was led by Goldschmidt in 1927, who worked on the orthorhombic $YAlO_3$ and $LaFeO_3$ compounds. Using a purely ionic model, he defined a factor of tolerance, t , to describe the ionic packing from the three ionic radii and predict the structural distortions at room temperature:

$$t = \frac{r_A + r_O}{\sqrt{2} \times (r_B + r_O)}$$

with r_A , r_B and r_O the ionic radii of elements A, B and oxygen, respectively.

The perovskite structure is stable for t values ranging between around 1.1 and 0.8. For $t > 1$, the structure is subjected to hexagonal distortions. It adopts a cubic symmetry when the Goldschmidt factor is equal to unity. Whether the size of A cations is smaller, or that of B cations is larger, the tolerance factor t decreases involving tilting of oxygen octahedra in order to compensate the induced bond stresses, by reducing the size of the cuboctahedral interstice of the oxygen sublattice. First, the crystal system transforms to the rhombohedral system, and then to the orthorhombic one as t is decreasing. This allows the equilibrium of A-O and B-O bonds to be maintained, and induces a break of the cubic symmetry. The tilts of the octahedra modify the B-O-B bond angles, and influence

strongly the coupling of the electron system to the lattice and thus the properties of the bulk material. Thus, according to the t value, it is possible to anticipate the distortions of the perovskite structure, which influence strongly its properties.

The topic of this thesis is focused on two perovskite materials, the lanthanum aluminate (LaAlO_3) and the strontium titanate (SrTiO_3). We can predict the distortions developed by these oxides by calculating their Goldschmidt factor, according to their characteristics found in Table I.1.

$$t_{\text{LaAlO}_3} = \frac{r_{\text{La}} + r_{\text{O}}}{\sqrt{2} \times (r_{\text{Al}} + r_{\text{O}})} \sim 1.01 ; \quad t_{\text{SrTiO}_3} = \frac{r_{\text{Sr}} + r_{\text{O}}}{\sqrt{2} \times (r_{\text{Ti}} + r_{\text{O}})} \sim 1.00$$

Ion	Charge	Coordination	Ionic Radii (Å)
La	+ 3	12	1.36
Al	+3	6	0.535
Sr	+ 2	12	1.44
Ti	+ 4	6	0.605
O	- 2	6	1.40

Table I.1 | Ionic radii obtained from Shannon Database

SrTiO_3 has a Goldschmidt factor closed to unity, and it is well known for having a cubic unit cell. Regarding LaAlO_3 , its structure should be subjected to hexagonal distortions. However, the steric model used by Goldschmidt assumes purely ionic bounds and thus does not take into account crystal field effects or polarisability. Therefore, the factor t should be used only as an indicator of the possible distortions induced.

I.2 SrTiO_3

The strontium titanate must be the most widely used perovskite material. It is associated into a multitude of combinations and comes to be indispensable in the modern all oxides electronic devices, notably due to its properties summarized in Table I.2. SrTiO_3 (STO) crystallizes in a cubic structure at room temperature with a lattice parameter of $a = 3.905 \text{ \AA}$. The overlap of the Ti 3d- t_{2g} orbitals with the O 2p- π ones leads to the formation of an empty π^* -type conduction band (or Ti-3d- t_{2g} band) and a full π -type valence band (or O 2p- π band), separated by a large band gap (3.2 eV, indirect). Pure stoichiometric STO is diamagnetic, paraelectric and a band-insulator with a resistivity over $10^9 \Omega \cdot \text{cm}$, but can be turned to semi-conductor by doping.

SrTiO₃	Properties	Units
	Crystal structure	Cubic
	Space group	$\text{Pm}\bar{3}\text{m}$
	Lattice constant	3.905 \AA
	Density	$5.12 \text{ g}\cdot\text{cm}^{-3}$
	Molar mass	$183.52 \text{ g}\cdot\text{mol}^{-1}$
	Melting temperature	2353 K
	Dielectric constant	300
	Thermal conductivity	$11.2 \text{ W}\cdot\text{m}^{-1}\cdot\text{K}^{-1}$
	Thermal expansion coefficient	$9.4 \cdot 10^{-6} \text{ K}^{-1}$
Band gap (Indirect)	3.2 eV	

Table I.2 | Properties of SrTiO_3 .

Chapter I | State-of-the-art

SrTiO₃ crystals are represented by a stacking of alternating neutral (SrO)⁰ and (TiO₂)⁰ layers in the [001] direction (Figure I.5a).

The STO crystal undergoes phase transitions from a cubic structure at room temperature to lower symmetry ones when the temperature decreases, due to a shortening of the bond lengths. Between 110 K and around 60 K, adjacent TiO₆ octahedra tilt around [001] in an opposite direction from each other along [100] and [010], and STO crystallizes in a tetragonal lattice. From 60 K, the strontium titanate adopts an orthorhombic lattice, and a phase transition to rhombohedral would occur for lower temperatures. These structural distortions are summarized in Figure I.2. These transitions influence strongly the coupling of the electronic system to the lattice [1] and thus the properties of the bulk material.

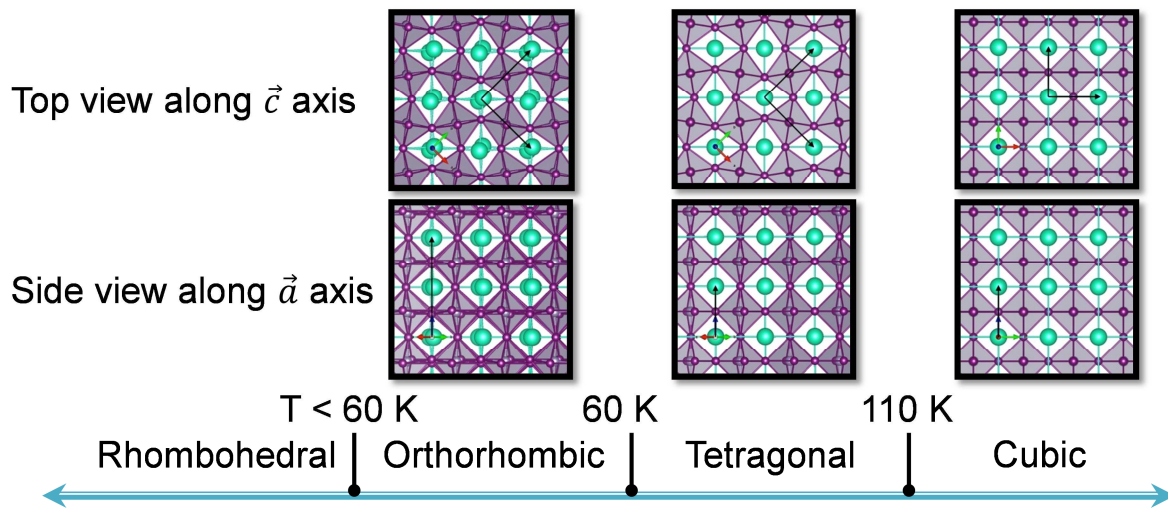


Figure I.2 | STO phase transitions as a function of bulk temperature. Adapted from the X.Gao work presented during the AFOSR Program review in 2015.

In addition to the cation size effect, change in Ti cation valence can imply additional structural changes with deep modifications in STO behavior due to the strong correlation between electrons of neighbor orbitals. The contribution of Sr cations on the electron energy levels of B cations is negligible, hence we have focused our attention on the Ti cations interactions with oxygen anions. Their electronic configuration is as follows:



For an isolated atom, the five d-electron levels of Ti (d_{xy} , d_{yz} , d_{xz} , $d_{x^2-y^2}$, d_{z^2}) have the same energy. In a perovskite structure, Ti is surrounded by six doubly negative oxygen ions in an octahedron environment. The interaction with the three p orbitals (p_x , p_y , p_z) of O provides a crystal field potential which brings a first lifting of the d levels degeneracy (Figure I.3).

The e_g orbitals ($d_{x^2-y^2}$ and d_{z^2}) point directly towards the oxygens, thus their electrons are submitted to a high coulombian repulsion from the electrons of the O orbitals. The t_{2g} orbitals (d_{xy} , d_{yz} , d_{zx}) point between the oxygens and the charge repulsion is weaker, therefore electrons in the t_{2g} orbitals have a lower energy than in the e_g ones.

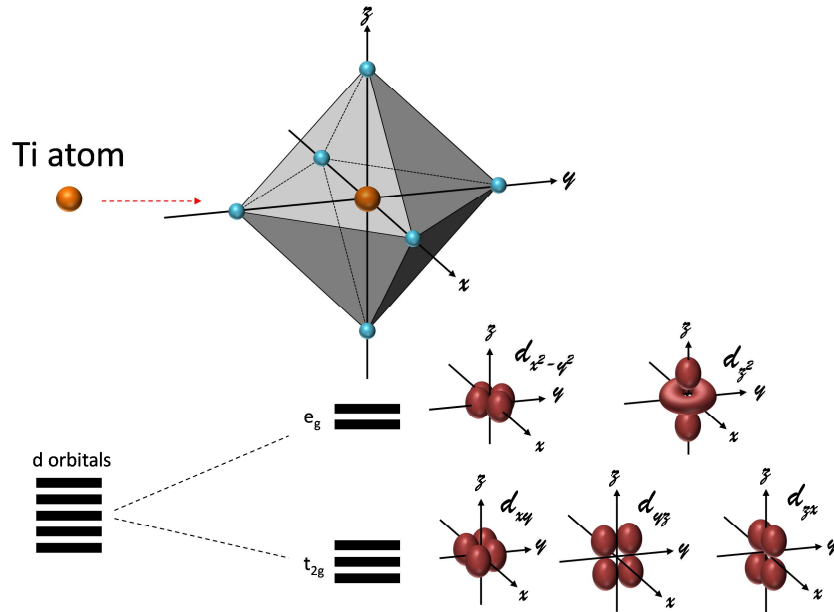


Figure I.3 | Crystal field theory. The octahedron environment provokes a splitting of the d orbitals.

If the first degeneracy has been lifted, the e_g and t_{2g} orbitals are still doubly and triply degenerated, respectively. Yet, Jahn and Teller [2] established that “All non-linear nuclear configurations are therefore unstable for an orbitally degenerate electronic state.”. In other words, when an electron can occupy several orbitals of same energy, the remaining degeneracy is lifted to stabilize the structure, resulting in a contraction (Figure I.4a) or an elongation (Figure I.4b) of the oxygen octahedra, and thus structural distortions.

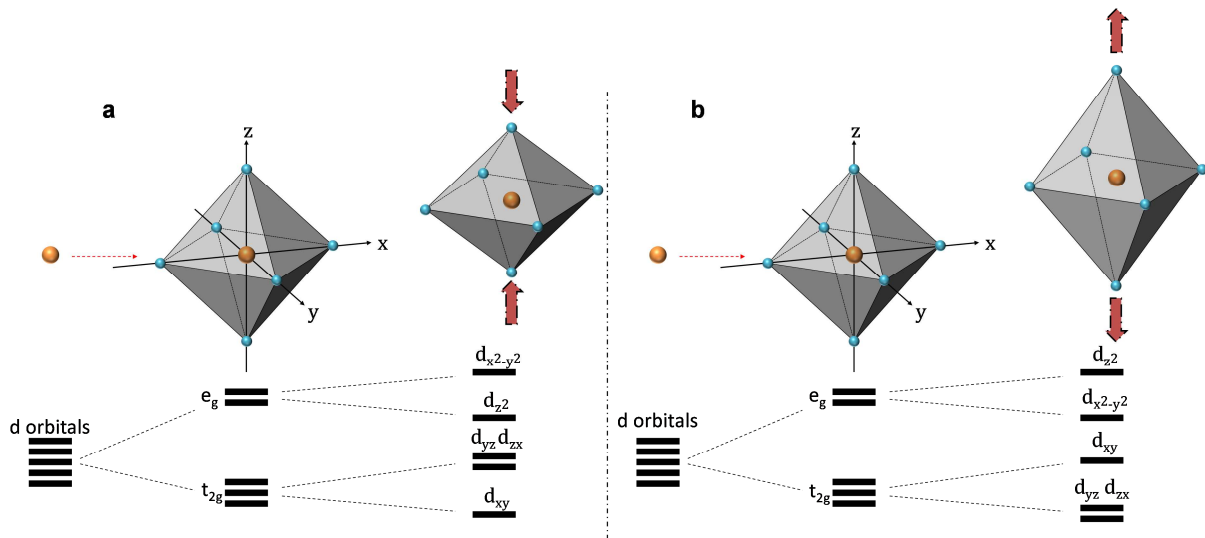


Figure I.4 | Jahn-Teller effect. a, Jahn-Teller effect splits the e_g and t_{2g} orbitals leading to a (a) compression (b) elongation of the octahedron.

In $\text{Sr}^{2+}\text{Ti}^{4+}\text{O}_3^{6-}$, the d orbitals of Ti do not contain electrons, thus there is not lift of the second degeneracy. However, as we will see later, Ti^{4+} is easily reduced into Ti^{3+} , thus a Jahn-Teller contraction of the TiO_6 octahedron is supposed to be promoted [3] and can have major impacts on the electron states in this strongly correlated electron system. Therefore, a particular attention will

be devoted to the cation oxidation state in our system to predict the deformation within the lattice and understand the electrical behavior of the heterostructure.

The large attraction focused on this perovskite is justified by its ability to accommodate a wide variety of point defects, which have been identified as the origin of the wide range of transport properties, notably, going from insulator to superconductor. Donor doping on the Sr sites (for example by La), or Ti sites (for example by Nb), leads to a dramatic change of the electronic properties, by promoting electrons in the conduction band. Extrinsic oxygen vacancies created in reducing environments are also able to produce an insulator-metal transition, by leaving two electrons by vacancy. The control of the conductivity makes STO a good candidate for capacitors, thermistors or Metal-Oxide-Semiconductor Field-Effect Transistor (MOSFET). Moreover, doped STO attracted more attention for thermoelectric devices, since the high effective mass of the mobile electrons provides large Seebeck coefficients. Yet, the greatest attraction for STO in the past decades may be due to the wide possibility of combinations with other oxides materials. The STO single crystal allows a good lattice match with many other perovskite crystals and is chemically inert, it is therefore commonly used as substrate for the epitaxial growth of many functional oxides giving rise to heterostructures with multiple exotic properties. As an example (taken totally randomly), the association of two insulators LaAlO_3 and SrTiO_3 gives rise to electronic conduction. The opportunities for tuning the heterostructure properties have been made possible even more by the ability to control the substrate termination in order to get a complete SrO- or TiO_2 -terminated STO substrates. We will see later that this parameter is primordial regarding the insulator/metal transition at the $\text{LaAlO}_3/\text{SrTiO}_3$ hetero-interfaces.

I.3 LaAlO_3

Lanthanum aluminate is the second part of the heterostructure studied in this thesis. LaAlO_3 (LAO) has a large band gap (5.6 eV, indirect) and is hardly turned into a conductor by doping or defect creation. LAO is a band insulator and is diamagnetic.

LaAlO_3	Properties	Units
	Crystal structure	Rhombohedral
	Space group	$R\bar{3}c$
	Lattice constant	$a = b = 5,365 \text{ \AA}$ $c = 13.11 \text{ \AA}$
	Density	6.52 g.cm^{-3}
	Molar mass	214 g.mol^{-1}
	Melting temperature	2373 K
	Dielectric constant	25
	Thermal conductivity	$11.6 \text{ W.m}^{-1}.\text{K}^{-1}$
	Thermal expansion coefficient	$11.6.10^{-6} \text{ K}^{-1}$
Band gap (Indirect)	5.6 eV	

Table I.3 | Properties of LaAlO_3 .

LaAlO_3 crystals adopt the perovskite structure. Contrary to SrTiO_3 , LaAlO_3 is a polar perovskite alternating positively charged $(\text{LaO})^{+1}$ and negatively charged $(\text{AlO}_2)^{-1}$ layers in the [001] direction (Figure I.5b).

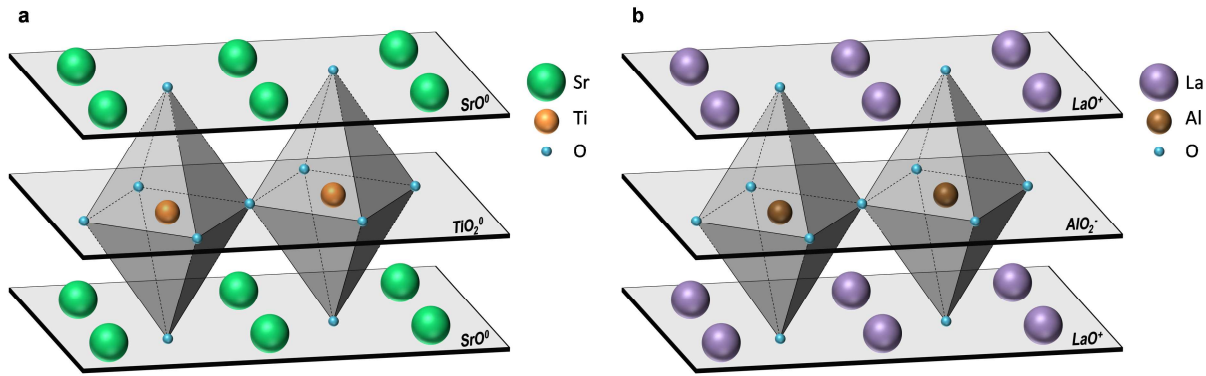


Figure I.5 | Crystalline structure of the studied perovskite. a, SrTiO₃ structure. The crystal consists in alternatively neutral-charged layers in the [001] direction. **b,** LaAlO₃ structure. The layers are alternatively charged positively and negatively in the [001] direction.

At high temperature LAO crystallizes in an ideal cubic structure with a lattice parameter $a = 3.778 \text{ \AA}$ and undergoes a phase transition around 813 K to a rhombohedral structure [4], space group $R\bar{3}m$, due to a slight antiphase rotation of oxygen octahedral around $\langle 111 \rangle$ of the rhombohedral cell (rotation of about 5° at room temperature). Using the related hexagonal unit cell the lattice parameters at room temperature are as follows, $a = b = 5.365 \text{ \AA}$ and $c = 13.11 \text{ \AA}$. However, because of the small tilts of the oxygen octahedral, the LAO crystalline structure will be considered as pseudocubic in this work, with $a = 3.791 \text{ \AA}$ ($\alpha = 90.096^\circ$). No Jahn-Teller distortions are expected for the AlO₆ octahedra due to the absence of electrons in d orbitals ($\text{Al}^{3+} = 1s^2 2s^2 2p^6$).

One of the main interests of the bulk LAO lies in the replacement of SiO₂ in microelectronic chips, the latter being a source of important leakage currents. Hence LAO unit cell, when rotated 45° relative to the silicon unit cell, has a small lattice mismatch allowing epitaxial growth and can be used as a high k gate oxide [5]. The moderate dielectric constant of LAO is attractive for achieving superconducting microwave devices [6], the band gap of LAO and its transparency find applications in optical devices [7], and maybe the most interesting features for this work, LAO shows a good lattice matching with various oxides, such as STO. Hence it can be used as substrate materials for developing heterostructures with specific electric or magnetic properties [7].

In our context, LAO is studied as a thin film deposited on a STO substrate. The misfit between the lattice parameters of the two perovskite is about 2.9%, allowing the formation of heterostructures by epitaxy, that exhibits a wide range of unexpected properties.

I.4 LaAlO₃/SrTiO₃ Heterostructure

The above sections have introduced the STO and LAO as insulators and diamagnetic perovskites. However, when these two compounds are brought together, intriguing new physical behaviors take place at the interface, which are emblematic of hetero-interface behaviors in complex oxides with strongly correlated electrons [8].

I.4.1 Two-dimensional electron gas with high mobility

In 2004, Ohtomo and Hwang [9] discovered a two-dimensional electron gas (2DEG) at the interface between LAO films deposited on STO substrates (illustrated in Figure I.6). This discovery gave rise to a rapid multiplication of publications aiming to elucidate this behavior. The review of the literature

reveals large discrepancies among the community in the electrical characteristics of the hetero-interface, such as charge carrier densities and carrier mobilities. This is mainly due variations in the film growth conditions, underlying how important the control of these parameters is. While the carrier density was reported [10] between 10^{13} cm^{-2} and 10^{17} cm^{-2} , the carrier mobility at 2 K was initially found [9] up to $10^4 \text{ cm}^2 \cdot \text{V}^{-1} \cdot \text{s}^{-1}$ and suggested to be unphysically high.

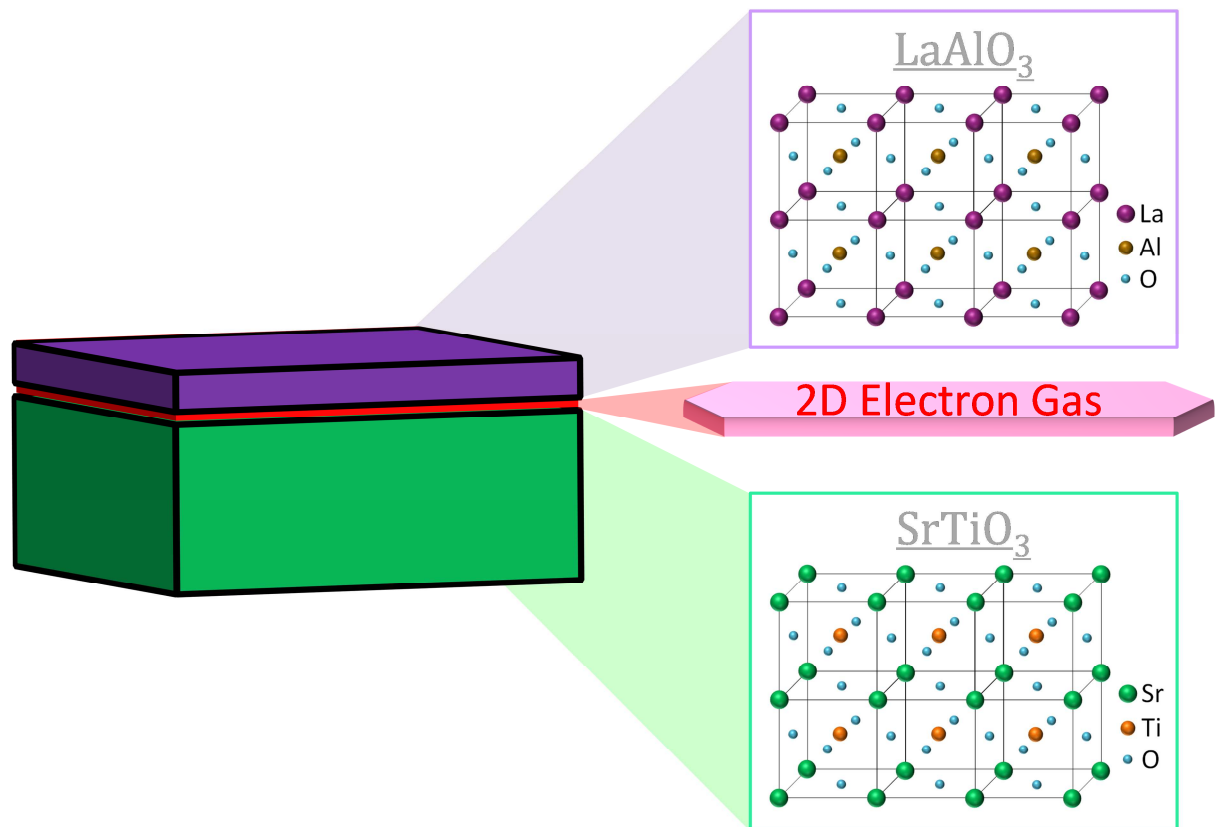


Figure I.6 | Illustration of the bi-dimensional electron gas at the interface of the LAO/STO heterostructure.

I.4.2 Superconductivity

Another exotic property, with no analog in the bulk undoped constituent materials, extends the field of functional application of LAO/STO heterostructures: the superconductivity [11–13]. Reyren *et al.* [11] characterized this behavior by growing films thicker than the critical value, and by excluding extrinsic defects, such as oxygen vacancies. At $\cong 200 \text{ mK}$ and $\cong 100 \text{ mK}$, respectively, the 8 unit cells and 15 unit cells samples underwent a transition into a state for which no resistance could be measured and specific correlation was demonstrated between voltage, current, temperature and magnetic field, as it is illustrated by Figure I.7a. The electron gas condensed into a superconducting phase below 200 mK, independently of the film thickness. Moreover, these authors demonstrated that this superconducting transition is consistent with a Berezinskii–Kosterlitz–Thouless (BKT) transition, characteristics of two-dimensional models. The confinement of the superconductivity to the LAO/STO hetero-interface was confirmed afterwards by the same group [12].

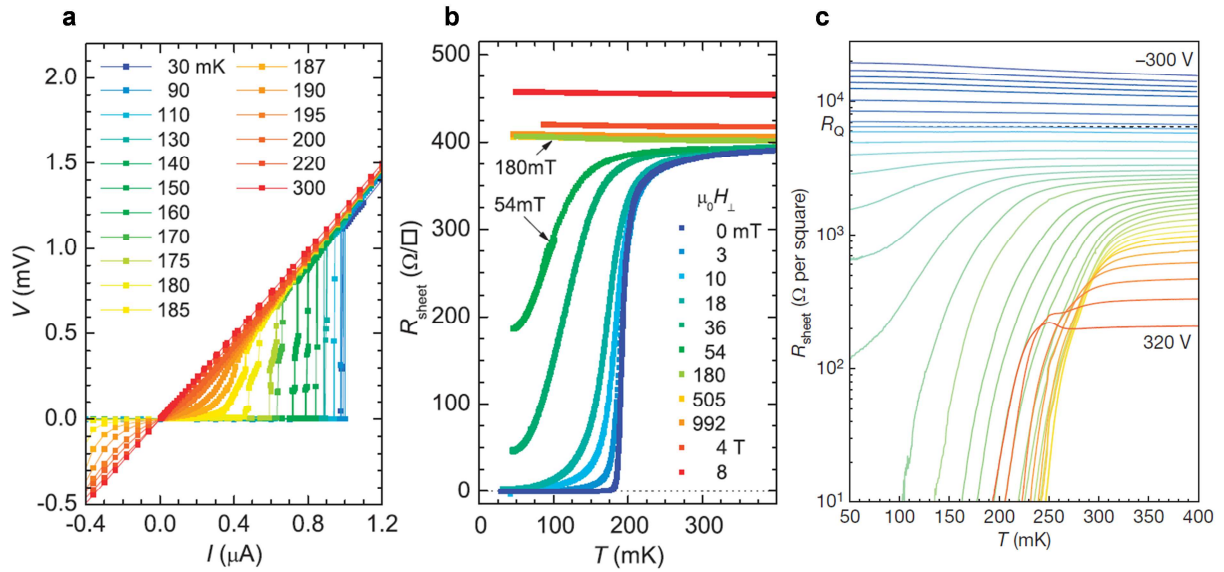


Figure I.7 | Transport measurements of LAO/STO heterostructures characterizing the superconductivity. **a**, Temperature-dependent voltage as a function of the current. From [11]. **b**, Superconductivity tuned with various magnetic fields applying perpendicular to the system interface. From [11]. **c**, Superconductivity tuned by electric field at the LAO/STO interface. From [12].

Figure I.7b and Figure I.7c display the influence of the magnetic or the electrical field on the sheet resistance at low temperatures. It can be seen that the superconductivity can be suppressed by the application of a magnetic or electric field perpendicular to the LAO/STO interface (Figure I.7c). Therefore, the superconductivity can be tuned opening opportunities to new applications.

1.4.3 Magnetism

Interestingly, magnetism properties would occur in the LAO/STO heterostructure, made of two non-magnetic bulks, once the critical thickness of four unit cells is reached [14–17], together with conductivity, suggesting an interplay between electric conduction and magnetism. Brinkman *et al.* [16] led the first experimental work, which revealed magnetism at the LAO/STO system (Figure I.8a and Figure I.8b). They attributed the large negative magnetoresistance at low temperature, and the logarithmic temperature dependence of the sheet resistance, to the spin scattering of conduction electrons at localized magnetic moments. This strong coupling between magnetic moments and the spin of mobile electrons is known as the Kondo effect. This was confirmed by the isotropic magnetoresistance found. These authors revealed likewise a hysteretic behavior of the sheet resistance at 0.3 K (Figure I.8c), indicating a formation of ferromagnetic domains which were characterized by Kalisky *et al.* [15] (Figure I.8d).

However, Reyren *et al.* [11] brought contradictory results since their samples did not exhibit hysteretic magnetoresistance. The superconducting ground state that they discovered should rule out magnetic ordering. Once again, the main distinction between these studies is based on the growth process. While Brinkman *et al.* [16] worked on 26 unit cells thick samples grown at 10^{-3} mbar ($\approx 7.5 \times 10^{-4}$ Torr), Reyren *et al.* [11] deposited 8 unit cells films at 10^{-5} mbar ($\approx 7.5 \times 10^{-6}$ Torr) and then annealed them. Therefore, they did not analyze similar samples, with the same amount of intrinsic/extrinsic defects, with analogous properties, and Kalisky *et al.* [15] highlighted the importance of extrinsic defects as a source of magnetism.

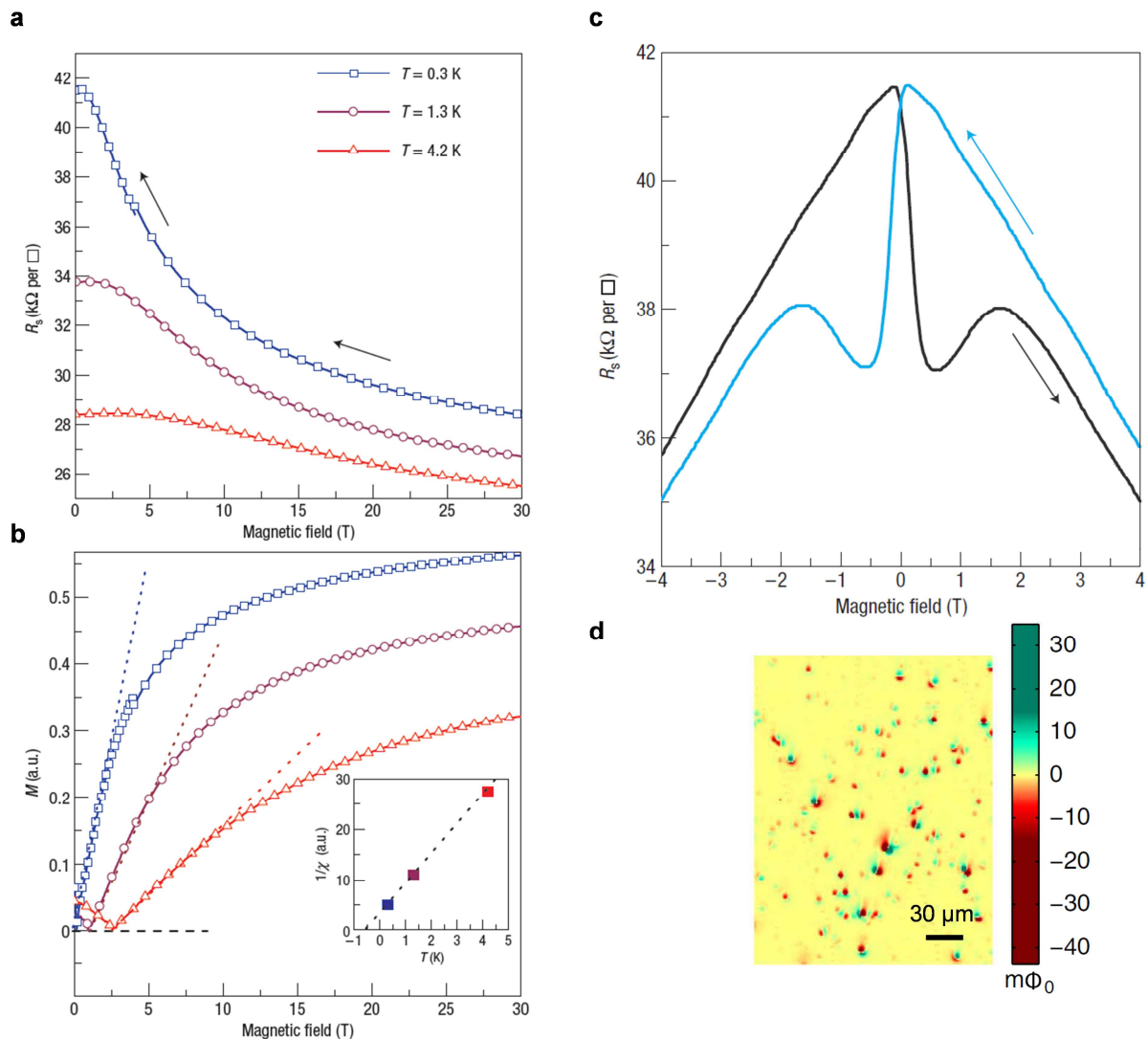


Figure I.8 | Magnetism in LAO/STO heterostructures. **a**, Sheet resistance as a function of magnetic field applied perpendicularly to the interface for various temperature. From [16]. **b**, Magnetization as a function of magnetic field for various temperature. From [16]. **c**, Magnetic hysteresis. From [16]. **d**, Scanning SQUID images showing ferromagnetic evidences of the surface of LAO(10 unit cells)/STO compound. From [11].

The missing consensus in the early literature about the occurrence of low temperature magnetism or superconductivity in the LAO/STO heterostructures [17,18] demonstrates, once again, the importance of growth process parameters to control their behavior and properties, especially in a perspective of applications. However, irrespective to the conduction model proposed, two pre-requirements were rapidly proposed to develop a conducting interface, which are the substrate termination and the film thickness.

1.4.4 Substrate termination

As mentioned previously, STO crystal alternates SrO and TiO₂ layers. STO cleaved surfaces exhibit SrO and TiO₂ terminated domains separated by step of half a unit cell, as it is illustrated in Figure I.10a. Therefore, a LAO film deposited on a STO substrate forms mixed AlO₂/SrO and LaO/TiO₂ interfaces and this was found to be responsible for the deterioration of the conduction properties developed at

the interface [9,19]. Hence, the growth of a single-terminated surface is a prerequisite in order to optimize the electrical behavior. Moreover Huijben *et al.* [19] demonstrated three orders of magnitude difference in the conductivity of pure AlO_2/SrO and LaO/TiO_2 as shown in Figure I.9. Ohtomo & Hwang [9] emphasized that the carrier density decreases significantly and proportionally with the insertion of SrO coverage. The origins of these discrepancies will be discussed in details in the next sections.

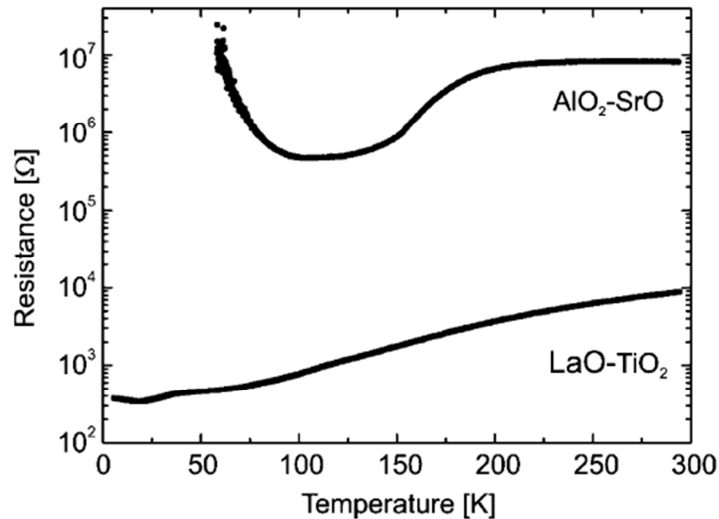


Figure I.9 | Evolution of resistance as a function of temperature for LaO/TiO_2 and AlO_2/SrO interfaces. From [19].

Several methods have been mentioned in the literature [13,19–24] to achieve the AO- or BO₂-terminated substrate.

For TiO₂-terminated surface (Figure I.10b), numerous techniques have been carried out to pick out the SrO sublayers, combining chemical and thermal treatments. SrO is soluble in various acids (e.g. hydrofluoric acid) contrary to TiO₂. Chemical etching is followed by thermal treatments to obtain TiO₂-terminated surfaces with well-defined terrace-step of about 0.4 nm in height [20,24,25]. However, the hazard of HF manipulation, and possible fluorine contamination [23], led to find substitute techniques to prepare the substrate. A mixture of HCl and HNO₃ could be a good candidate to replace HF, but a totally acid-etchant-free technique represents a more attractive perspective. Connell *et al.* [21] developed a thermal-annealing and deionized-water leaching procedure. Sr(OH)₂ compounds are formed at the substrate surface, and desorbed by thermal annealing. These authors showed very recently [26] that structural, optical and mainly electrical properties remain the same between substrates prepared using the water-leaching method and the buffered hydrofluoric acid (BHF) etching method. LaAlO₃ film grown on a TiO₂-terminated substrate results in a LaO/TiO₂ hetero-interface, called n-type interface, and exhibits the highest conductivity.

To obtain SrO-terminated surface, no particular chemical treatments could remove selectively TiO₂ monolayers [9]. However, the issue can be overcome by depositing SrO monolayers on a TiO₂-terminated substrate [9,19], illustrated in Figure I.10c and Figure I.10d. This leads to a AlO₂/SrO hetero-interface, called p-type, which is insulating.

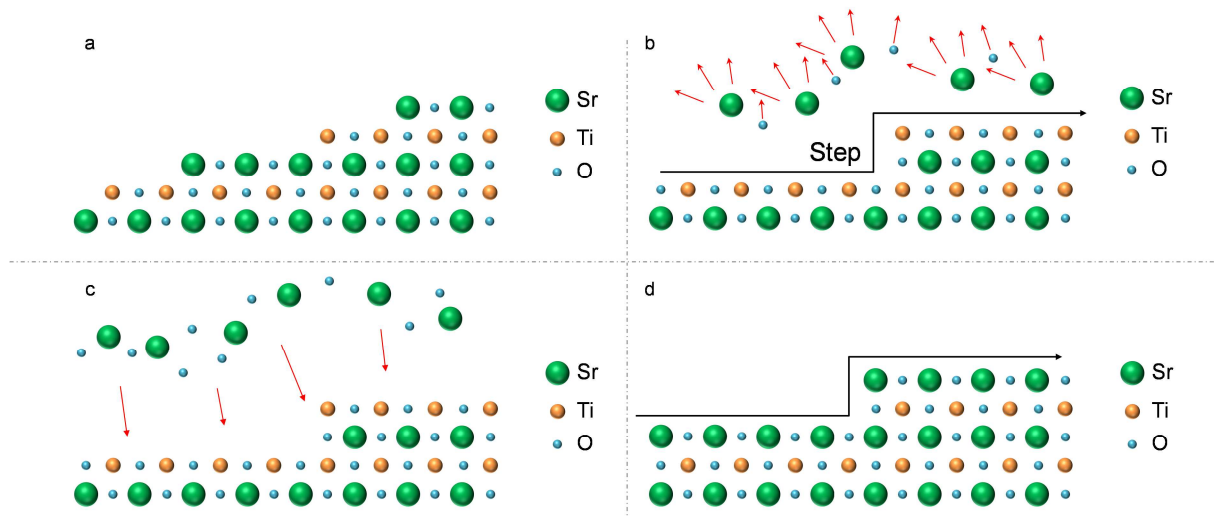


Figure I.10 | SrTiO₃ substrate termination. **a**, Mixed SrO/TiO₂ terminated surface. **b**, TiO₂-terminated substrate. **c**, Deposition of a SrO monolayer on a single-terminated TiO₂ surface. **d**, SrO-terminated substrate.

Attempts to create n-type STO_{film}/LAO_{substrate} mirror heterostructures, made by the deposition of a STO film on a LaO-terminated LaAlO₃ substrate, did not permit to reach the specific behavior of LAO_{film}/STO_{substrate} interfaces. Atomically controlled interfaces are difficult to obtain due to the polar character of LAO that favors surface re-construction and hinders the production of substrates with single terminated surface [19,22]. LaO-terminated surfaces could be obtained by a strict control of the temperature above 250°C [27] but the hetero-interfaces formed were found to be highly insulating [28]. Surface reconstruction during the growth or internal strains was suspected to be responsible for this behavior.

Actually, TiO₂-terminated substrate alone is not the sole parameter required to develop conducting interface; concomitantly, in the absence of external perturbation, a critical thickness of the polar film has to be reached.

1.4.5 Critical thickness

Covering a neutral TiO₂⁰ surface with a LaO⁺ layer induces a polar discontinuity at the interface, and the alternating AlO₂⁻/LaO⁺ layers that follows produces an accumulation of electrical dipole. Therefore the growth of a polar film on a non-polar substrate builds an electrostatic potential that increases linearly with the film thickness. Whatever the mechanism involved in the conduction of LAO/STO heterostructures, the thickness of the film plays a major role. Thiel *et al.* [29] were one of the firsts who established experimentally a striking thickness dependence of the conductivity. They measured the conductivity of several heterostructures with various LAO thicknesses, and they found a threshold at four unit cells (≈ 1.5 nm) deposited (Figure I.11), above which the LAO/STO system becomes electrically conductive. Below this critical value, the heterostructures remained insulating. This result was confirmed by many authors [8,19,30–36].

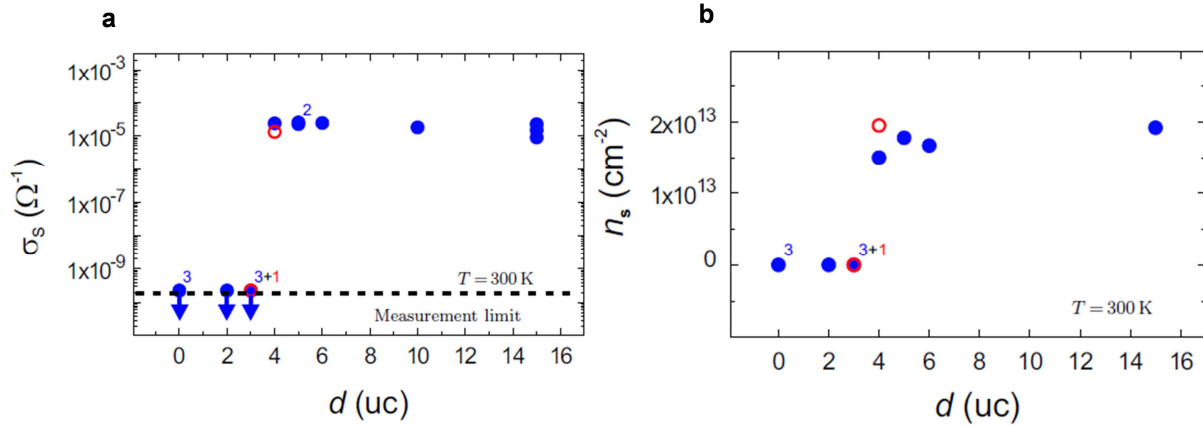


Figure I.11 | Influence of LAO thickness on the electrical measurements of LAO/STO heterostructures. From [29]. (a) Sheet conductance (b) Charge carrier density as a function LAO unit cells deposited on the STO substrate.

Once the threshold is reached, the LAO thickness does not influence the transport properties for most of the studies published [14,29,37,38], whereas for Bell *et al.* [35], increasing the film thickness above the 4 unit cells threshold decreased the sheet carrier density, and the sheet resistance was clearly higher for thicker films.

Nevertheless, over a certain thickness, the LAO/STO heterostructure turns back to insulating. The lattice mismatch between the film and substrate causes an elastic strain in the film and the elastic energy stored increases with the film thickness, up to inducing a periodic delamination of the film that suppresses the conductivity. Our SEM images of Figure I.12 show cracks and decohesions of LAO strips for a 50 nm-thick film. Pseudomorphic films up to a thickness of 22 nm could be obtained by Maurice *et al.* [39]. This upper threshold strongly depends on the process parameters used to grow the heterostructure. Authors found insulators system for a thickness larger than 25 unit cells [40], while others still have measurable electric properties for more than 65 unit cells thick films deposited at lower oxygen partial pressure [9].

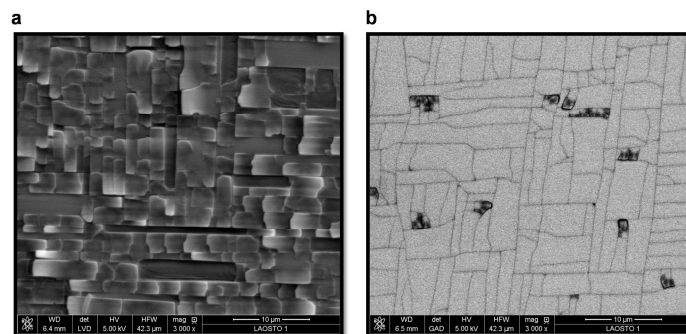


Figure I.12 | SEM Images of a 50 nm-thick LAO film on a STO substrate. a, Decoherence of LAO strips observed in SE mode. b, Cracks in the film observed in BSE mode.

1.4.6 Applications

The effort spending to understand the extraordinary behavior exhibited by the LAO/STO heterostructures is justified by the scientific challenge of addressing strongly correlated systems but

is also imperative for the practical development of reliable devices. Owing to their oxide nature and the pre-supposed confinement of its conductivity, the LAO/STO-based devices concepts are particularly appreciated. The miniaturization of electronic products, the subtle tunability of their response and the ability of using them in extreme environments, explain the growing interest towards possible electronic nanoscale applications. The 2DEG formed at the interface of non-oxide semiconductors are widely used under diverse forms, such as p-n junctions, Schottky diodes, memory devices and high-mobility transistors [8,41,42]. Similar devices are being achieved at the lab scale with oxide based hetero-interfaces, mostly allowed by the reversible switching capacity of the electron gas by using externally applied fields. The control of this confinement enables to conceive new field-effect transistors [30,41–43], with higher miniaturization levels than existing MOSFET. Moreover, an Atomic Force Microscope (AFM) probe applied at the surface of a 3 unit cells-thick film (limit of the threshold thickness), allows to get whether a local metallic interface by applying a positive voltage bias to the AFM tip, whether an insulating interface by applying a negative voltage. This opens up the possibility to build memory-based devices with the capacity to proceed several cycles of writing and erasing [43,44]. Lu *et al.* [42] found an alternative way to obtain such a reversible transformation, taking advantage of the Persistent PhotoConductivity (PPC) effect. Electrons and holes are generated by light illumination using 325 nm and 514 nm lasers. The photogenerated electrons are then trapped in the interfacial potential well, and this induces a lower resistance state. Then, once the light is off the electrons stay trapped at the interface because of the potential barrier to overcome. In order to get back to a higher resistance state, a positive back gate voltage is applied. The energy barrier being lowered, the electrons can refill the localized states and recombine with photogenerated holes [42]. This high nanoscale control allows designing potential barriers junctions [41,43]. Moreover, the exotic low temperature properties, mentioned previously, have also found a great interest for the industrial applications. This review has presented the very intriguing behaviors of LAO/STO heterostructures and proposed possible applications. A technological transfer to all-oxide microelectronic would require a total control of the system properties. Yet the mechanisms responsible for the 2DEG formation are still under intensive debates. We will discuss in the next section the different origins proposed in the literature to explain this behavior.

I.5 Origins 2DEG

An exponential number of articles have been published to understand the origins of this interfacial conductivity with a high electron mobility since its discovery by Ohtomo & Hwang [9] in 2004. Their pioneering work reported the formation of an electron gas with a large charge carrier density at the interface between the LAO film and the STO substrate. This first observation of a metallic sheet formation was attributed to a decrease in valence of Ti cations located in the first unit cell of STO, which will be discussed in details below. However the mechanisms of charge transfer and transport in this system are still not clearly established. Since then, some discrepancies between the charge carrier densities and mobilities predicted by this model and those measured experimentally have been reported [10,19,29,44–48]. This broadens the field of possible mechanisms responsible for the development of this surprising metallic behavior. Other structural and chemical changes have been revealed near the interface, including oxygen vacancies [10,13,19,34,36,44,49–58], cation intermixing [36,49,58–65], the dilatation of STO cells and polar distortions [3,31,34,39,60,66–71] and lanthanum deficiency in the film [37,72–77]. The specific roles of these phenomena in the interfacial conduction are yet not fully understood.

1.5.1 Polar Catastrophe

1.5.1.1 The pristine model

As seen previously, the abrupt polar/non-polar interface and the layer-by-layer growth of LAO induces an accumulation of dipoles and a built-in potential that grows proportionally with the LAO film thickness, as it is illustrated in Figure I.13. This energetically unstable charge distribution leads to the so called “polar catastrophe”. Nakagawa *et al.* [49] proposed a first model to compensate the potential, an electronic reconstruction was assumed to occur, allowed by a sufficient band bending for a charge transfer from (to) the LAO film surface to (from) the first STO unit cell below the interface in the case of a n-type (p-type) interface (Figure I.14).

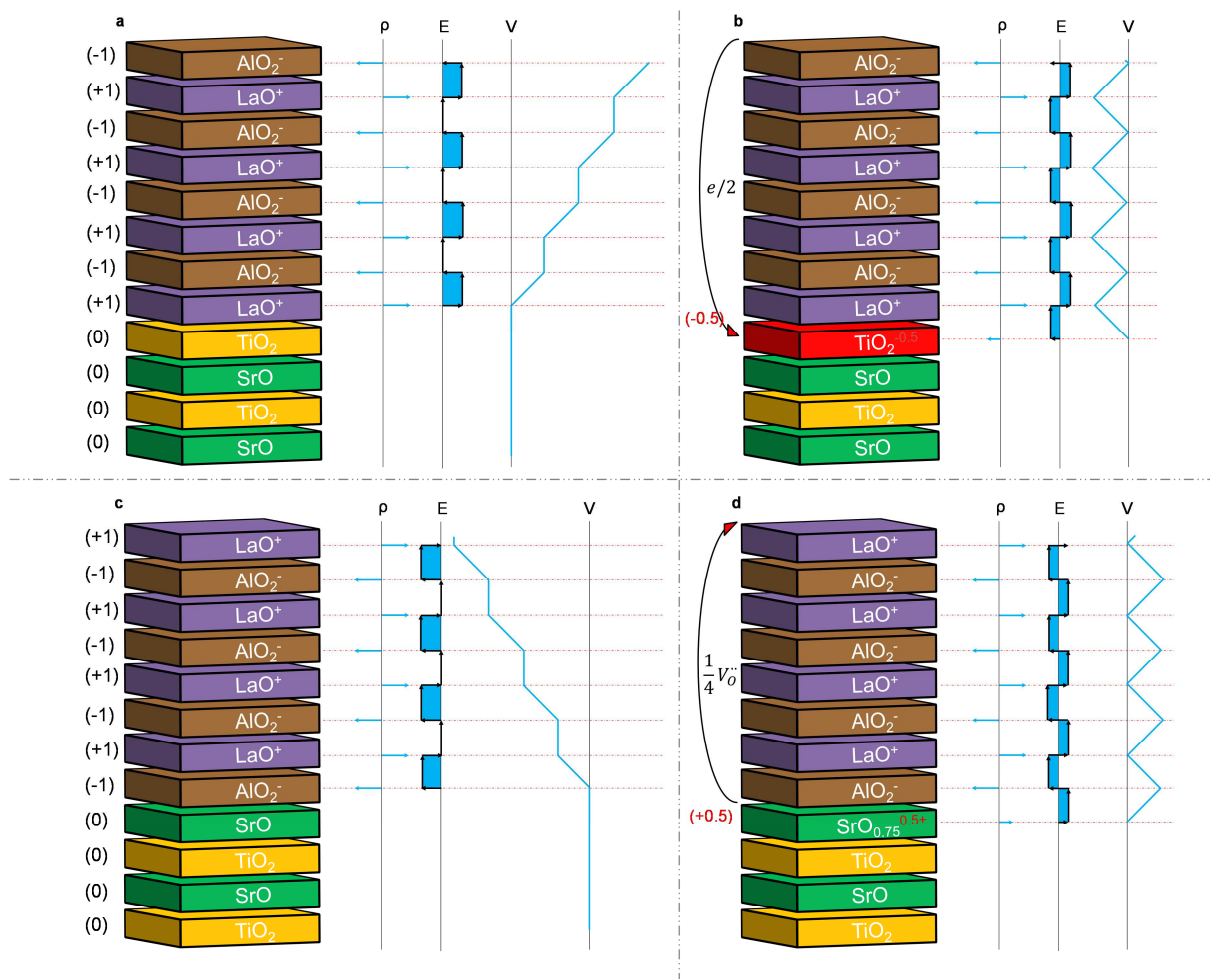


Figure I.13 | Polar Catastrophe models at the atomically abrupt interfaces LAO/STO. **a**, The n-type interface before the electronic reconstruction. The electrostatic potential is growing with the film thickness. **b**, A transfer of half an electron from the top surface to the LaO/TiO₂ interface allows the compensation of the diverging potential. **c**, The p-type interface exhibits a negative diverging potential due to the termination AlO₂⁻ of the LAO film. **d**, The potential build up is compensated by an atomic reconstruction, with the formation of oxygen vacancies providing electron to the surface.

Two interface configurations are found as a function of the substrate termination, as it was mentioned previously. Nakagawa *et al.* [49] suggested that the diverging potential at the n-type interface (Figure I.13a) can be removed with a transfer of half an electron, without the need of

structural changes (Figure I.13b). The remaining electric field oscillates around zero, the electrostatic potential no longer diverges, and the system is stabilized. This electronic reconstruction is possible because of the mixed valence states of Ti (Ti^{4+} and Ti^{3+}), which is energetically more favorable than ion redistribution see for instance when growing polar GaAs on non-polar Si [49]. Therefore, in a purely ionic model, half the Ti atoms at the interface receive one electron on their 3d electronic orbitals, resulting in an oxidation state of $\text{Ti}^{3.5+}$ on average at the interface. In fact, these electrons are not localized but delocalized in $3d_{xy-t_{2g}}$ sub band(s) and available to participate to the conductivity.

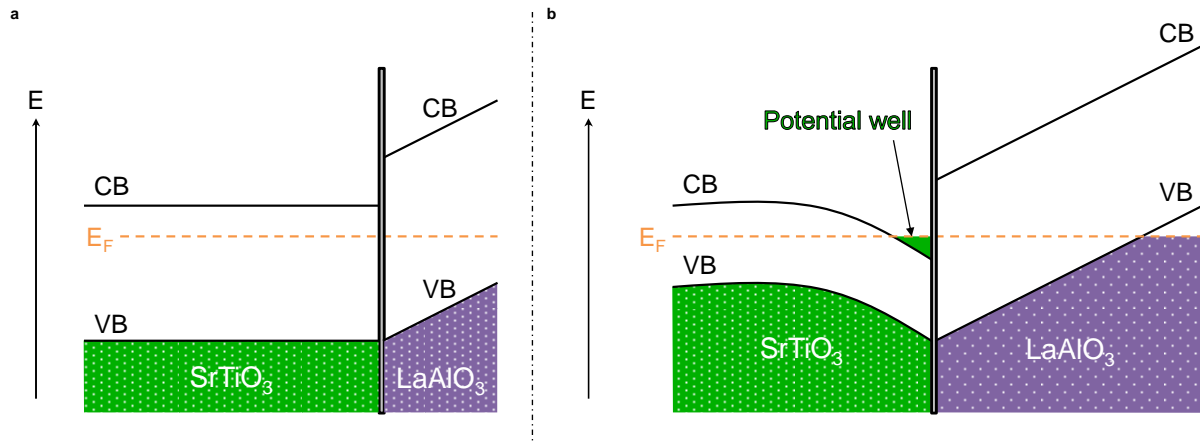


Figure I.14 | Illustration of the band diagram at the interface between the polar film LaAlO_3 and the non-polar substrate SrTiO_3 . **a**, Heterostructure with a film thickness below the critical threshold of 4 u.c.. **b**, Heterostructure with a film thickness above the critical threshold of 4 u.c., leading to electronic reconstruction.

In the case of p-type interfaces, the sign of the polar discontinuity at $(\text{AlO}_2)^-/(\text{SrO})^0$ interface is reversed and should support a 2D hole conductivity (Figure I.13c). The positive charged needed to compensate this disequilibrium at the interface and screen the potential divergence cannot come from a mixed valence states from any of the elements (energetically unfavorable), hence an atomic reconstruction at the interface is required [19,49]. Half an electron is removed from the interface via the formation of an oxygen vacancy ($V_{\text{O}}^{\bullet\bullet}$, carrying a positive double charge) for four SrO at the interface ($\text{SrO}_{0.75}$) (Figure I.13d). This atomic reconstruction does not provide mobile charges and the system remains insulating. It can be seen that the sign of the polar discontinuity is crucial in order to understand the discrepancies in terms of electrical properties between the two types of hetero-interfaces, shown in Figure I.9.

In this model, for both n and p configurations, once the electronic reconstruction has occurred, the potential does not diverge anymore when additional LAO layers are deposited. Because there is no need for supplementary charge carrier injection, the conductivity of the n-type interface should remain similar for any LAO thicknesses above the critical value.

I.5.1.2 Chemical modification of the film surface

This polar catastrophe model was the first mechanism proposed to explain the observed 2DEG at the LaO/TiO_2 interface. It should involve the formation of hole carriers at the film surface, the existence of these carriers could not be demonstrated experimentally [78]. Bristowe *et al.* [79] proposed an alternative model of the electronic reconstruction, based on a chemical modification of the film

surface. The free carriers at the LaO/TiO₂ interface were assumed to originate from redox reactions at the top surface, through the formation of oxygen vacancies [79] or the adsorption of hydrogen on surface oxygen [80]. Ab-initio calculations predict the formation energy of oxygen vacancies at the film surface strongly reduced by the electric field in the LAO film in comparison to their formation in STO sub interface [81], and their spontaneous appearance above 4 unit cell [51]. The positive surface defects created are immobile contrary to the surface mobile holes generated by the previous electronic reconstruction model.

I.5.1.3 Experimental evidence of the polar catastrophe model

Numerous studies attempt to provide experimental evidences of the theoretical polar catastrophe theory by verifying that transport properties were independent of LAO thickness above the 4 unit cells critical thickness [14,29,37,38]. Singh-Balla *et al.* [82] could measure a built-in electric field across the LAO film, which would confirm the theory, by performing tunneling measurements between the electron gas and metallic electrodes on LaAlO₃. Sing *et al.* [83] showed that the Ti 3d band was filled by extra electrons within STO, in accordance with the polar catastrophe theory, by achieving hard x-ray photoelectron spectroscopy (HAXPES). Nevertheless, the charge carrier concentration did not reach 0.5e⁻ at the interface, which was attributed by the authors to surface adsorbates, or polar distortions. The confinement of the conductivity matches also the polar catastrophe theory. Therefore, their work emphasized this scenario as the main driving mechanism for the conductivity at the LaO/TiO₂ hetero-interface.

I.5.1.4 Electron reconstruction below the critical thickness

Yet, more recent studies brought additional clues for a more complex model than the pristine polar catastrophe one. Takizawa *et al.* [48] performed core-level XPS measurements to probe the Ti³⁺ concentration within samples with different film thicknesses. Consistently with the polar catastrophe scenario, an increase of the Ti³⁺ component in the Ti 2p core-level was revealed at the interface for conducting interfaces. However, this Ti³⁺ component was found within samples with a film thickness below the critical threshold of four unit cells suggesting a gradual and continuous charge redistribution, consistently with other studies [44–47]. The observed abrupt change of the transport properties for 4 unit cells films would not only be due to the increase of the carrier density but also to that of the carrier mobility. Xie *et al.* [84] suggest the role of a surface film on LAO made of aligned polar adsorbates, such as water. This film would decrease the potential in the LAO film and allow an electrons transfer from adsorbate surface to the interface below the critical thickness. This would explain the presence of Ti³⁺ at the interface, and the localized charge carrier below four unit cells. Another mechanism of charge redistribution has been proposed by Asmara *et al.* [46] for insulating samples (≤ 3 unit cells), countering partially the polarization, by the transfer of about 0.5e⁻ from AlO₂ to LaO, as a consequence of the buckling of the LaAlO₃ lattice. This charge redistribution does not result in the creation of electrons and holes in the LaO and AlO₂ sublayers but rather an increase of covalence between these both sublayers.

This result questions the role of the built-in potential as the main initiator of electronic reconstruction. The presence of localized charge carrier at the interface below the 4 u.c. critical thickness and mobile above cannot support an electronic reconstruction triggered by a polar divergence since the potential slope would be already minimized below 4 u.c.. The reasons for the insulator/metal transition are still opened and the polar catastrophe theory cannot be considered as the unique driving force for the 2DEG.

I.5.1.5 Other incoherency of the polar catastrophe model

Verbeeck *et al.* [85] studied the oxidation state of Ti atoms at the LaO/TiO₂ interface by EELS measurements. The results undermined the role of polar catastrophe since the Ti valence was found close to +3.8, much smaller than the +3.5 expected from the electronic reconstruction model, and the authors introduced a concomitant effect of lattice distortions, as will be presented later. This result is consistent with previous studies in which the theoretical sheet carrier density of $3.10^{14} \text{ cm}^{-2}$ corresponding to 0.5 extra electrons per unit cell was never reached. Herranz *et al.* [86] focused their work on the orientation of the LAO/STO heterostructures, and the anisotropy of their electrical measurements. While the polar discontinuity at the (100)- and (111)-oriented interfaces (respectively LaO⁺/TiO₂⁰ and LaO₃³⁻/Ti⁴⁺) was able to provoke a conduction through the electronic reconstruction model, the (110)-oriented interface ABO⁴⁺/O₂⁴⁻ shows no polar discontinuity (the charge of the stacking is identical on both side of the interface), and so should stay insulating. Surprisingly, they could find an insulator/metal transition for a film thickness of seven unit cells deposited in the (110) direction. Therefore, they concluded that the polar catastrophe cannot be responsible, as a single mechanism, for the conductivity at the interface of the LAO/STO heterostructure but should rather be considered together with surface reconstruction of the substrate. Liu *et al.* [53] had more tempered conclusions, they measured the sheet resistance dependence on the post-oxygen annealing, in order to understand the role of extrinsic defects. They could show that the oxygen vacancies and polarization catastrophe contribute to the conductivity, as will be explained in the next section. However for oxygen-annealed samples, where all these vacancies are removed, they assumed that the polar catastrophe was the sole origin of interface conductivity.

In summary, the polar catastrophe model was the very first theoretical explanation proposed in order to explain the 2DEG at the LAO/STO interface. Several clues play in favor of this theory, such as the strong influence of the substrate termination on the conduction, the existence of the critical value of four unit cells for the occurrence of the conductivity, or the ability to reversibly generate conductivity by applying a bias at the LAO surface. This mechanism represented the main paradigm, widely spread in the community, to explain the observed transport properties. However, experimental results attest that the proposed simple model cannot be the unique driving force for the observed electrical conduction. Although a Ti³⁺ contribution was identified at the interface of most samples, consistently with the electronic reconstruction picture, the mean valence did not reach +3.5 as predicted by the model. Furthermore, it appeared that SrTiO₃ does not present exclusively ionic bonding, but owns a part of covalent character [79,87]. This results in a polar surface and leads, at least, to lower electronic discontinuity. Finally, the theory does not take into account the influence of growth conditions whereas its strong impact on the structures and properties is now admitted. Therefore, shortly after Ohtomo's major discovery, many authors have minimized or eliminated the occurrence of a polar catastrophe [3,10,13,19,31,33–36,44,51,55,60,61,74,88–91].

I.5.2 *Oxygen vacancies*

One source of carriers proposed to reduce the polar discontinuity at the LaO/TiO₂ interface was the formation of oxygen vacancies close to the substrate surface. The creation of oxygen vacancies by the evaporation of dioxygen provides two electrons per vacancy ($O_0^x = V_0^{\cdot\cdot} + 2e' + 1/2O_2$) that we will first supposed to be delocalized in the potential wedge at the hetero-interface. The formation mechanisms of these vacancies and their impact on the interface conductivity have been investigated by several authors [34,50–54,56,58,92].

I.5.2.1 The process as a source of oxygen vacancies in STO

Different mechanisms were proposed to induce oxygen vacancies, differing from the compensation mechanism involved in the polar catastrophe model for p-type interfaces. The process used to deposit the film on the substrate represents the principal source, since the STO substrate is initially insulating and does not contain such defects. Pulsed laser deposition (presented in more details further), which is the commonly growth method used, involves physical reactions between a laser, a target, a plume and a substrate. Several authors [10,34,56,58] put forward that oxygen vacancies would originate from the impingement of the high energy particles during the deposition process, or from chemical reactions with the ablation plume [54]. The oxygen partial pressure in the PLD chamber is pointed out as a major parameter to control the vacancy concentration, as it will be discussed in the next chapter. These positively-charged defects can be created by different external ways such as an annealing of the stoichiometric substrate at 800-1400°C in vacuum or in hydrogen [50], or by an Ar-ion bombardment [19,50]. Suwanwong *et al.* [57] could promote oxygen vacancies at the surface of STO (without LAO film) by an UV irradiation. Cleaving STO in ultra-high vacuum was also seen to produce a massive removal of surface oxygen and the formation of a 2DEG [93].

All these studies have furthermore underlined the role played by oxygen vacancies in the insulator/metal transition of the hetero-interfaces, or even of the sole STO surface in the two last works cited.

I.5.2.2 Oxygen vacancies and electrical conduction

Siemons *et al.* [56] in their early work followed the valence change from Ti^{4+} to Ti^{3+} by *in-situ* UPS as the oxygen pressure was lowered, together with a localized increase in charge carrier density at the LAO/STO hetero-interface. This suggested a strong dependence of the electrical conductivity of the heterostructure to the oxygen partial pressure used during the PLD growth. This point will be investigated in Chapter II.

Recent reports [34,54] demonstrated that conduction was dominated by a vacancy doping mechanism at oxygen partial pressures of around 10^{-4} Torr. Such conditions of growth gave rise to conducting interfaces for films with a thickness of 2 or 3 unit cells [34,54], which is below the critical thickness. This conductivity below 4 unit cells was eliminated by post heat treatments in oxidizing atmosphere, emphasizing the importance of these extrinsic defects (Figure I.15f). Kalabukhov *et al.* [50] observed a conductivity in LAO/STO heterostructures deposited at 10^{-4} mbar ($\approx 7.5 \times 10^{-5}$ Torr), which was not observed in a STO substrate treated at the same pressure condition. This suggests the specific role of the interface, more than a contribution of the bulk STO, for such growth conditions.

At partial pressure of 10^{-6} Torr, the substrate color changes from transparent to gray/black and blue light is emitted by cathode luminescence, which are characteristics of oxygen-reduced STO [50]. The vacancies are spread out in the bulk of the substrate and the conductivity is three dimensional. This three dimensionality of the conduction was confirmed by others authors [34,51,92], and could explain the unphysical “sheet” carrier densities measured originally by Ohtomo at this oxygen partial pressure [9]. This migration of the oxygen vacancies in the bulk can be predicted from their relatively high coefficient of diffusion D_v measured in STO. At 750°C for example, $D_v \approx 10^{-5}$ - 10^{-4} cm²/s [52,94], which allows migration over hundreds of microns during a duration of growth of about 10 s ($\ell \approx \sqrt{D_v t}$). Basletic *et al.* [92] mapped experimentally with a conducting-tip atomic force microscope, the extension of the mobile carriers on cross-sectional samples, and confirmed an extension of a high

mobility electron gas over 600 μm into the substrate for sample grown at $p_{\text{O}_2} \leq 10^{-5}$ mbar ($\approx 7.5 \times 10^{-6}$ Torr), $T = 750^\circ\text{C}$ (Figure I.15b). In all cited experiments the 3D conductivity vanished after post annealing in oxidizing atmosphere (Figure I.15).

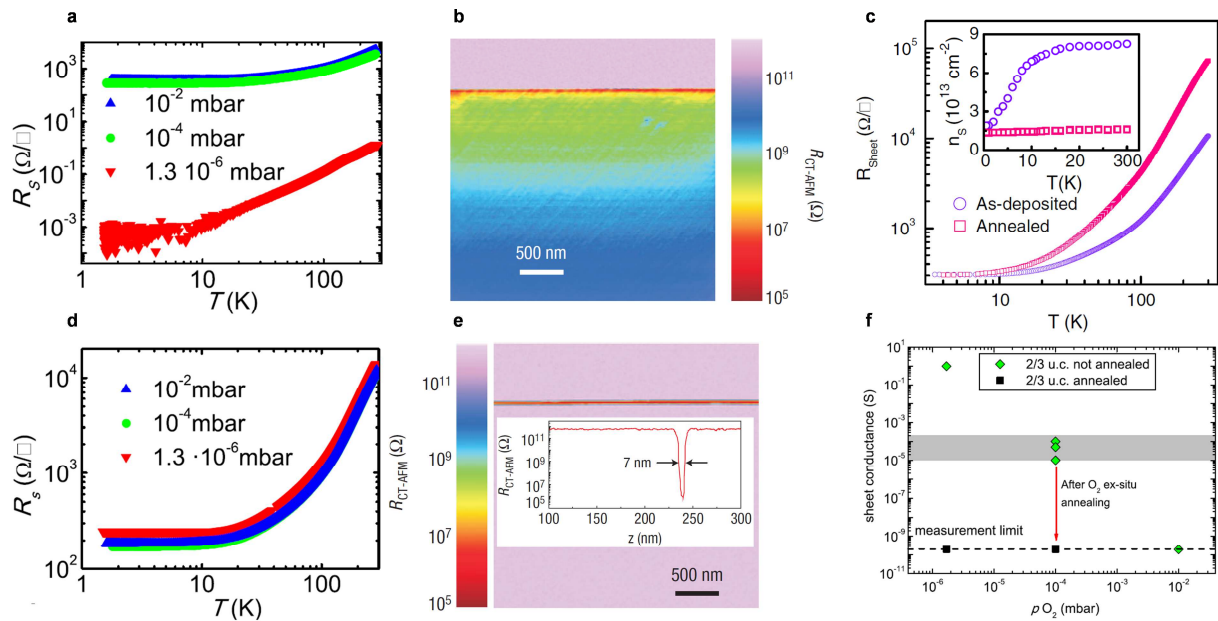


Figure I.15 | Transport properties of LAO/STO heterostructures as a function of oxygen-annealing process. **a**, Measurements for samples grown at various p_{O_2} before annealing. From [34]. **b**, CT-AFM resistance map for a sample prepared in reducing conditions. The conductive region extends through several micrometers. From [92]. **c**, Comparison of sheet resistance between annealed and as-deposited samples. The sheet resistance increases clearly once the sample is annealed. Inset shows that the charge carrier density collapses for annealed samples but they remain conductive. From [53]. **d**, Annealed samples compared to a. Samples with various oxygen pressure displayed similar sheet resistance after removing the oxygen vacancies. From [34]. **e**, CT-AFM resistance map for a sample annealed in oxygen. The conductive region is significantly reduced. From [92]. **f**, Sheet conduction evolution for various oxygen pressures of 2-3 unit cells samples annealed and non-annealed. From [34].

For growth at partial pressure of 10^{-2} Torr, the post-annealing did not modify the electrical behaviors of the samples [34] (Figure I.15d), which were conducting above 4 unit cells and insulating below. A growth at 10^{-3} mbar ($\approx 7.5 \times 10^{-4}$ Torr) was also reported to allow this clear transition [45]. In the same way, specimens grown between 10^{-6} and 10^{-2} Torr and post annealed in oxidizing atmosphere exhibit the same behavior with insulating/conducting transition for 4 unit cells [51]. In these last examples the conduction is no more driven by oxygen vacancies.

In summary, an oxygen vacancy scenario can be proposed at low oxygen partial pressures, and specific influence of the film deposition in the vacancy concentration below the interface is highlighted at medium partial pressure. However this scenario cannot explain the conductivity observed from 4 unit cells after annealing, nor the determinant role of the substrate termination.

1.5.3 Intermixing

After the 2DEG in LAO/STO was just being discovered by Ohtomo *et al.* [9], the first following publications commonly admitted that the interface was abrupt, i.e. without exchanges of cations between the film and the substrate. Nakagawa *et al.* [49] first assumed that the interface should not be abrupt. Numerous studies, using a combination of various techniques, confirmed the intermixing in the LAO/STO heterostructures. As $\text{La}_x\text{Sr}_{1-x}\text{TiO}_3$ is known to be conductor for a wide range of x [95], the intermixed layer was put forward as partially responsible for the conductivity. Two driving forces for this intermixing have been proposed, the physical deposition method used and a dipole compensation mechanism.

During a PLD film deposition, the energetic deposition flux of the pulsed ablation plume induces a drastic non-equilibrium defect structure in the substrate near surface, involving both oxygen and cation species. Implantation of film atoms into the substrate has been reported [61,65,96], as well as the filling of Sr^{2+} vacancies by La^{3+} [36].

The Ti valence measured in the first TiO_2 layer of STO could not support an electron reconstruction model confined to the first u.c.: the mobile electrons must be delocalized over several u.c. below the interface. This spreading of the charge carriers increases the interface dipole energy. A compensating dipole can be introduced by exchanging Sr^{2+} for La^{3+} cations across the interface [49].

Both proposed driving forces for intermixing have found contradictors. Willmott *et al.* [60] described an asymmetric A and B cation intermixing in their LAO/STO structure grown at 5×10^{-6} mbar ($\approx 3.8 \times 10^{-6}$ Torr) as seen on Figure I.16a. Al intermixed with Ti at shallower depths than La does with Sr, resulting in the formation of the compound $\text{La}_x\text{Sr}_{1-x}\text{TiO}_3$ on one or two monolayers. However the kinetic disruption caused by impinging deposition flux on the substrate should imply a deeper diffusion of Al than La, considering the size of A- and B-cations. This would rule out the mechanism of PLD deposition advanced as the main driving force of intermixing, consistently with conclusions of a distinct report [97]. Qiao *et al.* [64] assumed, in agreement with their calculation, that intermixing systematically occurs between a LAO film and a STO substrate. They explained this phenomenon by the thermodynamic instability met by an abrupt interface, as well as the reduction of the dipole created at the polar/non-polar interface. Mizoguchi *et al.* [98] contradicted the dipole compensation mechanism by analyzing non-polar heterostructures, $\text{BaTiO}_3/\text{Nb-doped SrTiO}_3/\text{SrTiO}_3$, with various techniques such as STEM, EDS, EELS, which will be described in the next chapter, and first-principles calculations. Barium was seen to diffuse into the Nb-doped STO in absence of any polar discontinuity. They proposed another mechanism to explain this diffusion based on formation and migration of Sr vacancies. The donor doping increased the Fermi level of STO which in turn decreased formation energy of the Sr vacancies, the latter being filled by a Ba cation.

The next paragraphs will present in more detail intermixing investigations carried out by several techniques with a particular focus on Medium Energy Ion Spectroscopy (MEIS), as this technique, together with electron microscopies, was the principal analytical tool of this thesis work. The advantage of MEIS is provided by the high energy loss of medium energy ions. They can probe the samples sub surface with an excellent depth resolution, better than the dimension of the perovskite unit cell, which is required for our problematic. We will bring more precision about this technique in the second chapter.

Kalabukhov *et al.* [36] realized MEIS analyses coupled with scanning Kelvin Probe Force Microscopy (KPFM) to characterize the cation intermixing in LAO/STO heterostructures elaborated at 10^{-4} mbar ($\approx 7.5 \times 10^{-5}$ Torr), varying from each other by their film thicknesses. Two distinct beam alignments were used with respect to the crystal orientation. They recorded spectra in “channeling mode”, aligning the incident ion beam along the [001] direction of the substrate, in order to record backscattered ions only from atoms situated at the top surface. Then, the “random mode” was chosen to avoid any particular crystallographic direction, with backscattered centers could be atoms located from the top surface to several u.c. below the interface. For an abrupt interface, a one unit cell-thick film, with La cations situated solely in the film at the top sample surface, should give rise to similar La contribution for spectra in channeling or random mode. However, as it is shown in Figure I.16b, the La peak, between 85 keV and 89 keV, is larger in the random mode, suggesting that La diffused into the substrate. Concerning the Sr cations, Figure I.16c presents the MEIS spectra between 82.5 keV and 85 keV obtained in channeling mode for film thicknesses between one and four unit cells. The Sr peak starts at similar energy for all thicknesses, indicating that Sr atoms diffused up to the film surface for all the films. The total count number in Sr signals decreased for thicker films revealing that the top surface contained less Sr as the thickness was increased. The intermixing was confirmed by KPFM which also revealed inhomogeneities in the surface potential with characteristic sizes of 100–1000 nm. Inhomogeneous compositional and, thus, “filamentary” interdiffusion were suggested. These MEIS results gave an insight into the chemical profile of LAO/STO heterostructures, but remained qualitative and comparative, without simulation of the spectra. Yet, the same authors confirmed the intermixing between La and Sr in a later work [63], suggesting that this cationic exchanges could be one contributor for the conductivity.

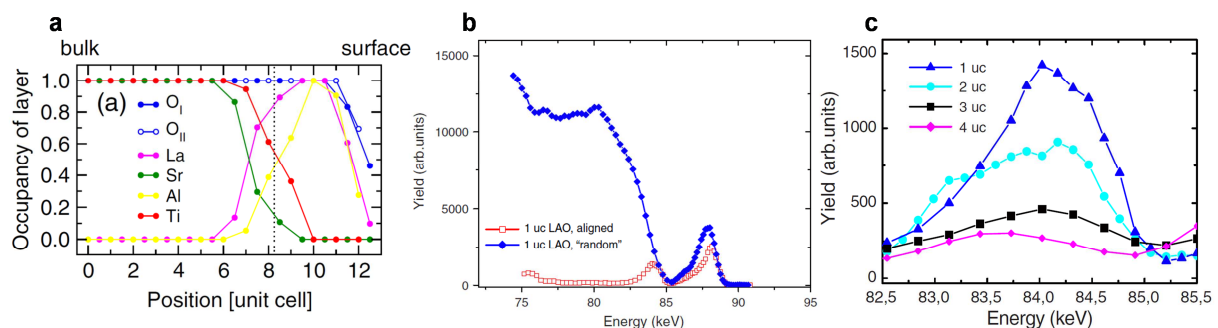


Figure I.16 | Intermixing characterizations. **a**, Chemical profiles with atomic resolution from structure refinement of SXR data (synchrotron radiation $\lambda = 0.775$ Å) determined from [60]. **b**, Comparison between MEIS spectra taken in aligned and random mode from LAO(1 uc)/STO sample. From [36]. **c**, MEIS Sr peaks from samples varying by their film thickness and recorded in channeling mode. Adapted from [36].

Chambers *et al.* [61] used also MEIS to characterize samples coming from two different laboratories. We will focus here on their study of a 4 unit cells film grown at about 10^{-5} mbar ($\approx 8 \times 10^{-6}$ Torr). Unlike the previous publication, MEIS spectrum simulations for abrupt and intermixed interfaces were provided (Figure I.17). The intermixed heterostructure allows clearly a better fit of the experiment, as seen in Figure I.17a. The broader La and Al peaks indicate that these atoms were located deeper than for an abrupt interface. Figure I.17b provides evidences of Sr and Ti diffusions up to the film, since the experimental edges for Sr and Ti were seen before what is expected for a substrate buried below the film with an abrupt interface.

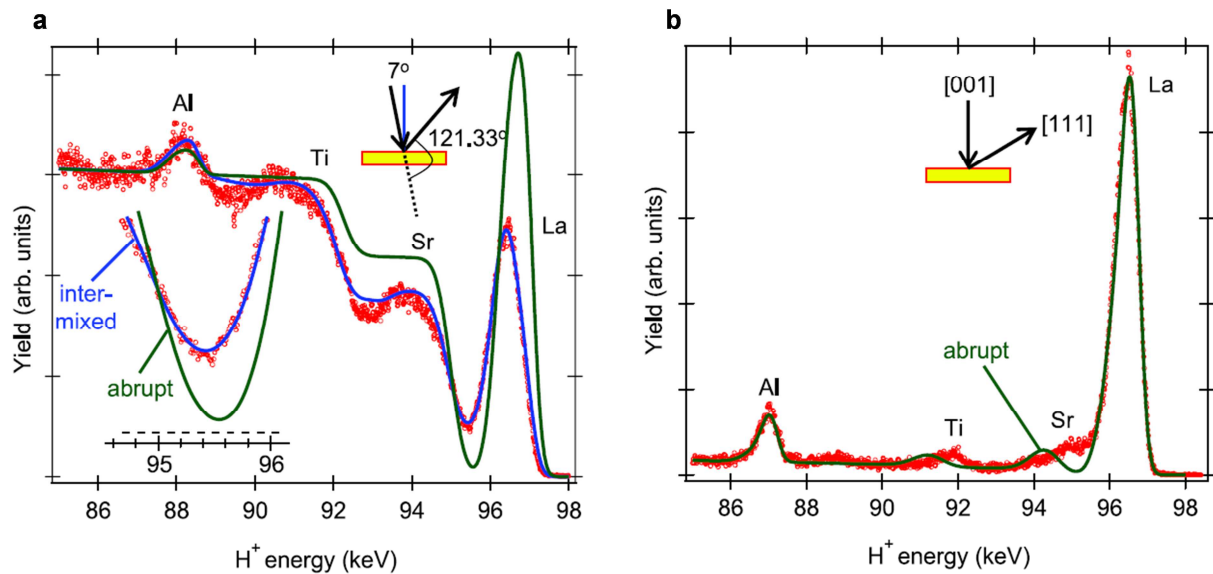


Figure I.17 | MEIS experimental spectra using H^+ particles with an energy of 99 keV. a, Random mode spectra on a sample with a film thickness of four unit cells. **b,** Aligned mode spectra on a sample with a film thickness of four unit cells. From [61].

Chambers *et al.* [61] crosschecked by multiple techniques in addition to MEIS the extension of this intermixing. Using Rutherford Backscattering Spectrometry (RBS), Time-of-Flight Secondary Ion Mass Spectrometry (ToF-SIMS), High-Angle Annular Dark Field Scanning Transmission Electron Microscopy and Electron Energy Loss Spectroscopy (HAADF STEM/EELS), and Angle-Resolved X-ray Photoelectron Spectroscopy (ARXPS), they established the occurrence of intermixing in the LAO/STO heterostructures over few unit cells from either side of the interface. In contrast with the previous report [60], here A-sites and B-sites cations were considered to diffuse over the same length.

More recently, Salvinelli *et al.* [62] performed Angle-Resolved X-ray Photoelectron Spectroscopy (ARXPS) on a 5 unit cells (conducting) and a 3 unit cells (insulating) films deposited at 10^{-3} mbar ($\approx 7.5 \times 10^{-4}$ Torr) and on a 5 unit cells (insulating) film deposited at 10^{-1} mbar ($\approx 7.5 \times 10^{-2}$ Torr). Intermixing was revealed for the three heterostructures, but to a different extent (Figure I.18). The 5 unit cells conductive sample exhibited the largest cation exchanges with a diffusion length of the film cations over four unit cells into the substrate, and Ti diffused up to the first unit cell of the film above the interface (Figure I.18a). For the 5 unit cells insulating sample grown at a higher oxygen pressure the film species diffusion length is reduced, but still observable (Figure I.18b). Hence, the cationic disorder seemed to be enhanced by increasing the oxygen pressure. For the 3 unit cells sample, elaborated at the same p_{O_2} as the conductive sample, the intermixing was found to extend over the shortest distance. It is interesting to note that Sr atoms were barely found within the film, and the La diffusion was never compensated. This would suggest that Sr vacancies were present within the substrate, leaving free sites for La cations diffusion. Therefore, intermixing was underlined for all samples, conductive and insulators, with a larger diffusion of La cations in the conducting sample. Hence the donor-doping is extended, and expected to contribute, at least partially, to the conductivity.

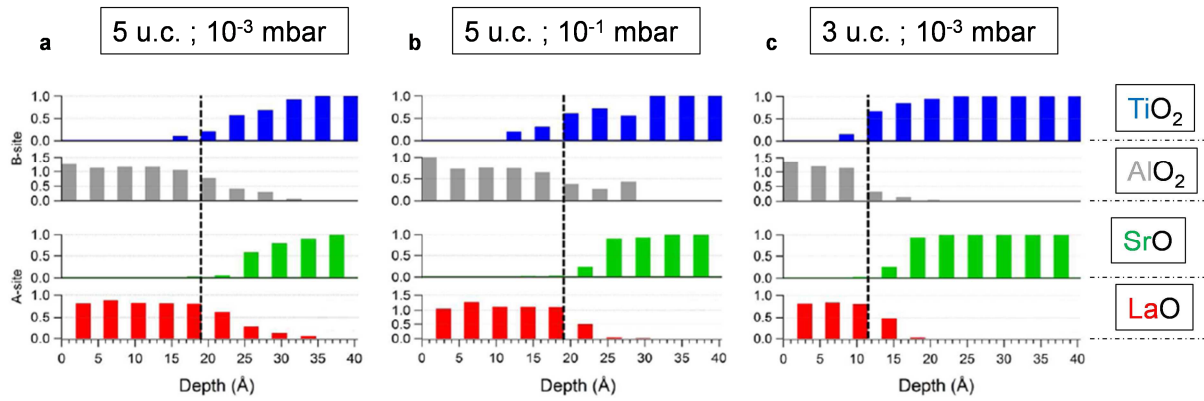


Figure I.18 | Cations occupancy and content around the LAO/STO interfaces. **a**, Conductive sample with a film thickness of five unit cells deposited at 10^{-3} mbar. **b**, Insulating sample with a film thickness of five unit cells deposited at 10^{-1} mbar. **c**, Insulating sample with a film thickness of three unit cells deposited at 10^{-3} mbar. Blue data displayed for TiO_2 , Gray data displayed for AlO_2 , Green data displayed for SrO , and Red data displayed for LaO . From [62].

We could keep going on quoting others reports in which the intermixing was experimentally shown [34,59,64,65,69], providing evidences that the interface between LAO and STO is not abrupt but consists in a graded composition of elements from the heterostructure.

If cationic exchanges seem to contribute to the conductivity, does it represent the main mechanism at the origin of 2DEG? All the available elements seem to diverge from such conclusions. As it was just mentioned above, Kalabukhov *et al.* [50] and Salvinelli *et al.* [62] highlighted intermixing in insulating samples, for film thicknesses smaller than the critical threshold of four unit cells. Furthermore, although p-type interfaces show no conduction, Yamamoto *et al.* [71] found cationic diffusion in such samples. Hence it is quite hard to believe that the cationic exchange is the triggering mechanism for electronic conduction. This doubt was shared by others authors [58,97,99] who advanced, either that the compound formed from a mixed composition of LAO and STO ($\text{La}_x\text{Al}_y\text{Sr}_{1-x}\text{Ti}_{1-y}\text{O}_3$) stays insulating [58,99], either cation intermixing could be minimized during the deposition, without precluding conduction [97]. Even though it seems questionable that intermixing could be the driving mechanism for an interface conduction as a sole doping effect, numerous works reported [60,62,69,100,101] its effects on the structural order of the heterostructure.

1.5.4 Structural Distortions

Despite the ambiguous role played by the cationic intermixing, ionic vacancies or polar discontinuities within the LAO/STO heterostructures, these phenomena are most of the time coupled with structural distortions. We will now discuss the influence of strain and structural distortions on the transport properties at the LaO/TiO_2 hetero-interfaces.

1.5.4.1 Effect of strain in perovskites

The effect of strain on the electron conductivity of perovskites and perovskite-based heterostructures has been reported by many authors using various experimental methodologies or theoretical models [5,102–105]. All conclude that strain affects the conductivity in these strongly correlated systems, through a modification of the electron effective mass and/or the density of states in the lower conduction bands. Strain induces a splitting of these bands, modify their

curvature or ranking. Due to the complexity of the mechanisms involved we will focus this review on the LAO/STO systems

I.5.4.2 Effect of epitaxial strain

We have seen in the previous section that the lattice parameters of LAO ($a = 3.791 \text{ \AA}$) and STO ($a = 3.905 \text{ \AA}$) differ slightly resulting in a lattice mismatch of about 2.9%. As the pseudomorphic growth was determined experimentally by several authors [39,70,88], the in-plane lattice parameters of the film fit that of the substrate, implying a contraction of the out-of-plane lattice parameter of the film. Numerous reports investigated further the influence of the epitaxial strain on the electrical properties [66,70,88,91]. Annadi *et al.* [66] grew various polar perovskites on STO substrates under the same conditions, with similar oxidation state and polar stacking layers in the [001] growth direction as for LAO. The analyzed combinations (and lattices mismatches tabulated by Moreira *et al.* [106]) are as follow, $\text{LaAlO}_3/\text{SrTiO}_3$ (2.9%), $\text{NdAlO}_3/\text{SrTiO}_3$ (3.9%), $\text{PrAlO}_3/\text{SrTiO}_3$ (3.8%) and $\text{NdGaO}_3/\text{SrTiO}_3$ (1.6%). At 300 K, the larger is the lattice mismatch, the larger is the in-plane tensile strain in the film and the weaker is the carrier density (Figure I.19a). Concerning the carriers mobility (Figure I.19b), μ , they were similar at 300 K but a strong dependency towards lattice mismatch was highlighted at 2 K, with μ decreasing for larger mismatches. Adding to these analyses, very recently Huang *et al.* [107] provided evidences of the influence of lattice mismatch on the transport properties. By replacing the LaAlO_3 by $\text{La}_{0.3}\text{Sr}_{0.7}\text{Al}_{0.65}\text{Ta}_{0.35}\text{O}_3$ (LSAT) which is also a polar perovskite insulator and exhibits closer lattice parameters in a cubic symmetry, they pointed out the role played by the strain mechanism. The authors linked the weaker lattice mismatch, with STO (1.0%) compared to LAO (2.9%), to the enhancement of the conductivity. The break of the symmetry, as well as the octahedral distortions induced by the lattice mismatch would result in a degradation of the carrier mobility [107]. Therefore, all these authors shed light on the control of the conductivity by both interfacial strain and the electronic correlations.

Bark *et al.* [88] grew (20 u.c.) LAO/(20 to 120 u.c.) STO interfaces on diverse substrates to vary the in-plane biaxial strains in STO intermediate thin layer. The authors showed that tensile strain made the heterostructure insulating, while compressive strains kept the conducting state, but increased the LAO critical thickness for insulating/metal transition (Figure I.19c) and decreased the carrier density (Figure I.19d). It is supposed that the strained STO develops a polarization that modifies the LAO polar field. However the mechanisms involved might be more complex as the substrates chosen were also polar, inducing additional charge discontinuity and relaxations in the STO. Even though it is difficult to isolate the role played by the strain in this study, it reveals that the conduction can be tuned by strain engineering.

The effect of epitaxial strain on charge transfer has also been reported by Lü *et al.* [108] who carried out electrical measurements at low temperatures. The cubic \rightarrow tetragonal \rightarrow rhombohedral phase transitions of SrTiO_3 substrate modify the in-plane cell parameters and thereby the misfit with the LAO film. The misfit is reduced by the cubic to tetragonal transition at 110 K and a metallic behavior is observed. An increase of the misfit by the tetragonal to rhombohedral transition at 55 K turns the interface to insulating. They correlate the observed abrupt variations of the resistivity around the transition temperatures to a strain driven modulation of the charge transfer. Furthermore, even though the phase transitions have been experimentally characterized for LAO/CTO/STO by Schoofs *et al.* [70] (Figure I.20a), no influence on transport properties has been emphasized on LAO/STO.

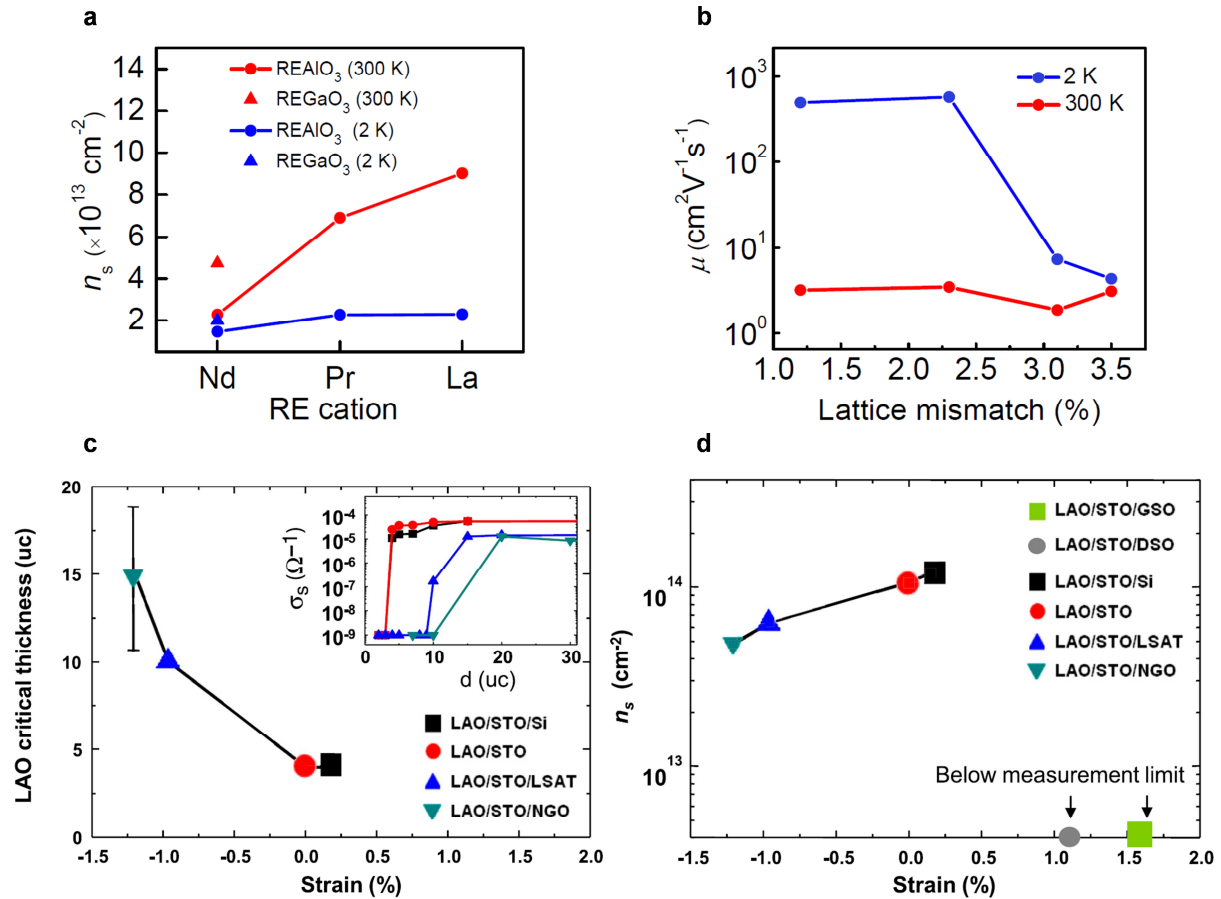


Figure I.19 | Influence of epitaxial strain on the electrical properties. **a**, Evolution of the carrier density as a function of oxides grown. From [66]. **b**, Evolution of the carrier mobility as a function of lattice mismatches. From [66]. **c**, Evolution of the critical thickness value as a function of the induced strain. Inset represents the conductivity as a function of the film thickness. From [88]. **d**, Evolution of the charge carrier density as a function of the induced strain. From [88].

I.5.4.3 Strain induced rotation and distortion of oxygen octahedra

Schoofs *et al.* [70] characterized the influence of structural distortions by inserting between LAO and STO a single unit cell layer of ATiO_3 ($A = \text{Ca}^{2+}, \text{Sr}^{2+}, \text{Sn}^{2+}, \text{Ba}^{2+}$) and $\text{Sr}_{0.5}\text{RE}_{0.5}\text{TiO}_3$ ($\text{RE} = \text{Dy}^{3+}, \text{Sm}^{3+}, \text{Nd}^{3+}, \text{La}^{3+}$) with cations listed by increasing order of their ionic radii. Interestingly in this study, the increasing of ionic radii modifies the epitaxial strain, without affecting the charge balance. Similarly to the above mentioned study, the strain induced a decrease of the conductivity; the larger the strain, the higher the resistance (Figure I.20a), except for BaTiO_3 suggesting that a much more complex scenario than only a steric one, drives the resistance. This is confirmed through the non-proportional relationship between the dopant ion size and the out-of-plane lattice parameter of LAO (Figure I.20b). Nonetheless the influence of strain was clearly established, shorter out-of-plane parameters of LAO, due to an increase of in-plane strain, is responsible for the increase of the carrier density. The large strains introduced in the film induce the rotation and distortion of their oxygen octahedra which are transferred into the first few unit cells below the interface to fully accommodate the strain. These structural distortions imply a local change in the band structure which would release the trapped carriers in the first STO unit cells under the interface, and thus would explain the conduction. Jia *et al.* [59] also provided experimental evidences of TiO_6 rotations

and distortions by using an aberration-corrected ultrahigh-resolution transmission electron microscopy in a system composed by a LAO film comprised between two STO layers. The lifting of degeneracies by symmetry reduction is put forward as a source for electronic reconstruction, although no electrical characterizations are given to establish this link.

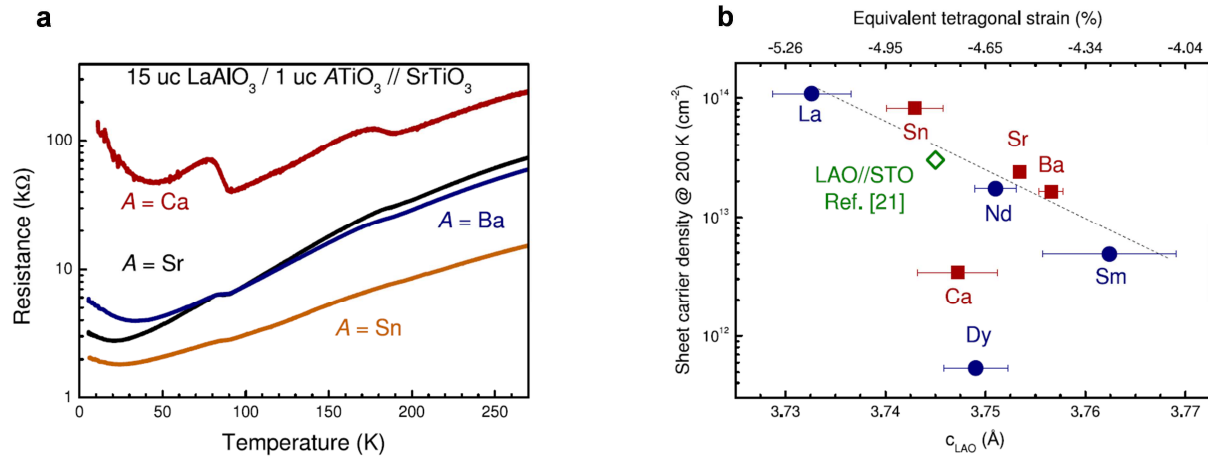


Figure I.20 | Influence of ionic dopant on the electrical measurements of LAO/STO heterostructures. From [70]. **a**, Resistance as a function of temperature for various cations. **b**, Evolution of sheet carrier density as a function of cationic dopants.

I.5.4.4 Elongation of the TiO₆ octahedra and Jahn-Teller effect

The origins of these structural distortions have been discussed widely in the literature. Maurice *et al.* [39] measured by HRTEM and STEM-HAADF (Figure I.21a) an elongation of the cells around the interface by at least 4%. They considered first a possible artefact in the image formation due to the deflection of the electron beam by the positively charged interface. The 3D character of the conduction leaves the positive fixed charges at the interface not charge balanced. However the change of distortion with defocus did not play in favor of a sole electrostatic effect. An intrinsic origin for the elongation of the cell is then related to the existence of Ti³⁺ cations below the interface and a Jahn-Teller effect (Figure I.4). In an unstrained bulk STO the octahedra would be contracted around Ti³⁺. Yet, these authors assumed that the observed elongation of the primitive cells can originate likewise from a Jahn-Teller-like effect where the minimization of the electron energy is achieved by an elongation of TiO₆. This conclusion was shared by several authors [70,109–111], and notably by Willmott *et al.* [60] who also characterized an elongation of the unit cells near the interface (Figure I.21b). In addition to the Jahn-Teller-like effect, Willmott *et al.* [60] proposed that the ionic radii of Ti³⁺, larger than Ti⁴⁺, could be a supplementary explanation for the expansion of the out-of-plane parameter. This elongation was confirmed by Synchrotron X-Ray Diffraction (SXR) analysis by the same group [69], who also pointed out the La diffusion as additional cause of the c-lattice expansion (Figure I.21c). If these last studies minimize the role of Jahn-Teller effect in the elongation of the interfacial cells, Yamamoto *et al.* [71] discarded this explanation. They measured the same amount of volume expansion around the interface for n- and p-type interfaces, which they attribute to a common origin. Since the p-type one does not induce Ti³⁺ formation, they attribute the expansion to oxygen vacancies, or small changes in the cation stoichiometry as Sr vacancies. In opposition to all the previous authors, Vonk *et al.* [3] reported a contraction of the TiO₆ octahedra measured *in-situ* in the PLD chamber by SXR. However we believe they described the initial structure of LaAlO₃ in the

first steps of the growth as the measurements were achieved for a deposition of less than one monolayer. They claimed that this result can be transferred to thicker films, assuming that their structure will not change; later publications will not support this assumption. Interestingly, Al-Ti and La-Sr distances across the interface measured by Vonk *et al.* [3] are coherent with the dilatation measured on HAADF images by Maurice *et al.* [55]. This is not in contradiction with a contraction of the octahedra as they pointed out a buckling of the AO and BO₂ layers around the interface. This buckling has been confirmed later on by many experimental and theoretical studies.

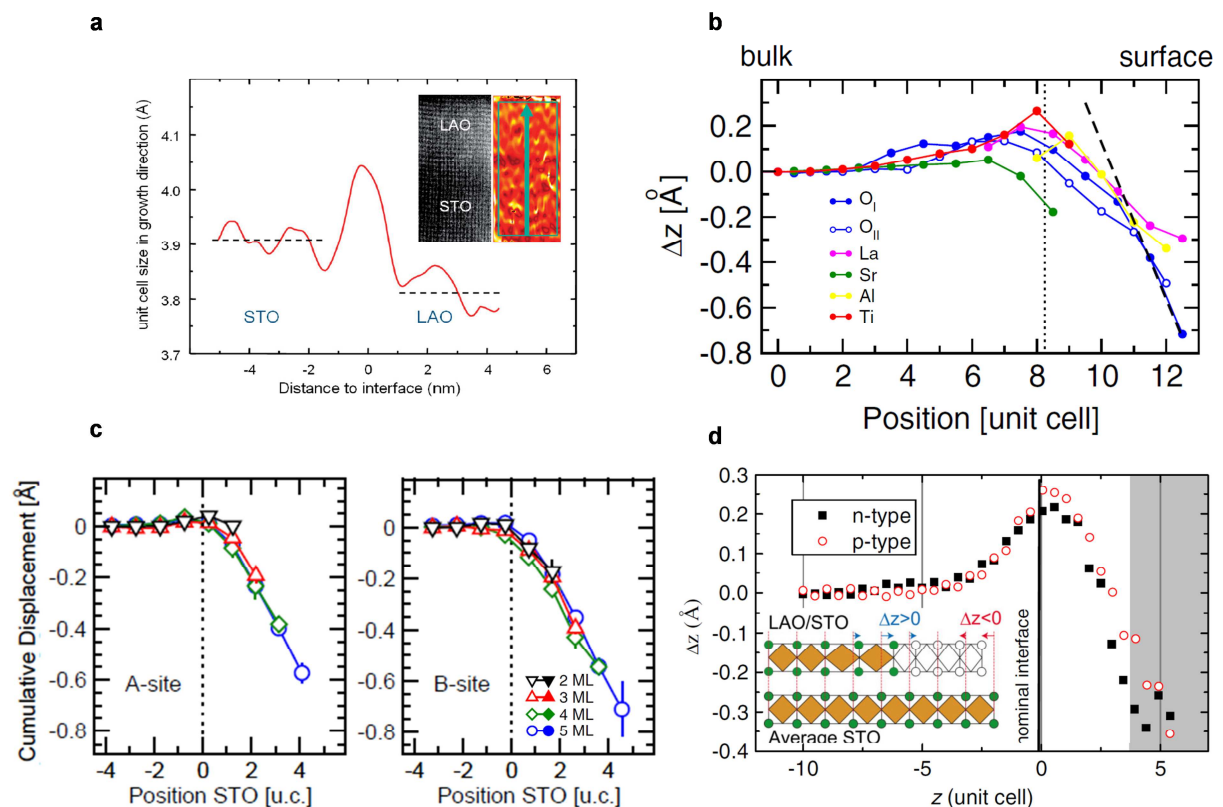


Figure I.21 | Structural distortions at the LAO/STO interface. **a**, Dilatation of the unit cell in the growth direction characterized from STEM-HAADF images. From [39]. **b**, Displacements of atoms around the LAO/STO interface. From [60]. **c**, Cumulative displacement of the A-sites and B-sites cations in the growth direction [001] relative to a reference bulk STO. Adapted from [69]. **d**, Evolution of the out-of-plane parameter throughout both n-type and p-type interfaces. From [71].

I.5.4.5 Buckling of AO and BO₂ layers

We have seen that the stacking of polar layers builds a polar field in the film. As a compensating mechanism, the layers buckle to modify the relative positions of the anions and cations and induce a depolarization field (Figure I.22). This buckling has been modeled by Density Functional Theory (DFT) methods by many groups [51,68,69,100,110,112], with A-sites and B-sites cations of the film moving away from the interface, relative to the oxygen ions. The lattice distortions of O-La-O chains are more pronounced than the lattice distortions of O-Al-O chains, even though quantitative values of the displacements for some film thicknesses differ from one publication to another. The buckling also affects the substrate. Schwingenschlögl *et al.* [68] calculated structural relaxations of the atomic positions in STO that drastically depend on the film thicknesses. Lowering of the LaAlO₃ film thickness below four unit cells lead to an inversion of the TiO₆ distortion pattern at the hetero-interface and an

insulating state. For Pauli *et al.* [69] the buckling increases the minimum thickness at which the electronic reconstruction occurs. At the critical thickness, the electronic injection reduces the polar field and the buckling is supposed to decrease. Strongly related to the buckling mechanism, another compensating mechanism is evidenced by these DFT models, consisting in a charge redistribution from the buckled AlO_2 to LaO layers [46,51]. This charge redistribution increases the covalence between the layers, and decreases the polar field. The buckling has been experimentally observed by Cantoni *et al.* [97] through EELS profiles and STEM-HAADF images. Even though the quantitative results are questionable, owing to the accuracy of such measurements, the buckling is clearly visible.

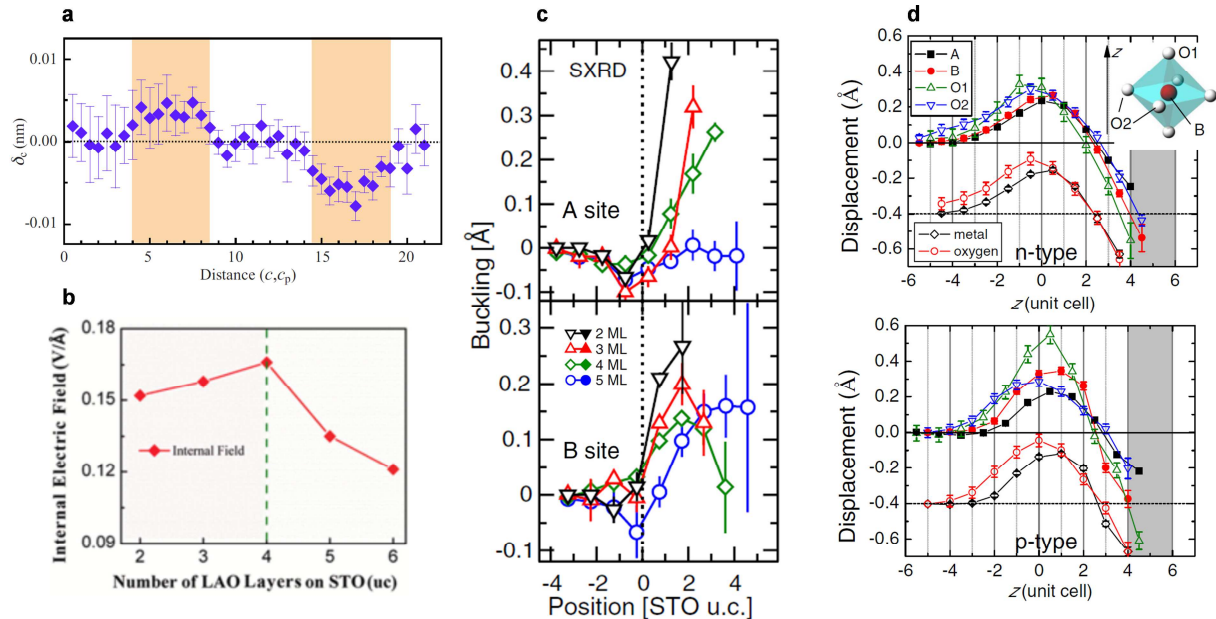


Figure I.22 | Buckling and polarization in the LAO/STO heterostructures. **a**, STO/LAO/STO multilayers. δ_c is the shifts of the oxygen octahedra center out of the Al plane in LAO and out of the Ti plane in the STO layers. The central LAO film is represented in white. The STO regions on the left and right are divided in two. The orange regions close to the interfaces exhibit larger shifts that give rise to a polarization. From [59]. **b**, The evolution of the electric field for various film thicknesses. Once the film reaches four unit cells (threshold for the insulator-to-metal transition), the internal electric field decreases as the film is thicker. Zhou *et al.* [51] associated this behavior to the polarization arisen from the lattice distortions. From [51]. **c**, Buckling of the A-site and B-site atomic planes around the interface for various film thicknesses leads inevitably to a polarization. Adapted from [69]. **d**, Atomic displacements near the interface for n-type and p-type interfaces. The displacement of metal cations and oxygen anions represented below were averaged over a unit cell in order to illustrate the polarization. Adapted from [71].

In summary, we have seen that epitaxial strain and polar field induce subtle changes in the atomic positions in the film and below the interface that can have major consequences in the electron transfer and in their mobilities. In turn, the charge transfer can induce distortion by, for example, the Jahn-Teller effect. Taking a step back from this abundant literature, it seems audacious to extract one single structural mechanism that could dictate the insulating/metal transition and the conduction behavior. Moreover the DFT calculations presented do not take into account the interplay of atomic displacements with point defects. Departure from ideal stoichiometry is likely to occur during the

growth and the charge defects introduced could have dramatic impact on local deformation and band structure.

I.5.5 *Film stoichiometry*

More recently, the formation of cation vacancies in the film was proposed as a potential knob for triggering the conduction in the LAO/STO heterostructure. These defects, which can be controlled by the process parameters, were reported to induce an expansion of the unit cell volume [72–74] and modify the transport properties of LAO/STO systems [37,72–77]. All results converged towards the conclusion that the LAO stoichiometry plays a significant role on the conduction.

I.5.5.1 Film stoichiometry and PLD process parameters.

Unsurprisingly, the deposition conditions such as the oxygen partial pressure, the laser fluence, the plume angle strongly influences the La/Al ratio in the film. Golalikhani *et al.* [72] investigated the effects of laser fluence ($0.7 \text{ J.cm}^{-2} - 2 \text{ J.cm}^{-2}$) and the oxygen pressure ($0.3 \text{ Torr} - 10^{-4} \text{ Torr}$) at a growth temperature of 730°C , by x-ray fluorescence (XRF) and by x-ray diffraction (XRD). They report stoichiometric film grown for oxygen pressures around 10^{-1} Torr with no clear dependence on the laser fluence. The films were Al-rich above 10^{-1} Torr and La-rich below with La/Al ratio as high as 1.5 at 10^{-2} Torr . Sato *et al.* [73] describe La/Al ratio varying from 0.883 to 1.155 only by varying the laser fluence from 0.7 to 1.9 J.cm^{-2} ($p_{\text{O}_2} = 10^{-5} \text{ Torr}$ and $T = 800^\circ\text{C}$). Modification of laser energy density impacts the target/light interaction and the stoichiometry of the plume. Although the La/Al ratios measured show a significant dispersion at a given fluence, a tendency toward La richer films were obtained for higher fluences. On the contrary Breckenfeld *et al.* [37] measured a deficiency in La when increasing fluence from 1.2 to 2.5 J.cm^{-2} ($p_{\text{O}_2} = 10^{-3} \text{ Torr}$ and $T = 750^\circ\text{C}$). However neither the processing parameters nor the chemical analysis methods are identical. Breckenfeld *et al.* [37] used RBS and only characterized La deficiency from La/(La+Sr) variations, since the Al signal was buried in the Ti plateau. Schoofs *et al.* [113] provided indirect experimental evidences of film stoichiometry variations with the laser fluence through variations of the out-of-plane lattice parameter, without giving quantification of the cationic ratio. More striking is their comparison of MEIS spectra obtained in random and channeling mode to assess the crystal quality of the film. A low ratio between the number of backscattered particles on La atoms in the channeling mode and the number of such particles in the random mode reveals a good crystal quality. They showed that the crystallinity was improved at higher fluences but suspected a near surface modification of the STO substrate. This methodology was firstly used by Kalabukhov *et al.* [36], from the same research network, for MEIS spectra recorded on a 1 unit cell-thick film as presented in the “intermixing” section (Figure I.16). As a remainder, they concluded that at the beginning of the deposition, La atoms were distributed non-homogeneously over the film, due to $\text{Sr} \leftrightarrow \text{La}$ intermixing. Stoichiometry was reached from a thickness of four unit cells.

I.5.5.2 Film stoichiometry and lattice parameters

The variation with process conditions of the out-of-plane parameter in the film has been described more or less accurately by several authors. The most precise study comes from Sato *et al.* [73] that reported a non-monotonic variation of the c parameter with the stoichiometry (Figure I.23): for a stoichiometric composition ($\text{La/Al} = 1$), the c parameter corresponds to the one predicted by an epitaxial strain on STO. For under and over stoichiometries in La, larger c were measured due to the formation of cation vacancies ($V_{\text{La}}^{3'}$ and $V_{\text{Al}}^{3'}$) causing Coulomb repulsion and lattice expansion (Figure

I.23b). It is stated that since the formation energy of $V_{La}^{3'}$ is lower than that of $V_{Al}^{3'}$, films are more easily La-deficient than Al-deficient. Surprisingly, antisites Al_{La}^X were not considered as a possible way to adjust La deficiency.

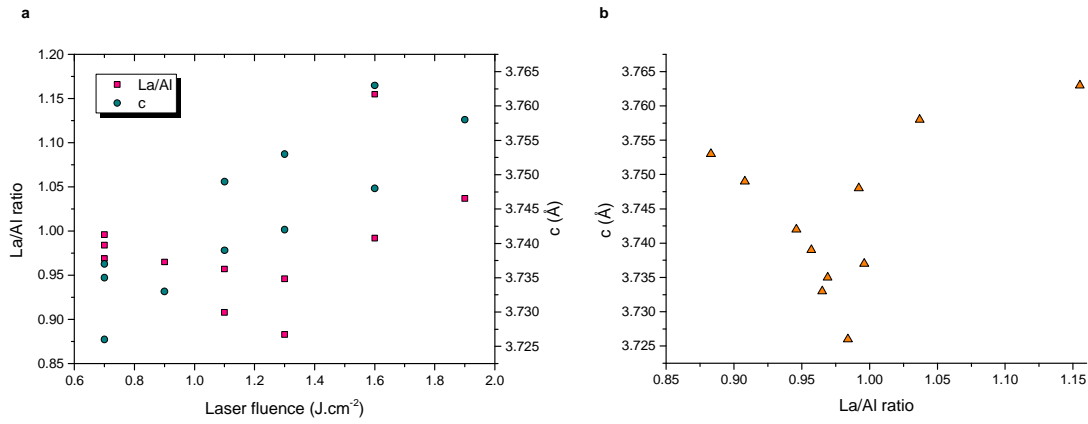


Figure I.23 | Influence of the LAO film stoichiometry on the out-of-plane lattice parameter. a, Variations of the film stoichiometry and of the c lattice with the laser fluence. **b,** Variations of the out-of-plane lattice parameter with the film stoichiometry. Adapted from [73].

I.5.5.3 Film stoichiometry and hetero-interface conductivity

We finally conclude this section by presenting the link between film stoichiometry and electron conductivity. For Sato *et al.* [73] the highest sheet carrier density and conductivity are measured for near stoichiometric films and were significantly decreased for under and over stoichiometries in La (Figure I.24a). It is presumed that cation vacancies ($V_{La}^{3'}$ and $V_{Al}^{3'}$) in non-stoichiometric films are charge balanced by oxygen vacancies. As a consequence, the polar discontinuity can be lowered by filling these anion vacancies by oxygen diffusion from the film surface, reducing the need for electronic reconstruction. We note that no proof of such mechanism was brought, the O vacancies were only hypothesized. Conversely, several authors did not find the highest conduction for stoichiometric films [37,74,75,77]. Although the films were processed by distinct methods, (Warusawithana *et al.* [74] and Rubano *et al.* [75] grew their films by MBE, Breckenfeld *et al.* [37] by PLD and Dildar *et al.* [77] by RF sputtering) they all concluded to an increase of the sheet conductivity for La-deficient films (Figure I.24b, Figure I.24c, Figure I.24d) with for some of them a steep conducting/insulating transition for La/Al \approx 1. Breckenfeld *et al.* [37] note that conduction behavior of the heterostructures with a La-deficient film becomes three dimensional and similar to that of reduced STO. Therefore they assume that the La in the non-stoichiometric film has promoted the reduction of the substrate by formation of O vacancies.

For Warusawithana *et al.* [74] the difference between the behavior of La-rich and La-poor film lays in the type of defects that accommodates the non-stoichiometry. By DFT they calculated that the defects for La/Al > 1 would consist in Al₂O₃ vacancy complexes (Figure I.25a and Figure I.25b). Such large complexes are periodic in the [001] direction and also remove oxygen from the nominal LaO⁺ layers. They are supposed to relieve more strain in the films and have lower energy than La_{Al}^X . Once formed, they offer conduits for Al³⁺ cations to move from the interface. The missing positive charges allow screening the polar field. Without need for electronic reconstruction, the interface remains insulating. For La/Al < 1, Al³⁺ substitutes for La³⁺, Al_{La}^X , and is displaced from the ideal La³⁺ position to

bond with five oxygen resulting in a dipole moment but no net charge (Figure I.25c and Figure I.25d). In this case, as no cation migration is possible, the electronic reconstruction is required to avoid the polar catastrophe and a two-dimensional electron conduction is reported. It has to be noted that no signature of such defects were presented in the HAADF images that could illustrate this theory.

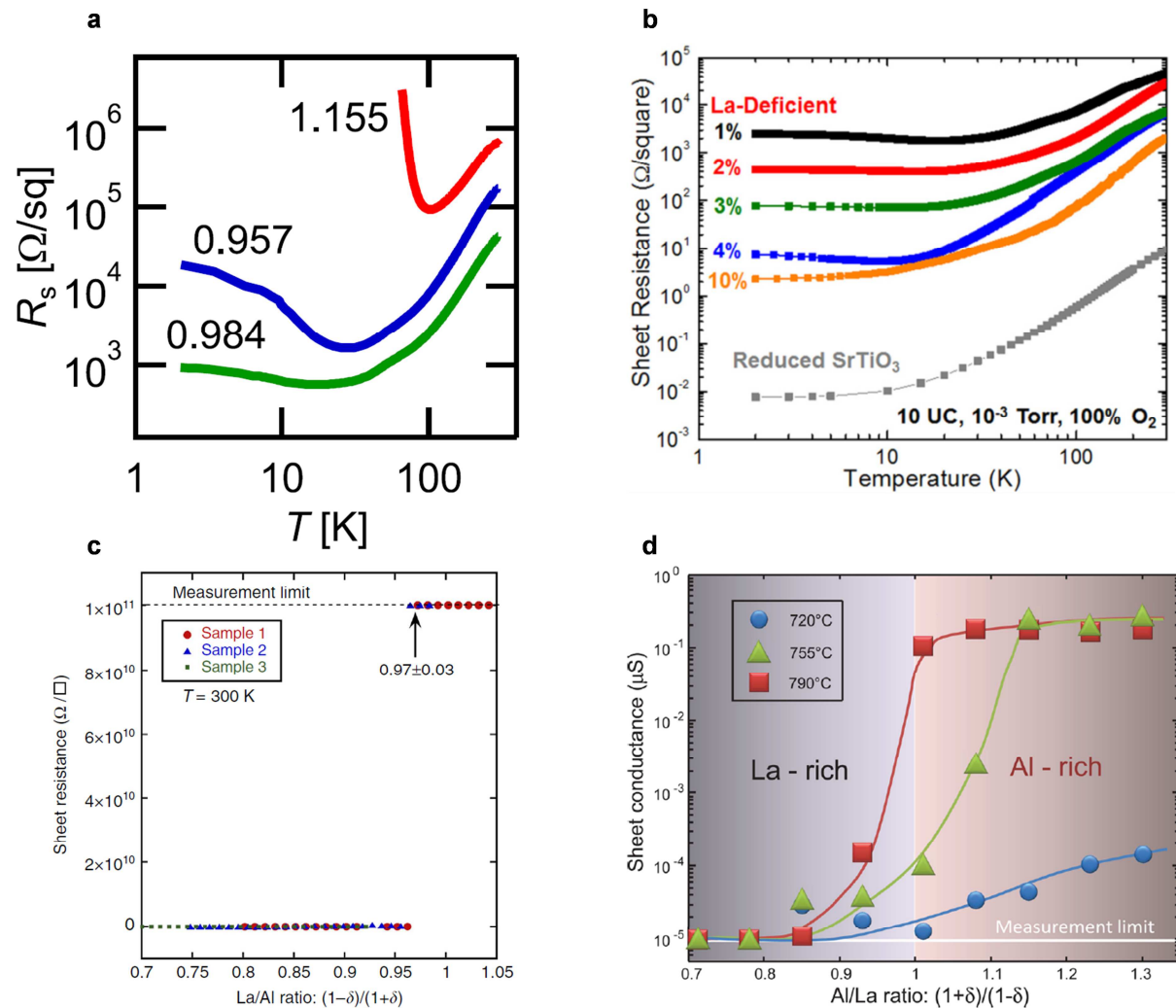


Figure I.24 | Effect of film stoichiometry on the sheet resistance. **a**, Evolution of the sheet resistance as a function of temperature for various film stoichiometries/laser fluences. The figures represent the La/Al ratio calculated from ICP. The sheet resistance decreases for less energetic laser. However, no linear dependence is seen between La/Al ratio, sheet resistance, and laser fluence. This indicates that other process parameters must impact the film stoichiometry. From [73]. **b**, Sheet resistance as a function of temperature for ten unit cells thick film with different levels of La-deficiency. The results demonstrate clearly that the electrical properties are improved for higher levels of La-deficiency. From [37]. **c**, Sheet resistance as a function of La/Al ratio. The LAO/STO heterostructure becomes resistive for La/Al ratio $\geq 0.97 \pm 0.03$. From [74]. **d**, Sheet resistance as a function of La/Al ratio for samples elaborated at different temperatures. Other than the influence of the growth conditions, which will be discussed later, the samples are confirmed to be conductive for La/Al ratio < 1 . From [75].

Once again no consensus on the effect of non-stoichiometry is reached, neither regarding the relation between La/Al value and the insulating/conducting transition nor on the mechanism involved (type of point defects created, 3D or 2D conduction). In addition the cation non-stoichiometry in the film is expected to be coupled with (or produce by) cation diffusion into a non-stoichiometric substrate and/or interdiffusion with Sr or Ti [62], which are not taken into account in these models. Therefore, it is clear that the film stoichiometry influences strongly the transport properties of the LAO/STO heterostructures, however this cannot be the only triggering factor for conduction.

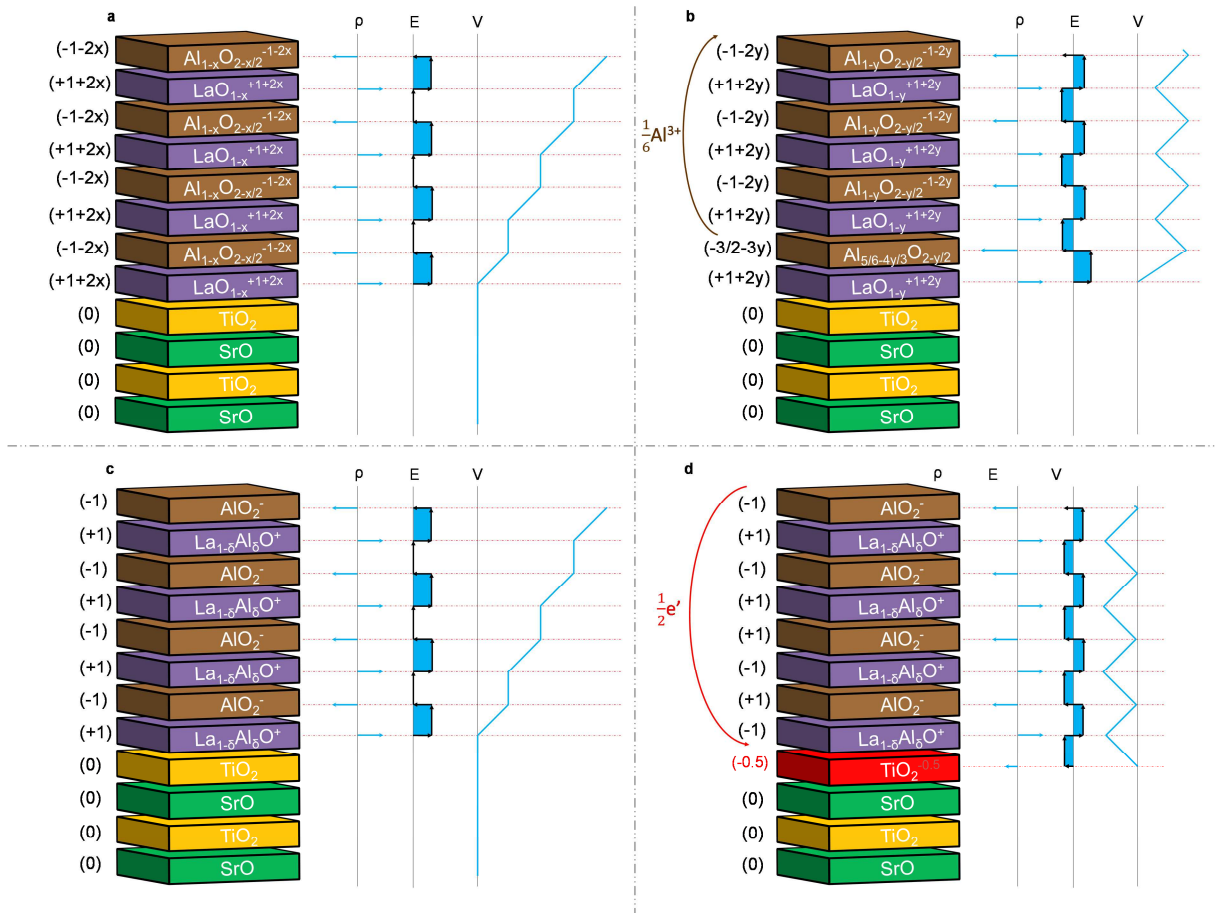


Figure I.25 | Polar Catastrophe models at interfaces LAO/STO with distinct La/Al ratio. Adapted from [74]. **a**, The interface for La/Al > 1 before the atomic reconstruction with the formation of Al₂O₃ vacancies. The electrostatic potential is growing as the film is thicker and encloses a higher concentration of vacancies. **b**, A transfer of one sixth of Al³⁺ counteracts the diverging electrostatic potential. **c**, The interface for La/Al < 1 before the electronic reconstruction with the substitution of La³⁺ by Al³⁺. The electrostatic potential is growing as the film is thicker and higher concentration of vacancies. **d**, A transfer of half an electron to the interface allows the compensation of the diverging potential.

I.6 Summary

This chapter presented a literature review of each mechanism assumed to promote the electronic gas at the LAO/STO interface. None of them was found exclusively responsible for the conduction and a strong synergy is rather expected. The absence of consensus we have underlined must also be understood as the consequence of the variety of deposition techniques and growth parameters used to synthesize the samples. The atomic structures of the hetero-interfaces investigated might often not be comparable. We believe that a deep understanding of the link between growth conditions and atomic structure is a prerequisite to predict and control the electron transport mechanism in this LAO/STO system.

Bibliography

- [1] R. Loetzsch, A. Lübcke, I. Uschmann, E. Förster, V. Große, M. Thuerk, T. Koettig, F. Schmidl, and P. Seidel, "The cubic to tetragonal phase transition in SrTiO₃ single crystals near its surface under internal and external strains," *Appl. Phys. Lett.* **96**, 71901 (2010).
- [2] H. A. Jahn and E. Teller, "Stability of Polyatomic Molecules in Degenerate Electronic States. I. Orbital Degeneracy," *Proc. R. Soc. Lond. Math. Phys. Eng. Sci.* **161**, 220–235 (1937).
- [3] V. Vonk, M. Huijben, K. J. I. Driessen, P. Tinnemans, A. Brinkman, S. Harkema, and H. Graafsma, "Interface structure of SrTiO₃/LaAlO₃ at elevated temperatures studied in situ by synchrotron x rays," *Phys. Rev. B* **75** (2007).
- [4] H. Lehnert, H. Boysen, J. Schneider, F. Frey, D. Hohlwein, P. Radaelli, and H. Ehrenberg, "A powder diffraction study of the phase transition in LaAlO₃," *Z. Krist.* **215**, 536 (2000).
- [5] L. Guan, L. T. Jin, W. Zhang, Q. Li, J. X. Guo, B. Geng, Q. X. Zhao, and B. T. Liu, "Atomic and Electronic Structure of LaAlO₃ and LaAlO₃:Mg from First-Principles Calculations," *Adv. Mater. Res.* **79–82**, 1257–1260 (2009).
- [6] X. Luo and B. Wang, "Structural and elastic properties of LaAlO₃ from first-principles calculations," *J. Appl. Phys.* **104**, 73518 (2008).
- [7] G. Murtaza and I. Ahmad, "Shift of indirect to direct bandgap and optical response of LaAlO₃ under pressure," *J. Appl. Phys.* **111**, 123116 (2012).
- [8] P. Zubko, S. Gariglio, M. Gabay, P. Ghosez, and J.-M. Triscone, "Interface Physics in Complex Oxide Heterostructures," *Annu. Rev. Condens. Matter Phys.* **2**, 141–165 (2011).
- [9] A. Ohtomo and H. Y. Hwang, "A high-mobility electron gas at the LaAlO₃/SrTiO₃ heterointerface," *Nature* **427**, 423–426 (2004).
- [10] S. A. Pauli and P. R. Willmott, "Conducting interfaces between polar and non-polar insulating perovskites," *J. Phys. Condens. Matter* **20**, 264012 (2008).
- [11] N. Reyren, S. Thiel, A. D. Caviglia, L. F. Kourkoutis, G. Hammerl, C. Richter, C. W. Schneider, T. Kopp, A.-S. Rüetschi, et al., "Superconducting Interfaces Between Insulating Oxides," *Science* **317**, 1196–1199 (2007).
- [12] A. D. Caviglia, S. Gariglio, N. Reyren, D. Jaccard, T. Schneider, M. Gabay, S. Thiel, G. Hammerl, J. Mannhart, et al., "Electric field control of the LaAlO₃/SrTiO₃ interface ground state," *Nature* **456**, 624–627 (2008).
- [13] J. Mannhart, D. H. A. Blank, H. Y. Hwang, A. J. Millis, and J.-M. Triscone, "Two-dimensional electron gases at oxide interfaces," *MRS Bull.* **33**, 1027–1034 (2008).
- [14] N. C. Plumb, M. Kobayashi, M. Salluzzo, E. Razzoli, C. Matt, V. N. Strocov, K.-J. Zhou, C. Monney, T. Schmitt, et al., "From the SrTiO₃ Surface to the LaAlO₃/SrTiO₃ Interface: How thickness is critical," *ArXiv13045948 Cond-Mat* (2013).

- [15] B. Kalisky, J. A. Bert, B. B. Klopfer, C. Bell, H. K. Sato, M. Hosoda, Y. Hikita, H. Y. Hwang, and K. A. Moler, "Critical thickness for ferromagnetism in LaAlO₃/SrTiO₃ heterostructures," *Nat. Commun.* **3**, 922 (2012).
- [16] A. Brinkman, "Magnetic effects at the interface between non-magnetic oxides," *Nat. Mater* **6**, 493–496 (2007).
- [17] H. Chen, A. M. Kolpak, and S. Ismail-Beigi, "Electronic and Magnetic Properties of SrTiO₃/LaAlO₃ Interfaces from First Principles," *Adv. Mater.* **22**, 2881–2899 (2010).
- [18] M. T. Gray, T. D. Sanders, C. A. Jenkins, P. Shafer, E. Arenholz, and Y. Suzuki, "Electronic and magnetic phenomena at the interface of LaAlO₃ and Ru doped SrTiO₃," *Appl. Phys. Lett.* **107**, 241603 (2015).
- [19] M. Huijben, A. Brinkman, G. Koster, G. Rijnders, H. Hilgenkamp, and D. H. A. Blank, "Structure-Property Relation of SrTiO₃/LaAlO₃ Interfaces," *Adv. Mater.* **21**, 1665–1677 (2009).
- [20] M. Kawasaki, A. Ohtomo, T. Arakane, K. Takahashi, M. Yoshimoto, and H. Koinuma, "Atomic control of SrTiO₃ surface for perfect epitaxy of perovskite oxides," *Appl. Surf. Sci.* **107**, 102–106 (1996).
- [21] J. G. Connell, B. J. Isaac, G. B. Ekanayake, D. R. Strachan, and S. S. A. Seo, "Preparation of atomically flat SrTiO₃ surfaces using a deionized-water leaching and thermal annealing procedure," *Appl. Phys. Lett.* **101**, 251607 (2012).
- [22] C. H. Lanier, J. M. Rondinelli, B. Deng, R. Kilaas, K. R. Poeppelmeier, and L. D. Marks, "Surface Reconstruction with a Fractional Hole: (√5x√5)R26.6° LaAlO₃ (001)," *Phys. Rev. Lett.* **98**, 86102 (2007).
- [23] S. A. Chambers, T. C. Droubay, C. Capan, and G. Y. Sun, "Unintentional F doping of SrTiO₃(001) etched in HF acid-structure and electronic properties," *Surf. Sci.* **606**, 554–558 (2012).
- [24] T. Ohnishi, K. Shibuya, M. Lippmaa, D. Kobayashi, H. Kumigashira, M. Oshima, and H. Koinuma, "Preparation of thermally stable TiO₂-terminated SrTiO₃(100) substrate surfaces," *Appl. Phys. Lett.* **85**, 272–274 (2004).
- [25] T. Nishimura, A. Ikeda, H. Namba, T. Morishita, and Y. Kido, "Structure change of TiO₂-terminated SrTiO₃(001) surfaces by annealing in O₂ atmosphere and ultrahigh vacuum," *Surf. Sci.* **421**, 273–278 (1999).
- [26] J. G. Connell, J. Nichols, J. H. Gruenewald, D.-W. Kim, and S. S. A. Seo, "Conducting LaAlO₃/SrTiO₃ heterointerfaces on atomically-flat substrates prepared by deionized-water," *Sci. Rep.* **6**, 23621 (2016).
- [27] J. Yao, P. B. Merrill, S. S. Perry, D. Marton, and J. W. Rabalais, "Thermal stimulation of the surface termination of LaAlO₃{100}," *J. Chem. Phys.* **108**, 1645–1652 (1998).

- [28] Z. Q. Liu, Z. Huang, W. M. Lü, K. Gopinadhan, X. Wang, A. Annadi, T. Venkatesan, and Ariando, "Atomically flat interface between a single-terminated LaAlO₃ substrate and SrTiO₃ thin film is insulating," *AIP Adv.* **2**, 12147 (2012).
- [29] S. Thiel, "Tunable Quasi-Two-Dimensional Electron Gases in Oxide Heterostructures," *Science* **313**, 1942–1945 (2006).
- [30] J. Mannhart and D. G. Schlom, "Oxide Interfaces--An Opportunity for Electronics," *Science* **327**, 1607–1611 (2010).
- [31] W. Wei and A. Sehirlioglu, "Strain relaxation analysis of LaAlO₃/SrTiO₃ heterostructure using reciprocal lattice mapping," *Appl. Phys. Lett.* **100**, 71901 (2012).
- [32] D. Stornaiuolo, S. Gariglio, N. J. G. Couto, A. Fête, A. D. Caviglia, G. Seyfarth, D. Jaccard, A. F. Morpurgo, and J.-M. Triscone, "In-plane electronic confinement in superconducting LaAlO₃/SrTiO₃ nanostructures," *Appl. Phys. Lett.* **101**, 222601 (2012).
- [33] M. Breitschaft, V. Tinkl, N. Pavlenko, S. Paetel, C. Richter, J. R. Kirtley, Y. C. Liao, G. Hammerl, V. Eyert, et al., "Two-dimensional electron liquid state at LaAlO₃-SrTiO₃ interfaces," *Phys. Rev. B* **81** (2010).
- [34] C. Cancellieri, N. Reyren, S. Gariglio, A. D. Caviglia, A. Fête, and J.-M. Triscone, "Influence of the growth conditions on the LaAlO₃/SrTiO₃ interface electronic properties," *EPL Europhys. Lett.* **91**, 17004 (2010).
- [35] C. Bell, S. Harashima, Y. Hikita, and H. Y. Hwang, "Thickness dependence of the mobility at the LaAlO₃/SrTiO₃ interface," *Appl. Phys. Lett.* **94**, 222111 (2009).
- [36] A. S. Kalabukhov, Y. A. Boikov, I. T. Serenkov, V. I. Sakharov, V. N. Popok, R. Gunnarsson, J. Börjesson, N. Ljustina, E. Olsson, et al., "Cationic Disorder and Phase Segregation in LaAlO₃/SrTiO₃ Heterointerfaces Evidenced by Medium-Energy Ion Spectroscopy," *Phys. Rev. Lett.* **103** (2009).
- [37] E. Breckenfeld, N. Bronn, N. Mason, and L. W. Martin, "Tunability of conduction at the LaAlO₃/SrTiO₃ heterointerface: Thickness and compositional studies," *Appl. Phys. Lett.* **105**, 121610 (2014).
- [38] E. Lesne, N. Reyren, D. Doennig, R. Mattana, H. Jaffrès, V. Cros, F. Petroff, F. Choueikani, P. Ohresser, et al., "Suppression of the critical thickness threshold for conductivity at the LaAlO₃/SrTiO₃ interface," *Nat. Commun.* **5** (2014).
- [39] J.-L. Maurice, C. Carrétéro, M.-J. Casanove, K. Bouzehouane, S. Guyard, é. Larquet, and J.-P. Contour, "Electronic conductivity and structural distortion at the interface between insulators SrTiO₃ and LaAlO₃," *Phys. Status Solidi A* **203**, 2209–2214 (2006).
- [40] S. P. Thiel, "Study of Interface Properties in LaAlO₃/SrTiO₃ Heterostructures."
- [41] C. Cen, S. Thiel, J. Mannhart, and J. Levy, "Oxide Nanoelectronics on Demand," *Science* **323**, 1026–1030 (2009).

- [42] H.-L. Lu, Z.-M. Liao, L. Zhang, W.-T. Yuan, Y. Wang, X.-M. Ma, and D.-P. Yu, "Reversible insulator-metal transition of LaAlO₃/SrTiO₃ interface for nonvolatile memory," *Sci. Rep.* **3** (2013).
- [43] E. Y. Tsymbal, E. R. A. Dagotto, C.-B. Eom, and R. Ramesh, Eds., *Multifunctional Oxide Heterostructures* (Oxford University Press, 2012).
- [44] S. A. Chambers, "Understanding the mechanism of conductivity at the LaAlO₃/SrTiO₃(001) interface," *Surf. Sci.* **605**, 1133–1140 (2011).
- [45] G. Drera, F. Banfi, F. F. Canova, P. Borghetti, L. Sangaletti, F. Bondino, E. Magnano, J. Huijben, M. Huijben, et al., "Spectroscopic evidence of in-gap states at the SrTiO₃/LaAlO₃ ultrathin interfaces," *Appl. Phys. Lett.* **98**, 52907 (2011).
- [46] T. C. Asmara, A. Annadi, I. Santoso, P. K. Gogoi, A. Kotlov, H. M. Omer, M. Motapothula, M. B. H. Breese, M. Rübhausen, et al., "Mechanisms of charge transfer and redistribution in LaAlO₃/SrTiO₃ revealed by high-energy optical conductivity," *Nat. Commun.* **5** (2014).
- [47] E. Slooten, Z. Zhong, H. J. A. Molegraaf, P. D. Eerkes, S. de Jong, F. Masee, E. van Heumen, M. K. Kruize, S. Wenderich, et al., "Hard x-ray photoemission and density functional theory study of the internal electric field in SrTiO₃/LaAlO₃ oxide heterostructures," *Phys. Rev. B* **87**, 85128 (2013).
- [48] M. Takizawa, S. Tsuda, T. Susaki, H. Y. Hwang, and A. Fujimori, "Electronic charges and electric potential at LaAlO₃/SrTiO₃ interfaces studied by core-level photoemission spectroscopy," *Phys. Rev. B* **84** (2011).
- [49] N. Nakagawa, H. Y. Hwang, and D. A. Muller, "Why some interfaces cannot be sharp," *Nat. Mater.* **5**, 204–209 (2006).
- [50] A. S. Kalabukhov, R. Gunnarsson, J. Börjesson, E. Olsson, T. Claeson, and D. Winkler, "Effect of oxygen vacancies in the SrTiO₃ substrate on the electrical properties of the LaAlO₃/SrTiO₃ interface," *Phys Rev B* **75**, 121404(R) (2007).
- [51] J. Zhou, T. C. Asmara, M. Yang, G. A. Sawatzky, Y. P. Feng, and A. Rusydi, "The interplay of electronic reconstructions, lattice distortions, and surface oxygen vacancies in insulator-metal transition of LaAlO₃/SrTiO₃," *Phys Rev B* **92** (2015).
- [52] G. Herranz, M. Basletić, M. Bibes, C. Carrétéro, E. Tafrá, E. Jacquet, K. Bouzouane, C. Deranlot, A. Hamzić, et al., "High mobility in LaAlO₃/SrTiO₃ heterostructures: origin, dimensionality, and perspectives," *Phys. Rev. Lett.* **98**, 216803 (2007).
- [53] Z. Q. Liu, C. J. Li, W. M. Lu, X. H. Huang, Z. Huang, S. W. Zeng, X. P. Qiu, L. S. Huang, A. Annadi, et al., "Origin of the Two-Dimensional Electron Gas at LaAlO₃/SrTiO₃ Interfaces: The Role of Oxygen Vacancies and Electronic Reconstruction," *Phys. Rev. X* **3**, 1010–1010 (2013).
- [54] Z. Q. Liu, L. Sun, Z. Huang, C. J. Li, S. W. Zeng, K. Han, W. M. Lü, T. Venkatesan, and Ariando, "Dominant role of oxygen vacancies in electrical properties of unannealed LaAlO₃/SrTiO₃ interfaces," *J. Appl. Phys.* **115**, 54303 (2014).

- [55] J.-L. Maurice, G. Herranz, C. Colliex, I. Devos, C. Carrétéro, A. Barthélémy, K. Bouzouane, S. Fusil, D. Imhoff, et al., "Electron energy loss spectroscopy determination of Ti oxidation state at the (001) LaAlO₃/SrTiO₃ interface as a function of LaAlO₃ growth conditions," *EPL Europhys. Lett.* **82**, 17003 (2008).
- [56] W. Siemons, "Origin of charge density at LaAlO₃ on SrTiO₃ heterointerfaces: Possibility of intrinsic doping," *Phys Rev Lett* **98**, 196802 (2007).
- [57] S. Suwanwong, T. Eknapakul, Y. Rattanachai, C. Masingboon, S. Rattanasuporn, R. Phatthanakun, H. Nakajima, P. D. C. King, S. K. Hodak, et al., "The dynamics of ultraviolet-induced oxygen vacancy at the surface of insulating SrTiO₃(001)," *Appl. Surf. Sci.* **355**, 210–212 (2015).
- [58] S. Gariglio, A. Fête, and J.-M. Triscone, "Electron confinement at the LaAlO₃/SrTiO₃ interface," *J. Phys. Condens. Matter* **27**, 283201 (2015).
- [59] C. L. Jia, S. B. Mi, M. Faley, U. Poppe, J. Schubert, and K. Urban, "Oxygen octahedron reconstruction in the SrTiO₃/LaAlO₃ heterointerfaces investigated using aberration-corrected ultrahigh-resolution transmission electron microscopy," *Phys. Rev. B* **79** (2009).
- [60] P. R. Willmott, S. A. Pauli, R. Herger, C. M. Schlepütz, D. Martocchia, B. D. Patterson, B. Delley, R. Clarke, D. Kumah, et al., "Structural basis for the conducting interface between LaAlO₃ and SrTiO₃," *Phys Rev Lett* **99**, 155502 (2007).
- [61] S. A. Chambers, M. H. Engelhard, V. Shutthanandan, Z. Zhu, T. C. Droubay, L. Qiao, P. V. Sushko, T. Feng, H. D. Lee, et al., "Instability, Intermixing and Electronic Structure at the Epitaxial LaAlO₃/SrTiO₃(001) Heterojunction," *Surf. Sci. Rep.* **65**, 317–352 (2010).
- [62] G. Salvinelli, G. Drera, A. Giampietri, and L. Sangaletti, "Layer-resolved cation diffusion and stoichiometry at the LaAlO₃/SrTiO₃ heterointerface probed by X-ray photoemission experiments and site occupancy modeling," *ACS Appl. Mater. Interfaces* **7**, 25648–25657 (2015).
- [63] A. Kalabukhov, Y. A. Boikov, I. T. Serenkov, V. I. Sakharov, J. Börjesson, N. Ljustina, E. Olsson, D. Winkler, and T. Claeson, "Improved cationic stoichiometry and insulating behavior at the interface of LaAlO₃/SrTiO₃ formed at high oxygen pressure during pulsed-laser deposition," *EPL Europhys. Lett.* **93**, 37001 (2011).
- [64] L. Qiao, T. C. Droubay, T. C. Kaspar, P. V. Sushko, and S. A. Chambers, "Cation mixing, band offsets and electric fields at LaAlO₃/SrTiO₃(001) heterojunctions with variable La:Al atom ratio," *Surf. Sci.* **605**, 1381–1387 (2011).
- [65] V. Vonk, J. Huijben, D. Kukuruznyak, A. Stierle, H. Hilgenkamp, A. Brinkman, and S. Harkema, "Polar-discontinuity-retaining A-site intermixing and vacancies at SrTiO₃/LaAlO₃ interfaces," *Phys. Rev. B* **85** (2012).
- [66] A. Annadi, A. Putra, Z. Q. Liu, X. Wang, K. Gopinadhan, Z. Huang, S. Dhar, T. Venkatesan, and Ariando, "Electronic correlation and strain effects at the interfaces between polar and nonpolar complex oxides," *Phys Rev B* **86**, 85450 (2012).

- [67] T. T. Fister, H. Zhou, Z. Luo, S. S. A. Seo, S. O. Hruszkewycz, D. L. Proffit, J. A. Eastman, P. H. Fuoss, P. M. Baldo, et al., "Octahedral rotations in strained LaAlO₃/SrTiO₃ (001) heterostructures," *APL Mater.* **2**, 21102 (2014).
- [68] U. Schwingenschlögl and C. Schuster, "Interface relaxation and electrostatic charge depletion in the oxide heterostructure LaAlO₃/SrTiO₃," *EPL Europhys. Lett.* **86**, 27005 (2009).
- [69] S. A. Pauli, S. J. Leake, B. Delley, M. Björck, C. W. Schneider, C. M. Schlepütz, D. Martocchia, S. Paetel, J. Mannhart, et al., "Evolution of the Interfacial Structure of LaAlO₃ on SrTiO₃," *Phys. Rev. Lett.* **106**, 36101 (2011).
- [70] F. Schoofs, M. A. Carpenter, M. E. Vickers, M. Egilmez, T. Fix, J. E. Kleibeuker, J. L. MacManus-Driscoll, and M. G. Blamire, "Carrier density modulation by structural distortions at modified LaAlO₃/SrTiO₃ interfaces," *J. Phys. Condens. Matter Inst. Phys. J.* **25**, 175005 (2013).
- [71] R. Yamamoto, C. Bell, Y. Hikita, H. Y. Hwang, H. Nakamura, T. Kimura, and Y. Wakabayashi, "Structural Comparison of n-Type and p-Type LaAlO₃/SrTiO₃ Interfaces," *Phys. Rev. Lett.* **107**, 36104 (2011).
- [72] M. Golalikhani, Q. Y. Lei, G. Chen, J. E. Spanier, H. Ghassemi, C. L. Johnson, M. L. Taheri, and X. X. Xi, "Stoichiometry of LaAlO₃ films grown on SrTiO₃ by pulsed laser deposition," *J. Appl. Phys.* **114**, 27008 (2013).
- [73] H. K. Sato, C. Bell, Y. Hikita, and H. Y. Hwang, "Stoichiometry control of the electronic properties of the LaAlO₃/SrTiO₃ heterointerface," *Appl. Phys. Lett.* **102**, 251602 (2013).
- [74] M. P. Warusawithana, C. Richter, J. A. Mundy, P. Roy, J. Ludwig, S. Paetel, T. Heeg, A. A. Pawlicki, L. F. Kourkoutis, et al., "LaAlO₃ stoichiometry is key to electron liquid formation at LaAlO₃/SrTiO₃ interfaces," *Nat. Commun.* **4** (2013).
- [75] A. Rubano, G. D. Luca, J. Schubert, Z. Wang, S. Zhu, D. G. Schlom, L. Marrucci, and D. Paparo, "Polar asymmetry of La(1- δ)Al(1+ δ)O₃/SrTiO₃ heterostructures probed by optical second harmonic generation," *Appl. Phys. Lett.* **107**, 101603 (2015).
- [76] G. Drera, G. Salvinelli, A. Brinkman, M. Huijben, G. Koster, H. Hilgenkamp, G. Rijnders, D. Visentin, and L. Sangaletti, "Band offsets and density of Ti³⁺ states probed by x-ray photoemission on LaAlO₃/SrTiO₃ heterointerfaces and their LaAlO₃ and SrTiO₃ bulk precursors," *Phys. Rev. B* **87**, 75435 (2013).
- [77] I. M. Dildar, D. B. Boltje, M. H. S. Hesselberth, J. Aarts, Q. Xu, H. W. Zandbergen, and S. Harkema, "Non-conducting interfaces of LaAlO₃/SrTiO₃ produced in sputter deposition: The role of stoichiometry," *Appl. Phys. Lett.* **102**, 121601 (2013).
- [78] S. Thiel, C. W. Schneider, L. F. Kourkoutis, D. A. Muller, N. Reyren, A. D. Caviglia, S. Gariglio, J.-M. Triscone, and J. Mannhart, "Electron Scattering at Dislocations in LaAlO₃/SrTiO₃ Interfaces," *Phys. Rev. Lett.* **102**, 46809 (2009).
- [79] N. C. Bristowe, P. Ghosez, P. B. Littlewood, and E. Artacho, "The origin of two-dimensional electron gases at oxide interfaces: insights from theory," *J. Phys. Condens. Matter* **26**, 143201 (2014).

- [80] W. Son, E. Cho, J. Lee, and S. Han, "Hydrogen adsorption and carrier generation in LaAlO₃-SrTiO₃ heterointerfaces: a first-principles study," *J. Phys. Condens. Matter* **22**, 315501 (2010).
- [81] Y. Li, S. N. Phattalung, S. Limpijumnong, J. Kim, and J. Yu, "Formation of oxygen vacancies and charge carriers induced in the n-type interface of a LaAlO₃ overlayer on SrTiO₃(001)," *Phys. Rev. B* **84**, 245307 (2011).
- [82] G. Singh-Bhalla, C. Bell, J. Ravichandran, W. Siemons, Y. Hikita, S. Salahuddin, A. F. Hebard, H. Y. Hwang, and R. Ramesh, "Built-in and induced polarization across LaAlO₃/SrTiO₃ heterojunctions," *Nat. Phys.* **7**, 80–86 (2011).
- [83] M. Sing, G. Berner, K. Goß, A. Müller, A. Ruff, A. Wetscherek, S. Thiel, J. Mannhart, S. A. Pauli, et al., "Profiling the Interface Electron Gas of LaAlO₃/SrTiO₃ Heterostructures with Hard X-Ray Photoelectron Spectroscopy," *Phys. Rev. Lett.* **102**, 176805 (2009).
- [84] Y. Xie, Y. Hikita, C. Bell, and H. Y. Hwang, "Control of electronic conduction at an oxide heterointerface using surface polar adsorbates," *Nat. Commun.* **2**, 494 (2011).
- [85] J. Verbeeck, S. Bals, A. N. Kravtsova, D. Lamoën, M. Luysberg, M. Huijben, G. Rijnders, A. Brinkman, H. Hilgenkamp, et al., "Electronic reconstruction at n-type SrTiO₃/LaAlO₃ interfaces," *Phys. Rev. B* **81** (2010).
- [86] G. Herranz, F. Sánchez, N. Dix, M. Scigaj, and J. Fontcuberta, "High mobility conduction at (110) and (111) LaAlO₃/SrTiO₃ interfaces," *Sci. Rep.* **2** (2012).
- [87] C. Noguera, "Polar oxide surfaces," *J. Phys. Condens. Matter* **12**, R367 (2000).
- [88] C. W. Bark, D. A. Felker, Y. Wang, Y. Zhang, H. W. Jang, C. M. Folkman, J. W. Park, S. H. Baek, H. Zhou, et al., "Tailoring a two-dimensional electron gas at the LaAlO₃/SrTiO₃ (001) interface by epitaxial strain," *Proc. Natl. Acad. Sci.* **108**, 4720–4724 (2011).
- [89] Y. Z. Chen, D. V. Christensen, F. Trier, N. Pryds, A. Smith, and S. Linderoth, "On the origin of metallic conductivity at the interface of LaAlO₃/SrTiO₃," *Appl. Surf. Sci.* **258**, 9242–9245 (2012).
- [90] F. Gunkel, S. Wicklein, S. Hoffmann-Eifert, P. Meuffels, P. Brinks, M. Huijben, G. Rijnders, R. Waser, and R. Dittmann, "Transport limits in defect-engineered LaAlO₃/SrTiO₃ bilayers," *Nanoscale* **7**, 1013–1022 (2015).
- [91] Y. Du, C. Wang, J. Li, X. Zhang, F. Wang, Y. Zhu, N. Yin, and L. Mei, "The effect of in-plane strain on the electronic properties of LaAlO₃/SrTiO₃ interface," *Comput. Mater. Sci.* **99**, 57–61 (2015).
- [92] M. Basletic, J.-L. Maurice, C. Carrétéro, G. Herranz, O. Copie, M. Bibes, É. Jacquet, K. Bouzehouane, S. Fusil, et al., "Mapping the spatial distribution of charge carriers in LaAlO₃/SrTiO₃ heterostructures," *Nat. Mater.* **7**, 621–625 (2008).
- [93] A. F. Santander-Syro, O. Copie, T. Kondo, F. Fortuna, S. Pailhès, R. Weht, X. G. Qiu, F. Bertran, A. Nicolaou, et al., "Two-dimensional electron gas with universal subbands at the surface of SrTiO₃," *Nature* **469**, 189–193 (2011).

- [94] R. A. De Souza, V. Metlenko, D. Park, and T. E. Weirich, "Behavior of oxygen vacancies in single-crystal SrTiO₃: Equilibrium distribution and diffusion kinetics," *Phys. Rev. B* **85**, 174109 (2012).
- [95] M. Takizawa, H. Wadati, K. Tanaka, M. Hashimoto, T. Yoshida, A. Fujimori, A. Chikamatsu, H. Kumigashira, M. Oshima, et al., "Photoemission from Buried Interfaces in SrTiO₃/LaTiO₃ Superlattices," *Phys. Rev. Lett.* **97**, 57601 (2006).
- [96] P. R. Willmott and J. R. Huber, "Pulsed laser vaporization and deposition," *Rev. Mod. Phys.* **72**, 315 (2000).
- [97] C. Cantoni, J. Gazquez, F. Miletto Granozio, M. P. Oxley, M. Varela, A. R. Lupini, S. J. Pennycook, C. Aruta, U. S. di Uccio, et al., "Electron Transfer and Ionic Displacements at the Origin of the 2D Electron Gas at the LAO/STO Interface: Direct Measurements with Atomic-Column Spatial Resolution," *Adv. Mater.* **24**, 3952–3957 (2012).
- [98] T. Mizoguchi, H. Ohta, H.-S. Lee, N. Takahashi, and Y. Ikuhara, "Controlling Interface Intermixing and Properties of SrTiO₃-Based Superlattices," *Adv. Funct. Mater.* **21**, 2258–2263 (2011).
- [99] M. L. Reinle-Schmitt, C. Cancellieri, D. Li, D. Fontaine, M. Medarde, E. Pomjakushina, C. W. Schneider, S. Gariglio, P. Ghosez, et al., "Tunable conductivity threshold at polar oxide interfaces," *Nat. Commun.* **3**, 932 (2012).
- [100] I. Fongkaew, S. Limpijumnong, and W. R. L. Lambrecht, "Effects of structural relaxation, interdiffusion, and surface termination on two-dimensional electron gas formation at the LaAlO₃/SrTiO₃ interface," *Phys. Rev. B* **92**, 155416 (2015).
- [101] J. J. Pulikkotil, S. Auluck, P. Kumar, A. Dogra, and R. C. Budhani, "Energetics and electronic structure of La/Sr disorder at the interface of SrTiO₃/LaTiO₃ heterostructure," *Appl. Phys. Lett.* **99**, 81915 (2011).
- [102] B. Jalan, S. J. Allen, G. E. Beltz, P. Moetakef, and S. Stemmer, "Enhancing the electron mobility of SrTiO₃ with strain," *Appl. Phys. Lett.* **98**, 132102 (2011).
- [103] H. W. Jang, D. A. Felker, C. W. Bark, Y. Wang, M. K. Niranjana, C. T. Nelson, Y. Zhang, D. Su, C. M. Folkman, et al., "Metallic and Insulating Oxide Interfaces Controlled by Electronic Correlations," *Science* **331**, 886–889 (2011).
- [104] F. J. Wong, S.-H. Baek, R. V. Chopdekar, V. V. Mehta, H.-W. Jang, C.-B. Eom, and Y. Suzuki, "Metallicity in LaTiO₃ thin films induced by lattice deformation," *Phys. Rev. B* **81**, 161101 (2010).
- [105] A. Janotti, D. Steiauf, and C. G. Van de Walle, "Strain effects on the electronic structure of SrTiO₃: Toward high electron mobilities," *Phys. Rev. B* **84**, 201304(R) (2011).
- [106] R. L. Moreira and A. Dias, "Comment on 'Prediction of lattice constant in cubic perovskites,'" *J. Phys. Chem. Solids* **68**, 1617–1622 (2007).
- [107] Z. Huang, K. Han, S. Zeng, M. Motapothula, A. Y. Borisevich, S. Ghosh, W. Lü, C. Li, W. Zhou, et al., "The Effect of Polar Fluctuation and Lattice Mismatch on Carrier Mobility at Oxide Interfaces," *Nano Lett.* **16**, 2307–2313 (2016).

- [108] W. M. Lü, X. Wang, Z. Q. Liu, S. Dhar, A. Annadi, K. Gopinadhan, A. R. Barman, H. B. Su, T. Venkatesan, et al., “Metal-insulator transition at a depleted LaAlO₃/SrTiO₃ interface: Evidence for charge transfer induced by SrTiO₃ phase transitions,” *Appl. Phys. Lett.* **99**, 172103 (2011).
- [109] F. Bi, M. Huang, C.-W. Bark, S. Ryu, S. Lee, C.-B. Eom, P. Irvin, and J. Levy, “Electro-mechanical response of top-gated LaAlO₃/SrTiO₃,” *J. Appl. Phys.* **119**, 25309 (2016).
- [110] M. S. Park, S. H. Rhim, and A. J. Freeman, “Charge compensation and mixed valency in LaAlO₃/SrTiO₃ heterointerfaces studied by the FLAPW method,” *Phys Rev B* **74**, 205416 (2006).
- [111] J. Lee and A. A. Demkov, “Charge origin and localization at the n-type SrTiO₃/LaAlO₃ interface,” *Phys. Rev. B* **78**, 193104 (2008).
- [112] R. Pentcheva and W. E. Pickett, “Avoiding the polarization catastrophe in LaAlO₃ overlayers on SrTiO₃ through polar distortion,” *Phys. Rev. Lett.* **102**, 107602 (2009).
- [113] F. Schoofs, T. Fix, A. S. Kalabukhov, D. Winkler, Y. Boikov, I. Serenkov, V. Sakharov, T. Claeson, J. L. MacManus-Driscoll, et al., “Optimized transport properties of LaAlO₃/SrTiO₃ heterointerfaces by variation of pulsed laser fluence,” *J. Phys. Condens. Matter* **23**, 305002 (2011).

Chapitre I – Résumé

La chapitre I a pour ambition d'introduire la thèse en contextualisant le sujet lié à l'apparition d'un gaz bidimensionnel à l'interface des hétérostructures $\text{LaAlO}_3/\text{SrTiO}_3$. La famille de matériaux de structure perovskite, de formule ABX_3 , a connu un essor considérable de par la grande diversité d'éléments qui peut être insérée afin d'élaborer la structure cristalline. Dans cette thèse, nous nous sommes intéressés en premier lieu au titanate de strontium (SrTiO_3) dont les propriétés en font un des matériaux le plus utilisé dans la conception d'hétérostructures. Il cristallise dans une structure cubique ($a = 3.905 \text{ \AA}$) à température ambiante, faite d'une alternance de plans neutres $(\text{SrO})^0/(\text{TiO}_2)^0$ et dont le gap (3.2 eV) le place à la frontière entre les matériaux isolants et semi-conducteurs. Toutefois, le cristal est soumis à de nombreuses distorsions, notamment, suivant la configuration électronique des atomes du matériau. En effet, suite à la première levée de dégénérescence des cinq orbitales 3d du titane, due au champ cristallin octaédrique que forment les anions d'oxygènes autour de l'atome de titane, ces orbitales sont dédoublées suivant leur orientation vis-à-vis des orbitales p des oxygènes. De la même façon, en fonction de l'occupation des orbitales d du titane, une seconde levée de dégénérescence apparaît afin de stabiliser la structure. Cet effet, connu sous le nom d'effet Jahn-Teller, a pour conséquence une contraction ou une elongation des octaèdres d'O. Ainsi, ces modifications structurales peuvent avoir de profondes conséquences sur ces systèmes à électrons fortement corrélés. Dans un deuxième temps, on s'est concentré sur l'aluminate de lanthane (LaAlO_3) qui se présente sous la forme d'une structure pseudo-cubique avec un paramètre de maille proche de SrTiO_3 ($a = 3.791 \text{ \AA}$), avec une alternance de plan polaire $(\text{LaO})^+/(\text{AlO}_2)^-$, et avec un gap plus grand (5.6 eV) ce qui en fait donc un isolant. Nous nous sommes ensuite concentrés sur le matériau essentiel de cette thèse, l'hétérostructure $\text{LaAlO}_3/\text{SrTiO}_3$. Nous avons abordé ses principales propriétés, à savoir la supraconductivité, le magnétisme, et surtout le gaz électronique bidimensionnel à haute mobilité (2DEG). Notamment, nous avons défini les conditions à respecter, et comment les réaliser, pour optimiser la conduction à l'interface de ce système que sont la terminaison TiO_2 à la surface du substrat SrTiO_3 , ainsi qu'une épaisseur de film critique de quatre mailles élémentaires. Malgré le fait que le 2DEG ait été mesuré à l'interface de l'hétérostructure, les mécanismes à l'origine de cette conduction font débat. Nous avons donc effectué une vaste étude bibliographique sur chacun des mécanismes afin d'apporter un éclairage global sur la littérature et comprendre ce manque de consensus au sein de la communauté scientifique.

Lors de la découverte du gaz électronique à l'interface en 2004, une première hypothèse a été émise pour expliquer ce phénomène. La croissance d'un film polaire sur un substrat non polaire engendre l'apparition d'un potentiel électrostatique qui diverge linéairement avec l'épaisseur du film déposé. A

partir d'une épaisseur de quatre mailles élémentaire, un phénomène appelé catastrophe polaire se produit et aboutit au transfert d'un demi électron (en moyenne) de la surface du film vers un atome de titane présent à l'interface. Néanmoins, bien que plusieurs éléments aillent dans le sens de ce modèle théorique, les résultats expérimentaux publiés dans la littérature démontrent que la catastrophe polaire ne peut être avancée comme étant le seul mécanisme à l'origine de la conduction. Ensuite, les lacunes d'oxygènes ont été mentionnées comme un mécanisme alternatif à la présence en grande quantité de porteurs de charges. Ces défauts intrinsèques libèrent deux électrons qui migrent vers l'interface afin de compenser le potentiel divergeant. Ces porteurs sont donc fortement suspectés de participer à la conduction. Les lacunes d'oxygènes peuvent être formées de différentes manières, toutefois la pression partielle d'oxygène, utilisée lors de la croissance des films LaAlO_3 , a été avancée comme étant le principal paramètre contrôlant la concentration de ces défauts. Notamment, la disparition de la conduction à l'interface d'échantillons élaborés à basse pression d'oxygène puis soumis à un recuit, a permis d'établir une influence certaine des lacunes d'oxygènes sur les propriétés électriques. Par contre, certaines publications ont montré que des échantillons réalisés à plus haute pression d'oxygène conservaient leur caractère conducteur, même après avoir éliminé les lacunes d'oxygènes (recuit). De plus, la présence de ces défauts n'explique pas l'épaisseur critique nécessaire à l'apparition du 2DEG, de même que la terminaison préférentielle du substrat. Ceci tend à démontrer que, bien qu'elles aient une influence, les lacunes d'oxygènes ne représentent pas le seul mécanisme responsable de la conduction. Le troisième mécanisme évoqué dans la littérature est l'interdiffusion des espèces cationiques. En effet, initialement l'interface des hétérostructures était communément considérée comme étant abrupte, sans aucun échange entre les atomes du film et du substrat. Or depuis, un nombre considérable d'études a démontré la présence d'une interdiffusion, engendrée par la technique de dépôts et/ou pour compenser le dipôle à l'interface. Ce phénomène résulte d'une part en la formation du composé $\text{La}_x\text{Sr}_{1-x}\text{TiO}_3$, connu pour être conducteur avec la substitution de cations Sr^{2+} par La^{3+} , qui va fournir des électrons afin de compenser le déséquilibre électronique. Les propriétés électroniques s'en retrouvent donc améliorées. Toutefois, le mécanisme d'interdiffusion ne peut pas prétendre non plus à être seul à l'origine du déclenchement de la conduction. En effet, la découverte de ces échanges cationiques au sein d'hétérostructures isolantes ne favorise pas cette démarche. Il n'en reste pas moins vrai que l'interdiffusion influe fortement sur les propriétés du système. Par exemple, la substitution des cations A, de taille différente, implique une déformation du réseau. Ces distorsions structurales représentent également un facteur important à considérer dans les mécanismes liés à la conduction. Plusieurs études ont montré que la déformation, qu'elle soit en tension ou en compression, dégrade la conductivité voir la détruit. Les distorsions structurales peuvent prendre différentes formes suivant l'environnement des éléments impliqués. Dans un premier temps, la déformation épitaxiale, due à la différence de mailles des réseaux cristallins du film et du substrat, débouche sur une diminution du paramètre c du film, qui se retrouve en compression selon [001]. Puis, l'état d'oxydation du titane peut également apporter une déformation supplémentaire via l'effet Jahn-Teller. De même, la présence de lacunes cationiques, et notamment les lacunes de strontium, ont été évoquées comme sources potentielles d'une expansion de la maille. De plus, le champ polaire présent dans le film peut également provoquer le flambement du réseau cristallin. La distance entre les cations et les anions induit un champ de dépolarisation. Par contre, une fois encore, il semble difficilement concevable de considérer que les distorsions structurales soient à l'origine de la conduction. Tout d'abord car elles ont été caractérisées dans des systèmes isolants, et ensuite car elles ne permettent pas d'apporter des porteurs de charge ni d'améliorer leur

mobilité, au contraire. Le dernier mécanisme proposé dans la littérature pour expliquer l'apparition du 2DEG à l'interface LaO/TiO₂ est la stœchiométrie du film. Lors du dépôt du film, suivants les paramètres de croissance définis, des lacunes cationiques peuvent apparaître dans le film, et impacter de façon significative la taille du réseau cristallin ainsi que les propriétés de l'hétérostructure. Néanmoins, des avis divergents apparaissent sur la relation étroite entre le taux de La/Al et la transition isolant/conducteur. De plus, ce phénomène est largement associé avec les échanges cationiques entre film et substrat, ce qui jette un peu plus de doutes sur le caractère exclusif de l'influence de la stœchiométrie du film sur la conduction à l'interface de LaAlO₃/SrTiO₃.

Pour conclure sur ce chapitre, aucun des mécanismes suspectés d'être à l'origine du 2DEG à l'interface des hétérostructures LaAlO₃/SrTiO₃ n'a pu être identifié comme étant l'unique responsable de la conduction. Une synergie entre tous ces phénomènes semblent être une théorie plus réaliste. Le manque de consensus au sein de la communauté provient finalement de l'immense variété de techniques et de conditions utilisées pour élaborer les hétérostructures. Les structures étudiées sont donc différentes, avec des propriétés distinctes, et donc une grande variabilité des conclusions établies. Une profonde compréhension du lien entre les conditions de croissance et la structure atomique est nécessaire afin de prévoir et de contrôler les défauts introduits et les mécanismes de transport dans ces systèmes à base d'oxydes.

Chapter II

Experimental methods

This chapter will be focused on the description of the experimental methods performed during the thesis. The film growth via Pulsed Laser Deposition will be first developed as well as the influence of the process parameters on the heterostructure properties. Then the electron microscopy tools used and their associated spectroscopies will be detailed. Following this, the ion beam analysis methods will be presented by distinguishing two techniques differing by the incident particles energy used. Finally, the method to measure the transport properties will be exposed.

It is noteworthy that all samples studied in this thesis were prepared and synthesized at NASA Glenn Research Center, in Cleveland, Ohio (USA), by Richard Akrobetu under the supervision of Prof. Alp Sehirlioglu. The electrical measurements were carried out by Nicholas Goble under the supervision of Prof. Xuan Gao at the Department of Physics of Case Western Reserve University in Cleveland, Ohio (USA). I was kindly welcomed four months in these laboratories in Cleveland in order to improve my understanding on the process and to investigate the transport measurements performed on our systems.

Most of experimental results were obtained through several deep collaborations. The TEM investigations were mainly led at Laboratoire de Physique des Solides, Université Paris-Sud, with Michael Walls, while the RBS works were achieved at the CEA Saclay DRF/IRAMIS/NIMBE/Laboratory for the study of light elements (LEEL) with Pascal Berger, and the MEIS measurements were performed at the laboratory CEA tech/Leti/DTSI/SCMC in Grenoble, with Denis Jalabert.

II.1 Pulsed Laser Deposition (PLD)

II.1.1 Substrate Preparation

As mentioned in the previous chapter, the as-received STO samples exhibited a mixed surface termination with SrO and TiO₂ layers. In order to optimize the transport properties and obtain a TiO₂-terminated substrate, a chemical pre-treatment has to be applied to the substrate before film

deposition. The STO substrates were etched with a chemical solution of ammonium fluoride and hydrofluoric acid at pH = 6 for 10 s. TiO_2 is chemically stable contrary to SrO which dissolved in the chemical bath. The substrates were then rinsed in deionized water. In order to optimize the termination of the substrates and improve the recrystallization, they were submitted to an annealing process at 950°C in a tube-furnace for one hour in an oxygen-rich atmosphere. The substrates were then cooled down to room temperature. The surface morphology was checked with AFM (Agilent Technologies). An example is presented in Figure II.1c.

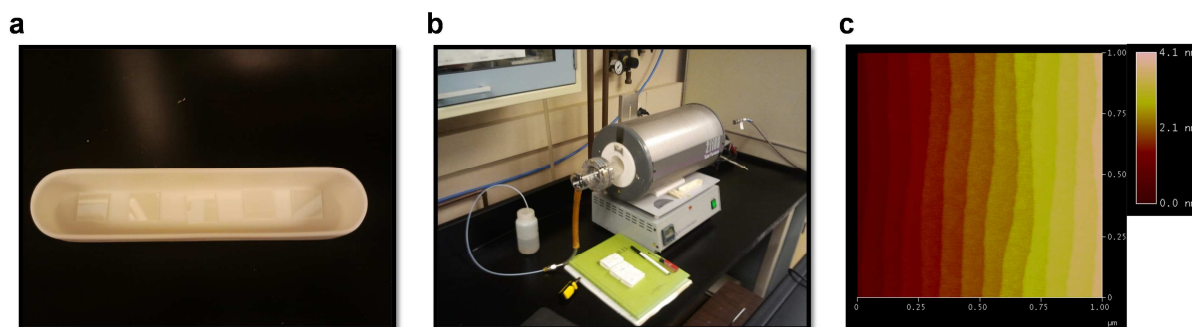


Figure II.1 | Substrate preparation. **a**, As-received substrates after chemical treatments. **b**, Tube-furnace used to anneal the substrates. **c**, AFM image of pH = 6 BHF acid etched STO substrate resulting in Ti-termination with no visible etch pits. From R.Akrobetu's data.

II.1.2 PLD Process

A large number of techniques were developed to deposit films over many kind of substrates. The most widespread ones include the Pulsed Laser Deposition (PLD), the Molecular Beam Epitaxy (MBE), the Atomic Layer Deposition (ALD); the Chemical Vapor Deposition (CVD), and the Magnetron Sputtering (MS). The main distinction dividing these deposition techniques is the physical/chemical mechanisms involved to produce the plasma/gaseous beam that impact the film structure and properties of the system [1]. For epitaxial film growth, and in particular LAO growth on STO substrates, PLD is the most popular technique used in the literature for research purpose. This can be understood by its good performances, the capability for stoichiometric transfer of material from target to substrate and the relatively high growth rate compared to ALD and MBE, the ease of use and above all, the relative low costs of its equipment. The technique was first used in the middle of sixties for the preparation of semiconductors [2], and was popularized in the late eighties by the work on the superconductors [2,3]. Nowadays, the PLD technique is chosen to develop a wide combination of oxides.

The PLD process consists in sending a high-energetic pulsed (typically 20 ns) excimer laser onto a target of desired film composition, via a system of mirrors. The laser is absorbed by the target and the photons are converted first into electronic excitations and then into thermal, chemical, and mechanical energy inducing the target ablation when the energy per surface area deposited exceeds an ablation threshold. The target's species, including neutrals, ions and electrons, are ejected and expand forward in the form of a dense plasma plume towards the substrate. Then the plume species condense on the substrate, located perpendicularly inside the ultrahigh-vacuum PLD chamber, and the film grows. The principle of PLD is schematized in Figure II.2, and the PLD device is presented in Figure II.15.

The growth of the film is carried out in three different modes, either layer-by-layer (2D, Frank – Van Der Merwe) with a good surface quality, either by islands formation (3D, Volmer-Weber) inducing surface roughness, or a combination of bi-dimensional and three-dimensional growth (Stranski – Krastanov). We will detail briefly these growth modes later.

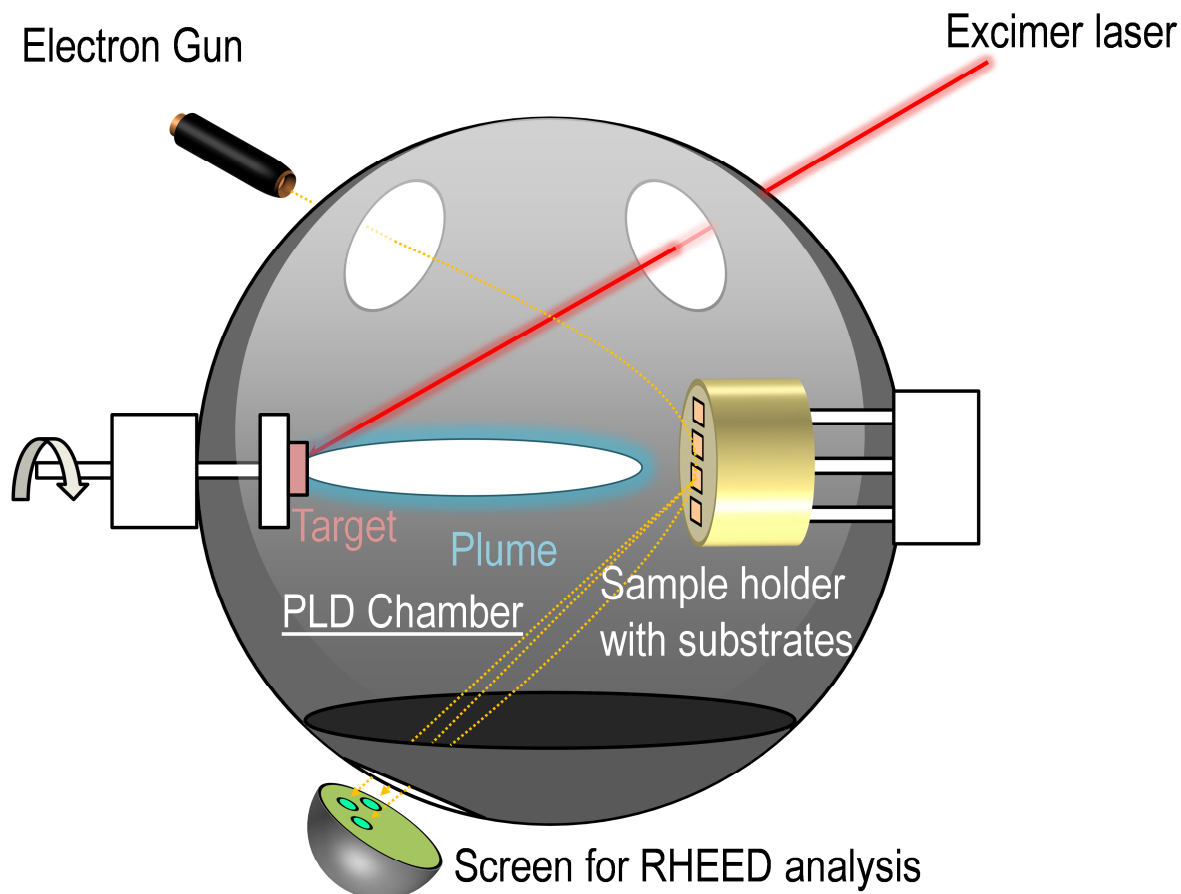


Figure II.2 | Illustration of the PLD process. The laser beam impacts the target from which species are ejected in the form of a plasma plume in the direction of substrates located perpendicularly. The growth is followed by Reflection High Energy Electron Diffraction.

The growth depends strongly on the process parameters, such as the pressure within the PLD chamber, the plume angle with the substrate, the substrate temperature, the laser fluence, the laser frequency, the target-to-substrate distance etc. While the pressure impacts directly the plume, as it will be specified in the following part, variations of the plume angle modify the stoichiometry of the deposit. The temperature influences the mobility of species, their diffusion and their adherence on the substrate. The target-to-substrate distance is also decisive for the film growth. An increase of this distance decreases the density of the plume reaching the substrate and the energy of the species impinging the surface, and reduces the damage induced. However it also reduces the growth rate so that an optimum value is searched for each system processed. The frequency and pulse duration of the laser influence the energy deposited in the target and the amount of species ablated. One of the key parameters in the perspective of film growth is the fluence of the laser. This notion is defined by the energy delivered by an impulsion of the laser, per unit area impacted. The fluence directly impacts the particle flux and growth mechanism. Lower fluences promote three-dimensional growth,

while excessive ones damage the substrate surface and thus the heterostructure properties. As stated by Golalikhani *et al.* [4], looking for a layer-by-layer growth of stoichiometric LAO on STO by PLD, a narrow harmony has to be respected in order to induce this perfect film growth. We will discuss the influences of the growth conditions on the LAO/STO heterostructures properties in more details in the next sections.

II.1.2.1 Plasma mechanisms

The phenomena involved in the PLD growth are strongly dependent on the interaction occurring between the laser and the target, giving rise to the plasma plume. The mechanisms of the target species ablation, the creation and the expansion of the plume are very complex and not well understood [1,3,5]. The pulsed laser impinges the target with sufficient energy to melt, evaporate and ionize its surface species (Figure II.3b) that are ejected in the form of a plasma plume. The short pulsation duration allows minimizing thermal destructions of the target and phase segregation. The dense plume ejection originates from the thermal and pressure gradients between the melted target surface and the PLD chamber and/or the electrostatic repulsion with the species ionized by the laser interaction with the plume. As the plume is expanding, the very short laser pulsation is still impacting the target. This results in an interaction between the laser and the plume (Figure II.3c) and an excitation and ionization of its species [5]. After the laser pulsation, the target re-solidification occurs, with asperities left by the part ejected (Figure II.3d). This simple model provides a first approach to the complex mechanisms contributing to the formation of the plasma and to thin film depositions.

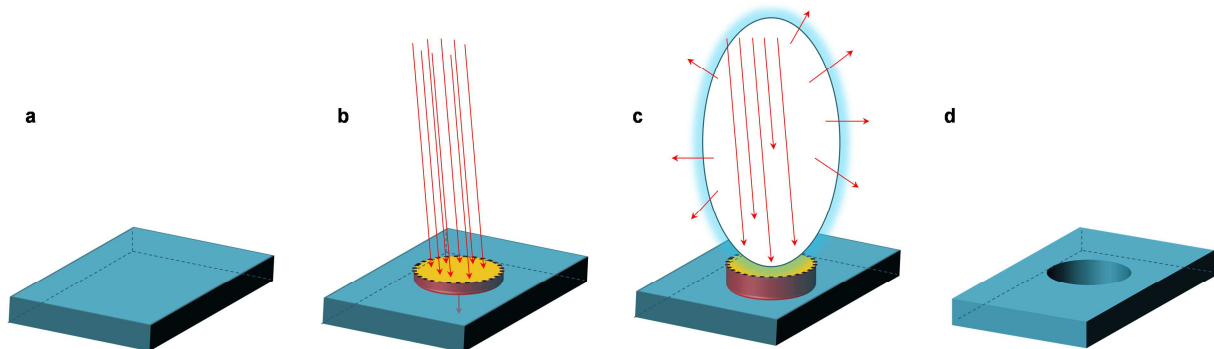


Figure II.3 | Illustrations of the target extraction and projection. a, Target material. **b,** Laser absorption and target melted area formed. **c,** Formation and expansion of the plume, and interaction with the laser. **d,** Re-solidification of the target after the laser impingement.

II.1.2.2 Growth monitoring by RHEED

An *in-situ* monitoring of the layer-by-layer film growth is achieved by via Reflection High Energy Electron Diffraction (RHEED). A high energy electron beam ($V = 30$ kV, Emission current = -0.05 μ A in our study) hits the substrate surface with a shallow incident angle of a few degrees (between 1° and 2°). The grazing incidence makes the electron beam more sensitive to the sample surface. One part of the beam is diffracted by the sample surface, and the diffraction pattern is collected on a fluorescent screen or recorded with a CCD camera. The construction of a RHEED pattern of a thin film can be understood in the reciprocal space. The two-dimensional array of the surface atoms turns into vertical lines in the reciprocal space, the *reciprocal rods*. When these rods cross the Ewald sphere the condition for Bragg diffraction are fulfilled. The intersection of the rods with the Ewald sphere results in streaks disposed along a Laue circle (Figure II.4). The shape of the streaks (height and width) allows

following the deposition and the quality of the film growth. In addition Kikuchi lines can be formed from electrons which have been firstly inelastically scattered and subsequently diffracted. They indicate a structure well crystallized.

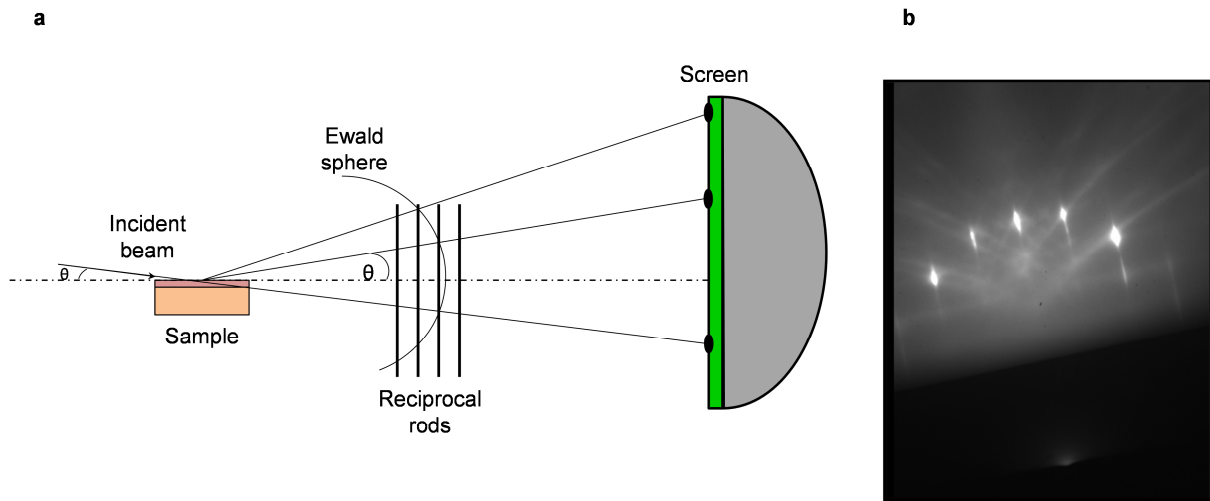


Figure II.4 | RHEED pattern. **a**, Illustration of the RHEED principle. Streaks are formed by the intersections of the reciprocal lattice rods with the Ewald sphere. **b**, Experimental RHEED pattern, provided by R.Akrobetu. Streaks are clearly seen, forming a semi-circle, as well as thin Kikuchi lines.

In order to control the thickness and crystallinity of the film, the RHEED signal is followed for growth monitoring during the deposition. The different steps of the layer-by-layer growth lead to oscillations in the RHEED signal intensity. The morphology of the growing monolayer implies variations of the signal. The atomic roughness created by an uncomplete coverage leads to a decrease of the electronic signal intensity. The film atoms behave like scattering centers resulting in a weaker RHEED signal. The intensity is maximal once a layer is completed, and decreases again while an upper monolayer is in formation, as shown in Figure II.5. Therefore, these oscillations give the number of unit cells deposited accurately during the PLD process. Figure II.6a gives an example for a 10 unit cells film deposited. Figure II.6b shows that each oscillation encloses higher frequency ones representing the number of laser pulsations. A complete period of a RHEED intensity oscillation corresponds to a unit cell deposited. This model is however not adapted to explain the experimental RHEED pattern variations for growth modes other than bi-dimensional.

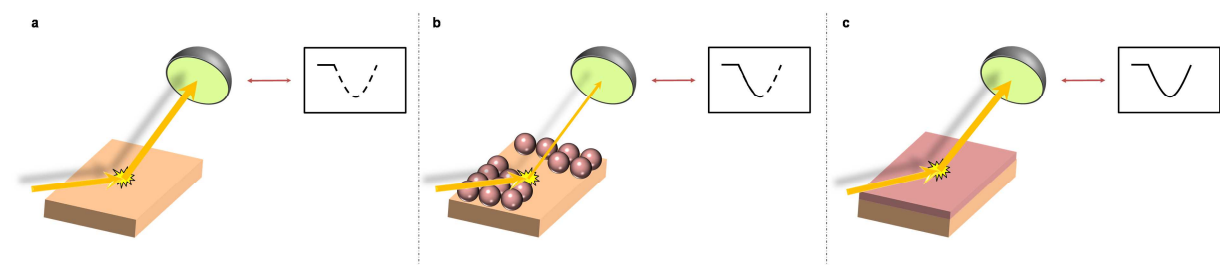


Figure II.5 | Illustration of the RHEED intensity modulation during a bi-dimensional film growth. **a**, The flat surface of the substrate does not engender deep modifications of the incident electron beam intensity. **b**, The intensity detected on the screen decreases due to the roughness surface occurring during the layer-by-layer growth. **c**, Once a unit cell is deposited, the flat surface reflected higher signal intensity.

RHEED patterns and their oscillations give information on the surface structure and morphology, the thickness of the film and the growth modes during the deposition. In principle, it is also possible to determine the lattice constants from the diffraction patterns.

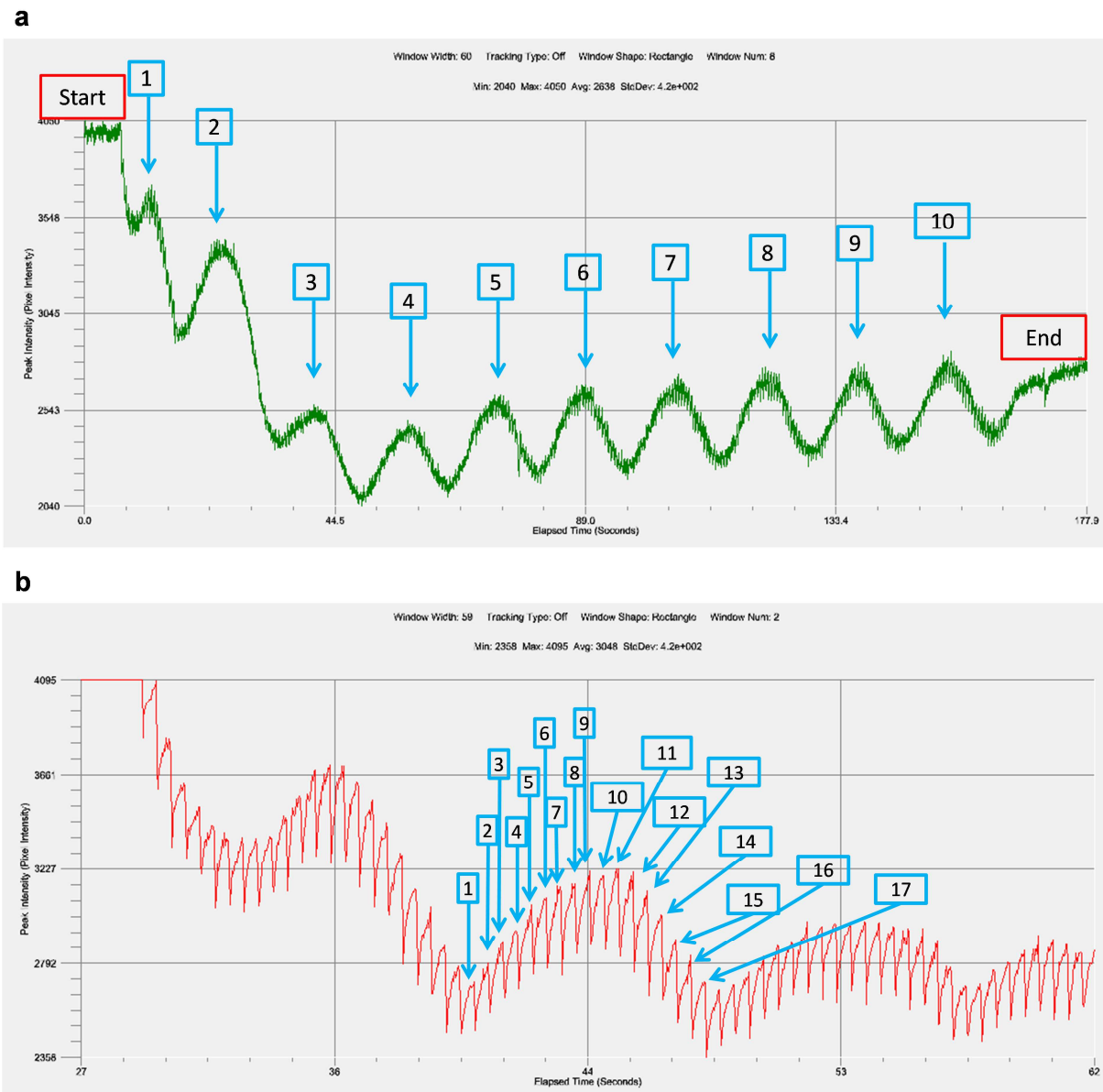


Figure II.6 | Modulations of RHEED signal intensity. From R. Akrobetu work. **a**, Each oscillation corresponds to a unit cell deposited. Here we show an example of a ten unit cells film deposited. **b**, Magnification of an oscillation. As seen, each oscillation is made of several laser pulsations, hence here 17 pulsations were necessary to grown one unit cell.

Pulsed Laser Deposition is a deposition technique well dedicated to academic research. Willmott *et al.* [3] enumerated the numerous advantages of PLD process. Among them, the wide choice in the nature of the target, including complex oxides to metals, and even polymers, the ability to pulse the laser allowing controlling the film growth rate, or the position of the laser, outside the PLD chamber, permitting a larger device flexibility. The parameters can be tuned quite easily, often empirically, in order to promote the best thin film deposition. In terms of disadvantages, some appear to be crucial in the objective of the film quality [3]. Notably the defects produced at the substrate surface by the

high energetic impingement of the plume, the inhomogeneous angular energy distribution of the ablated species in the plume resulting in variations of composition across the film. Maybe one of the most difficult obstacles to overcome is the ejection of droplets from the target and carried by the plume that dramatically degrade the heterostructure quality. These droplets of condensed sputtered materials originate from the synergy between three phenomena, the boiling of the target surface, the recoil ejection and the exfoliation. More details of these phenomena can be found in [3]. In order to avoid the formation of such contamination, Gorbunov *et al.* [6] proposed a simultaneous ablation of two targets with crossed plasma plumes, or an off-axis deposition. Alternatively, the rotation of the target minimizes the development of these droplets. Finally PLD is not really considered for industrial applications since the growth rate and the surface covered are too low to be industrially efficient.

The main challenge surrounding PLD is to identify the influence of each growth parameter on the mechanisms involved in the growth process, and overall in the properties of the heterostructures.

II.2 Film growth

Ideally the growth of a thin film on a substrate is initiated by a nucleation process with the formation of nanoclusters of the deposited particles, followed by the development of these agglomerates that gives rise to the film growth. Actually, the process is much more complex as, in addition to the adsorption of the particles impacting the substrate, the desorption and diffusion along the surface have to be taken into account in the film formation.

We have mentioned previously three distinct growth modes which can be induced, depending on the free energies of the substrate and film surfaces, and of their interface. If the sum of the film surface and film/substrate interface free energies is weaker than the substrate surface free energy, the system will lower its total energy by covering the substrate, and the film grows layer-by-layer (Figure II.7a). This bi-dimensional growth mode, named Frank - Van der Merwe mode, results in flat surfaces, with the best deposition quality. In contrast, if the sum of the film surface and film/substrate interface free energies is higher than the substrate surface free energy, the film follows the Volmer - Weber growth (Figure II.7b). The low surface reactivity disadvantage particles-substrate bonds and the low surface energy of the substrate favors free surface. Thus the first clusters grow into islands in order to minimize the contact between the particles from the film and the substrate, and the film is formed by coalescence of these islands. This three-dimensional growth mode leads to rough film surfaces. The last mode consists in the intermediate case between the bi-dimensional and the three-dimensional growth, and is called Stranski – Krastanov (Figure II.7c). The film growth starts by a 2D layer-by-layer mode and turns to islands formation. One possible origin for this transition is the release of elastic energy stored due to epitaxial strain. This simplified description of these models, hides more parameters included in the free energies and that influence significantly the growth mode adopted by the film such as the film thickness, the substrate temperature or the pressure.

Studies investigating heterostructures and their interface phenomena generally require a Frank – Van der Merwe growth mode with a continuity of lattice plane across the interface. Such an epitaxial growth is defined according to the relative crystalline orientation of the film and substrate. Two types of epitaxy are distinguishable, the homoepitaxy for which the film and the substrate are made of the same compound, and the heteroepitaxy for which the film and the substrate are distinct. In the latter case, the lattice parameters are, most of the time, different resulting in lattice mismatch.

For small mismatches (below $\approx 3\%$, depending on the elastic constants of the film) a coherent growth can be obtained for thin films. The growing film is storing elastic energy which is proportional to the thickness deposited. Above a thickness threshold the elastic limit is reached and the strain is accommodated plastically by structural relaxations [7]. Misfit dislocations or Stranski – Krastanov islands are created that strongly affect the heterostructures properties.

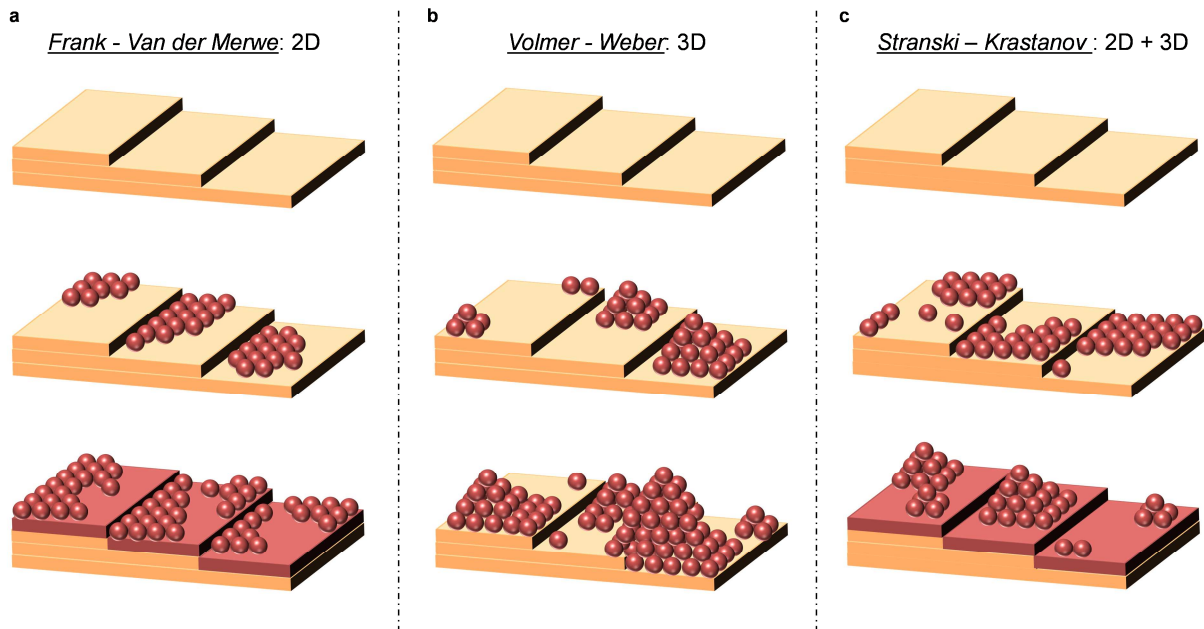


Figure II.7 | Illustrations of film growth modes on a substrate. a, Frank – Van der Merwe. **b,** Volmer – Weber. **c,** Stranski – Krastanov.

In conclusion several conditions must be fulfilled to deliver high quality hetero-interfaces. The deposition process should not be too energetic in order to minimize the creation of defects on the substrate surface, a layer-by-layer growth mode should occur, the lattice parameters between the film and the substrate should closely match to minimize the defects at the interface, phase transformations should be avoided, coefficient of thermal expansion should be similar between film and substrate to limit thermal residual stresses on cooling, and no chemical reactions between the film and the substrate should occur [8].

II.3 PLD growth conditions

The PLD process is often described as a perfect method dedicated to thin films depositions thank to an atomic layer precision of the growth maintaining the stoichiometry between the target and the film. In practice several authors emphasized the complexity of this deposition technique [4,9–23]. Depending on the process parameters chosen, modification of the substrate surface, growth defects, non-stoichiometry can occur that will impact the electron gas spatial extension or modify the conduction mechanisms of the hetero-interface. The main PLD growth parameters to control are the laser fluence, the plume, the deposition angle, the target-to-substrate distance, the oxygen background pressure and the temperature.

II.3.1 Laser Fluence

In the first stage of the PLD, the laser beam is focused onto the surface of the target to eject its species towards the substrate. The laser fluence is defined as the energy deposited on the target per

unit of surface by the electromagnetic radiation. Laser fluence impacts the ablation mode, the film structure and stoichiometry, and thereby the properties of the interface.

II.3.1.1 Film stoichiometry

Several authors emphasized the strong role played by the laser fluence on the film stoichiometry [22,24,25]. They agree that B-sites cations are preferentially ablated from the target at high laser fluence, resulting in B-rich films, while A-sites cations are preferentially ablated for lower fluence, resulting in A-rich films. However the fluence threshold for a stoichiometric growth is subjected to debate. Ohnishi *et al.* [24] have grown Ti-rich Nb-doped STO films for fluences higher than 0.3 J.cm^{-2} . Wicklein *et al.* [22] revealed from XPS measurements that homoepitaxial STO film exhibited Sr-deficiency at higher laser fluence (i.e. 1.7 J.cm^{-2}). Finally, Breckenfeld *et al.* [25] emphasized similar results for heteroepitaxial LAO films grown on STO. The authors could characterize the effect of laser fluence on film stoichiometry using XPS and RBS (Figure II.9a). Depositing at higher fluence than 1.6 J.cm^{-2} led to Al-rich films and lowering laser fluence resulted in Al-deficient films.

II.3.1.2 Film structure

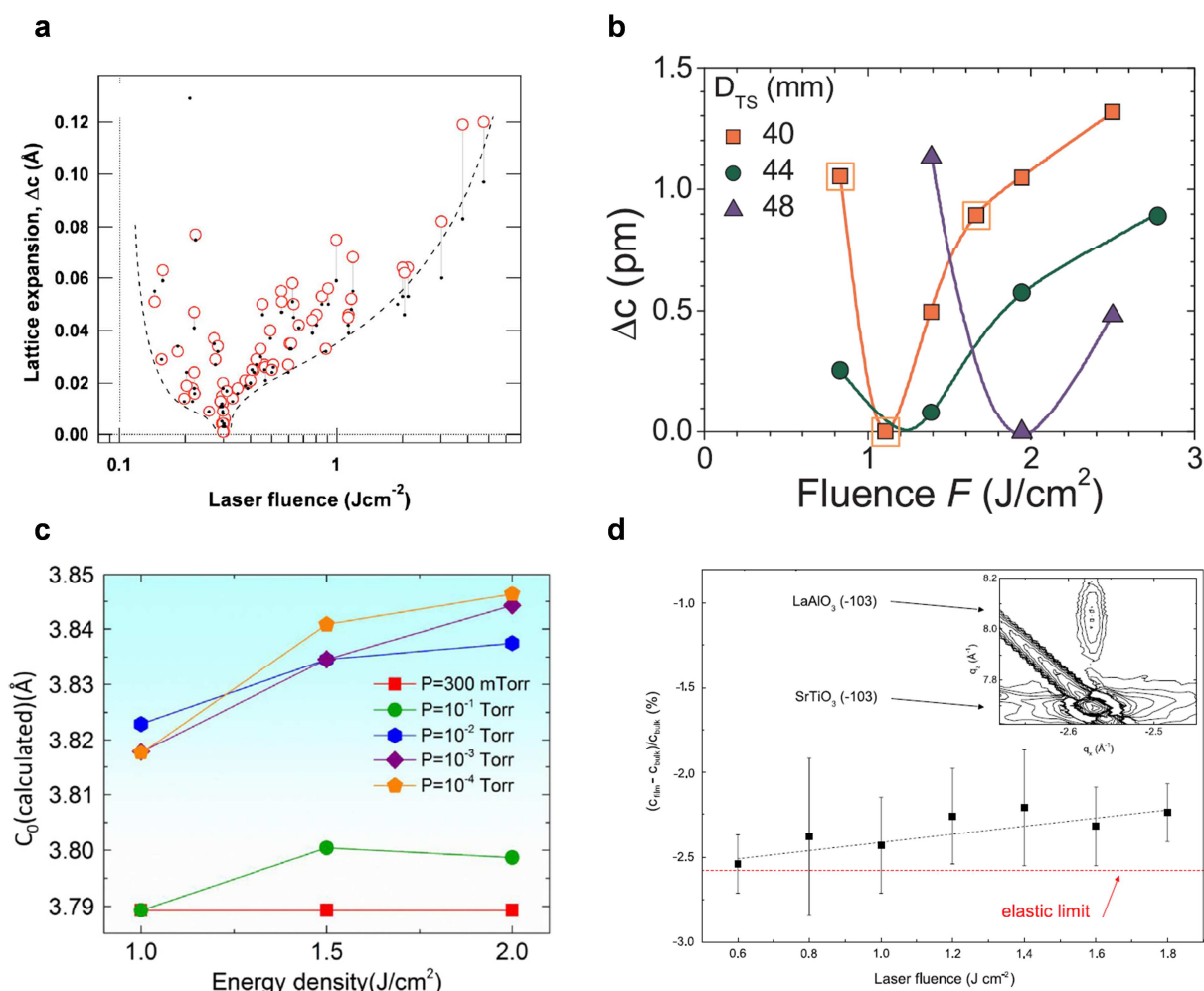


Figure II.8 | Influence of laser fluence on out-of-plane lattice parameter. a, Expansion of the Nb-STO film lattice parameter deposited at different laser fluences. From [24]. **b**, The c-lattice expansion of STO films as a function of laser fluence for various distance target-to-substrate distances. From [22].

c, Evolution of the LAO lattice parameter calculated depending on laser fluence. From [4]. **d**, Strain caused by the c-lattice modifications depending on the laser fluence. From [13].

Few months ago, Golalikhani *et al.* [4] worked on homoepitaxial LAO films and confirmed conclusions from a previous report [25] that the layer-by-layer growth mode is promoted for high laser energy densities, whereas island mode is observed for lower fluence. Moreover, the research group [4] illustrated the relationship between the out-of-plane lattice parameter and the laser fluence, reported in Figure II.8c. The laser fluence, and thus the non-stoichiometry, impacts directly the structure of the films [24] (Figure II.8a) by promoting c-lattice expansion [12,22,25] (Figure II.8b. Schoofs *et al.* [13] shared these conclusions by shedding light on the improvement of film crystallinity, and stoichiometry, for higher laser fluence through the MEIS spectra, while the structural characterizations confirmed the strong connection between the increase of this laser parameter and the c-lattice expansion (Figure II.8d). Higher fluence implies higher kinetic energy of the species impinging the surface, leading to formation of defects (i.e. vacancies, intermixing etc.), and thus to structural distortions. It is interesting to note here that the expansion of the lattice is observed for both high and low laser fluence, suggesting that the cationic vacancies is at the origin of the elongation whatever the nature of the vacancy (i.e. A-site or B-site). On the contrary, the c-axis of STO film exhibits no deviations from the bulk STO when the film is stoichiometric.

II.3.1.3 Electrical properties

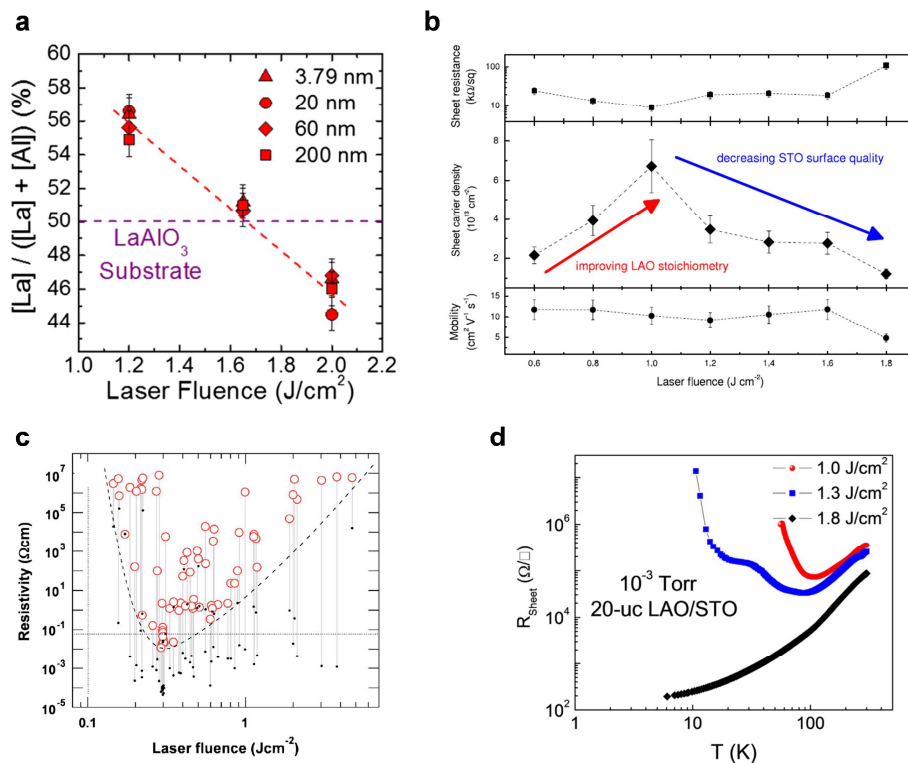


Figure II.9 | Influence of laser fluence on intrinsic properties of systems studied. **a**, LAO film stoichiometry variations as a function of laser fluence. From [25]. The films exhibited B-cations rich films for low laser energy density while they were B-cations deficient for high fluence. **b**, Electrical properties vs laser fluence in LAO/STO heterostructures. From [13]. **c**, Evolution of the resistivity in Nb-STO films deposited at different laser fluences. From [24]. **d**, Sheet resistance of LAO/STO heterostructures as a function of temperature for various laser fluence. From [21].

We have seen in Chapter I that the film stoichiometry impacts drastically the electrical properties of the LAO/STO heterostructures. Thus, varying the laser fluence should also result in variations in transport properties. This is reflected by Figure II.9. While the sheet resistance and mobility seem to be less subjected to the laser fluence variations, unless for the highest value, the carrier density is significantly affected (Figure II.9b). Furthermore, Liu *et al.* [21] showed that the temperature dependence of the sheet resistance varies with the laser fluence (Figure II.9d). While a resistance upturn is exhibited at low laser energy density, the metallicity is promoted at higher fluence. They attributed this result to the chemical affinity of Al with O, leading to donor vacancies. Since high laser fluence leads to Al-rich films, Liu *et al.* [21] assumed that this excess of Al reacts with O and promotes the formation oxygen vacancy at STO surface. Chambers *et al.* [26] estimated that the intermixing is not driven by the laser energy density. This is not in agreement with other works showing that even if a slight variation would be insufficient to cause dramatic damages, high laser fluence involves high kinetics species impacting the substrate surface, causing defects [27] and intermixing [13]. Gariglio *et al.* [28] proposed this alternative scenario, with the growth temperature, to show the intermixing dependence on the laser fluence.

These experimental results show that the laser fluence impacts the film stoichiometry and the out-of-plane lattice parameter. Owing to the influence of structural distortions and the film stoichiometry on the electrical properties of LAO/STO described in the previous chapter, it follows that the laser parameters have a dramatic impact on the electrical behavior of LAO/STO heterostructures.

II.3.2 Plasma plume

If the laser parameters display a strong influence on the LAO/STO properties, numerous other conditions affect the systems grown by PLD. Indeed, Wicklein *et al.* [22] showed that for the exact same laser fluence, the film stoichiometry can vary, as well as the size of the lattice, due to the distance target-to-substrate distance (Figure II.8b).

II.3.2.1 Target-to-substrate distance

The target-to-substrate distance fixes the probability for the plume species to interact with background gas species. When this distance increases, since the plume species are slowed by these collisions, they reach the substrate surface softly causing fewer damages. The target-to-substrate distance was also suggested as a possible parameter for adjusting the film stoichiometry [22]. Reducing this distance would allow the compensation of the B-cations deficiency induced by low laser fluence.

II.3.2.2 Plume Angle

Furthermore, besides the incongruent ablation and deposition state of the PLD process [18,22], laser fluence variations modify significantly the shape of the plume and its composition profile [24]. Notably, Droubay *et al.* [18] focused their researches on the angular distribution of the target elements within the plasma plume. They showed that the film composition varies as a function of the plume angle, by performing RBS measurements (Figure II.10). One observes that according to the plume angle, the composition of the film differs strongly, as well as the deposition rate of the film thickness. This is understandable since the species are more concentrated in the middle of the plume than in its extremities. This results in stoichiometric variations as a function of the angle between the substrate (orthogonal direction) and the plasma plume axis, La richer films being obtained at zero plume angle.

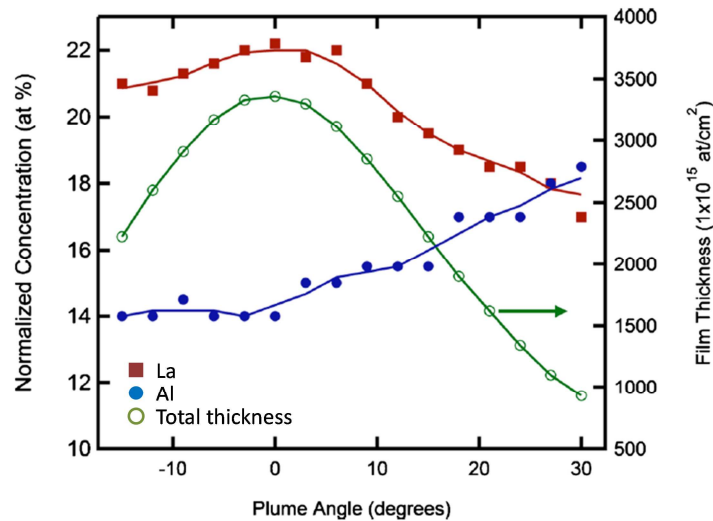


Figure II.10 | Distributions of LAO film cations and thickness as a function of the angle of the plume. Adapted from [18].

Qiao *et al.* [29] showed that, consistently with the above mentioned report [18], tuning the center of the plume on the substrate gives rise to non-stoichiometric films with Al-deficiency. In order to improve the stoichiometry, the authors advised to shift the substrate off the plume axis. Nevertheless, if the plume is not homogeneous, one expects to obtain heterogeneous distributions of cations over the substrate surface with significant differences for a large surface area.

II.3.3 Oxygen pressure

Laser ablation, plume expansion and film deposition occur in a chamber with a tunable background pressure, involving supplementary interactions. Figure II.8c shows that the lattice expansion at a given laser fluence varies with the oxygen pressure used in the PLD chamber during the growth of the homoepitaxial LAO. For high pressure conditions (3×10^{-1} Torr), the lattice parameters of the film remain close to the bulk value ones, regardless of laser fluence. However, decreasing the growth pressure from 10^{-1} Torr to 10^{-2} Torr increases the c lattice parameter, which varied with the laser fluence. It is noteworthy that the larger dilation of the cell occurs for the highest fluence combined with the lowest O pressure. This result confirms and strengthens the importance of the background pressure in the PLD chamber during the growth.

II.3.3.1 Film stoichiometry

Golalikhani *et al.* [30] revealed earlier that the oxygen pressure drives the LAO film stoichiometry. They measured the cation ratio by x-ray fluorescence as a function of the oxygen pressure, shown in Figure II.11a. For pressures between 10^{-4} Torr and 10^{-2} Torr, the films were La-rich with a larger deviation to stoichiometry as the pressure increased. At 10^{-1} Torr the films were nearly stoichiometric independently of laser fluence. This was in total contrast to a previous work lead by Kalabukhov *et al.* [20] who found that low oxygen pressures (10^{-4} mbar $\approx 7.5 \times 10^{-5}$ Torr) promote La-deficient films. Once again the distinct growth parameters such as the film thickness, the growth temperature, the laser fluence, or the cooling process, must be at the origin of such discrepancies. In any case, the variations of p_{O_2} have an impact on the film stoichiometry.

II.3.3.2 Film growth

Savinelli *et al.* [31], as well as Huijben *et al.* [32] correlated the quality and the growth mode to the O pressure. Maurice *et al.* [10] showed by using AFM and Transmission Electron Microscopy (TEM) that samples grown at high oxygen pressures (3×10^{-1} Torr) developed a three-dimensional growth with islands formations, associated with three-dimensional strain relaxations. This was confirmed later by Drera *et al.* [17]. This may explain the lattice distortions observed by Kalabukhov *et al.* [20] at higher O pressure.

II.3.3.3 Intrinsic defects

One of the most significant effects of the oxidation conditions is the promotion of donor intrinsic defects, the oxygen vacancies. As it was discussed in the previous chapter, the intrinsic defects have a crucial impact on the structure and the transport properties of LAO/STO heterostructures. It is now clearly established that low oxygen pressures ($\leq 10^{-5}$ Torr) result in oxygen vacancies formation [10,15,21,28,33,34], providing charge carriers to the system. While Chen *et al.* [16] pointed out the effect of the oxygen pressure on amorphous–crystalline LAO/STO heterostructures, numerous reports [15,25,33,35,36] emphasized that higher O_2 pressures imply weaker electrical properties with less sheet carrier density, and smaller carrier mobility (Figure II.11).

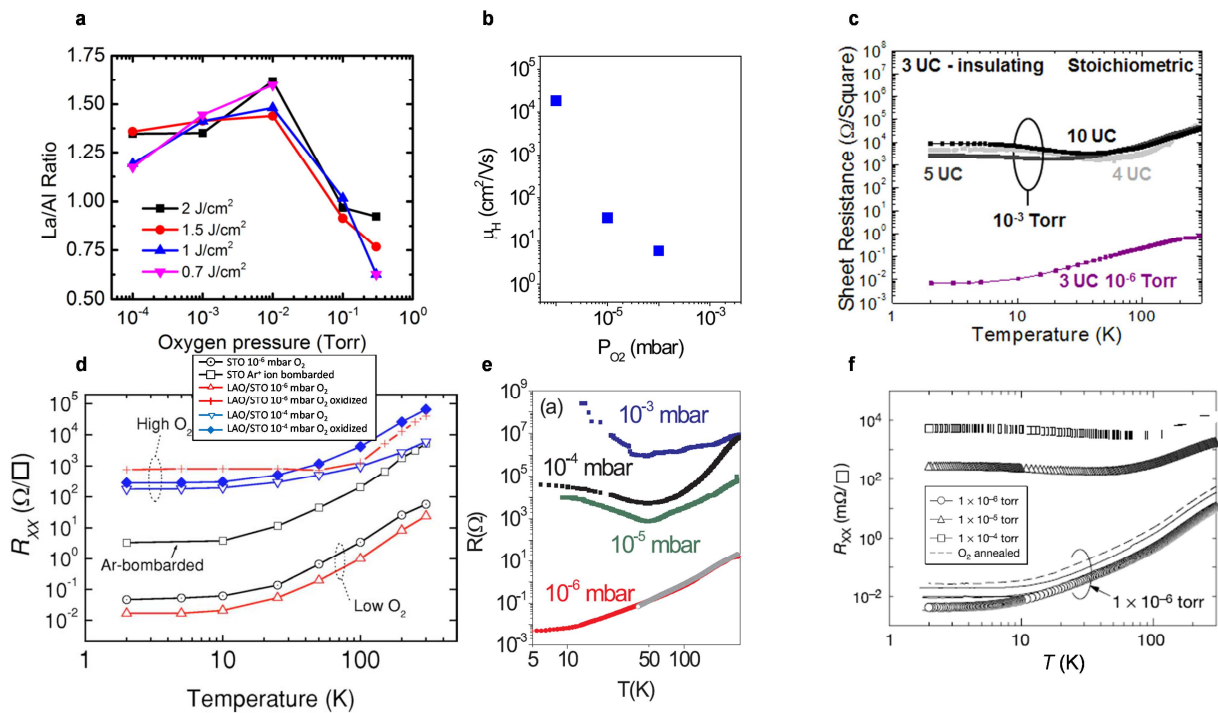


Figure II.11 | Influence of the oxygen pressure on the properties of LAO/STO heterostructures. **a**, Variations of the film stoichiometry at different oxygen pressures for diverse laser fluences. From [30]. **b**, Carrier mobility as a function of the oxygen pressure. From [33]. **c**, Dependence of the sheet resistance on the temperature for high and low oxygen pressure. From [12]. **d**, Effect of p_{O_2} and oxidizing on the sheet resistance. Electrical properties are degraded at higher O pressure, and even more after a re-oxygenation when the high density of defects are removed. From [35]. **e**, Effect of p_{O_2} on the sheet resistance. From [33]. **f**, Effect of p_{O_2} on the sheet resistance. From [36]. (10^{-4} Torr $\approx 1.33 \times 10^{-4}$ mbar).

II.3.3.4 Conduction extension

Furthermore, several authors highlighted the importance of the O pressure in the confinement of the interfacial conductive layer [11,12,15,17,20,28,33]. While the conduction is constrained to the first unit cells at the interface for high pressures [28], above 10^{-4} mbar ($\approx 7.5 \times 10^{-5}$ Torr), it is extended through the STO substrate for low pressures [11,15,28,33], below 10^{-5} mbar ($\approx 7.5 \times 10^{-6}$ Torr).

II.3.3.5 Cationic exchanges

In addition to the density of intrinsic defects, the growth oxygen partial pressure modifies the level of intermixing [20,31]. Kalabukhov *et al.* [20] acquired MEIS spectra in channeling mode, which is particularly sensitive to elements present in sample (film) surface. They found a larger intermixing between Sr and La cations at lower oxygen pressures. It is shown on Figure II.12 that the Sr peak is higher for the sample made at lower pressure, revealing higher content of Sr into the film. This result suggests a strong correlation between oxygen vacancies and cationic diffusion. This is totally in accordance with a more recent report [31] in which the $\text{La} \leftrightarrow \text{Sr}$ intermixing was shown reduced for higher pressure (10^{-1} mbar $\approx 7.5 \times 10^{-2}$ Torr) compared to the lower one (10^{-3} mbar $\approx 7.5 \times 10^{-4}$ Torr). Maurice *et al.* [10] related low-pressure growth to high energy particles reaching the substrate surface, resulting in an acceleration of the cationic diffusion and an enhancement of oxygen vacancies concentration.

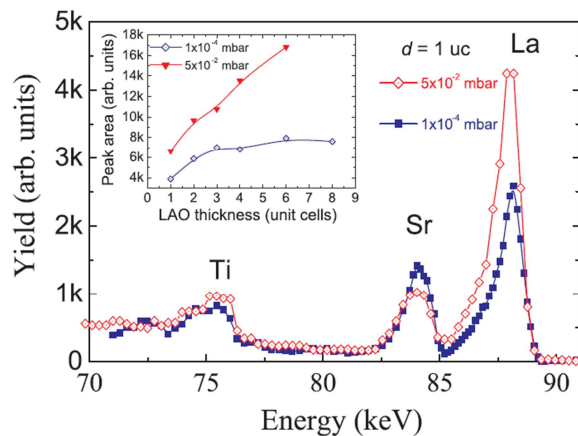


Figure II.12 | MEIS aligned experimental spectra for (one unit cell) LAO/STO samples grown at 5×10^{-2} mbar ($\approx 3.75 \times 10^{-3}$ Torr) and 10^{-4} mbar ($\approx 7.5 \times 10^{-5}$ Torr). From [20]. While the La peak is larger for higher O pressure due to structural distortions, the Sr peak is smaller suggesting that the Sr content is weaker within the STO film at higher O pressure.

II.3.3.6 Cationic defects

Recent reports [31,37] linked the formation of Sr vacancies to the oxygen pressure used during the LAO film growth, which are known to be factors implying structural distortions, and notably c-lattice expansion [1,24], and influencing the electrical properties. It was initially suggested that the Sr vacancies represent a charge compensation mechanism of the positive interfacial charge or donor-charge defects (e.g. La_{Sr}) occurring in samples elaborated at high oxygen partial pressure, while electronic compensation mechanism would be promoted for synthesis at low-oxygen pressures [37–39]. The type of charge compensation (electronic or ionic), determined partly by the oxygen partial pressure used during the deposition, is primordial to understand the behavior of our oxides combination.

To conclude on the oxygen pressure, we have seen how critical this parameter is for the film and substrate stoichiometry, the lattice distortions, the growth mode, the oxygen and cationic vacancies, the intermixing. The oxygen partial pressure seemed to be in the heart of our subject for achieving high quality LAO/STO heterostructures with optimized transport properties.

II.3.4 Temperature

Besides the oxygen partial pressure, the temperature is another essential growth parameter for the control of the behavior of LAO/STO heterostructures [15,19,28,40].

II.3.4.1 Film growth

Fête *et al.* [19] indicated that according to their experimental RHEED diffraction patterns, all the films grew bi-dimensionally, layer-by-layer, independently of the growth temperature in the range 650°C to 900°C ($p_{O_2} \approx 6 \times 10^{-5}$ Torr). Pseudomorphic growth was also obtained at 550°C ($p_{O_2} \approx 7.5 \times 10^{-4}$ Torr) by Bark *et al.* [41]. At room temperature (10^{-6} Torr $< p_{O_2} < 10^{-1}$ Torr) the film obtained by Liu *et al.* [21,42] was amorphous, except the very first atomic layers that were aligned parallel to the substrate surface. Beside the influence on the crystallinity of the film, the temperature affects the level of intermixing during the growth. One would expect that this parameter implies modifications in terms of surface and depth diffusion (intermixing), with structural deteriorations and damaging the quality of the deposition.

II.3.4.2 Lattice structure

To investigate the role of the temperature in the atomic interface structure, Vonk *et al.* [23] studied by in-situ SXRD sub-monolayer coverages of LAO on STO grown at 1123 K and 473 K. They observed variations of the lattice distortions as a function of the growth temperature. At high temperatures the atoms above and below the interface are situated on the ABO_3 quadratic lattice sites, with a c parameter of LAO expanding to 3.824 Å (slightly higher than the high T relaxed value). At low temperatures this c parameter is 3.797 Å (close to its RT relaxed value) and atomic layers are buckled with anions displaced towards, and cations away from, the underlying substrate. In the substrate, interface atoms of the covered parts relax with a O-Ti-O buckling giving rise to distortions similar to ferroelectric ones. The uncovered parts of the substrate keep the same structure as the bulk. In addition, the strontium vacancies can also be favored at lower temperature to compensate the electronic disequilibrium. Yet, the cationic vacancies are well known to induce lattice expansion. We have discussed in the previous chapter the deep modifications that these distortions can bring on the transport properties.

II.3.4.3 Electrical properties

Fête *et al.* [19] varied the growth temperature from 650°C to 900°C and analyzed the consequences on the transport measurements. The authors showed that for higher growth temperature, the mobility is reduced (Figure II.13a) and the carrier density is enhanced. The latter was used to explain the lower sheet resistance observed at higher growth temperature (Figure II.13b). This is in agreement with a distinct report [40] showing higher conductivities of stoichiometric LAO/STO heterostructures for higher growth temperature, as displayed in Figure I.24d.

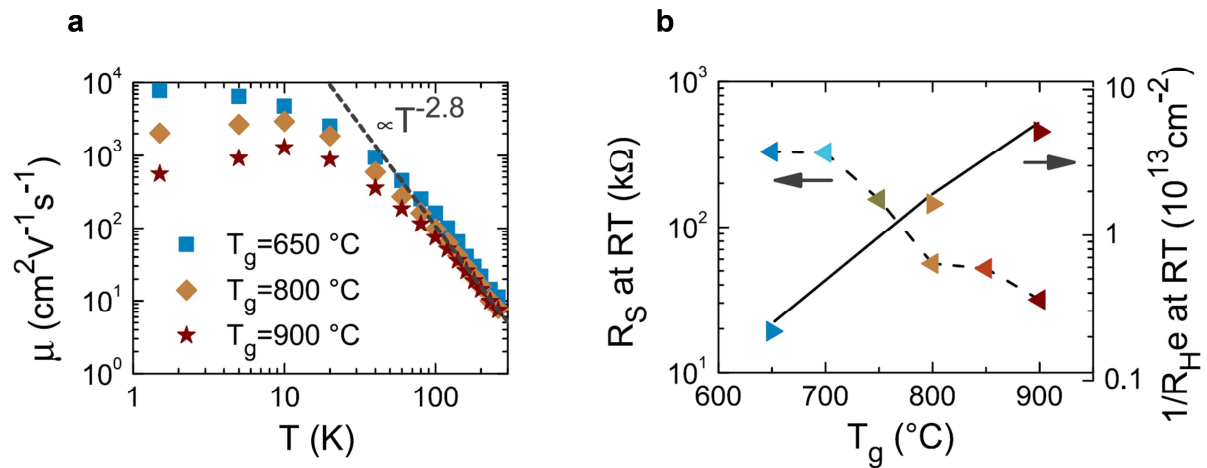


Figure II.13 | Influence of the growth temperature on the electrical properties. From [19].

a, Variations of the mobility as a function of temperature for various growth temperatures. **b**, Sheet resistance dependence on the growth temperature.

This literature review on the PLD process for LAO film deposition demonstrates the critical influence of the growth parameters on the LAO/STO heterostructures properties. Furthermore, strong correlations exist between these parameters (for example the plume structure and the oxygen partial pressure) that makes a parametric study complex but essential to understand the conduction mechanisms at the LAO/STO hetero-interface. In the plentiful literature about this system, various mechanisms for the 2DEG formation are put forward. The experimental investigations are carried out on systems obtained using distinct process parameters. A critical and comparative review of these models must always be done in the light of the growth conditions used, that makes the analysis of the published results less straightforward.

II.3.5 PLD growth relative to this thesis

The etched and annealed substrate was glued by silver paint on the sample holder to ensure a good thermal contact between the holder and the substrate. The plume angle was defined by the lateral position of the substrate on the sample holder, regarding the plasma plume. A mask was applied in order to keep the exact same position for each sample (Figure II.14a). The target was a single crystal of LAO mounted on a dedicated holder (Figure II.14b). During the deposition, the target was rotated continuously to allow a uniform laser ablation.

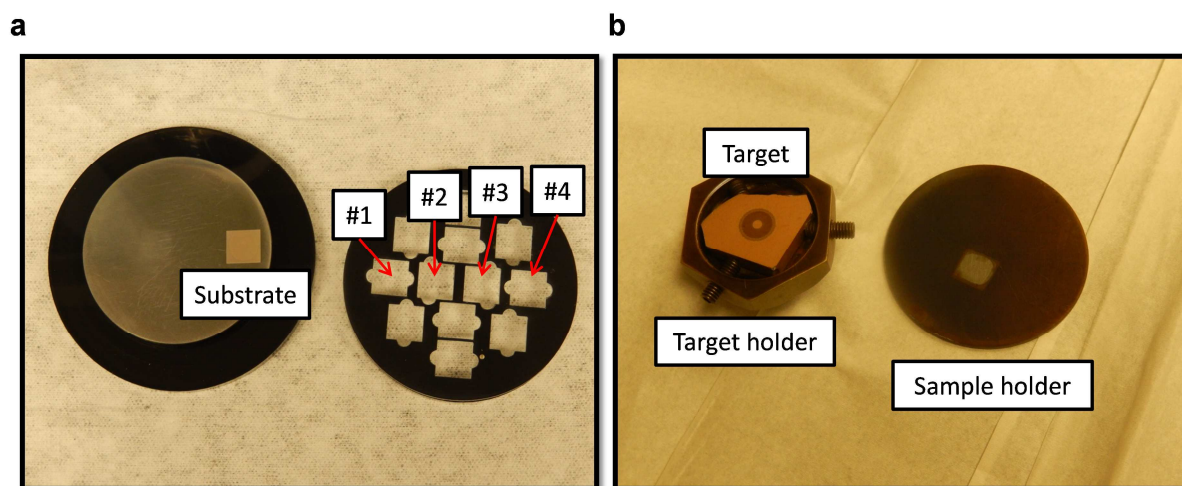
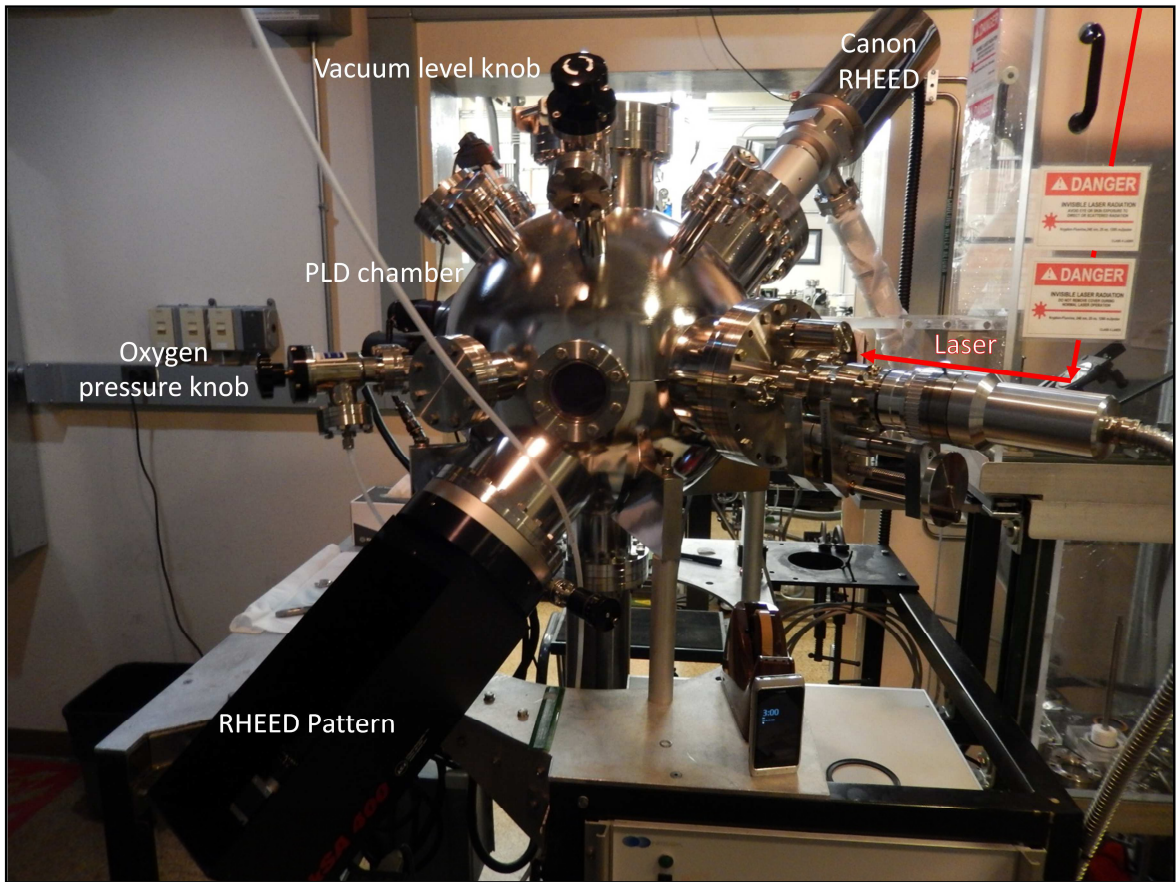


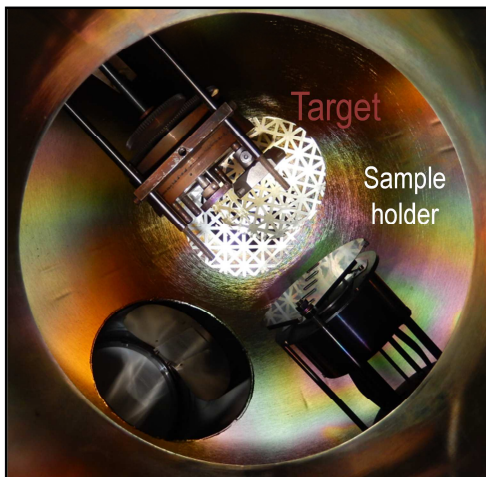
Figure II.14 | Sample preparations. **a**, A mask allows to fix the position of the substrate on the sample holder. The STO substrate is located on the position #4. **b**, The target and the sample holder after a film deposition on a substrate situated on the position #2. The circular mark on the target results from laser impacts from a previous PLD deposition.

In this thesis most of the samples were grown with the following PLD parameters: the chamber was ultrahigh vacuumed to 10^{-9} Torr and the desired O_2 partial pressure was adjusted via an MKS Mass Flow Controller and Cold Cathode. The target-to-substrate distance was fixed to 4 inches (≈ 10.16 cm). To optimize the crystallinity of the film and its epitaxial growth, the growth was performed at a temperature of about 750°C (unless otherwise specified) with an initial ramping rate of about $10^\circ\text{C}/\text{min}$ up to 500°C and then about $30^\circ\text{C}/\text{min}$ up to the deposition temperature. The LAO target was ablated using a 248 nm KrF excimer (Coherent Inc.) laser with a fluence ranging from $1.2 \text{ J}/\text{cm}^2$ to $2 \text{ J}/\text{cm}^2$ depending on the deposition angle and a repetition rate of 2 Hz. LAO films were grown at a deposition rate ranging from 7 ppl (pulses per layer) to 30 ppl, due to the various laser calibrations over the years, and the growth rate was followed *in-situ* by oscillations in Reflection High-Energy Electron Diffraction (RHEED) patterns (STAIB Instruments), as explained in the following sections. After deposition, films were brought to room temperature at cooling rates of about $10^\circ\text{C}/\text{min}$, maintaining the same O_2 partial pressure as during the film growth, then about $5^\circ\text{C}/\text{min}$. Once the latter cooling rate is applied, the mass flow controller is turned off along with the turbo pump, so the pressure increases slowly up to the roughing pump range, which is around 10^{-2} Torr.

a



b



c

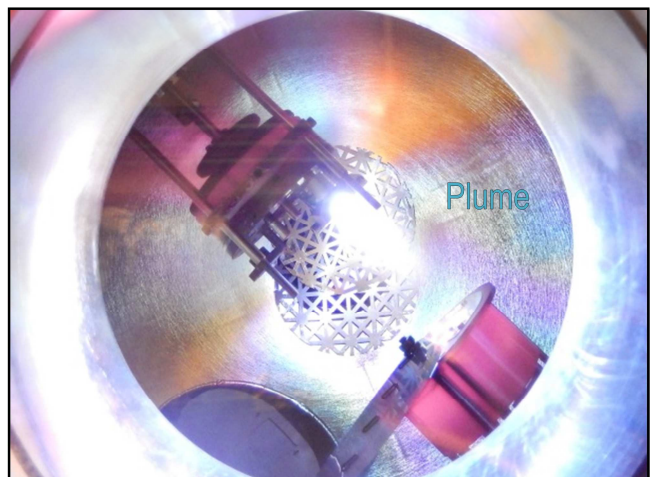


Figure II.15 | Pulsed Laser Deposition Technique at NASA Glenn research center. a, Picture of the PLD device. **b**, Picture inside the PLD chamber before deposition. **c**, Picture inside the PLD chamber during the film deposition.

II.4 Transmission Electron Microscopy (TEM)

Ernst Ruska invented and developed with Max Knoll the first Transmission Electron Microscope (TEM) device in the beginning of the 1930's, replacing photons by electrons and using magnetic coils rather than glass lenses. Thanks to the shorter electron wave length used (several orders magnitude below that of photons), the resolution of this first generation TEM exceeded for the first time that of optical microscopes. Nowadays sub-angstrom resolution can be obtained thank to the improvement in the stability of electron source, the lens characteristics and the addition of aberration correctors. This imaging technique is therefore suitable to the investigations of our hetero-interface. A major limitation however comes from the strong interaction between electrons and matter. For the electrons to pass through the specimen, thicknesses lower than 100 nm are required. This imposes a preliminary and delicate step: the thin foil preparation.

II.4.1 Sample preparation for TEM investigations

Two techniques were used to prepared samples for our TEM works. First, we decided to focus our effort on the tripod polisher technique, and afterwards FIB milling was alternatively used.

II.4.1.1 Mechanical Polishing

II.4.1.1.1 Tripod polishing

LAO/STO samples (dimensioned as following: $10 \times 10 \times 0.5 \text{ mm}^3$), received from NASA Glenn Research Center laboratory, grown by PLD were cut by using a SiC blade into $2.5 \times 2 \times 0.5 \text{ mm}^3$ to fit to dimensions of the 3 mm diameter TEM sample holder. To prepare transverse sections, minimize the degradation during polishing and increase observable areas, two pieces were glued together with an epoxy-phenolic adhesive (M-BOND 610), film on film, and pressed together using self-gripping tweezers (Figure II.16a). Afterwards, the sample is glued with a thermal adhesive (QuickStick mounting wax) on the tripod pyrex foot.

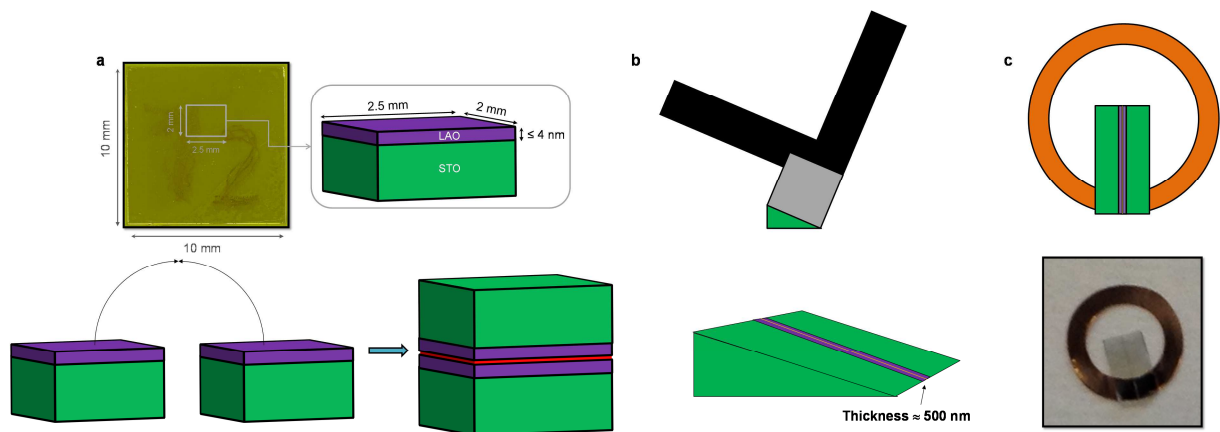


Figure II.16 | Mechanical polishing. **a**, Samples cuts are removed from the as-received material, adapted to the sample holder size. Samples are assembled before starting the mechanical polishing with the tripod. **b**, Polishing of the sample second face by introducing a wedge. **c**, Once the polishing is ended up, the sample is glued on a copper grid.

The tripod polishing is a mechanical polishing allowing a precise control of the angle between the upper and lower sides of the sample. The polishing is carried out step by step with successive diamond lapping polymer films from $30 \mu\text{m}$ to $0.1 \mu\text{m}$ in terms of granulometry [43]. The first side is

mirror polished, and then a wedge of about 0.57 degree is imposed to polish the second face (Figure II.16b). The thickness at the tip of the wedge needed to be reduced to less than 1 μm , with color fringes observable. Eventually the sample is glued on a copper grid (Figure II.16c) and placed into an ion-milling device in order to reach electron transparency ($< 100 \text{ nm}$).

II.4.1.1.2 Ion-milling

Electron transparency was obtained by Ar^+ ion-milling using a Precision Ion Polishing System (Gatan PIPS 691) (Figure II.17). To reduce thinning artefacts, the ion milling duration must be as short as possible, that is to say the sample introduced must be as thin as possible. A compromise between the risk of failure during tripod polishing and of damage during the ion-milling was found for a thickness of about 5 μm .

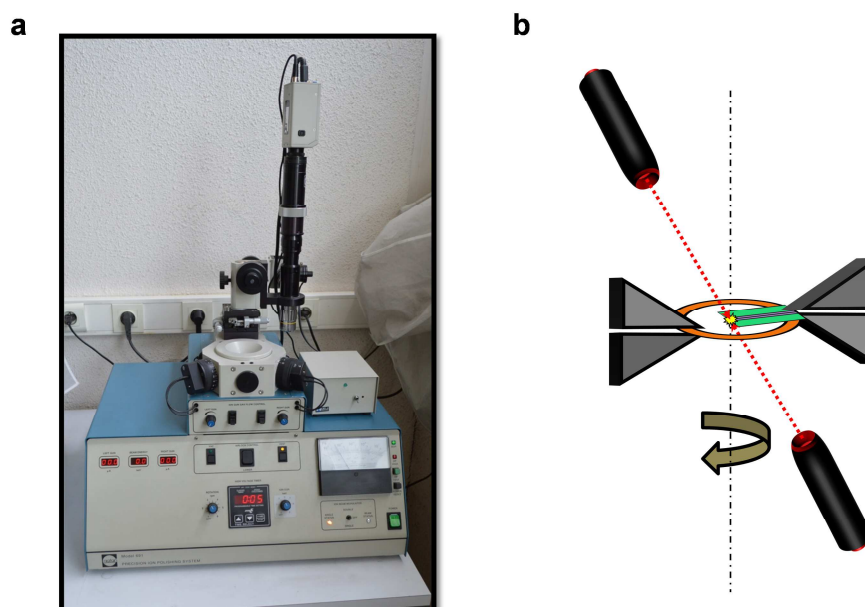


Figure II.17 | Ion-milling technique. **a**, Ion-milling device. **b**, Ion-milling process. The ion guns are directed in order to thin preferentially the thinnest part of the sample.

Another compromise lies in the ion-milling parameters. The higher the energy of the particles and the angle of the guns are, the faster the sample is thinned, but the more artefacts are introduced such as amorphous phases, Ar^+ implantation etc. On the other side, for reduced energies and angles, the thinning duration is increased, giving rise to re-deposition, surface rippling, preferential thinning of the glue line, thinning of the PIPS sample holder etc. A thinning at 4 kV to 3 kV Ar^+ and 6° was chosen. To reduce specimen heating and promote a thinning direction perpendicular to the interface, the guns were switched off sequentially on both side of glue line during 2/3 of a sample revolution.

II.4.1.1.3 Difficulties faced during tripod/ion thinning

The above protocol, when carried out through the end, gave us a couple of thin foils of good quality. However, numerous specimens were wasted during the mechanical polishing down to 1 μm by STO cleavage, not to mention the loss of the samples between different steps of the preparation. Thicker samples ($> 1 \mu\text{m}$) imposed too long ion-milling duration resulting in re-deposition of species that recrystallized under the electron beam of the microscope, as shown on the bright field image of Figure II.18. These issues led us to switch to a more efficient thinning method, the Focused Ion Beam (FIB).

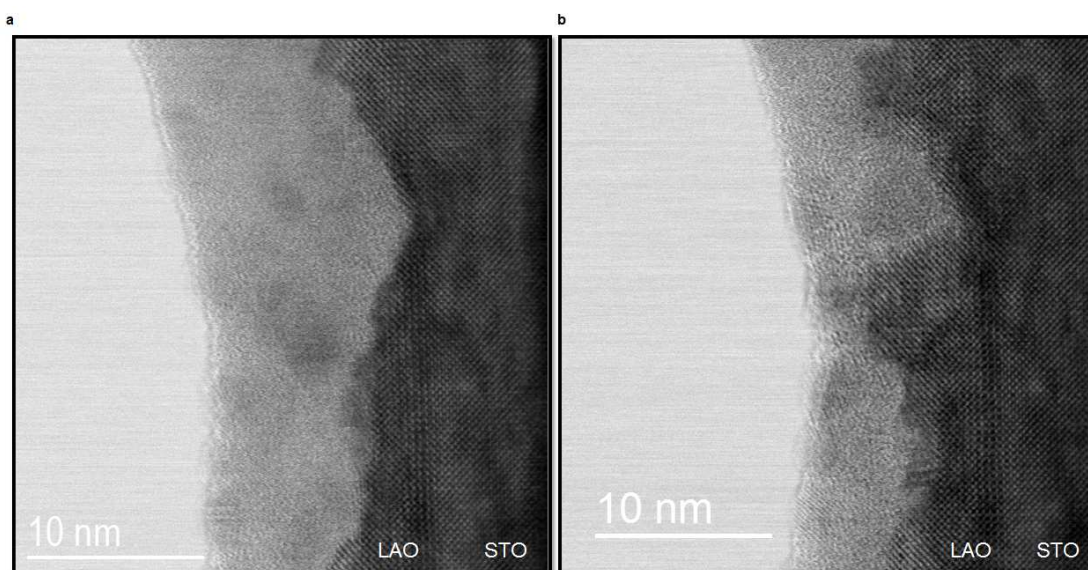


Figure II.18 | Representative Bright Field (BF) images of a sample prepared by mechanical polishing. a, BF picture of a sample area with the LAO film before analyzing. **b,** BF picture of a sample area with the LAO film after analyzing. We clearly see recrystallization under the beam.

II.4.1.2 Focused Ion Beam (FIB)

The FIB cuts were done at CEA, Saclay (DMN/SRMP), with Sylvie Poissonnet, as well as at Case Western Reserve University by Elahe Farghadany following the protocol we developed with S.Poissonnet. An amorphous carbon layer was first deposited to protect the surface, using carbon rod evaporator in a secondary vacuum. The sample was introduced in the FIB chamber and a 1.5 μm -thick Pt wall was added on the region of interest.

The extraction started by digging both sides of the region of interest with gallium ions (Figure II.19a). They were accelerated to 30 kV and hit the surface at 90° with a current of 21 nA. This first milling was stopped when a thickness of about 2 μm was reached on a 10 x 1.5 μm^2 area. Then the as obtained slice was cut out from the surrounding parts (Figure II.19d) and fixed to a copper comb with Pt (Figure II.19c). A final thinning was carried out by gradually decreasing the current and (Figure II.19d), to eliminate defects created by the previous energetic process (Table II.1).

Tension	Current	Angle vs LAO/STO [001] direction	Aimed thickness
30 kV	0.79 nA/0.43 nA	± 1.5	1 μm
30 kV	0.23 nA	± 1.5	500 nm
30 kV	0.08 nA	± 1.2	100 nm
5 kV	0.041 nA	± 5	Thinning restricted to an upper window. Up to partial transparency to 5 keV electrons
2 kV	0.023 nA	± 6	Finishing step and cleaning
1 kV	0.028 nA	0	Finishing step and cleaning

Table II.1 | Experimental protocol for FIB cuts preparation.

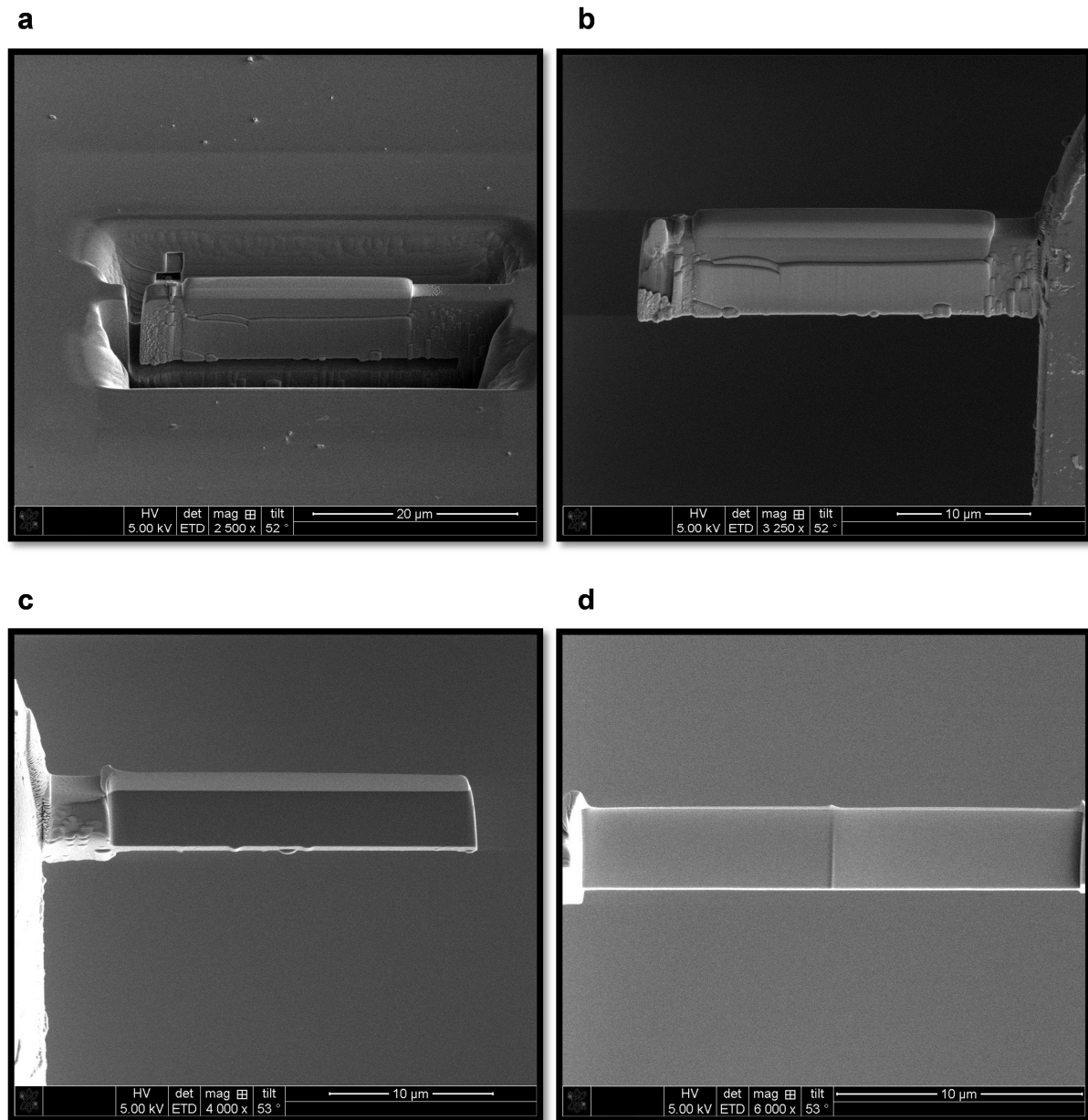


Figure II.19 | SEM pictures obtained by Secondary Electrons of one TEM sample prepared by FIB. a, The FIB cut after the first thinning, before its extraction from the surrounding parts of the heterostructure. **b,** The FIB cut fixed on the copper comb. **c,** The FIB cut after an additional stage of thinning. **d,** The FIB cut in its final state, ready for TEM analysis.

The main advantages of FIB technique compared to the tripod/PIPS one are its success rate and relative rapidity. We could obtain a cut within 3 hours whereas mechanical polishing could take at least 3 days. Furthermore the uniform sample thickness provided is attractive for TEM analyses, although thinner samples can be obtained by tripod. We could avoid redistribution of species but implantation of Ga was not excluded.

II.4.2 TEM-STEM imaging

In this work, the very first investigations were led with a 200 kV TEM-STEM equipped with a field emission gun (FEI Tecnai F20-ST at Mines ParisTech). The spherical aberration of this microscope is

$C_s = 1.2$ mm, the resolution at Scherzer defocus is 2.3 \AA and information limit is about 1.4 \AA . A typical contrast image recorded with this TEM is shown in Figure II.20. The resolution obtained limits the field of investigations. The FEI Tecnai F20 ST was mainly used to check the quality of the growth, the thickness of the prepared TEM samples, locate the LAO film and record electron diffraction patterns. We have thus developed collaborations with Michael Walls, from the Laboratoire de Physique des Solides (Université Paris-Sud), via the METSA platform, who gave us access to the Ultra-STEM (USTEM) Nion.

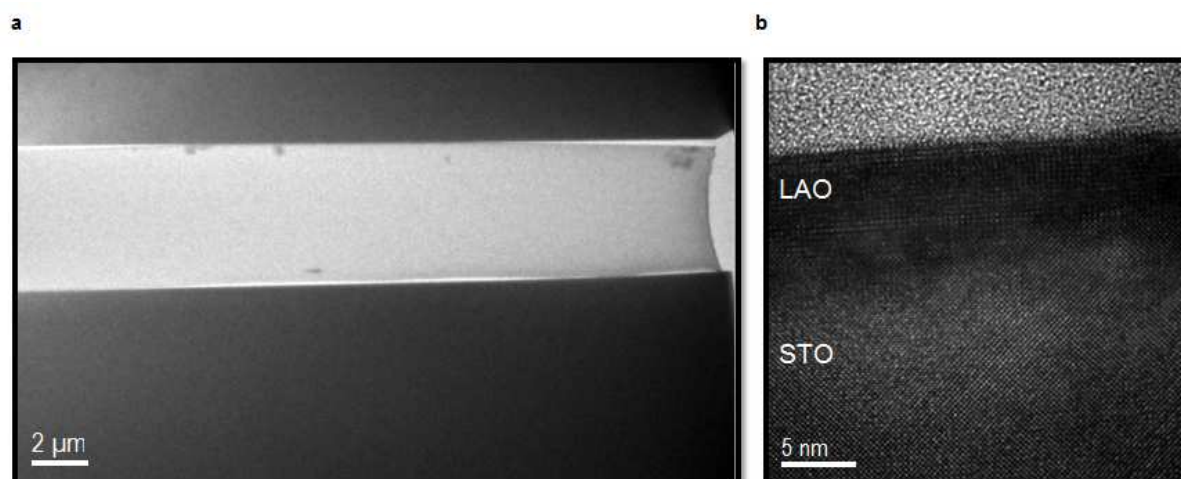


Figure II.20 | High-Resolution TEM image of a LAO/STO heterostructure prepared by mechanical polishing.

All the samples were analyzed using a Nion UltraSTEM (USTEM) 200 operating at 100 kV and a High-Angle Annular Dark-Field (HAADF) detector with an inner collection angle of 70 mrad. The microscope was equipped with a spherical aberration corrector, which enabled a probe-size of under 0.1 nm to be obtained.

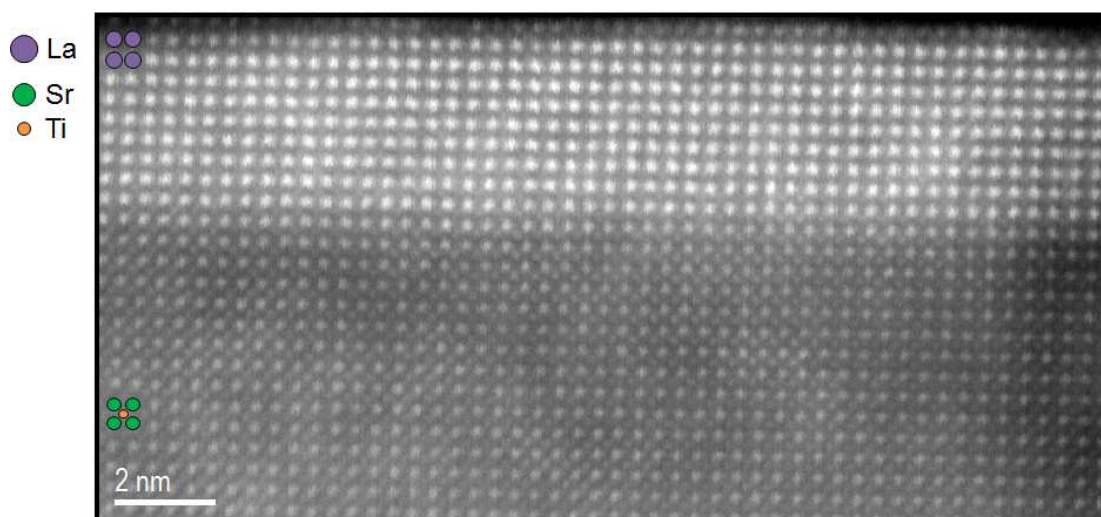


Figure II.21 | STEM-HAADF image of a LAO/STO heterostructure prepared by mechanical polishing. The chemical contrast permits to distinguish on the A-site the lanthanum atoms (brighter) from strontium atoms (darker). Titanium could be seen on the B-site, aluminium and oxygen where too light to be detected.

The HAADF detector collects electrons scattered by atoms, with scattering angles larger angle than Bragg diffraction angles. The success of this method is explainable by the more intuitive interpretation of its pictures compared to phase contrast images. The intensity, I , of the signal is related to the atomic number, Z with $I \propto Z^n$, with $1 \leq n \leq 2$. Figure II.21 shows clearly the typical chemical contrast of HAADF images, with heavier atoms brighter than the lighter ones. Thickness variations of the foil can lead to an additional absorption contrast that has to be taken into account in the interpretation of the image.

HAADF was used to investigate the quality of the pseudomorphic growth, the presence or absence of misfit dislocations. HAADF intensity profiles along A-cations rows across the interface were used to study the Sr-La intermixing across the interface since La ($Z = 57$) atoms were displayed brighter than Sr ones ($Z = 38$). The Al and O atoms were too light to be observable through this technique. The cations detected on B-sites in the film side corresponded mostly to the Ti atoms, revealing diffusion of B-cations from the substrate and the film.

II.4.3 Electron Energy Loss Spectroscopy (EELS)

The EEL spectroscopy is an analytical technique based on the energy distribution of all the inelastically scattered electrons passing through the thin foil. More details can be found in Williams & Carter [44]. In this work we focused on the core loss part of the EELS spectrum and more specifically on its oscillations after the absorption edges of Ti-L_{2,3} and O-K (energy loss near edge structure). Excitation of inner-shell electrons by the electron beam implies transitions of the core electrons to empty states above the Fermi level. The energy-loss near-edge structure (ELNES) of a core-level EELS edge reflects the local density of these empty states [45]. Any changes in the valence of the atom, or in nearest-neighbour position/nature, modify the near edge structure. We also quantified the extent of La and Ti intermixing by EELS profile or spectrum images in the interface region. EELS spectra were acquired with the Nion USTEM with a Gatan Enfina spectrometer and a custom-made EELS camera. The energy resolution for this set of experiments was 0.5 eV and the probe size of about 0.1 nm.

II.4.3.1 Ti valence

We have performed EELS measurements around the Ti-L₂L₃ edge at the interface to investigate variations in the valence of Ti atoms. The Ti-L₂L₃ edges correspond to the $2p_{1/2} \rightarrow 3d$ and $2p_{3/2} \rightarrow 3d$ transitions respectively. In TiO₆ octahedral environment the d energy level is split into t_{2g} and e_g (section I.2). The d level is empty for Ti⁴⁺ whereas the t_{2g} level is partially occupied for Ti³⁺. Therefore changes in Ti valences result in modifications of the ELNES spectra. The Ti³⁺ EELS spectrum exhibits a shift towards lower energies and a vanishing of the t_{2g} peaks for L₂ and L₃ edges (Figure II.22). We have used two methods to quantify these changes, a multivariable analysis and a linear combination of reference spectra.

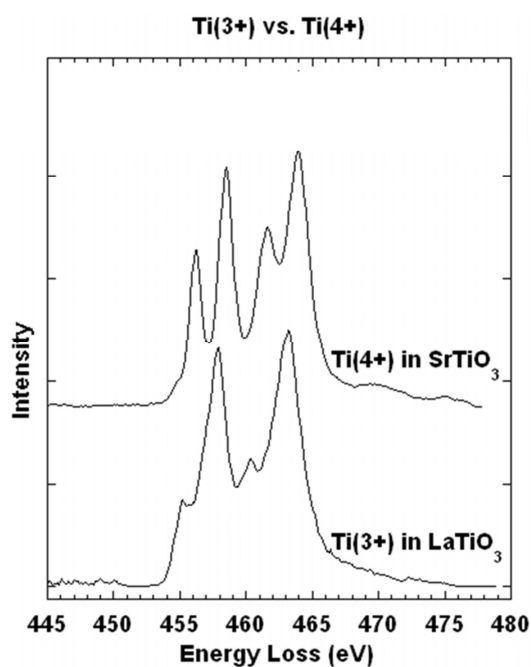


Figure II.22 | Spectra measured by Muller's group with a FEI Tecnai T20. From Muller group EELS database.

II.4.3.1.1 Multivariate Analysis

We suppose that the $\text{Ti-L}_{2,3}$ EELS spectra in the interface region enclose contributions of Ti^{3+} and Ti^{4+} . We tried to map and quantify their respective contributions to spectrum images without needing external reference spectra. We analyzed our experimental spectrum image of the $\text{Ti-L}_{2,3}$ absorption edges by a multivariate analysis method (MVA) developed by Francesco DelaPeña [46], called Independent Component Analysis (ICA). This computational method can retrieve mutually independent components linearly added in a set of spectra, without previous knowledge of these contributions. A Principal Component Analysis (PCA) was carried out before the ICA to separate the noise from high variance components. This reduction of the dimensionality by PCA considerably lowers the computation time of ICA. For this PCA/ICA analysis, we used the code developed in Python by Francesco DelaPeña, called Hyperspy.

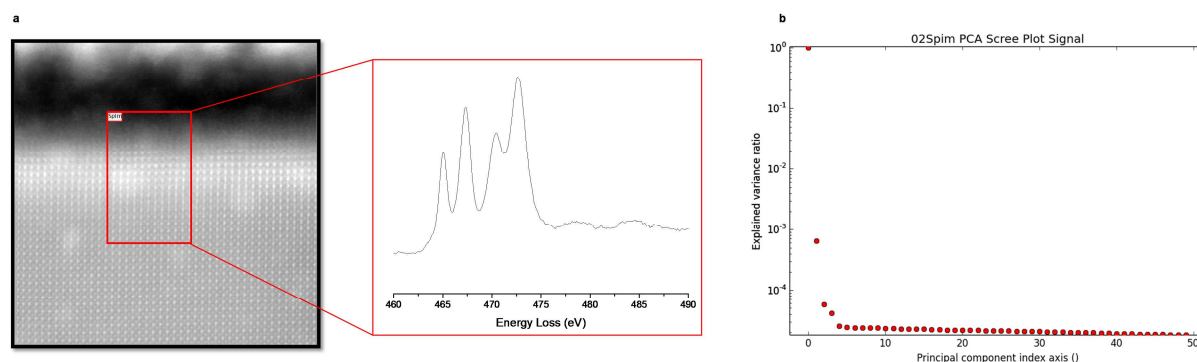


Figure II.23 | Principal Component Analysis process. **a**, $\text{Ti-L}_{2,3}$ EELS spectrum, sum of all the spectra recorded by scanning the red framed area on the STEM-HAADF image. **b**, Total variance explained by the principal components for an EELS spectrum restricted to the $\text{Ti-L}_{2,3}$ absorption edge.

An example of such computational analysis is given, carried out on a spectrum image, restricted to the energy range corresponding to Ti-L_{2,3} edges, in the interface region of 5 u.c.-thick LAO/STO (Figure II.23a). PCA identified four main independent components (Figure II.23b). This means that contributions to Ti-L_{2,3} absorption edges other than Ti⁴⁺ and Ti³⁺ would exist in this area, or that the assumption of linearity is not fulfilled due to multiple scattering [46]. These components and their spatial distributions were then extracted by ICA (Figure II.24). In the present example the second component, “BSS Factor 1”, could be attributed to Ti⁴⁺. In addition, a component with a negative intensity “BSS Factor 0” was extracted which is physically incoherent. The third component “BSS Factor 2” also contains negative parts and could not be attributed to a known fingerprint. The fourth one was almost null. This method was applied several times to numerous samples, and did not highlight reliable contributions other than that of Ti⁴⁺. The weak contribution of Ti³⁺ to the total spectrum image might contribute to these unsuccessful results.

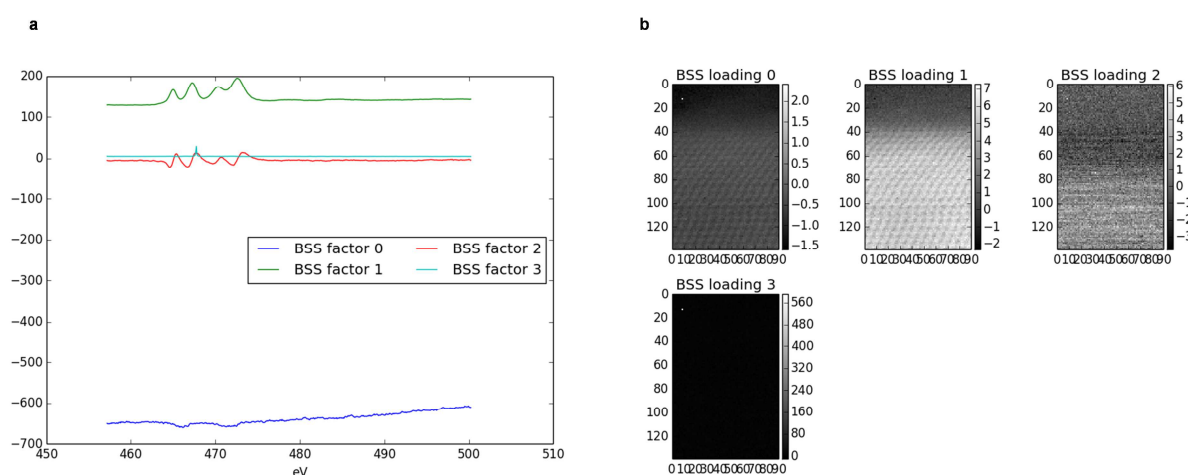


Figure II.24 | PCA/ICA Results. **a**, Independent components identified from the original EELS spectrum of a sample with a 5 u.c.-thick sample restricted to the Ti-L_{2,3} absorption edge. **b**, Maps representing the spatial distribution of each independent components.

II.4.3.1.2 Linear combinations of EELS reference spectra

As the elegant PCA/ICA method was not well suited to our samples, we decided to determine the Ti oxidation state, $+(4 - x)$, around the interface by a more conventional technique, using reference spectra for the two boundaries +4 and +3. For Ti⁴⁺, the more reliable spectrum is obtained in the deepest part of the STO substrate of the sample, in a region of the equivalent thickness. For films grown at $p_{O_2} < 10^{-4}$ Torr, the Ti⁴⁺ reference spectrum was that obtained at 10^{-4} Torr. As the Ti³⁺ reference cannot be obtained from our samples, Michael Walls provided us EELS spectra of Ti₂O₃ obtained in the same experimental conditions as our sample measurements (Figure II.25). The energy calibration was based on the Muller’s group data (Figure II.22). The contributions of Ti⁴⁺ and Ti³⁺ to the Ti edge were deduced from a linear combination of the two reference spectra. The method of least squares was used to fit the experimental and the simulation spectra.

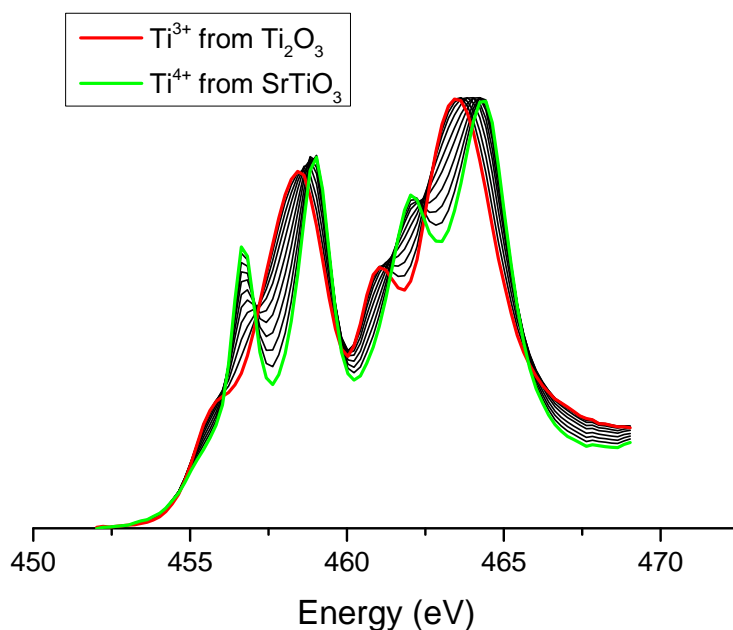


Figure II.25 | EELS Spectra Ti^{3+} vs. Ti^{4+} . Experimental spectra for Ti^{3+} and Ti^{4+} measured with the Nion USTEM at LPS, University of Paris Sud. Linear combinations of Ti^{3+} and Ti^{4+} are represented 10% by 10% by black curves.

II.4.3.2 Oxygen vacancies

The oxygen vacancies have been advanced by many groups as the main contributor of the conduction at the LAO/STO interface due to strong dependence of the conducting layer properties on the oxidation conditions during growth and post-treatments. One way to investigate these oxygen vacancies is to analyze EELS O-K absorption edges which depend on the environment surrounding the oxygens. The introduction of an oxygen vacancy in the perovskite cell induces opposite shifts of the cations and anions around the vacancy (Figure II.26). The environments of the first and second oxygen neighbors are then modified, these changes being visible on the ELNES O-K spectrum.

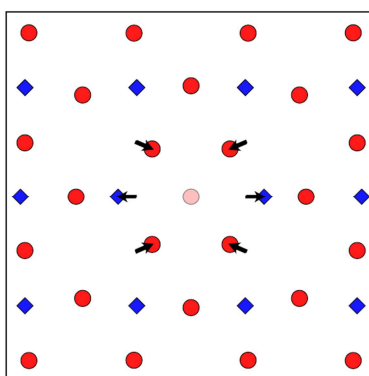


Figure II.26 | Influence of oxygen vacancies on the lattice structure. Oxygen (Titanium) atoms are represented by red circles (blue diamonds). The oxygen vacancy is represented by a transparent red circle. From [47].

For the interpretation of an O-K EELS absorption edge, we discriminated the spectrum measured from the STO bulk (Figure II.27a) into five peaks (A, B, C, D, E) characteristics of the O environment [48]. While the peak A represents a weak π hybridization of the Ti-3d t_{2g} with the O 2p orbitals, the

peak B results from σ hybridization of Ti-3d e_g with O 2p orbitals. The A and B peaks allow probing the presence of Ti throughout the sample, and particularly in the film as this peak is not found for LaAlO_3 , Al having no d electrons (Figure II.27b). Moreover, the shape of these two peaks allows discriminating O in LaTiO_3 and SrTiO_3 environments (Figure II.27c). We note here that once O is linked to Ti^{3+} , the signal of the peak A decreases as the t_{2g} level is partially occupied. Furthermore, Varela *et al.* [49] suggested that the energy difference between the peaks A and C represents an indicator of the B-site cations oxidation state. Hence, a smaller energy difference is related to a valence decreasing. Then, Kourkoutis *et al.* [48], based on De Groot *et al.* work [50], associated the peak C to the interactions with A-site cations, and more particularly to the hybridization of the O 2p orbitals with the Sr 4d ones in the case of SrTiO_3 or with the La 5d for LaAlO_3 . The shift of this peak towards the lower energies reveals substitution of Sr by La as it is verified by Figure II.27b and Figure II.27c where the A cations are represented by La^{3+} . The peaks D and E represent respectively the Sr 5p and Ti 4sp contributions [48].

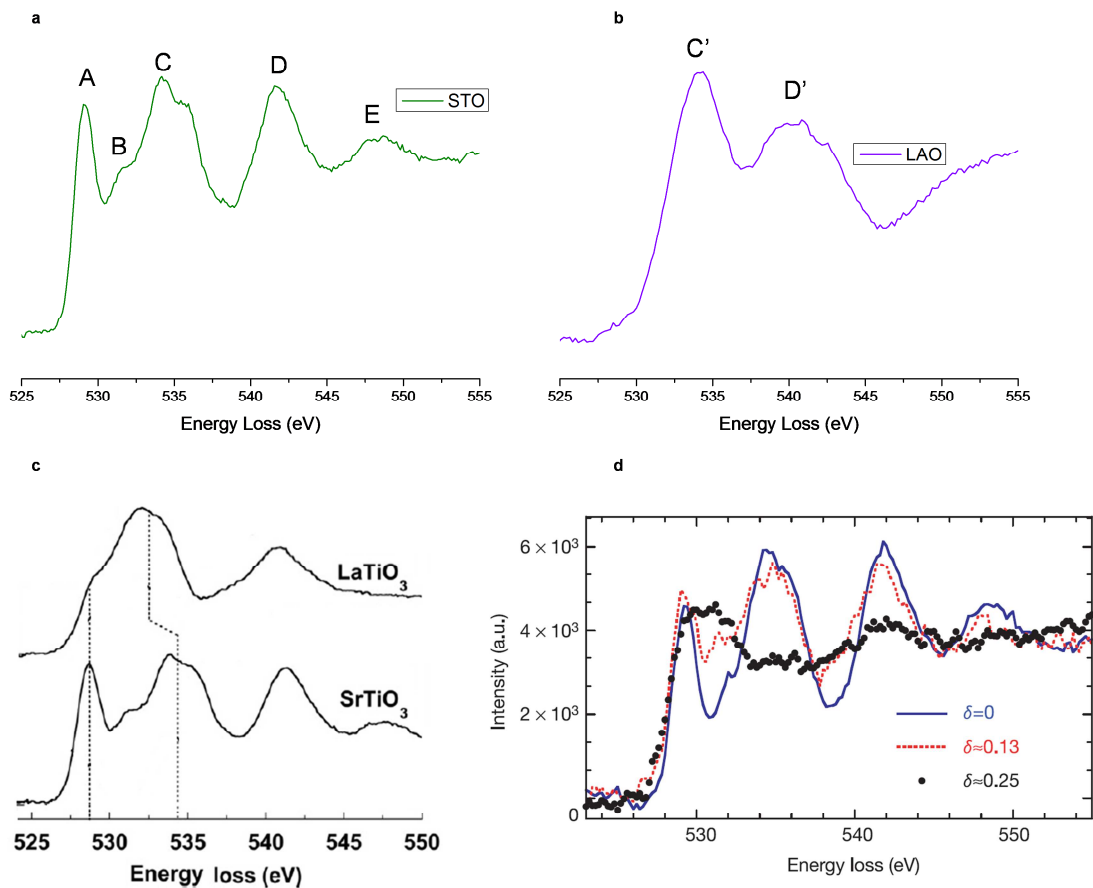


Figure II.27 | Interpretation of EELS O-K absorption edges. **a**, Experimental spectrum SrTiO_3 away from the interface taken in a heterostructure with a thicker film. **b**, Experimental spectrum for LaAlO_3 (purple) away from the interface taken in a heterostructure with a thicker film. **c**, Comparison between EELS O-K spectra from LaTiO_3 and SrTiO_3 . Adapted from [48]. **d**, Reference taken to evaluate the presence of oxygen vacancies. From [51].

Finally, the oxygen vacancies are detected via the reference obtained by Muller *et al.* [51], presented in the Figure II.27d. The peak A broadens and overlaps the peak B. Moreover, the peaks C, D and E

tend to vanish, as well as the valley between the peaks A and C, and C and D. All these data give us significant clues to interpret the experimental EELS O-K absorption edges.

II.5 Nuclear Spectroscopies

At the beginning of the XXth century, Ernest Rutherford discovered that alpha particles could be backscattered when impacting a gold foil and built his planetary model of the atom. Rutherford Backscattering Spectroscopy (RBS) analyses Coulomb scattering events of incident ions by nuclei in the solid. This non-destructive method is dedicated to the investigation of the stoichiometry, structure and depth composition profiles of coatings, surface layers, etc. In RBS primary particles, typically $^4\text{He}^+$ or $^1\text{H}^+$, are accelerated to an energy ranging from about 0.5 MeV to 5 MeV. They probe a solid down to a few micrometers in depth, with a depth resolution of about 10-20 nm. Medium-Energy Ion Scattering (MEIS) is based on the same physics of Coulomb scattering but using incident particles of a few 100 keV and an angular and energy detector with higher resolution. MEIS is more dedicated to thin film analysis and provides the in-depth atomic resolution needed for the investigation of our hetero-interface. Before presenting how RBS and MEIS investigations were carried out for our study, we will summarize some concepts of the physics of ion-solid interactions. The “kinematic factor” will introduce the mass resolution, the “stopping power” the depth resolution and the “scattering cross section” the qualitative composition analysis.

II.5.1 Fundamentals of physics of ion-solid interactions

With the range of particle energy used in RBS, the nature of the interactions with the target atoms can be divided into two categories, the inelastic interactions with the electrons, and the scattering with the nuclei [52]. The incident particles lose most of their kinetic energy by Coulomb interactions with the electrons of the target atoms, their trajectory is only slightly deflected and the energy lost is dissipated through the electron cloud into thermal vibrations [52]. The atoms are ionized by the particles beam, and the subsequent decay gives rise to the emission of X photons or Auger electrons. A very small fraction of the particles have trajectories approaching close enough the nucleus to be scattered by the nucleus or even backscattered for frontal interactions.

II.5.1.1 Kinematic factor

Figure II.28 illustrates the elastic scattering to an angle θ_{sc} of a particle of mass m impinging a stationary atom with a mass M , with $m \ll M$. The incident particle energy is written E_0 before the scattering event, and E_1 after. The elastic collision implies a conservation of the kinetic energy and the momentum. The ratio E_1/E_0 , called the kinematic factor k , can be deduced from these conservation laws:

$$k = \frac{E_1}{E_0} = \left[\frac{\sqrt{M^2 - m^2 \sin^2 \theta_{sc}} + m \cos \theta_{sc}}{M + m} \right]^2 = k(M, m, \theta_{sc})$$

It can be seen that k is independent from E_0 . This equation motivates the strategy to increase the mass resolution of RBS (or MEIS): higher scattering angles allow a larger energy separation $\Delta E_1 = E_1'' - E_1'$ for two distinct masses M'' and M' .

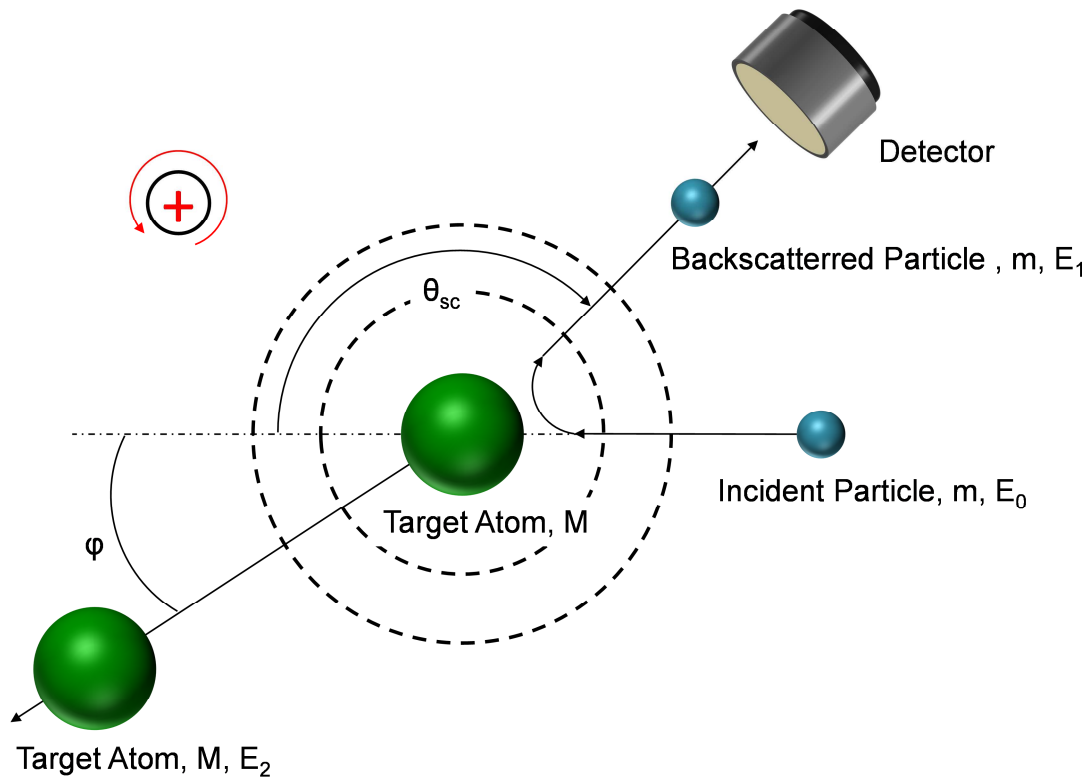


Figure II.28 | Illustration of the elastic collision of an incident particle (m, E_0) with a stationary target atom (M). The impingement with the atom backscatters the particle with an angle θ_{sc} , giving an energy E_2 to the atom which deviates with an angle ϕ from its initial position.

II.5.1.2 Electronic / Nuclear Stopping power

The kinematic factor allows the identification of target surface atoms from the measurement of the energy and angle of the backscattered particles. For scattering centers below the surface (i.e. deep within the bulk), an additional energy is lost on the incoming and out-coming path. The particles are progressively slowed down by the electronic and nuclear interactions which control the stopping power of a media, i.e. the energy dE lost by the particle along the path length dx :

$$\frac{dE}{dx} = \left(\frac{dE}{dx}\right)_{\text{electronic}} + \left(\frac{dE}{dx}\right)_{\text{nuclear}}$$

The relative weight of the two processes depends on the energy E and the atomic number Z of the incident ion. Nuclear collisions dominate at low energies/heavier ion and electronic collisions at high energies/light ions.

The identification of the depth coordinate of the scattering center is now possible since the additional energy lost is related to the length of the incoming and out-coming paths (Figure II.29). Better depth resolutions are obtained for higher stopping powers. It is noteworthy here that the energy resolution of the detector has also a strong influence on the depth resolution. Therefore conventional detectors, made with Si, used in RBS cannot be applied for MEIS analyses, due to their limited energy resolution.

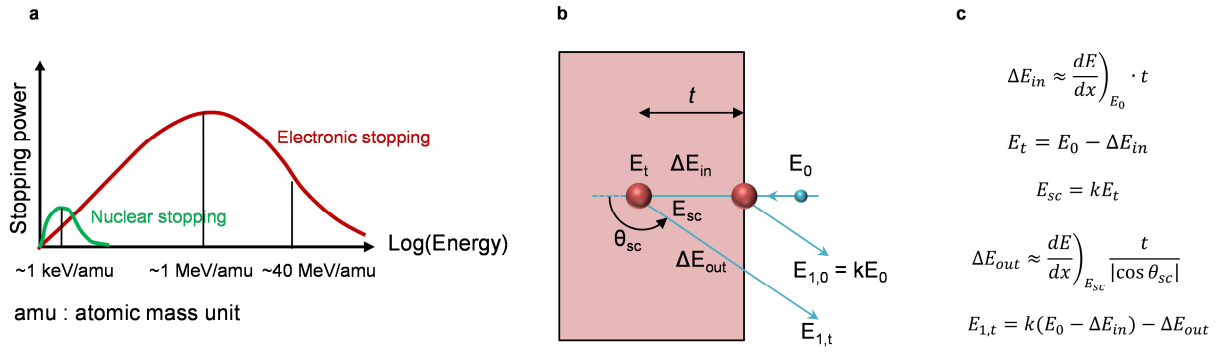


Figure II.29 | Stopping power. **a**, Illustration of the stopping power as a function of the energy. **b**, Illustration of the depth effect on the incident particle energy. **c**, Equations giving the energy of the out-coming particle after depth crossing.

The formulation of the stopping power used considers a continuous energy loss along the trajectory. However, the statistical processes involved in the slowdown lead to energy loss fluctuations, commonly called energy straggling. Moreover the probability for particle to be scattered by atomic nucleus increases as their energy decreases, implying modifications in their path direction within the sample [53]. This explains why the depth from which analytical information can be obtained is lower than the penetration depth.

II.5.1.3 Scattering cross section

For quantitative analysis of the atomic composition by RBS, the count number recorded at a given scattering angle and energy is converted into a concentration by knowing the backscattering yield on this atom at this angle and energy. This yield is related to the scattering cross section, in other words the probability for the incident particles to be scattered. We make the assumption that the scattering is exclusively due to Coulomb repulsion. The scattering cross-section σ_{Ruth} , called the Rutherford cross section, is then equal to:

$$\sigma_{Ruth} = \left(\frac{Z_1 Z_2}{4E_0} \cdot \frac{e^2}{4\pi\epsilon_0} \right)^2 \frac{4}{\sin^4 \theta_{sc}} \frac{\left[\sqrt{1 - \left(\frac{m}{M} \sin \theta_{sc} \right)^2} + \cos \theta_{sc} \right]^2}{\sqrt{1 - \left(\frac{m}{M} \sin \theta_{sc} \right)^2}}$$

With Z_1 the atomic number of the incident particle of mass m and energy E_0 , Z_2 the atomic number of the target atom of mass M , θ_{sc} the scattering angle.

The approximation of Rutherford cross section is effective for high energy incident particles, as in RBS. For lower energies, the screening of the nuclear charge by the electrons of the target cannot be neglected and the Rutherford cross section is no longer valid. Consequently, a correction factor has to be added to the Rutherford cross section:

$$\sigma = F \sigma_{Ruth}$$

Chapter II | Experimental methods

In the range of scattering angles we will work with ($\theta_{sc} > 90^\circ$), the correction factor proposed by L'Ecuyer *et al.* [55] is widely used:

$$F_{Lec} = 1 - \frac{0.04873Z_1Z_2^{\frac{4}{3}}}{E_0(keV)}$$

For ${}^4\text{He}^+$ sent at 3 Mev, $F_{Lec} > 0.99$ for La and Sr, the Rutherford cross section is valid. At 100 keV the correction factors $F_{Lec} = 0.785$ for La and 0.875 for Sr will be applied.

The number of particles collected, A , by a detector of solid angle, Ω , for a total number of incident particles, Q , hitting a target with an areal density N_s (in atoms/cm²), defined by the product of the number density, N , (in atoms/cm³) and the thickness, t , which is the parameter directly obtained from RBS, is obtained by the following equation:

$$A = \sigma\Omega N_s Q$$

The parameters defining this equation are illustrated in Figure II.30.

The scattering cross section, σ , will dictate the sensitivity of the measurements, which is higher for lower scattering angle contrary to the mass selectivity given by the kinematic factor. Therefore a compromise has to be found in the choice of the collection scattering angle. Scattering cross section also increases for lower energy and for higher M .

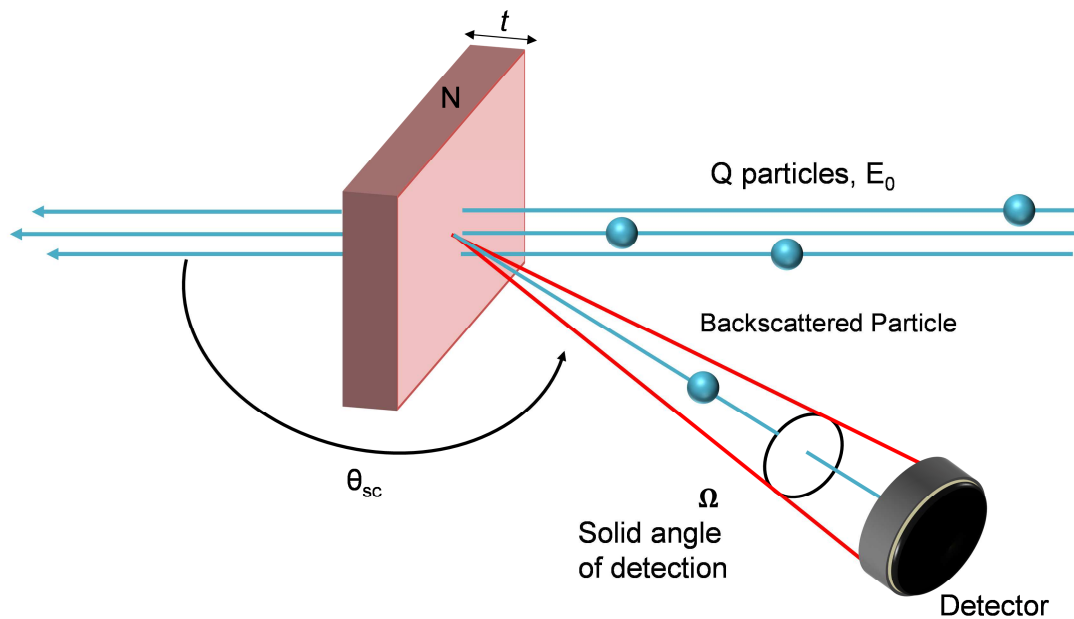


Figure II.30 | Illustration of the particles collected.

II.5.2 Rutherford Backscattered Spectroscopy (RBS)

RBS spectra plot, for a fixed position of the detector, the number of backscattered particles recorded as a function of their energies. Figure II.31 outlines a spectrum for a La film covering a Sr matrix.

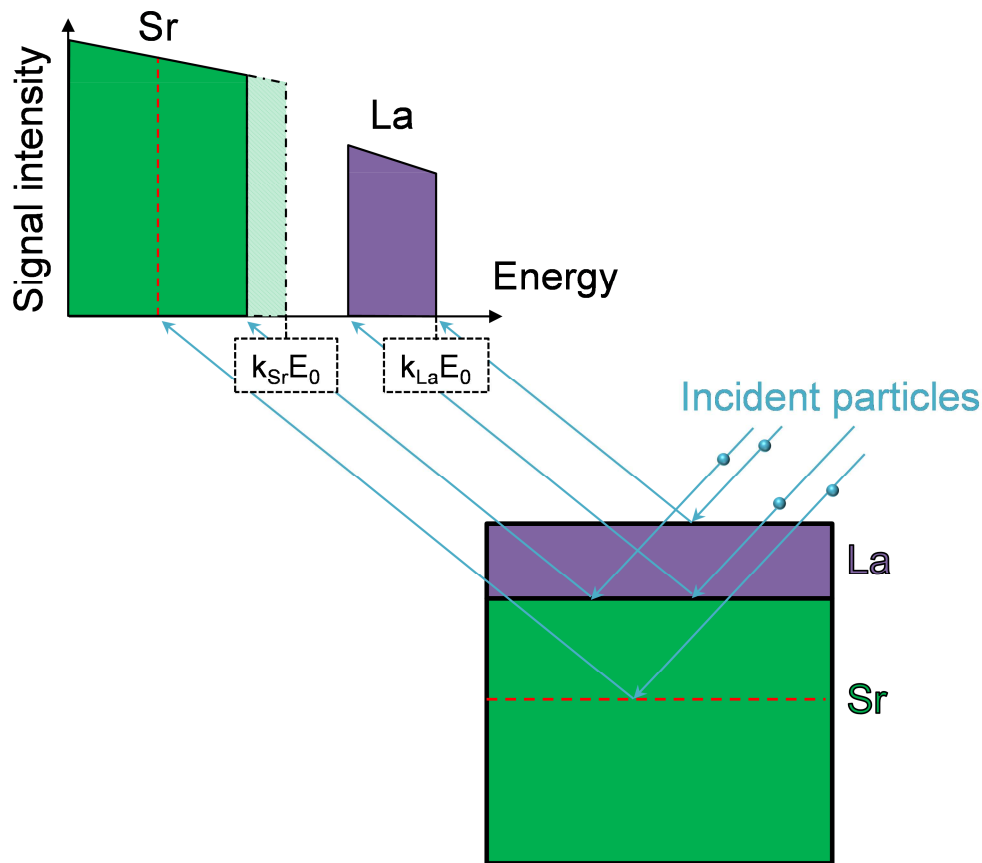


Figure II.31 | Illustration of the RBS measurements.

The lanthanum atoms on the top surface produce a signal at $k_{La}E_0$, the La threshold. The surface concentration is calculated from the height of signal at $k_{La}E_0$. Signals at lower energy than this threshold originate from La scattering centers below the surface, as additional energy is lost by travelling in the target. Since the thickness of the film is smaller than the probed depth, the signal has a “rectangular” shape rather than an extended plateau (Figure II.31).

The strontium atoms are lighter than La ones, $M_{Sr} < M_{La}$, therefore $k_{Sr} < k_{La}$. The Sr threshold (or signal from Sr atoms at the surface) would be seen at lower energy than La threshold. Here the first Sr are found below the La film, so that the first particles scattered on Sr have to cross the La film, they come out at an energy lower than $k_{Sr}E_0$ and no signal is recorded in the hatched area. The thickness of the substrate is larger than the probed depth and its composition constant, thus the Sr signal increases constantly below its step since the cross section increases when the particles penetrate the substrate in depth. The slope of the plateau is thus produced by the increase of σ when E_0 (or E_t in Figure II.29) decreases.

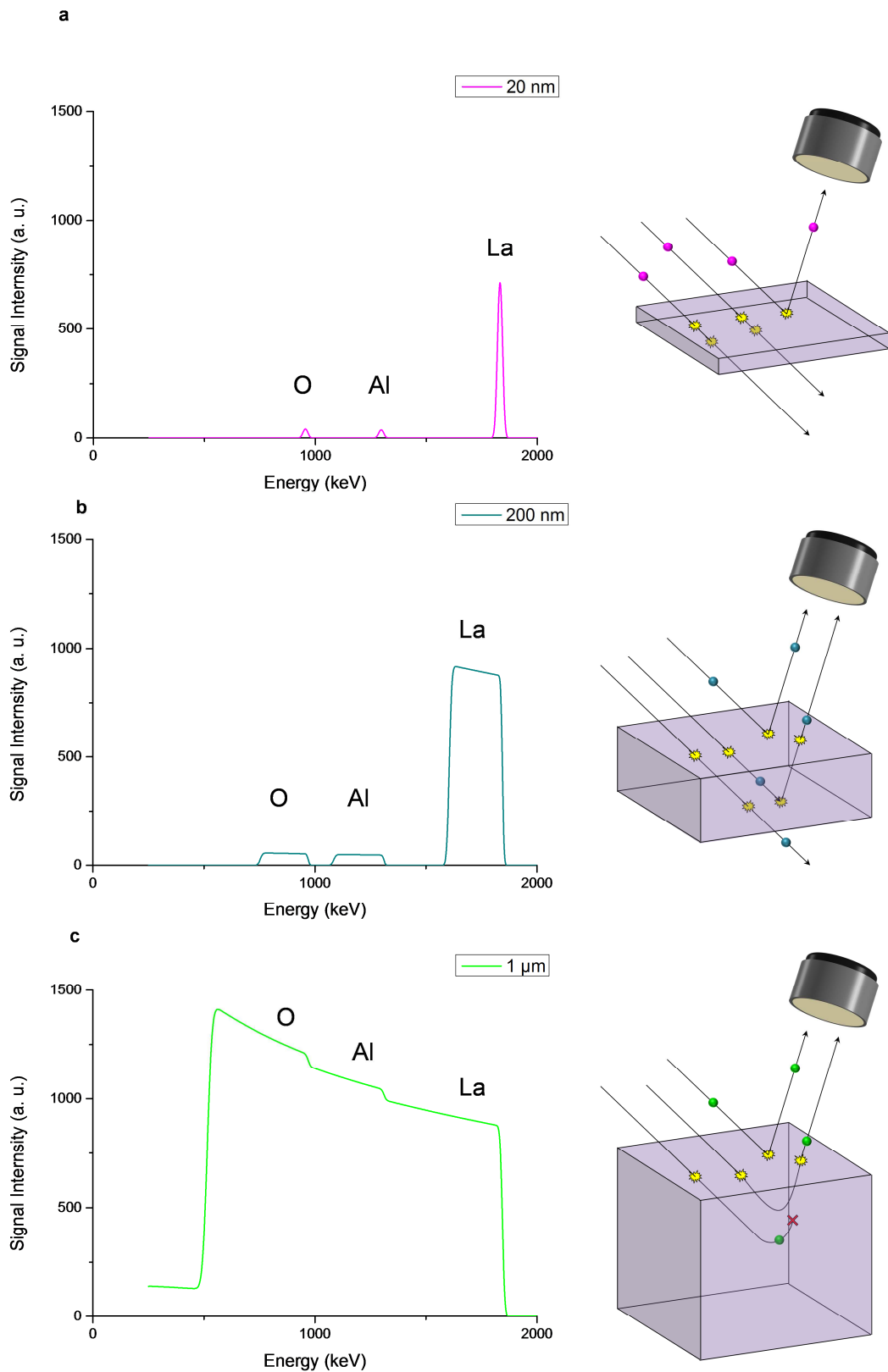


Figure II.32 | Simulated RBS spectra of LaAlO_3 bulk with various thicknesses, with a He^+ incident beam of 2 MeV and particles collected with an angle of 114.5° , associated to an illustration of the system simulated. a, RBS spectrum of a 20 nm-thick LAO. b, RBS spectrum of a 200 nm-thick LAO. c, RBS spectrum of a 1 μm -thick LAO.

We have simulated RBS spectra (${}^4\text{He}^+$ sent with energy of 2 MeV, scattered with angle 114.5°) of a single phase LaAlO_3 with various thicknesses (Figure II.32). Figure II.32a exhibits a simulation for a number of atoms per surface area, N_s , that corresponds to a 20 nm-thick LAO sample (20 nm is within the depth resolution limit of the technique). The mass ranking $M_{\text{O}} < M_{\text{Al}} < M_{\text{La}}$ is again found in the threshold ranking for the three elements. The reduced thickness of the bulk results in signals with a spike shape. It is noticeable for stoichiometric LAO, the area density of the Al peak, as well as the O peak, is much lower than for the La peak since, as it was suggested in the previous section, the cross section increases with the mass of the target atom.

When the LAO thickness increases to 200 nm, we are still below the probe distance, the width of the three signals increases (Figure II.32b) – as well as their height – compared to the former thinner sample (Figure II.32a) since the measurements were within the depth resolution in the former case. The “rectangular” shape attests that the sample thickness is larger than the energy resolution. Finally, for large thicknesses (Figure II.32c), the sample can be considered as infinite and this results in a large plateau in the RBS spectrum.

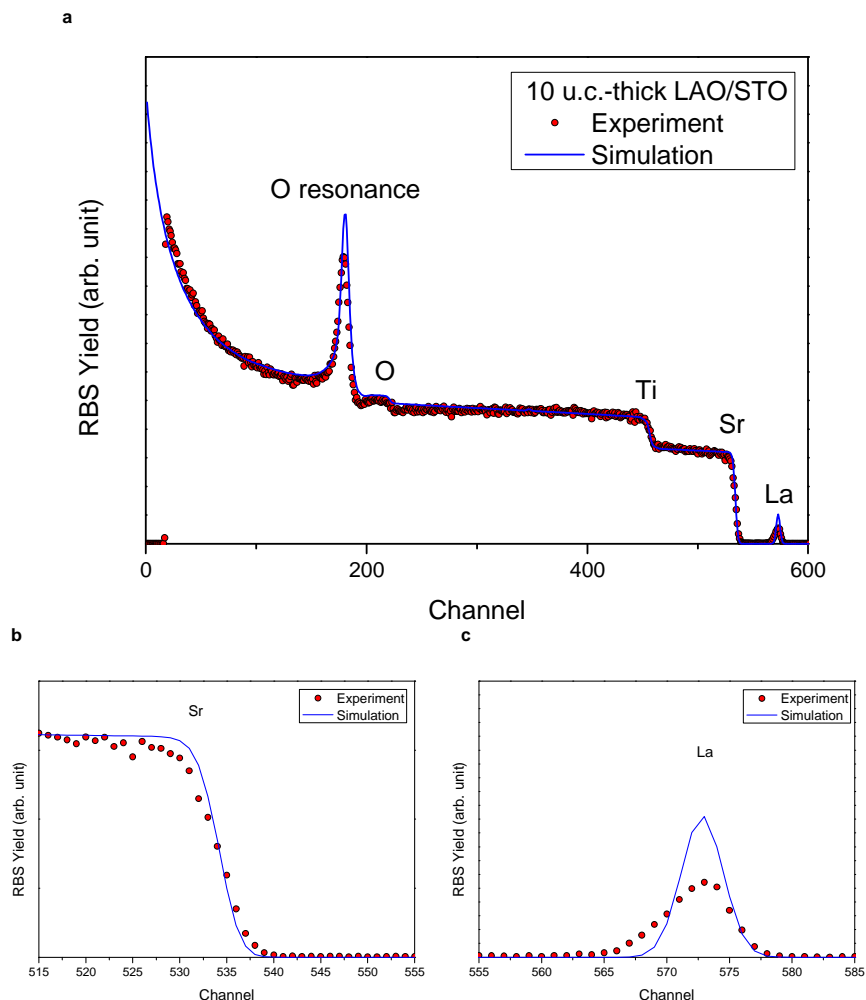


Figure II.33 | 3 MeV He^+ Random RBS experimental (red dots) and simulated (blue curve) spectra for a sample with a film thickness of 10 u.c. associated with simulated spectra. The blue curve simulates an ideal stoichiometric heterostructure with an abrupt interface. a, RBS spectrum spread over the whole energy range. All elements are identified except Al, the peak of which is buried in the

Ti plateau due to the low sensibility of the method for light elements. The large peak situated at the approximately channel 180 corresponds to the resonance peak of O. The critic variations of the cross sections occur while the incident particle energy corresponds to one of the discrete stationary energy state of the nucleus [52]. In other words, this nuclear excitation leads the nucleus to higher energetic state. **b**, Zoom on the Sr step. The experimental spectrum starts at higher energy, revealing diffusion into the LAO film. **c**, RBS spectrum focusing on the energetic distribution of La peak. The experimental spectrum does not fit the simulation revealing diffusion into the STO substrate.

After these simulations, Figure II.33 presents an experimental RBS spectrum of a 10 u.c.-thick LAO/STO heterostructure, obtained with 3 MeV helium particles sent in a direction avoiding channeling. The simulation of the same system with abrupt interface (no intermixing in fully stoichiometric LAO films) is displayed in blue. The quality of the fit is poor, due to lower tilting of the Sr step (Figure II.33b) and lower energy tails of La peaks (Figure II.33c). This means that La was distributed over a larger depth than the film thickness and the Sr signal started above the substrate surface clearly demonstrating La \leftrightarrow Sr intermixing. However, the resolution of the technique does not permit to simulate the composition gradient with the unit cell resolution required for our analyses. P.Berger thus advised us to focus on a similar technique using lower energetic incident particles, the MEIS.

II.5.3 Medium Energy Ion Scattering (MEIS)

As we seen before, in Medium-Energy Ion Scattering (MEIS) the particle energy used (a few hundred keV) gives to the target a high stopping power, allowing an analysis of the composition unit cell by unit cell. Yet, owing to the straggling phenomenon, this high depth resolution is deteriorated for particles penetrating deeper inside the sample. Therefore MEIS is a near-surface analyzing technique, with an atomic-scale resolution through 10 nm to 20 nm.

The sample is mounted on a three-axis goniometer inside the ultra-high vacuum ($\approx 10^{-10}$ mbar/ 7.5×10^{-11} Torr) chamber of the MEIS. For our study 100 keV $^4\text{He}^+$ were sent towards the sample. The backscattered ones were collected by a high resolution electrostatic detector, a Toroidal Electrostatic Analyzer (TEA) (Figure II.34a), measuring their angular positions energies. It should be noted that some of the particles becomes neutral after interacting with the electronic cloud of the atoms at such medium energy, and thus were not measured by the TEA. This phenomenon is now well taken into account for MEIS quantification. The energy resolution was equal to $\Delta E/E = 3 \times 10^{-3}$, in other words 300 eV for a beam of 100 keV, and the angular resolution was 0.1° .

Thus the standard method using the MEIS technique consists in aligning the incident particles in a crystallographic direction of the sample on the angle-resolved detector entrance and scanning the energy of the scattered ions with an electrostatic energy analyzer. Figure II.34b schematizes the three degrees of freedom (θ , ψ , φ) for angular orientation of the sample fixed on the goniometer. This set of angles controls the yield of the backscattered ions and a variety of information on the chemistry, the cell parameters and the atomic displacements can be obtained from distinct scattering geometries.

A first step consists in the identification of the geometries giving rise to these distinct scattering behaviors, by building an orientation map. A typical map is shown in Figure II.36a. The beam was hitting the sample with an angle θ_i (here $\theta_i = 26.1^\circ$), with respect to the surface orthogonal direction

([001] axis), the angles θ and ψ were fixed at -26° and 2.5° . The sample was rotating around [001] from $\varphi = -60^\circ$ to $+60^\circ$. The detector recorded the particles scattered to $\theta_{sc} = [-113^\circ, -87^\circ]$ and with energy fixed to 85.77 eV, which corresponds to Sr scattering centers located in the substrate. For each rotation angle φ , the count number N was recorded as a function of θ_{sc} .

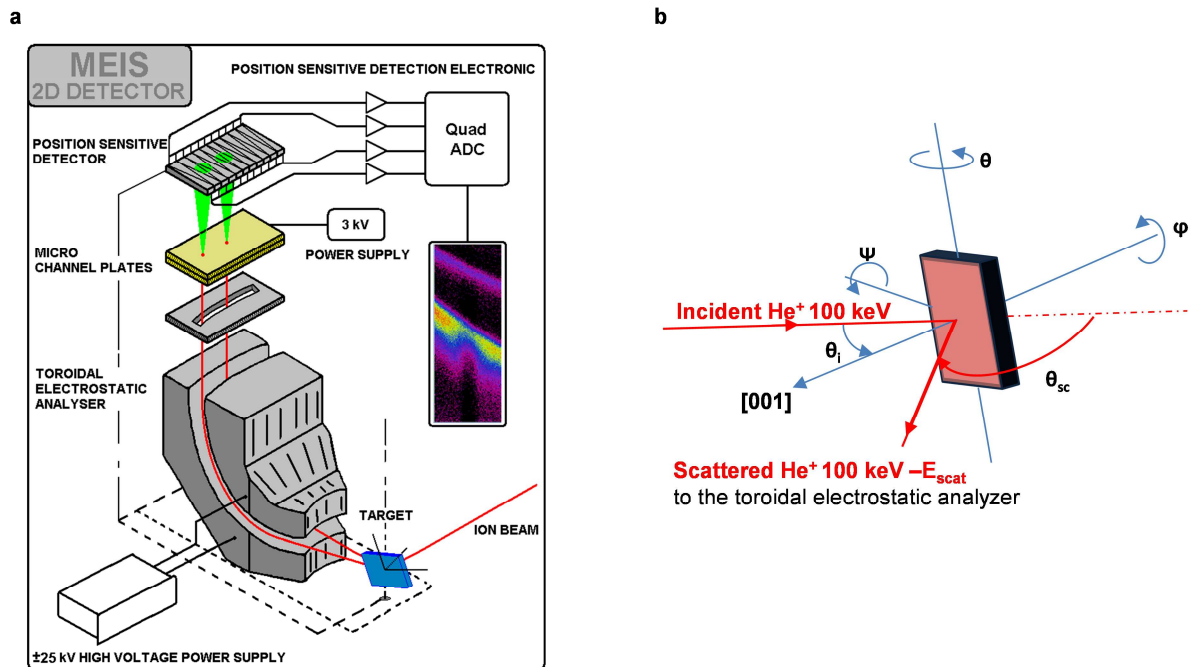


Figure II.34 | MEIS measurement method. a, MEIS Equipment. From D. Jalabert's work. **b**, Definition of the angles used to orientate the sample fixed on the MEIS goniometer.

This map (φ , θ_{sc} , N) encloses large horizontal darker strips at given angles φ . This strong decrease in the signal occurs when the beam is aligned on a low index crystal direction. The particles are then caught and guided into a channel between two parallel atomic planes experiencing small scattering angle (Figure II. 35). This particle channeling dramatically reduces the scattering probability.

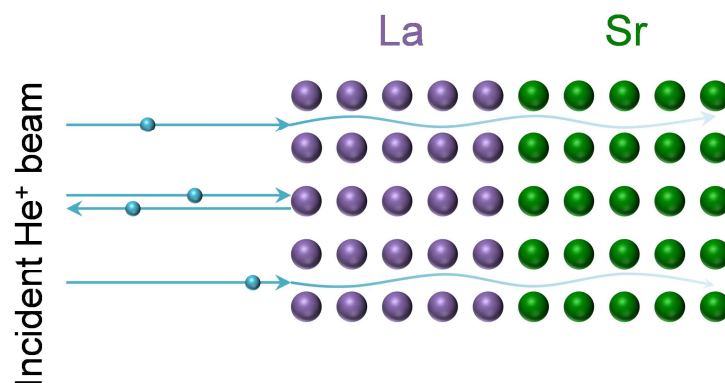


Figure II. 35 | Illustration of the incoming particles path in channeling mode.

The thinner horizontal or curved and tilted lines correspond to blocking planes due to scattered particles deflected from their initial outward trajectories by the nuclei of the first upper layers. The

intersections of such blocking lines (planes) correspond to blocking directions (“holes” in the Figure II.36c).

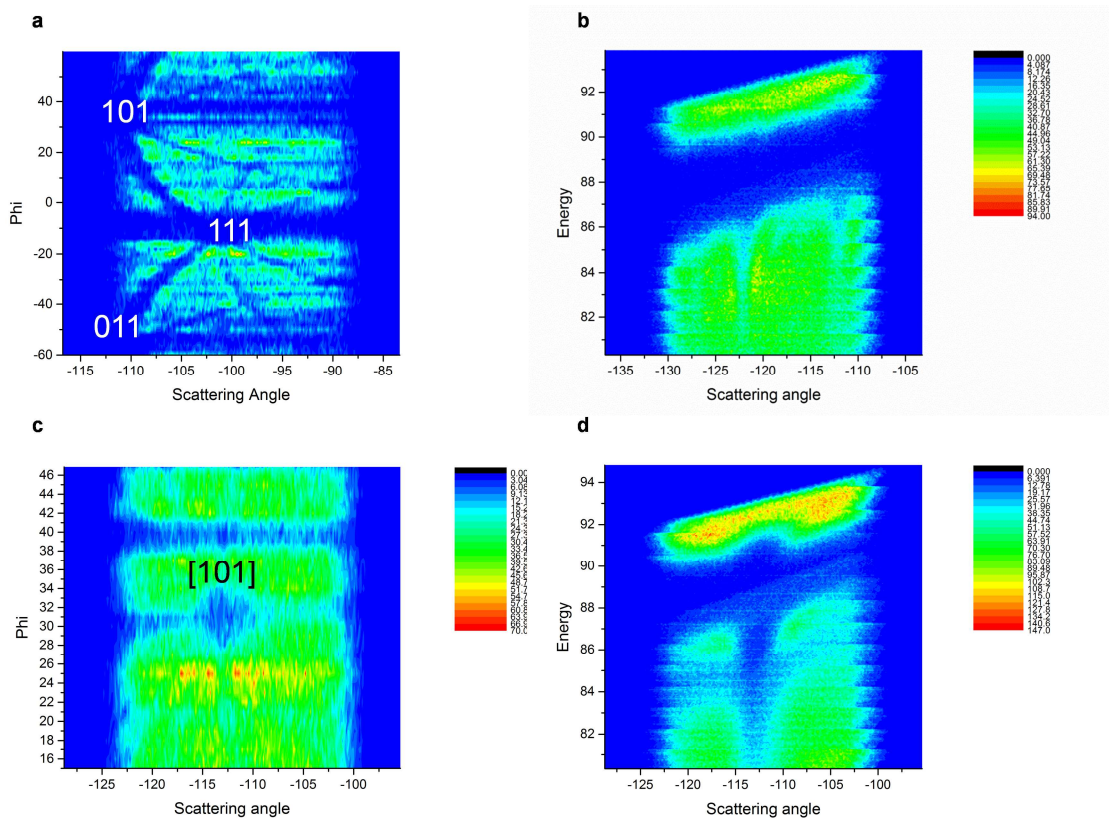


Figure II.36 | MEIS experimental maps of a LAO/STO heterostructures. a, Typical MEIS cartography (φ , θ_{sc} , N) recorded at a fixed energy corresponding to the substrate region and for a large range of φ in order to identify blocking and channeling geometries; N is the count number. **b**, Random mode 3D MEIS spectrum characterizing La (upper part) and Sr (lower part). **c**, Similar MEIS map (φ , θ_{sc} , N) using a shorter range of φ to localize more precisely the [101] blocking direction. **d**, Blocking mode 3D MEIS spectrum characterizing La (upper part) and Sr (lower part).

The map exhibits the symmetry of the cubic crystal and can be indexed in a similar way to a stereographic projection [56]. The orientation of the sample can thus be adapted to the desired MEIS mode. Figure II.36 presents the experimental maps used to characterize the sample according to “Random” and “Blocking” modes:

- Random: Channeling of the beam by dense atomic planes of the target is avoided by rotating the sample and aligning the beam direction away from a simple crystal axis. In addition the geometry for the random mode minimized the probability of a second scattering for the scattered He^+ on their way out. According to Figure II.36a, the orientation $\varphi = -21.5^\circ$ gives the highest yield. An intensity map in mode called “random” (Figure II.36b) was achieved with this set of goniometer angles. The particle energies were selected between 80.3 eV and 93.8 eV to collect the particles backscattered by La and Sr atoms.

- Blocking: The orientation map of Figure II.36a shows drops of the intensity for [101], [011] and [111] blocking directions. We selected the [101] one to get information about the c/a variations as will be explained later. The rotation angle φ and scattering angle θ_{101} for this blocking direction were more precisely determined on a second (φ , θ_{sc}) map built with smaller steps for the φ scan (Figure II.36c). Finally, similarly to random mode, the energy was varied between 80.3 eV and 93.8 eV and we measured the signal as a function of the scattering angle around θ_{101} (Figure II.36d).

We have seen the experimental setup for recording MEIS spectra. The following sections will detail the protocol to process the data obtained in random and blocking modes.

II.5.3.1 Random mode

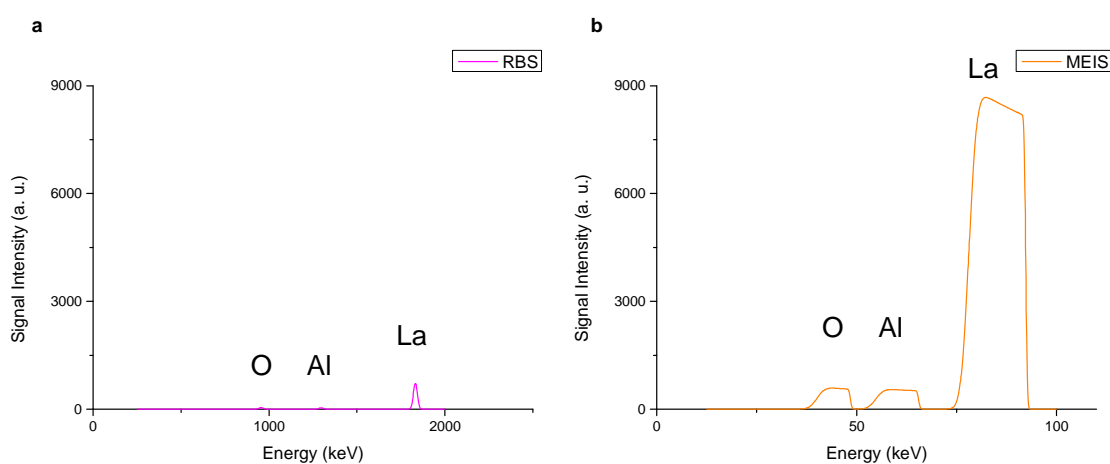


Figure II.37 | Simulated RBS and MEIS spectra of LaAlO_3 bulk with a thickness of 20 nm, and particles collected with an angle of 114.5° . **a**, RBS spectrum of a 20 nm-thick LAO and an incident particles beam of 2 MeV. **b**, MEIS spectrum of a 20 nm-thick LAO and an incident particles beam of 100 keV.

As mentioned above, the random mode avoids specific crystallographic directions (channeling and blocking). Figure II.37 highlights the main discrepancies between RBS and MEIS spectra. For the exact same simulation parameters, except for the energy of the incident beam, the MEIS $N(E_1)$ spectrum (Figure II.37b) harvested much more particles than the RBS one (Figure II.37a). The combination of larger scattering cross-sections and higher stopping powers will open up the possibility to probe the atomic exchanges unit cell by unit cell in our heterostructure.

Experimental protocol to investigate $\text{La} \leftrightarrow \text{Sr}$ intermixing

The electrostatic analyzer was tuned to collect He^+ particles backscattered by lanthanum and strontium atoms located from the film surface to around 15 u.c. under the interface. The measurements were focused on this limited energy range in order to optimize the energy resolution. The investigation of the $\text{Al} \leftrightarrow \text{Ti}$ intermixing was not possible since the Al signal was buried into the Ti plateau, making reliable quantification extremely difficult.

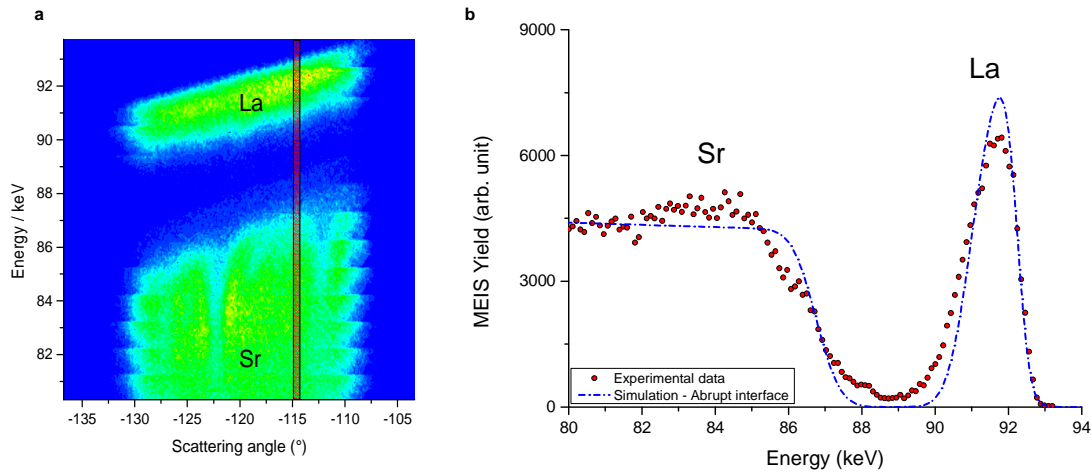


Figure II.38 | MEIS data in random mode. Incident particles : 100 keV He^+ ions. **a**, MEIS random maps (E_1 , θ_{sc} , N) of a 5 u.c.-thick LAO/STO sample. Top (-bottom) region of highest (-lowest) energies correspond to He^+ particles backscattered on La (-Sr) respectively. The red lines locates the scattering angle from which the profile was extracted. **b**, Random MEIS experimental and simulated spectra of the 5 u.c. sample with a backscattering angle of $114,5^\circ$. The blue curve simulates the MEIS theoretical spectrum for non-intermixed, fully stoichiometric LAO/STO heterostructure.

Figure II.38a shows the random map (E , θ_{sc} , N) recorded for a 5 u.c.-thick LAO/STO sample. The $N = f(E)$ curve extracted from this map at a fixed θ_{sc} (Red line in Figure II.38a) is shown in Figure II.38b where the red dots correspond to the experimental data. The experimental spectrum was compared to a simulation of an abrupt LAO/STO heterostructure with no cationic exchanges (Blue curve in Figure II.38b). The simulated spectrum does not fit the experimental spectrum, confirming that La was present deeper than the film thickness and Sr was found above the substrate surface clearly exhibiting $\text{La} \leftrightarrow \text{Sr}$ intermixing.

In order to quantify the intermixing, the experimental MEIS chemical profiles have been simulated using an in-house software similar to commercially available programs for RBS (for instance SIMNRA [57]) but with specific parameters more adapted to the medium energy range used. As an example, the screening of the nuclei charge by the surrounding electrons is modeled with the L'Ecuyer approximation [55] and the energy straggling is based on the calculations of Chu [58]. In our simulations, we made the assumption of a full occupancy of the A-site by La or Sr and of B-site by Al or Ti. The compositions ascribed to the layers should be $(\text{La}_x\text{Sr}_{1-x})(\text{Al}_y\text{Ti}_{1-y})\text{O}_3$. To simplify the $\text{La} \leftrightarrow \text{Sr}$ intermixing investigation, y values were set to 1 in the film and 0 in the substrate. It must be noted that equalizing y to x (same amount of intermixing on A- and B-sites cations) did not induce detectable variations in the fit of the Sr and La signals.

The $\text{La} \leftrightarrow \text{Sr}$ intermixing was quantified by modeling the sample with a pile up of unit cell-thick layers of distinct compositions. This allows a simulation of composition gradients with unit cell resolution. The as obtained simulated curve shown in black curve in Figure II.39 matches the experimental one except between La peak and Sr edge (between 87.5 and 89.5 keV). This suggests that element(s) with atomic numbers between that of Sr and La could be present within the heterostructure. The fit was improved when less than 1 at % of Mo, Nb or Ag were added inside the

layers (Green curve in Figure II.39). The first two elements could come from the Inconel disk supporting the STO substrate in the PLD chamber and the last one from the silver paint used to fix the substrate. Other artifacts, related to the use of an energy analyzer, could contribute to the signal in this energy range such as multiple ion scatterings or photon emission.

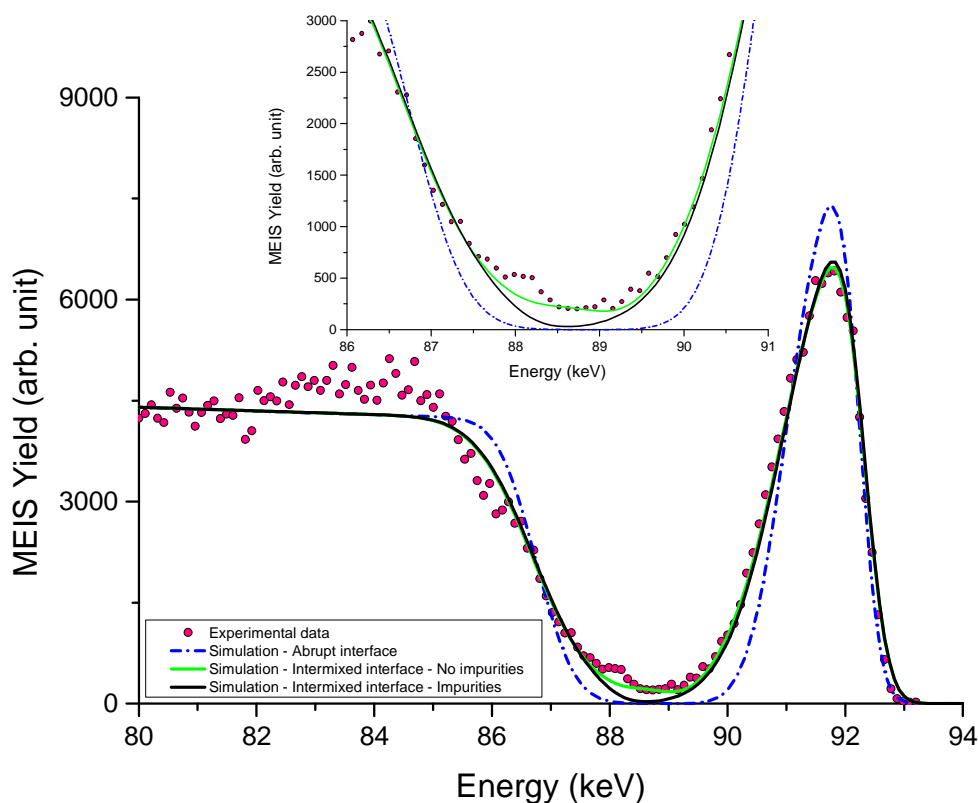


Figure II.39 | 100 keV He^+ Random MEIS experimental spectrum (red dots) collected with a backscattering angle of $114,5^\circ$ and simulated spectra (continuous curves) from LAO(5 u.c.)/STO system. The blue curve simulates an ideal stoichiometric heterostructure with an abrupt interface. The black and green curves were obtained by simulating the heterostructure with stacks of 1 u.c. slices of distinct La and Sr compositions. The stacks used for these two curves differ from each other only by the impurity concentrations introduced. The black curve is a simulation without impurity, which does not fit the signal recorded between 87.5 and 89.5 keV.

II.5.3.2 Channeling mode

When the incident beam is orientated towards a low index direction of our LAO epitaxial film/STO [001] substrate, the particles are either backscattered by the first atoms the sample surface or channeled between the atomic rows reducing the probability of being backscattered by deeper atoms as was illustrated in Figure II.40a. In the former case, the first atom backscattering the incident particle induces a shadowing cone which screens the atoms located deeper inside the material (Figure II.40b). MEIS spectra in channeling mode reflects the sample surface rather than its depth, with a decreased yield compared to random mode. It also probes the defect structure since interstitial atoms or atom positions shifted from their ideal positions will dechannel and backscatter the particles. We have only used this mode once the crystallinity of one of our film was put in doubt.

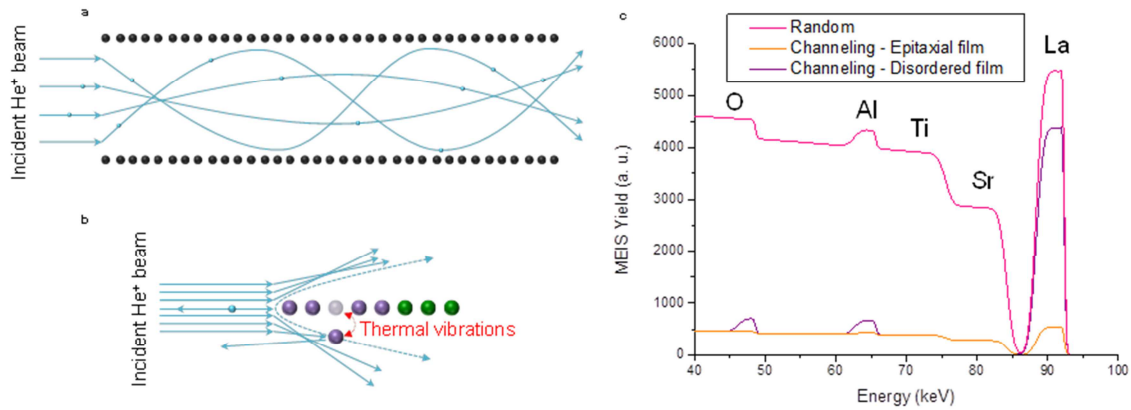


Figure II.40 | Channeling mode. **a**, Trajectories of the incident particles in an atomic row. **b**, Shadowing effect. **c**, Simulated 100 keV MEIS spectra in Random and Channeling modes of a non-intermixed 4 nm thick LAO film on a 100 nm thick STO substrate. The disordered film/substrate assembly (purple spectrum) was simulated with 20% of channeling within the film and 90% of channeling within the substrate. The epitaxial film/substrate assembly (orange spectrum) was simulated with 90% of channeling throughout the heterostructure.

Figure II.40c illustrates the discrepancies between MEIS spectra of heterostructures made of 4 nm-thick LAO/STO measured in random mode and in channeling mode with poor/good film crystallinity. The disordered LAO film impedes channeling of the particles. The count numbers for La are close to that recorded in random mode.

II.5.3.3 Blocking mode

Blocking mode consists in sending particles in a direction that promotes additional scattering by atoms situated one layer above the first backscattering center (Figure II.41a). This involves fewer particles collected by the detector, in the outgoing path. This shadow pattern is called “blocking dip” pattern and is intimately linked to the position of the second scattering atom (Figure II.41b). The (E_{sc} , N) map of Figure II.36d illustrates a typical shadowing effect at around -113° , here along [101].

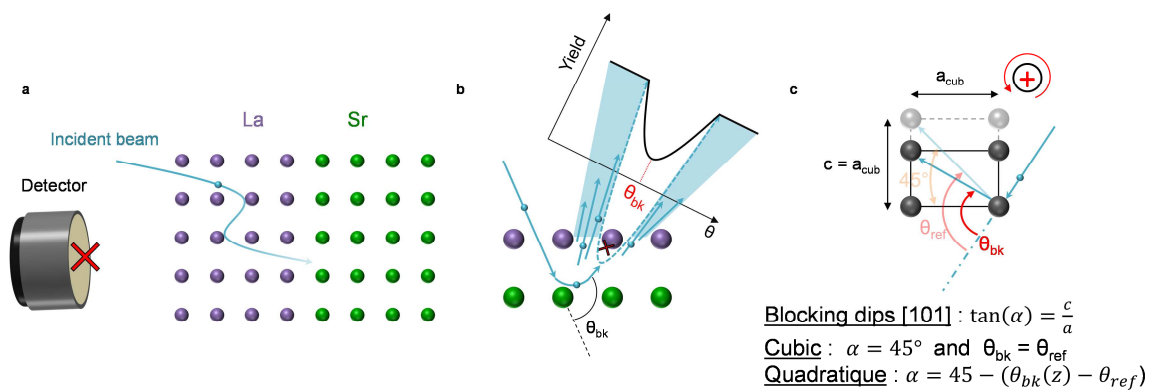


Figure II.41 | Blocking Mode features. **a**, Illustration of the blocking process. The incoming particle is scattered by the atom situated above the first scattering center and cannot escape the sample. **b**, Illustration of a blocking dip pattern formation. The particle blocked is not collected by the detector resulting in a “shadow” in the pattern. **c**, Schematic drawing of the geometry allowing to link blocking

angle and cell geometry. The blocking along [101] in a cubic structure occurs at a fix angle $\theta_{bk} = \theta_{ref}$ for an angle of 45° between the scattering and blocking atom, and depart from θ_{ref} for $c/a \neq 1$.

Experimental protocol to measure the strain profile

The variations in θ_{bk} with E_1 for blocking along [101] give access to the depth variations in the cell parameter ratio c/a . We made the assumption that the deepest analyzed unit cell within the STO substrate was not strained and cubic, with $a = c = 0.3905$ nm. The corresponding [101] blocking angle was taken as a reference, $\theta_{bk}(ref)$, for $c/a = 1$, as schematized in Figure II.41c. The variation in c/a at a depth z was then derived from $\theta_{bk}(z)$ via the following equation :

$$\frac{c}{a}(z) = \tan[45 - (\theta_{bk}(z) - \theta_{bk}(ref))]$$

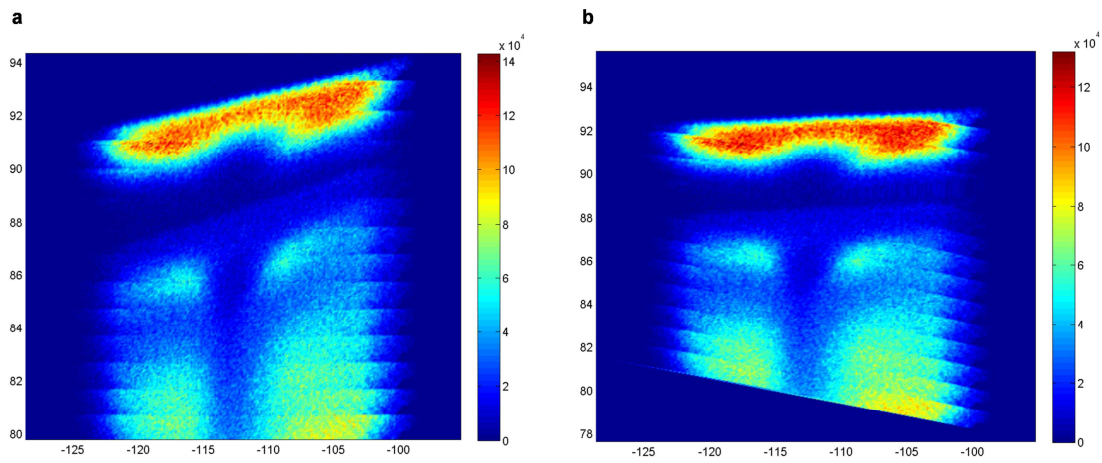


Figure II.42 | MEIS maps (E , θ_{sc} , N) obtained in Blocking mode. a, Original map. b, Original map after redress.

We also consider the in-plane parameters fixed to those of unstrained cubic STO (0.3905 nm). This assumption is justified by a previously published work [59] showing that the in-plane cell parameter of a 4.9 nm thick LAO film was 0.39028 nm (0.06% difference from that of STO) as measured by reciprocal lattice mapping (RLM). Therefore if $\theta_{bk}(z)$ differs from $\theta_{bk}(ref)$, it means that the structure is no longer cubic. Blocking dip patterns shifting to the right (left) indicates a decrease (increase) of c .

We have to determine the position of the blocking dip for each unit cell-thick layer by plotting intensity profile of $N = f(\theta_{sc})$ at iso-depth. As the kinematic factor k decreases for higher $|\theta_{sc}|$, the scattered particles coming from the same depth at higher $|\theta_{sc}|$ have lower energies. This explains the tilt of the La and Sr zones on the map of Figure II.36d and Figure II.42a. For an easier data processing, the iso-depth signals have been put on the same horizontal line. We have considered that particles, scattered at θ_{sc1} and θ_{sc2} from atoms of same mass M at the same depth, will escape the material with energies E_1 and E_2 with $\frac{E_1}{E_2} = \frac{k_1(\theta_{sc1}, M)}{k_2(\theta_{sc2}, M)}$. This assumes that the difference ($E_{1out} - E_{2out}$) between the energies lost by the particles on their way out at θ_{sc1} (path length L_1 , energy lost E_{1out}) and θ_{sc2} (path length L_2 , energy lost E_{2out}) could be neglected. The stopping power over a distance ($L_1 - L_2$) was assumed to introduce only a second order effect. Figure II.42b displays the map “rotated” around the mean scattering angle θ_{mean} using the kinematic factors $k(\theta_{sc}, La)$ and $k(\theta_{sc}, Sr)$. The depth coordinates

at θ_{mean} is assigned to each horizontal line. A blocking dip profile can be plotted at iso-depth as illustrated in Figure II.43, the angular position of the dip maximum at this depth, θ_{bk} , is determined by fitting the dip with a parabola and taking its minimum. This data processing is iterated for all the depths, for La and Sr scattering centers, and $c/a = f(z)$ profiles are plotted.

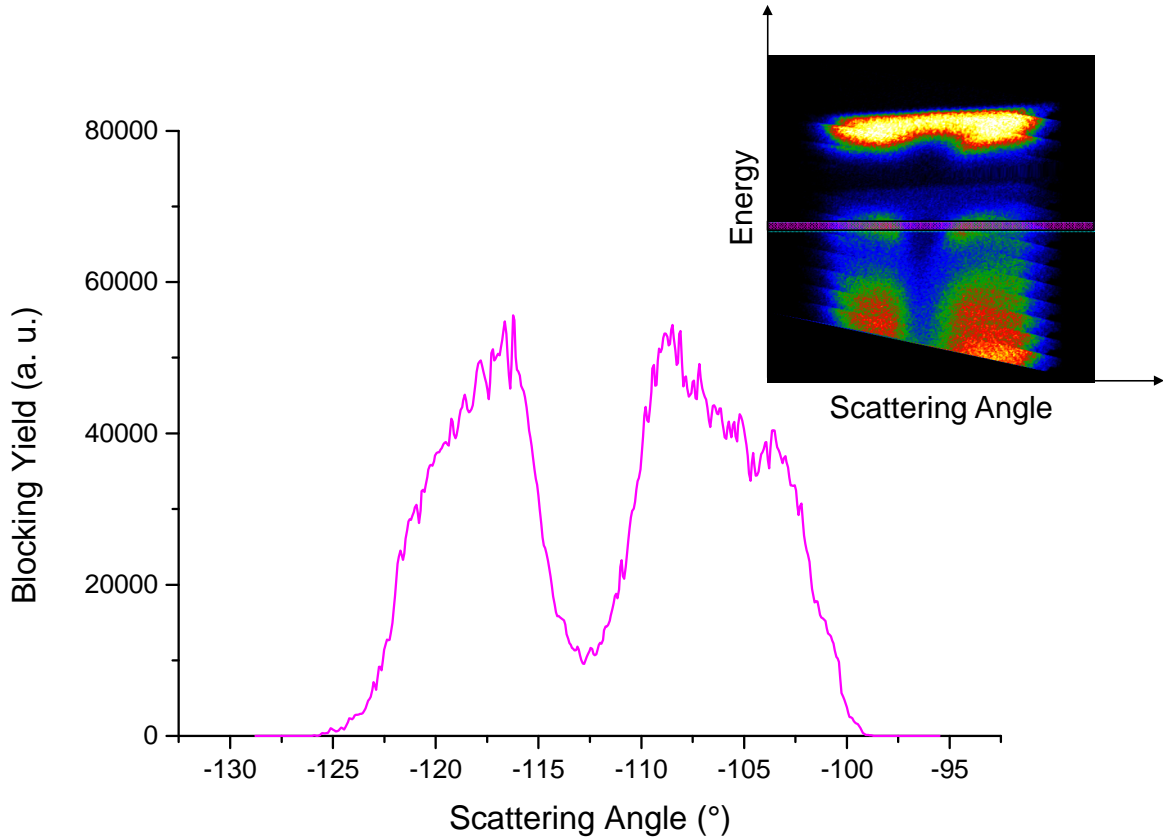


Figure II.43 | Experimental Blocking dip corresponding to particles backscattered by Sr atoms situated closed to the sample surface.

II.5.3.4 Buckling profiles

The analysis of the angular positions of the blocking dips gave us access to the variations of the distances between the A cations along [101]. We have interpreted them as c/a variations or homothetic lattice distortions. In addition we will see that local distortions around hosted cations or ferroelectric distortions can induce a buckling of the layers. In order to investigate these particular structural distortions, the blocking dips data are once again processed. However this time, instead of evaluating the angular position of the blocking dips, their angular width (FWHM) will be measured, unit cell by unit cell. The width of the shadow cone created by the second scattering on the blocking atom is linked to the nature and position of this atom (Figure II.44). The width of the blocking pattern will give information about the environment of the scattering center. This innovative method, inspired by Denis Jalabert, has never been published yet, to my knowledge, and it remains at a test level.

The angular width ω of the blocking dip is related to the radius of the shadow cone R_M , the amplitude of thermal vibrations ρ and the distance d between the blocking atom and the scattering center through the equation [53]:

$$\omega \cong 2\arctan\left(\frac{\rho + R_M}{2d}\right)$$

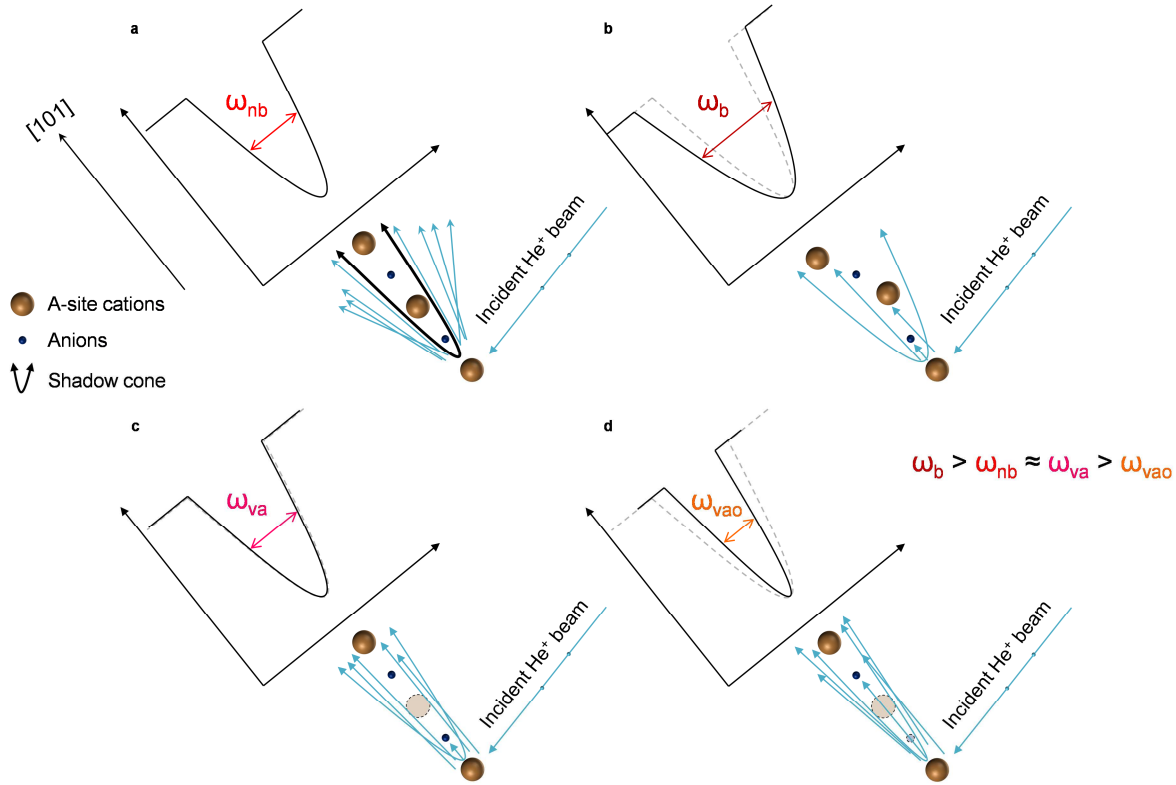


Figure II.44 | Illustration of [101] blocking events generating various blocking width in a perovskite.

a, Blocking dip generated for a non-buckled structure. Particles scattered on A-site cations and blocked along [101]. The blocking width is controlled by the first A neighbor of the scattered center in the [101] direction. **b**, Blocking dip generated for a buckled structure. The shift of the cations widens the blocking width. **c**, Blocking dip generated in a structure with one Sr vacancy. In the presence of one Sr vacancy: the blocking is now controlled by the first oxygen atom. **d**, Blocking dip generated in a structure with one Sr and O vacancy: the width is controlled by the blocking by the fourth neighbor (i.e. A cation) leading to a thinning of the blocking dips.

The width of the blocking dip will also depend, through R_M , on the atomic number of the scattering center and the blocking center, the energy at which helium particles leave the material. The variations of the blocking dip width with respect to the scattered energy of He^+ and to the scattered/blocking atoms in a crystal can be plotted. Such curves are displayed in Figure II.45a, Figure II.45b, Figure II.45c, and Figure II.45d for $\text{Sr}_{\text{scat}}/\text{Sr}_{\text{bloc}[101]}$ in STO, $\text{Sr}_{\text{scat}}/\text{O}_{\text{bloc}[101]}$ in STO, $\text{La}_{\text{scat}}/\text{La}_{\text{bloc}[101]}$ in LAO and $\text{La}_{\text{scat}}/\text{O}_{\text{bloc}[101]}$ in LAO respectively. As the exact amount of thermal vibrations at 300K was not known three indicative values were chosen (0 Å, 0.05 Å, 0.10 Å). These curves will be used as abaci for perfect STO and LAO structures. It is important to note here that the theoretical blocking width increases as the measurements reached the sample surface (i.e. at lower energy). The thermal vibration values will be determined from the width of the blocking dip in the deep non-buckled substrate and corresponding curve drawn. Then an experimental blocking width/energy couple that

cannot be plotted on this curve indicates that the corresponding blocking and/or scattering atom were not on the ideal position.

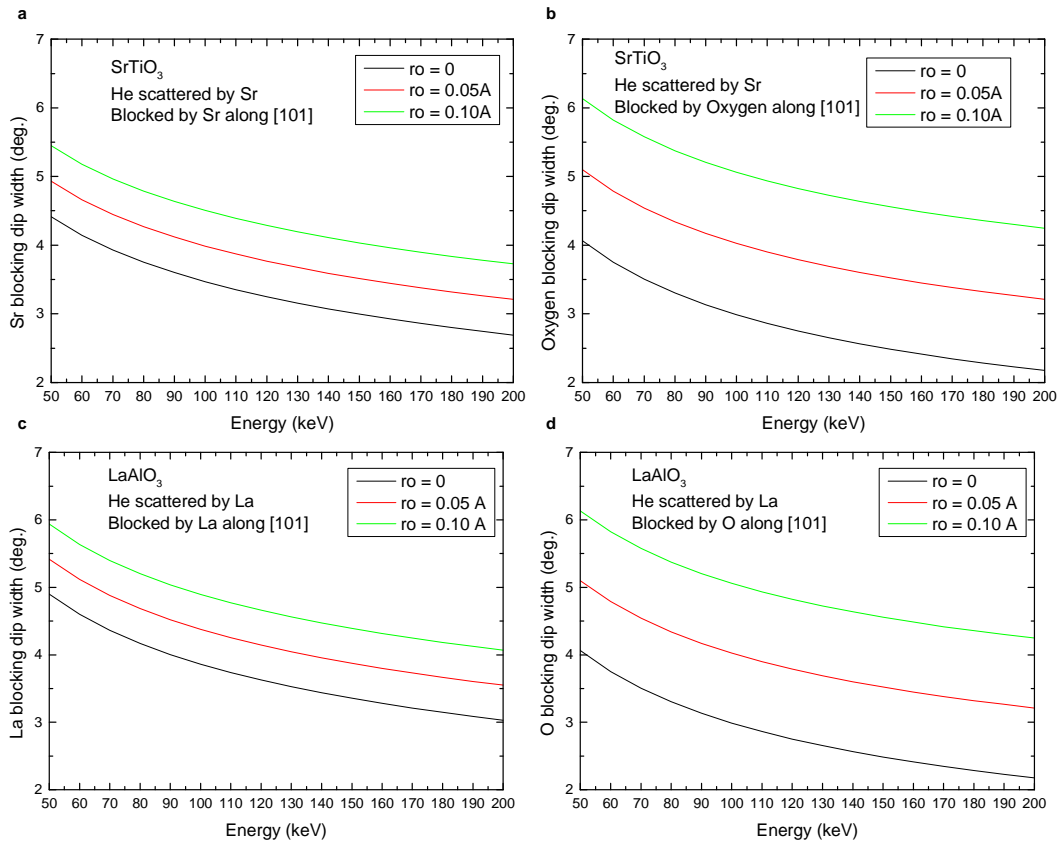


Figure II.45 | Abaci defining the theoretical blocking width for perfect STO and LAO structures. Blocking dip width as a function of scattered energy for helium ions scattered by (a, b) Sr (c, d) La and blocked by (a) Sr (c) La (b, d) O along the [101] direction in STO for various thermal vibrations at 300 K. Based on D. Jalabert’s work.

II.6 Electrical measurements

The last, but not least, section of this chapter describes the transport properties measurements of the LAO/STO heterostructures. Although I did not perform these investigations by myself, I could attend the electrical characterizations at the Department of Physics in CWRU.

In this thesis, the work was focused on the sheet resistance, carrier density and Hall mobility which were obtained by Hall Effect measurements in a four-probe Van der Pauw configuration [60]. It consists in etching the sample to reach the LAO/STO interface, where the contacts are required for a Van der Pauw geometry (Figure II.46b). Then, the scratches are filled by indium to create the contacts (Figure II.46c). Gold wires connect these contacts to the measurement sample holder (Figure II.46d and Figure II.46e). After confirming the Ohmic behavior of contacts, the transport properties are measured using standard lock-in technique with less than 1 mV excitation at 13 Hz. Electrical transport measurements were made in a physical property measurement system (PPMS, Quantum Design Inc.) with temperature varying from 2 K to room temperature, and magnetic fields up to +/- 9 T.

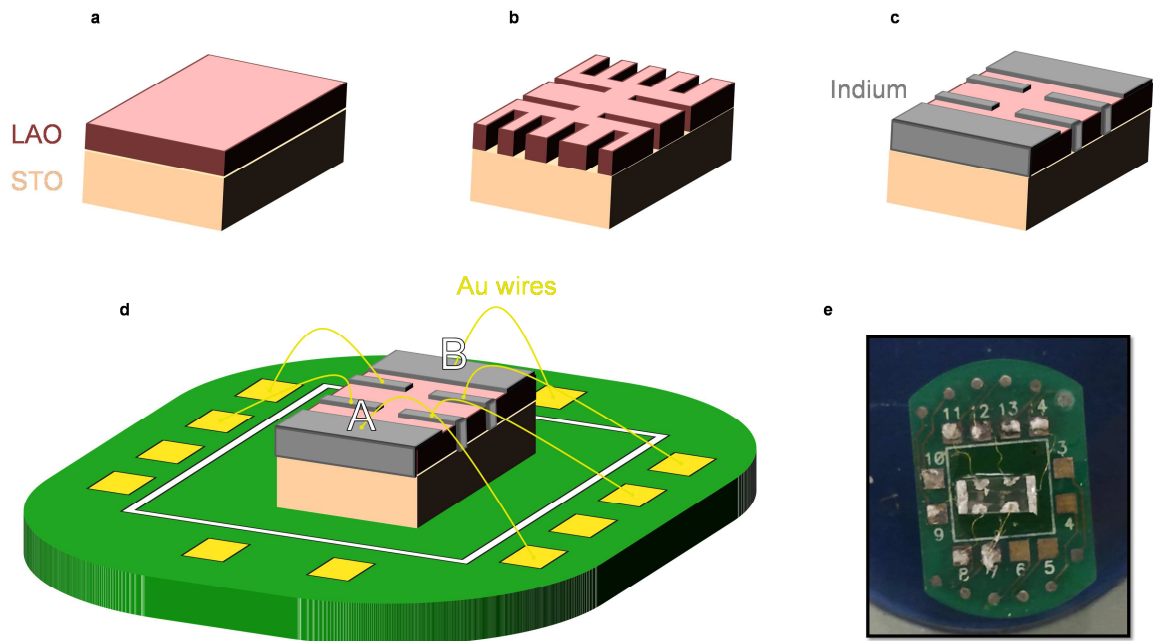


Figure II.46 | Electrical properties measurement via Van der Pauw geometry. **a**, A LAO/STO sample. **b**, Scratches are dug in the LAO film to reach the interface. **c**, Indium is deposited inside the scratches to create contacts. **d**, Gold wires are connected to the sample via the indium contacts. **e**, Picture of the device illustrated in **d**.

The electric current flows from A to B and a magnetic field is imposed perpendicular to the interface. The magnetic field exerts a transverse Lorentz force on the moving charge carriers which tends to push them to one lateral side of the conductor. This buildup of charge at the sides of the conductor will balance this magnetic influence and a measurable equilibrium voltage V_{xy} is produced between the two sides of the conductor (Figure II.47b). The presence of this measurable transverse voltage is called the Hall effect. The Hall resistance R_{xy} can be measured as a function of the applied magnetic field B . The Hall coefficient R_H is defined by the slope of the corresponding curve:

$$R_H = \frac{\partial R_{xy}}{\partial B}$$

The charge carrier density n is thus determined by:

$$n = \frac{1}{R_H \cdot e}$$

And the mobility is extracted from:

$$\mu = \frac{\sigma}{n \cdot e}$$

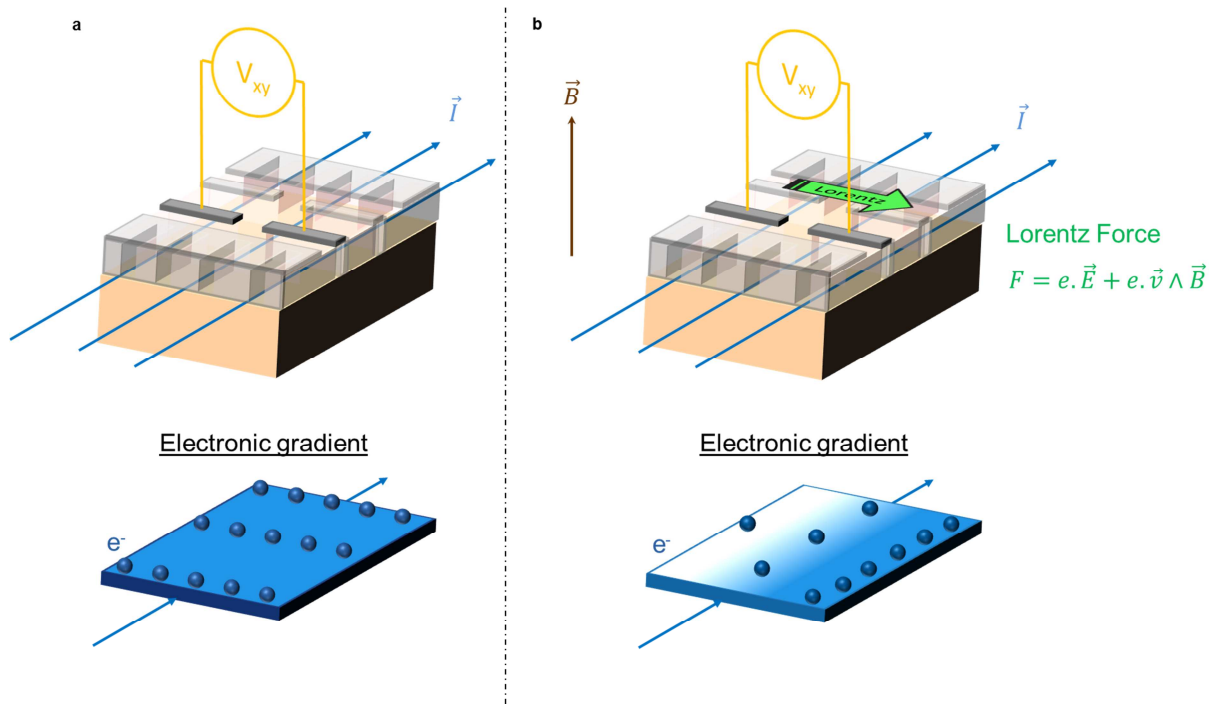


Figure II.47 | Principles of Hall measurements. **a**, System not subjected to magnetic field. In the absence of magnetic field, the electrons should be the same at each contact points of the measurement, resulting in a null Hall voltage V_{xy} . **b**, System subjected to a perpendicular magnetic field. The charged carriers differ at each contact points of the measurement, resulting in a non-null Hall voltage V_{xy} .

Others properties can be investigated by this measurement configuration, such as the low temperature magneto-resistance, or the effect of the electric field on the conduction. We restricted our measurements to the determination of the charge carrier density and mobility for the different film growth conditions. The mechanism responsible for the conducting properties at the LAO/STO interface will be searched in association with the structural characterizations carried out by STEM EELS and MEIS.

II.7 Summary

This chapter evoked the experimental methods employed through this thesis work. First, the PLD deposition process was presented. The sample preparation performed by Richard Akrobetu at NASA Glenn Research Center led to perfect TiO_2 -terminated substrates. It should be noted here that all samples studied in this thesis have a n-type interface. We have seen how dramatic can be the PLD parameters, during the growth, on the LAO/STO heterostructures properties. The TEM and MEIS investigations, shed light in this chapter, have thus been led to understand the influence of the growth conditions on the system behavior.

Bibliography

- [1] S. A. Chambers, "Epitaxial Growth and Properties of Doped Transition Metal and Complex Oxide Films," *Adv. Mater.* **22**, 219–248 (2010).
- [2] H.-U. Krebs, M. Weisheit, J. Faupel, E. Süske, T. Scharf, C. Fuhse, M. Störmer, K. Sturm, M. Seibt, et al., "Pulsed Laser Deposition (PLD) -- A Versatile Thin Film Technique," in *Adv. Solid State Phys.*, B. Kramer, Ed. (Springer Berlin Heidelberg, 2003).
- [3] P. R. Willmott and J. R. Huber, "Pulsed laser vaporization and deposition," *Rev. Mod. Phys.* **72**, 315 (2000).
- [4] M. Golalikhani, Q. Y. Lei, M. A. Wolak, B. A. Davidson, and X. X. Xi, "Narrow growth window for stoichiometric, layer-by-layer growth of LaAlO₃ thin films using pulsed laser deposition," *J. Cryst. Growth* **443**, 50–53 (2016).
- [5] M. N. R. Ashfold, F. Claeysens, G. M. Fuge, and S. J. Henley, "Pulsed laser ablation and deposition of thin films," 23–31 (2004).
- [6] A. A. Gorbunov, W. Pompe, A. Sewing, S. V. Gaponov, A. D. Akhsakhalyan, I. G. Zabrodin, I. A. Kas'kov, E. B. Klyenkov, A. P. Morozov, et al., "Ultrathin film deposition by pulsed laser ablation using crossed beams," *Appl. Surf. Sci.* **96**, 649–655 (1996).
- [7] J. Tersoff and F. K. LeGoues, "Competing relaxation mechanisms in strained layers," *Phys. Rev. Lett.* **72**, 3570–3573 (1994).
- [8] Z. L. Wang and A. J. Shapiro, "Studies of LaAlO₃{100} surfaces using RHEED and REM. I: twins, steps and dislocations," *Surf. Sci.* **328**, 141–158 (1995).
- [9] L. Qiao, T. C. Droubay, T. C. Kaspar, P. V. Sushko, and S. A. Chambers, "Cation mixing, band offsets and electric fields at LaAlO₃/SrTiO₃(001) heterojunctions with variable La:Al atom ratio," *Surf. Sci.* **605**, 1381–1387 (2011).
- [10] J.-L. Maurice, G. Herranz, C. Colliex, I. Devos, C. Carrétéro, A. Barthélémy, K. Bouzehouane, S. Fusil, D. Imhoff, et al., "Electron energy loss spectroscopy determination of Ti oxidation state at the (001) LaAlO₃/SrTiO₃ interface as a function of LaAlO₃ growth conditions," *Eur. Lett* **82**, 17003 (2008).
- [11] M. Basletic, J.-L. Maurice, C. Carrétéro, G. Herranz, O. Copie, M. Bibes, É. Jacquet, K. Bouzehouane, S. Fusil, et al., "Mapping the spatial distribution of charge carriers in LaAlO₃/SrTiO₃ heterostructures," *Nat. Mater.* **7**, 621–625 (2008).
- [12] E. Breckenfeld, N. Bronn, N. Mason, and L. W. Martin, "Tunability of conduction at the LaAlO₃/SrTiO₃ heterointerface: Thickness and compositional studies," *Appl. Phys. Lett.* **105**, 121610 (2014).
- [13] F. Schoofs, T. Fix, A. S. Kalabukhov, D. Winkler, Y. Boikov, I. Serenkov, V. Sakharov, T. Claeson, J. L. MacManus-Driscoll, et al., "Optimized transport properties of LaAlO₃/SrTiO₃ heterointerfaces by variation of pulsed laser fluence," *J. Phys. Condens. Matter* **23**, 305002 (2011).

- [14] H. K. Sato, C. Bell, Y. Hikita, and H. Y. Hwang, "Stoichiometry control of the electronic properties of the LaAlO₃/SrTiO₃ heterointerface," *Appl. Phys. Lett.* **102**, 251602 (2013).
- [15] C. Cancellieri, N. Reyren, S. Gariglio, A. D. Caviglia, A. Fête, and J.-M. Triscone, "Influence of the growth conditions on the LaAlO₃/SrTiO₃ interface electronic properties," *EPL Europhys. Lett.* **91**, 17004 (2010).
- [16] Y. Z. Chen, D. V. Christensen, F. Trier, N. Pryds, A. Smith, and S. Linderoth, "On the origin of metallic conductivity at the interface of LaAlO₃/SrTiO₃," *Appl. Surf. Sci.* **258**, 9242–9245 (2012).
- [17] G. Drera, G. Salvinelli, A. Brinkman, M. Huijben, G. Koster, H. Hilgenkamp, G. Rijnders, D. Visentin, and L. Sangaletti, "Band offsets and density of Ti³⁺ states probed by x-ray photoemission on LaAlO₃/SrTiO₃ heterointerfaces and their LaAlO₃ and SrTiO₃ bulk precursors," *Phys. Rev. B* **87**, 75435 (2013).
- [18] T. C. Droubay, L. Qiao, T. C. Kaspar, M. H. Engelhard, V. Shutthanandan, and S. A. Chambers, "Nonstoichiometric material transfer in the pulsed laser deposition of LaAlO₃," *Appl. Phys. Lett.* **97**, 124105 (2010).
- [19] A. Fête, C. Cancellieri, D. Li, D. Stornaiuolo, A. D. Caviglia, S. Gariglio, and J.-M. Triscone, "Growth-induced electron mobility enhancement at the LaAlO₃/SrTiO₃ interface," *Appl. Phys. Lett.* **106**, 51604 (2015).
- [20] A. Kalabukhov, Y. A. Boikov, I. T. Serenkov, V. I. Sakharov, J. Börjesson, N. Ljustina, E. Olsson, D. Winkler, and T. Claeson, "Improved cationic stoichiometry and insulating behavior at the interface of LaAlO₃/SrTiO₃ formed at high oxygen pressure during pulsed-laser deposition," *EPL Europhys. Lett.* **93**, 37001 (2011).
- [21] Z. Q. Liu, L. Sun, Z. Huang, C. J. Li, S. W. Zeng, K. Han, W. M. Lü, T. Venkatesan, and Ariando, "Dominant role of oxygen vacancies in electrical properties of unannealed LaAlO₃/SrTiO₃ interfaces," *J. Appl. Phys.* **115**, 54303 (2014).
- [22] S. Wicklein, A. Sambri, S. Amoruso, X. Wang, R. Bruzzese, A. Koehl, and R. Dittmann, "Pulsed laser ablation of complex oxides: The role of congruent ablation and preferential scattering for the film stoichiometry," *Appl. Phys. Lett.* **101**, 131601 (2012).
- [23] V. Vonk, M. Huijben, K. J. I. Driessen, P. Tinnemans, A. Brinkman, S. Harkema, and H. Graafsma, "Interface structure of SrTiO₃/LaAlO₃ at elevated temperatures studied in situ by synchrotron X rays," *Phys Rev B* **75**, 235417 (2007).
- [24] T. Ohnishi, K. Shibuya, T. Yamamoto, and M. Lippmaa, "Defects and transport in complex oxide thin films," *J. Appl. Phys.* **103**, 103703 (2008).
- [25] E. Breckenfeld, N. Bronn, J. Karthik, A. R. Damodaran, S. Lee, N. Mason, and L. W. Martin, "Effect of Growth Induced (Non)Stoichiometry on Interfacial Conductance in LaAlO₃/SrTiO₃," *Phys. Rev. Lett.* **110**, 196804 (2013).

- [26] S. A. Chambers, M. H. Engelhard, V. Shutthanandan, Z. Zhu, T. C. Droubay, L. Qiao, P. V. Sushko, T. Feng, H. D. Lee, et al., "Instability, Intermixing and Electronic Structure at the Epitaxial LaAlO₃/SrTiO₃(001) Heterojunction," *Surf. Sci. Rep.* **65**, 317–352 (2010).
- [27] W. Siemons, G. Koster, H. Yamamoto, W. A. Harrison, G. Lucovsky, T. H. Geballe, D. H. Blank, and M. R. Beasley, "Origin of charge density at LaAlO₃ on SrTiO₃ heterointerfaces: possibility of intrinsic doping," *Phys. Rev. Lett.* **98**, 196802 (2007).
- [28] S. Gariglio, A. Fête, and J.-M. Triscone, "Electron confinement at the LaAlO₃/SrTiO₃ interface," *J. Phys. Condens. Matter* **27**, 283201 (2015).
- [29] L. Qiao, T. C. Droubay, T. Varga, M. E. Bowden, V. Shutthanandan, Z. Zhu, T. C. Kaspar, and S. A. Chambers, "Epitaxial growth, structure, and intermixing at the LaAlO₃/SrTiO₃ interface as the film stoichiometry is varied," *Phys. Rev. B* **83**, 85408 (2011).
- [30] M. Golalikhani, Q. Y. Lei, G. Chen, J. E. Spanier, H. Ghassemi, C. L. Johnson, M. L. Taheri, and X. X. Xi, "Stoichiometry of LaAlO₃ films grown on SrTiO₃ by pulsed laser deposition," *J. Appl. Phys.* **114**, 27008 (2013).
- [31] G. Salvinelli, G. Drera, A. Giampietri, and L. Sangaletti, "Layer-resolved cation diffusion and stoichiometry at the LaAlO₃/SrTiO₃ heterointerface probed by X-ray photoemission experiments and site occupancy modeling," *ACS Appl. Mater. Interfaces* **7**, 25648–25657 (2015).
- [32] M. Huijben, A. Brinkman, G. Koster, G. Rijnders, H. Hilgenkamp, and D. H. A. Blank, "Structure-Property Relation of SrTiO₃/LaAlO₃ Interfaces," *Adv. Mater.* **21**, 1665–1677 (2009).
- [33] G. Herranz, M. Basletić, M. Bibes, C. Carrétéro, E. Tafra, E. Jacquet, K. Bouzehouane, C. Deranlot, A. Hamzić, et al., "High mobility in LaAlO₃/SrTiO₃ heterostructures: origin, dimensionality, and perspectives," *Phys. Rev. Lett.* **98**, 216803 (2007).
- [34] M. L. Scullin, J. Ravichandran, C. Yu, M. Huijben, J. Seidel, A. Majumdar, and R. Ramesh, "Pulsed laser deposition-induced reduction of SrTiO₃ crystals," *Acta Mater.* **58**, 457–463 (2010).
- [35] A. S. Kalabukhov, R. Gunnarsson, J. Börjesson, E. Olsson, T. Claeson, and D. Winkler, "Effect of oxygen vacancies in the SrTiO₃ substrate on the electrical properties of the LaAlO₃/SrTiO₃ interface," *Phys Rev B* **75**, 121404(R) (2007).
- [36] A. Ohtomo and H. Y. Hwang, "A high-mobility electron gas at the LaAlO₃/SrTiO₃ heterointerface," *Nature* **427**, 423–426 (2004).
- [37] F. Gunkel, R. Waser, A. H. H. Ramadan, R. A. De Souza, S. Hoffmann-Eifert, and R. Dittmann, "Space charges and defect concentration profiles at complex oxide interfaces," *Phys. Rev. B* **93**, 245431 (2016).
- [38] U. Balachandran and N. G. Eror, "Electrical Conductivity in Lanthanum-Doped Strontium Titanate," *J. Electrochem. Soc.* **129**, 1021–1026 (1982).
- [39] Y. Kozuka, Y. Hikita, C. Bell, and H. Y. Hwang, "Dramatic mobility enhancements in doped SrTiO₃ thin films by defect management," *Appl. Phys. Lett.* **97**, 12107 (2010).

- [40] A. Rubano, G. D. Luca, J. Schubert, Z. Wang, S. Zhu, D. G. Schlom, L. Marrucci, and D. Paparo, "Polar asymmetry of $\text{La}(1-\delta)\text{Al}(1+\delta)\text{O}_3/\text{SrTiO}_3$ heterostructures probed by optical second harmonic generation," *Appl. Phys. Lett.* **107**, 101603 (2015).
- [41] C. W. Bark, D. A. Felker, Y. Wang, Y. Zhang, H. W. Jang, C. M. Folkman, J. W. Park, S. H. Baek, H. Zhou, et al., "Tailoring a two-dimensional electron gas at the $\text{LaAlO}_3/\text{SrTiO}_3$ (001) interface by epitaxial strain," *Proc. Natl. Acad. Sci.* **108**, 4720–4724 (2011).
- [42] Z. Q. Liu, C. J. Li, W. M. Lu, X. H. Huang, Z. Huang, S. W. Zeng, X. P. Qiu, L. S. Huang, A. Annadi, et al., "Origin of the Two-Dimensional Electron Gas at $\text{LaAlO}_3/\text{SrTiO}_3$ Interfaces: The Role of Oxygen Vacancies and Electronic Reconstruction," *Phys. Rev. X* **3**, 1010–1010 (2013).
- [43] J. Ayache, L. Beaunier, J. Boumendil, G. Ehret, and D. Laub, *Guide de préparation des échantillons pour la Microscopie électronique en transmission. Tome 2, Techniques - Jeanne Ayache, Luc Beaunier, Jacqueline Pottu- Boumendil, Gabrielle Ehret, Danièle Laub* (Publications de l'Université de Saint-Etienne).
- [44] D. B. Williams and C. B. Carter, *Transmission Electron Microscopy* (Springer US, Boston, MA, 2009).
- [45] R. F. Egerton, "Electron energy-loss spectroscopy in the TEM," *Rep. Prog. Phys.* **72**, 16502 (2009).
- [46] F. de la Peña, M.-H. Berger, J.-F. Hochepeid, F. Dynys, O. Stephan, and M. Walls, "Mapping titanium and tin oxide phases using EELS: An application of independent component analysis," *Ultramicroscopy* **111**, 169–176 (2011).
- [47] D. A. Freedman, D. Roundy, and T. A. Arias, "Elastic effects of vacancies in strontium titanate: Short- and long-range strain fields, elastic dipole tensors, and chemical strain," *Phys Rev B* **80**, 64108 (2009).
- [48] L. F. Kourkoutis, H. L. Xin, T. Higuchi, Y. Hotta, J. H. Lee, Y. Hikita, D. G. Schlom, H. Y. Hwang, and D. A. Muller, "Atomic-resolution spectroscopic imaging of oxide interfaces," *Philos. Mag.* **90**, 4731–4749 (2010).
- [49] M. Varela, M. P. Oxley, W. Luo, J. Tao, M. Watanabe, A. R. Lupini, S. T. Pantelides, and S. J. Pennycook, "Atomic-resolution imaging of oxidation states in manganites," *Phys. Rev. B* **79**, 85117 (2009).
- [50] F. M. F. de Groot, J. Faber, J. J. M. Michiels, M. T. Czyżyk, M. Abbate, and J. C. Fuggle, "Oxygen 1s x-ray absorption of tetravalent titanium oxides: A comparison with single-particle calculations," *Phys. Rev. B* **48**, 2074–2080 (1993).
- [51] D. A. Muller, N. Nakagawa, A. Ohtomo, J. L. Grazul, and H. Y. Hwang, "Atomic-scale imaging of nanoengineered oxygen vacancy profiles in SrTiO_3 ," *Nature* **430**, 657–661 (2004).
- [52] P. Berger and G. Revel, "Microsonde nucléaire: Principe et appareillage," *Tech. Ing. Anal. Caractér.* (2005).

- [53] D. Jalabert, I. Vickridge, and A. Chabli, *Swift Ion Beam Analysis in Nanosciences*, 1 edition (Wiley-ISTE, Place of publication not identified, 2016).
- [54] W.-K. Chu, J. W. Mayer, and M.-A. Nicolet, *Backscattering Spectrometry* (Academic Press, London, 1978).
- [55] J. L'Ecuyer, J. A. Davies, and N. Matsunami, "How accurate are absolute rutherford backscattering yields," *Nucl. Instrum. Methods* **160**, 337–346 (1979).
- [56] D. Jalabert, "Real space structural analysis using 3D MEIS spectra from a toroidal electrostatic analyzer with 2D detector," *Nucl. Instrum. Methods Phys. Res. Sect. B Beam Interact. Mater. At.* **270**, 19–22 (2012).
- [57] M. Mayer, "SIMNRA, a simulation program for the analysis of NRA, RBS and ERDA," in *AIP Conf. Proc.* **475**, (AIP Publishing, 1999).
- [58] W. K. Chu, "Calculation of energy straggling for protons and helium ions," *Phys. Rev. A* **13**, 2057–2060 (1976).
- [59] W. Wei and A. Sehirlioglu, "Strain relaxation analysis of LaAlO₃/SrTiO₃ heterostructure using reciprocal lattice mapping," *Appl. Phys. Lett.* **100**, 71901 (2012).
- [60] D. P. Van, "A method of measuring specific resistivity and hall effect of disks of arbitrary shape," *Philips Res Rep* **13**, 1–9 (1958).

Chapitre II – Résumé

Le chapitre II se concentre autour des méthodes expérimentales utilisées lors de cette thèse, que ça soit lors de l'élaboration des hétérostructures, ou de leurs caractérisations. Il est important de noter ici que la synthèse de nos échantillons a été effectuée au laboratoire NASA Glenn Research Center à Cleveland (OH, USA) par R.Akrobetu et A.Sehirlioglu, alors que les mesures électriques ont été faites au Department of Physics de l'université Case Western Reserve University à Cleveland (OH, USA) par N.Goble and X.Gao. En ce qui concerne la caractérisation de nos échantillons, les investigations MET ont été menées avec l'aide de M.Walls du Laboratoire des Physiques du solide, de l'université Paris-Sud, et finalement les études de spectroscopies nucléaires ont été dirigées, en partie par P.Berger (RBS) du laboratoire Pierre Süe, du CEA à Saclay, et principalement par D.Jalabert (MEIS) du laboratoire CEA tech/Leti/DTSI/SCMC à Grenoble.

Plusieurs prérequis ont été mentionnés dans le précédent chapitre sur l'optimisation des propriétés électriques des hétérostructures LAO/STO, et notamment la terminaison TiO_2 du substrat. Pour réaliser cette étape, les plaquettes monocristallines de STO sont placées dans une solution chimique qui va dissoudre exclusivement les groupements SrO, puis sont recuits dans une atmosphère oxydante, pour améliorer la recristallisation. La technique de dépôts de nos films LAO sur les substrats avec une terminaison TiO_2 correspond à la plus répandue dans la littérature, à savoir la technique d'ablation par laser pulsé (PLD). Elle consiste à envoyer un faisceau laser hautement énergétique vers un matériau cible, via un système de miroirs. Le laser est alors absorbé par la cible qui va être éjectée sous forme d'une plume, contenant les atomes du matériau cible, qui se condense à la surface du substrat. La croissance du film se fait ainsi successivement aux pulsations du laser, et est suivie en direct par la diffraction d'un faisceau d'électrons en incidence rasante (RHEED), à la surface de l'échantillon, interceptée par un écran fluorescent. Néanmoins, la qualité du dépôt est sujette à un nombre important de fluctuations qui dépendent des paramètres utilisés lors de la croissance, et liés à la technique PLD. La fluence du laser, définie par la densité énergétique du laser, a un impact important sur les propriétés de l'échantillon. En effet, un laser avec une haute fluence va avoir tendance à extraire préférentiellement les cations B de la cible, ce qui va résulter en un film ayant un excès de cations B. De plus, à haute densité énergétique le laser va introduire plus de défauts cristallins lors de l'impact de la plume sur le substrat. Ceci, ajouté à la non-stœchiométrie du film, induit des distorsions structurales qui ont une forte influence sur les propriétés électriques. La plume en elle-même joue également un rôle important sur le comportement électrique des échantillons. On a vu que la cinétique du plasma pouvait avoir des conséquences irréversibles, toutefois il est possible d'ajuster la distance entre la cible et le substrat pour les minimiser. De plus, la position du substrat vis-à-vis de la plume comme la pression partielle d'oxygène dans la chambre

sont primordiales pour contrôler la stœchiométrie du film. La présence de lacunes d'oxygènes a été établie lors d'élaborations d'échantillons à basse pression d'oxygène. Ces défauts intrinsèques apportent des électrons supplémentaires, améliorant ainsi la conductivité de l'échantillon. Dans le même temps, plusieurs études ont montré que la pression partielle d'oxygène permet de réguler le mécanisme de compensation de la discontinuité électronique présente dans les hétérostructures LAO/STO. Notamment, augmenter ce paramètre favorise l'apparition de lacunes de Sr, alors qu'en l'abaissant le déséquilibre est compensé par des électrons. On n'a pas cité l'interdiffusion, les distorsions structurales ou encore le mode de croissance sur lesquels la pression partielle d'oxygène a un effet, mais on observe que c'est un facteur extrêmement important dans l'élaboration des échantillons. Finalement, nous avons montré que la température de croissance influe tout autant sur le comportement de nos échantillons, avec de meilleurs propriétés conductrices lorsqu'ils sont déposés à plus haute température.

Afin de comprendre le comportement des hétérostructures LAO/STO, nous avons utilisé plusieurs outils de caractérisations, allant de la microscopie en transmission (MET) en passant par l'analyse par faisceau d'ions, et plus précisément l'analyse haute-résolution à moyenne énergie (MEIS). Dans le premier cas, après avoir rappelé les techniques de préparation des échantillons MET, à savoir le polissage mécanique (tripode + bombardement ionique) et le polissage ionique (FIB), nous nous sommes concentrés sur l'appareil MET dont nous nous sommes principalement servis, le Nion UltraSTEM avec une résolution spatiale inférieure à 0.1 nm. Les méthodes annexes, utilisées avec cet appareil, ont également fait l'objet d'un bref descriptif telles que le MET en mode balayage à grand angle (STEM-HAADF) et la spectroscopie en pertes d'énergies (EELS). Alors que la méthode STEM-HAADF nous a permis d'obtenir des informations sur la chimie de nos échantillons grâce au contraste en Z (numéro atomique), les spectres EELS ont été mesurés pour détecter la présence lacunes d'oxygènes, pour quantifier la distance d'interdiffusion, ou encore pour suivre l'état d'oxydation du titane autour de l'interface LaO/TiO₂. Dans ce dernier cas, nous avons opté pour une comparaison entre le spectre EELS à l'interface et une combinaison linéaire de deux références des spectres EELS Ti⁴⁺ (mesurée dans le substrat STO) et Ti³⁺ (mesurée dans les mêmes conditions sur du Ti₂O₃), par la méthode des moindres carrés. Dans un deuxième temps, après avoir rappelé les principes fondamentaux des mécanismes mis en jeu lors des réactions nucléaires, nous avons développé les techniques d'analyses par faisceau d'ions que nous avons utilisé dans cette thèse. En particulier, la technique MEIS consiste à mesurer la distribution énergétique et angulaire de particules rétrodiffusées par le solide étudié. La spécificité de cette méthode réside dans la gamme énergétique des particules envoyées, de l'ordre de quelques keV, qui confère une meilleure résolution énergétique, et donc en profondeur, aux mesures. Cette singularité permet ainsi d'obtenir des informations précises couche atomique par couche atomique sur une profondeur de l'ordre d'une dizaine de nanomètres. Un des avantages de ce type de mesures est la variété des informations que l'on peut obtenir suivant l'orientation de l'échantillon. Aussi, trois modes principaux se dégagent des données MEIS. Tout d'abord le mode « Random », dans lequel le faisceau d'ions est envoyé dans une direction évitant toute perte de signal par une canalisation quelconque et par diffusions supplémentaires des particules par des atomes des couches supérieures. Ainsi, les particules rétrodiffusées apportent des informations sur le profil chimique de l'échantillon avec une résolution atomique. Ensuite, nous avons abordé le mode « Channeling ». Il consiste à orienter le faisceau de telle façon à ce qu'il soit parallèle aux plans denses du cristal. En effet, puisqu'on analyse un système fait de monocristaux, les particules d'ions canalisent entre les colonnes atomiques, ce qui réduit leur

probabilité d'être rétrodiffusés vers le détecteur. L'information mesurée est donc spécifique à la surface de l'échantillon. Enfin, le dernier mode, appelé « Blocking », est obtenu lorsque les particules incidentes subissent une seconde rétrodiffusion, lors de leur sortie vers le détecteur, de la part d'atomes situés sur une couche atomique au-dessus des premiers centres diffuseurs. Ceci implique un nombre de particules collectées bien inférieur que si le faisceau avait été dirigé dans une direction « Random ». L'effet d'ombrage engendré est intimement lié à la position des atomes faisant office de seconds centres de diffusions. Ainsi, un déplacement de ces cations va provoquer un déplacement angulaire du cône d'ombrage. On obtient donc des informations sur la structure des échantillons analysés. De plus, la taille de ces cônes d'ombrage nous révèle également des informations sur l'environnement des centres de diffusion. En effet, suivant la présence de lacunes, d'atomes de substitution, ou même de flambage, la largeur angulaire des cônes varie ce qui permet d'en savoir plus sur le réseau cristallin entourant les atomes « bloquant ». Ce chapitre se termine sur la présentation de la méthode des mesures électriques qui ont été effectuées par la méthode de Van der Pauw, consistant à mesurer le gradient électronique créé par effet Hall.

Chapter III

Origin(s) of the q-2DEG at the LAO/STO hetero-interface

In this chapter, the objective is to go through the mechanisms responsible for the conduction at the LaO/TiO₂ interface described in Chapter I and to investigate their validity for a set of heterostructures grown in the same conditions with film thicknesses below and above the presumed critical thickness. This chapter is built mainly from our article [1]: Zaid, H. *et al.* Atomic-resolved depth profile of strain and cation intermixing around LaAlO₃ /SrTiO₃ interfaces. *Sci. Rep.* **6**, 28118 (2016). In Table III.1 below, the PLD growth parameters, used to synthesize the samples described in this chapter, are presented. Attempt was made to avoid the bulk conductivity described at lower partial pressure, to reduce the density of growth defects seen at lower temperature, to optimize the quality of the growth by centering the substrate relatively to the plasma plume.

Sample	TEM preparation	Thickness	P _{O₂}	Laser Fluence	Plume angle	Temperature
<i>UC10</i>	Mechanical	10 u.c.	10 ⁻⁴ Torr	1.2 J/cm ²	#2	750°C
<i>UC5</i>	FIB	5 u.c.	10 ⁻⁴ Torr	1.2 J/cm ²	#2	750°C
<i>UC3</i>	FIB	3 u.c.	10 ⁻⁴ Torr	1.2 J/cm ²	#2	750°C

Table III.1 | Growth parameters of the samples studied in this chapter.

III.1 Film growth

First of all, the growth quality of the film will be evaluated through TEM works. We will focus on a ten unit cells (u.c.) LAO film deposited on a TiO₂-terminated substrate. Indeed this is the thickest sample we have ever deposited during this thesis. If growth defects, such as those caused by epitaxial strain, cannot be observed for a 10 u.c.-thick film they will not be developed for thinner films grown in the same conditions. This sample, called *UC10*, was realized by PLD according to the above mentioned growth parameters (Table III.1).

Chapter III | Origin(s) of the q-2DEG

The *UC10* thin foil for TEM investigations was carefully prepared by mechanical (tripod) polishing followed by a rapid 4 keV Ar⁺ milling. The first step was to check the quality of the growth. Indeed, as we mentioned in the first chapter, the misfit between the LAO and STO lattices is 2.9%. In case of a pseudomorphic growth, the in-plane lattice parameters of LAO would be stretched to fit that of STO. If no relaxation is involved, this elastic deformation would induce a contraction of the out-of-plane lattice parameter of the LAO. In a model with no intermixing and no relaxation, this lattice parameter is reduced to about 3.72 Å ($v_{LAO} = 0.24$) [2]. This allows a spot separations to be seen on SAED patterns along the [001]* direction, whereas no splitting is observed along [100]*. This is illustrated in Figure III.1a and Figure III.1b. The experimental SAED pattern shows a splitting on the high order 00 l spots not seen on the h00 ones (Figure III.1d), this confirmed the pseudomorphic growth of LAO on STO.

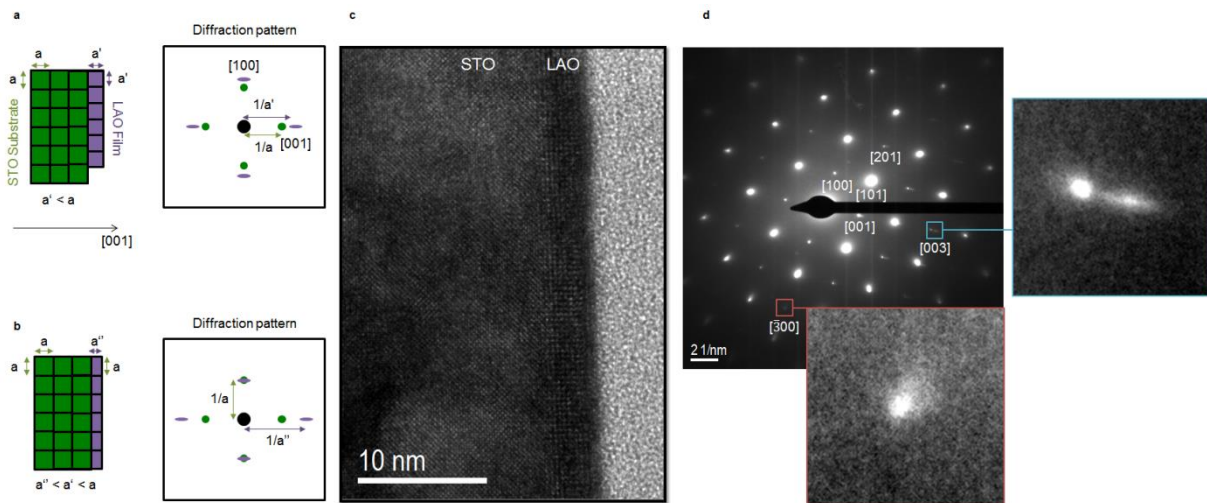


Figure III.1 | Characterization of LAO pseudomorphic growth on STO substrate. **a**, Schematic diagram of a diffraction pattern for totally relaxed film growth. The zone axis is [010] with 100 and 001 spots drawn. The cell parameters of bulk STO and LAO are written a and a' respectively with $a > a'$. In this relaxed configuration $d_{100,STO}^* = d_{001,STO}^* = 1/a < d_{100,LAO}^* = d_{001,LAO}^* = 1/a'$. LAO spots are elongated due to the finite dimension in the film thickness direction. **b**, Diffraction pattern for an epitaxial non relaxed film growth. In this configuration, $d_{100,LAO}^* = d_{100,STO}^* = d_{001,STO}^* = 1/a$ and $d_{001,LAO}^* = 1/a'' > 1/a'$ due to the lower out-of-plane lattice parameter of the film, a'' . **c**, HRTEM image of *UC10* taken with Tecnai ST-F20. **d**, Experimental diffraction pattern corresponding to *UC10*. One observes that the spots are separated in the [001]* direction while they are at the same position in the [100]* direction, confirming the pseudomorphic growth.

The USTEM observations confirmed that the growth was coherent: the in-plane lattice parameters of the film fit with the substrate ones and no misfit dislocations are detected along the foil observed, as seen on Figure III.2. In addition, the thickness of the film is in agreement with the RHEED pattern and oscillations numbers communicated by R.Akrobetu, that corresponded to 10 u.c. deposited.

The chemical contrast permits to identify the La ($Z = 57$), Sr ($Z = 38$) and Ti ($Z = 22$) atoms with brighter contrast for higher Z on STEM-HAADF images. As we specified previously, the Al and O atoms are too light to be observable by STEM-HAADF here, unless in the very first film unit cell (which the thinnest part of the TEM cut) where the B-site cations may be Al atoms. The interface is indicated by a red arrow in Figure III.2 below.

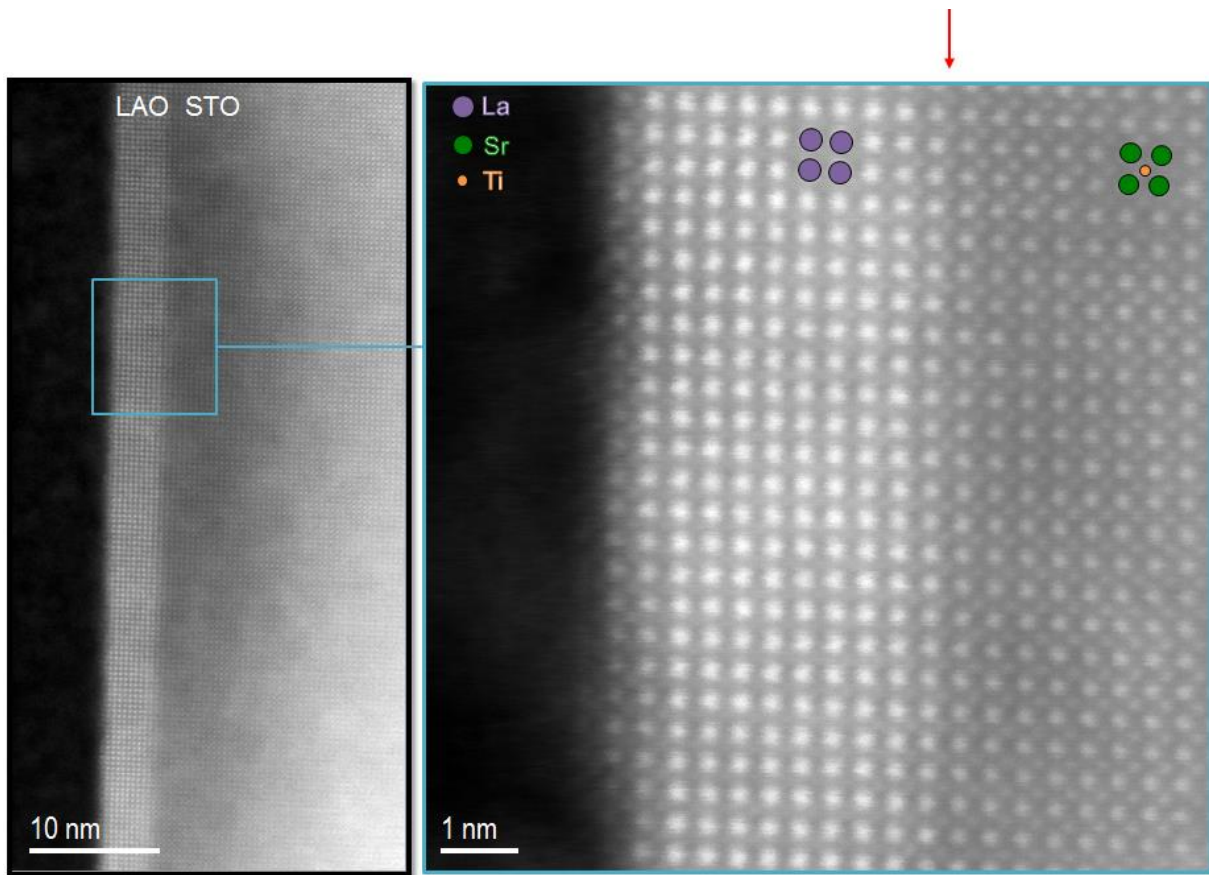


Figure III.2 | Representative HAADF images of LaAlO_3 films grown pseudomorphically on SrTiO_3 (UC10). The interface is shown by a red arrow, La (Sr) {Ti} atoms are illustrated by purple (green) {orange} circles. No misfit dislocations could be detected at LAO/STO interfaces along the entire distance observed via Nion UltraSTEM.

III.2 Polar catastrophe

III.2.1 Critical thickness

We have seen in the first chapter (section I.5.1) that the polar catastrophe model involved the build-up of an electrostatic field across the thickness of the polar LAO film deposited on the non-polar STO substrate. Once the critical value of 4 u.c. is reached, the diverging electrostatic potential is removed by the transfer of half an electron per unit cell into the first STO layer below the interface. A theoretical average valence of $\text{Ti}^{3.5+}$ would be thus expected resulting in a 2D carrier density of $3.3 \times 10^{14} \text{ cm}^{-2}$. The electrical properties of the samples UC5 and UC3 tend to support such model. The sample UC5 exhibited a conductive interface, with a 2D charge carrier density at 5 K of $\approx 3 \times 10^{14} \text{ cm}^{-2}$ while for the 3 u.c. film the resistance exceeded our instrumental limits ($> 100 \text{ M}\Omega$) (Figure III.3). Thus, consistently with previous studies [3–7], the critical thickness lies between 3 and 5 u.c.. However it is noteworthy that the carrier density obtained at room temperature, $n \approx 1.25 \times 10^{15} \text{ cm}^{-2}$, is four times higher than the theoretical one and adding to this the theoretical Ti valence at the interface should be equal to +2.15 to reach this density, suggesting that the carriers were not confined in a 2D layer.

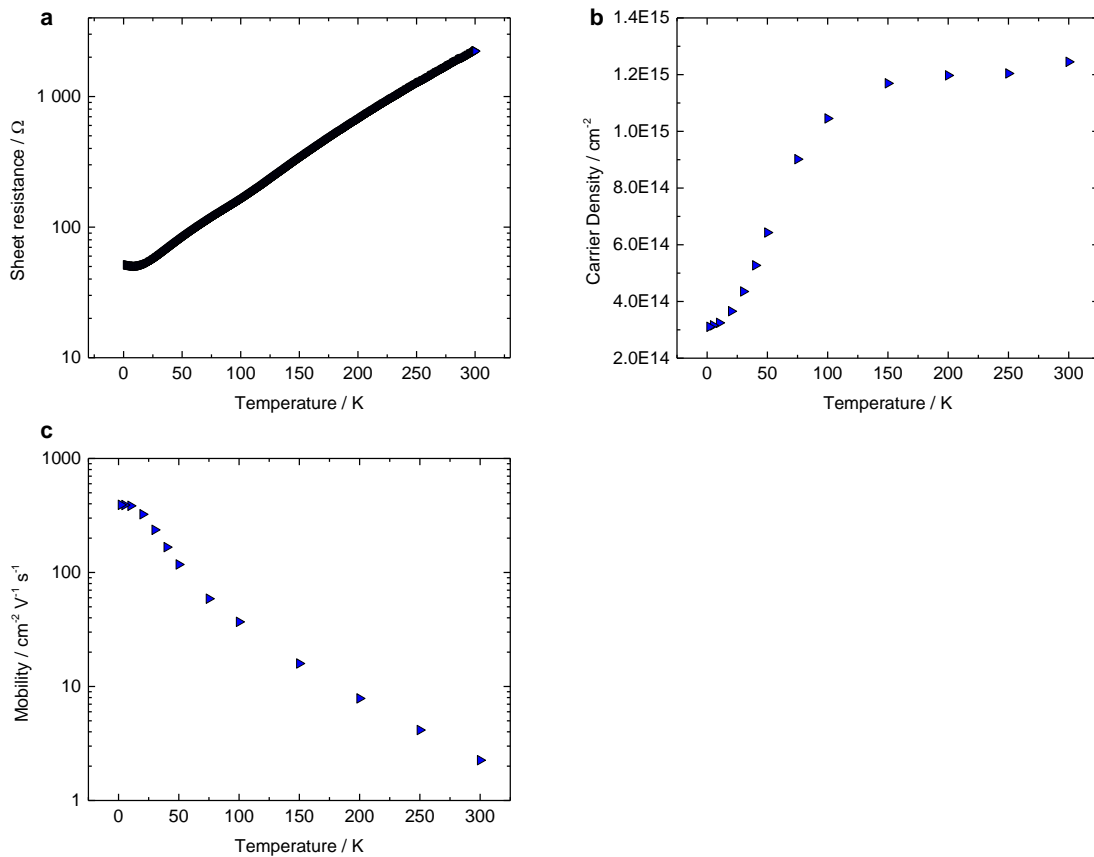


Figure III.3 | Electrical measurements of the sample UC5. Evolution of (a) sheet resistance, (b) carrier density, (c) Hall mobility, as a function of temperature. The sample exhibits metallic conductivity with a carrier density larger than $1.2 \times 10^{15} \text{ cm}^{-2}$ at room temperature.

We have then performed EELS investigations at the interface to probe the valence of Ti atoms and its accordance with the polar catastrophe model. Indeed, we mentioned in Chapter II (section II.4.3.1) that valence changes influence significantly the shape of the absorption edges [8].

III.2.2 Ti valence

EELS spectrum images and profiles across the interface of the samples UC5 and UC3 were used to deduce the contribution of Ti³⁺ to the Ti-L_{2,3} absorption edges, as presented in Figure III.4. First we note that the quality of the growth (Figure III.4a and Figure III.4c) is similar to the sample UC10. Then, a minimum valence of about Ti^{3.9+ (+/- 0.05)} was found located in the first unit cell below the interface for both samples (Figure III.4b and Figure III.4d). This would lead to a maximum theoretical density of free charge carriers of $6.6 \times 10^{13} (+/- 3.28 \times 10^{13}) \text{ cm}^{-2}$.

These results, leading to Ti oxidation state higher than the +3.5 value predicted by the polar catastrophe model for a conducting interface, are consistent with multiple studies led by EELS [9–12], as well as XPS [13–17] for a wide range of growth conditions.

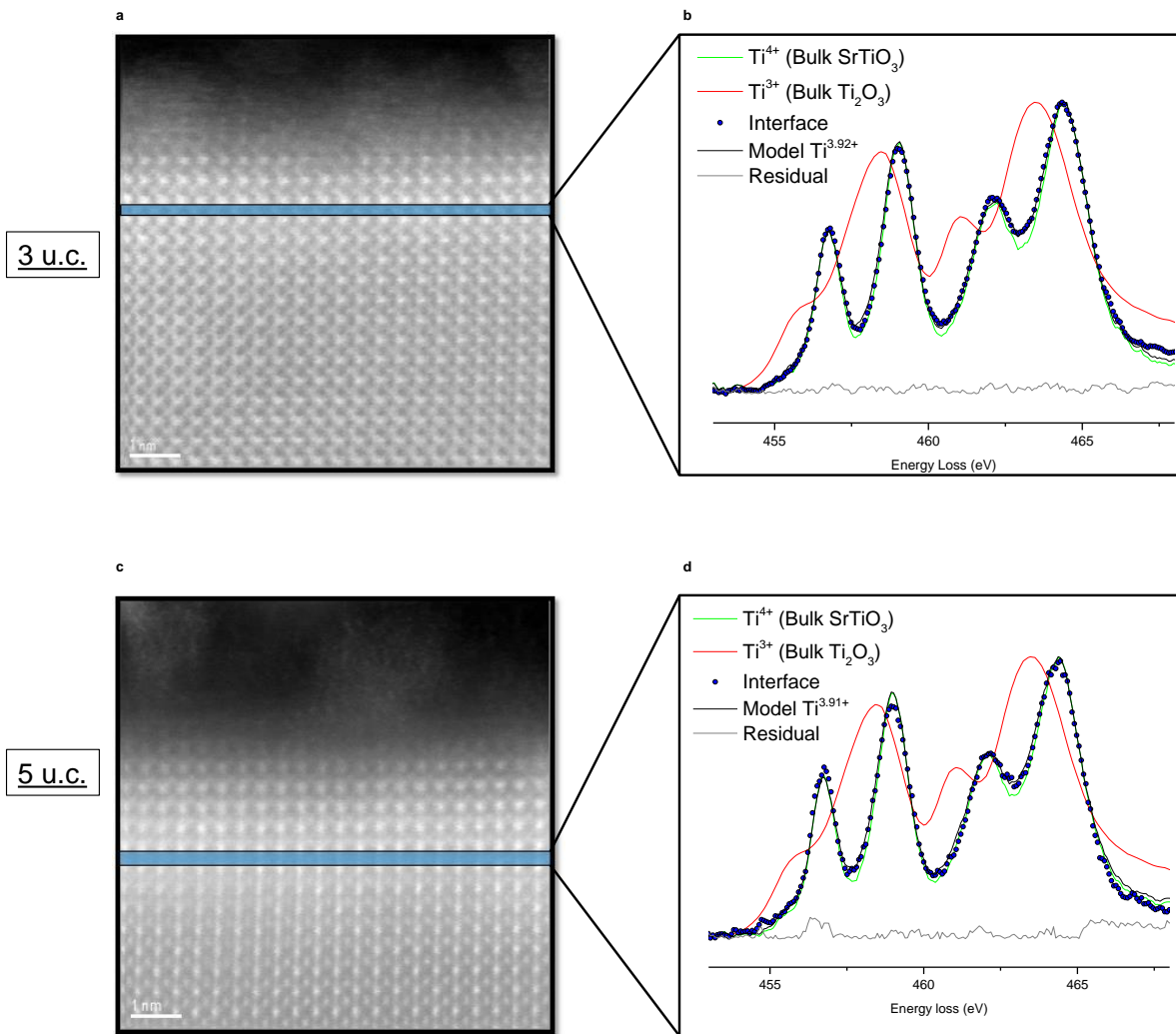


Figure III.4 | Ti-L_{2,3} edge EELS taken at the LaAlO₃/SrTiO₃ interface. a-c, HAADF image of the region of interest probed to measure the Ti EELS spectrum at the interface of (a) UC3 (c) UC5. **b-d**, EELS spectrum at the interface of the sample (b) UC3 (d) UC5. The blue dots spectra correspond to the experimental EELS measurement at the very first unit cell below the interface. The contributions of Ti⁴⁺ and Ti³⁺ to the Ti edge were deduced from a linear combination of two reference spectra, a green one for Ti⁴⁺ (in the substrate SrTiO₃ away from the interface) a red one Ti³⁺ (Bulk Ti₂O₃) recorded on the same spectrometer. The black curves represent the best simulation that fitted the experimental spectrum. The gray curves are the residual of the method of least squares. Ti oxidation states are similar between the conductive and insulating samples grown in the same conditions.

The 2D charge carrier density at room temperature ($n > 1.2 \times 10^{15} \text{ cm}^{-2}$), was much higher than the density calculated based on EELS valence measurements restricted to the first unit cell below the interface. The comparison of charge carrier densities obtained from Hall measurements on bulk samples with those measured on thin foils from EELS could be questionable. We are aware of the electronic modifications that can occur during ion milling (FIB or PIPS) and electron irradiation (STEM) or surface oxidation of Ti³⁺. However we will see in the next chapter that variations of the Ti oxidation state as a function of the growth conditions can be recorded by EELS. Moreover XPS measurements conducted on bulk samples tend to confirm the range of oxidation rate we measured [13–17]. This suggests that the EELS measurements, if not fully quantitative, remain reliable. The

Chapter III | Origin(s) of the q-2DEG

lower carrier density found below the interface by EELS indicates that the conduction was not purely bi-dimensional, once again in contrast to the polar catastrophe model. A second hypothesis of a quasi 2D conduction zone restricted to the first layers above and below the interface has been evaluated. The additional Ti oxidation state taken 1 u.c. above (Figure III.5a and Figure III.5b) and below (Figure III.5c and Figure III.5d) the LaO/TiO₂ interface permitted to reach a maximum carrier density of about $1.5 \times 10^{14} \text{ cm}^{-2}$, still underestimates by a factor 10 the charge carrier density with respect to the Hall measurements. This result would confirm that the conduction is not strictly confined in the first STO unit cells. As shown in Chapter I (section I.5.2.2), several authors emphasized the extension of the carrier zone throughout the LAO/STO heterostructure [7,18,19]. This delocalization of the carriers normal to the interface was suggested to explain the weak contribution of Ti³⁺ on the EELS measurements at the interface [18,20,21].

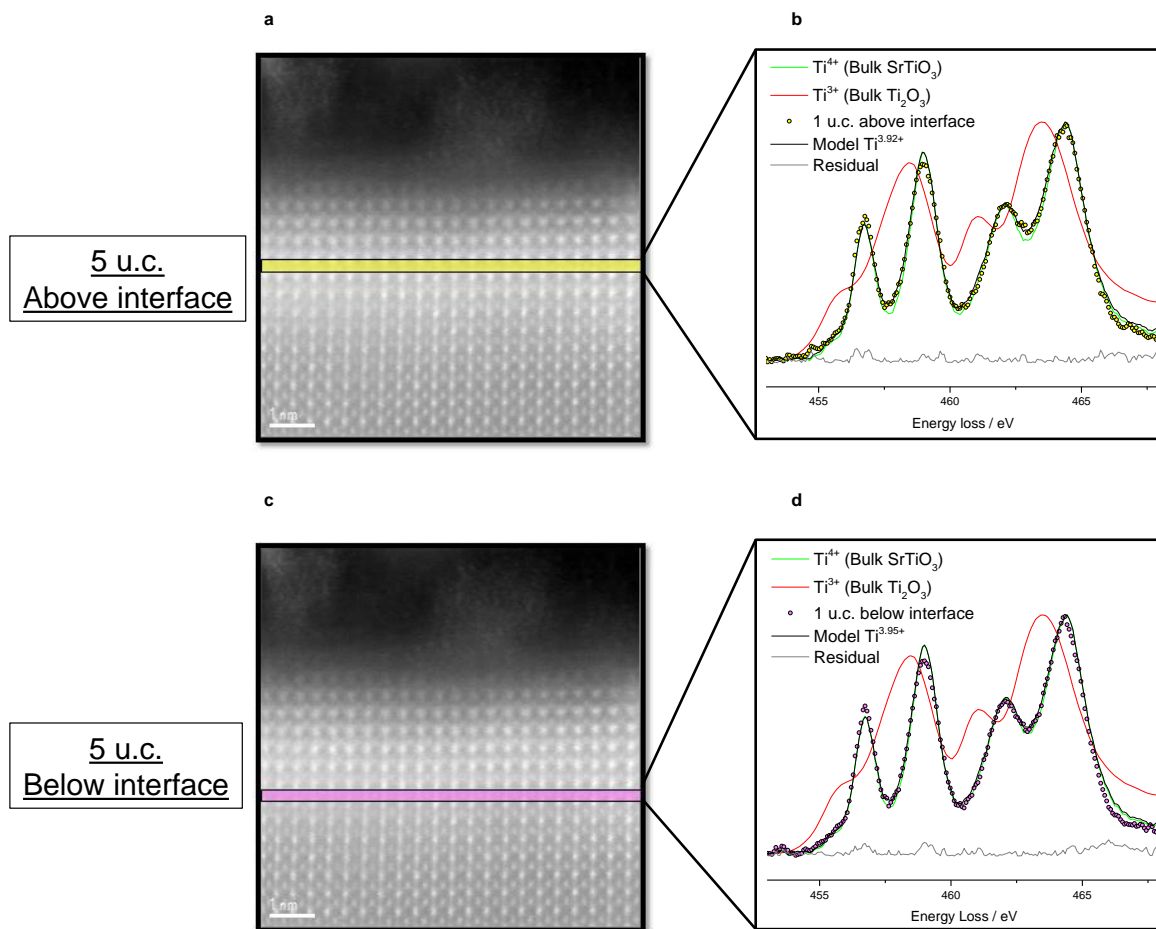


Figure III.5 | Ti-L_{2,3} edge EELS taken near the LaAlO₃/SrTiO₃ interface of UC5. a-c, Same HAADF image of the region of interest probed Ti EELS one unit cell (b) above (d) under the interface of UC5 sample. The experimental spectra are fitted using the same methodology as in Figure III.4. Taking into account charge carriers located in the unit cell under, above and at the interface, results in a carrier density lower than $1.5 \times 10^{14} \text{ cm}^{-2}$. This indicates that the conduction measured in the 5 u.c. film sample is not confined to a two dimension layer.

The similar Ti valences measured below the interfaces in the conducting and insulating samples does not play in favor of charge injection only activated by a polar catastrophe [20–22], at least for such film thicknesses. We will have to find out, in the next sections, the origins of such Ti³⁺ contribution.

To conclude here, the polar catastrophe model cannot be designated as the single mechanism triggering the conduction at the LAO/STO hetero-interface. The theoretical Ti valence of +3.5 was not reached at the interface for the conductive sample, and it was even close to the value of the insulating sample. This suggests an alternative origin to the carriers at least below the critical thickness. The discrepancies between the electrical properties and the Ti oxidation state measured for the conducting sample revealed that the carrier should be dispersed deeper in the STO substrate than the presumed 2D layer. However, consistently with this model based on the electrostatic potential built-in, we have found that the critical thickness for conduction lies between 3 and 5 u.c.. These results also emphasize the role of the carrier mobility to explain the observed discrepancies in terms of electrical conduction between the two samples. The factors impacting this mobility will have to be determined.

III.3 Oxygen vacancies

We have investigated the role played by the oxygen vacancies by performing EELS measurements at the interface between LaO and TiO₂ in the samples *UC3* and *UC5*. In Figure III.6, we observe differences in the shape of the EELS spectra between the O-K edge taken into the STO bulk and the one measured at the interface for both samples, suggesting modifications of the anion environment around the interface.

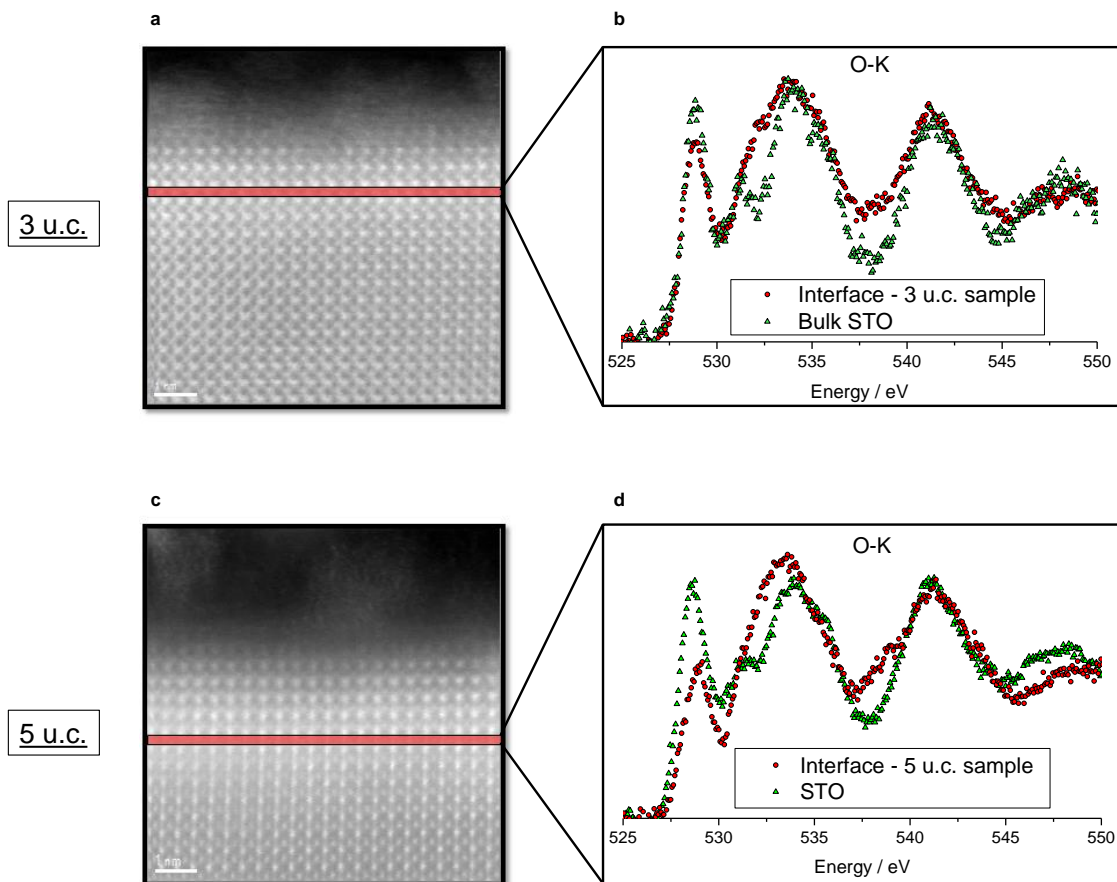


Figure III.6 | Experimental EELS fine structure of the O-K absorption edge across LaAlO₃/SrTiO₃ heterostructures. a-c, HAADF image of the region of interest probed to measure the O-K EELS spectrum at the interface of (a) *UC3* (c) *UC5*. b-d, EELS spectrum at the interface (red triangles) and within the STO bulk (green dots) of the sample (b) *UC3* (d) *UC5*.

However the fingerprint of oxygen vacancies, as presented in Chapter II (section II.4.3.2), has been found neither in the substrate nor around the interface for both samples (Figure III.6b and Figure III.6d). This is consistent with the weak contribution of Ti^{3+} on the Ti-L_{2,3} absorption edge measured at the interface of these samples (Figure III.5). We can conclude that oxygen vacancies are not detected at the interface for samples grown at 10^{-4} Torr. This seems to contradict Liu *et al.* [23] who found conductive samples made at the exact same oxygen pressure with a film thickness of 3 u.c.. They attributed the transport properties to the occurrence oxygen vacancies, without providing proof of the presence of these extrinsic defects. Moreover the film growth was achieved using a shorter target-to-substrate distance, implying more energetic impingement of the target particles on the substrate, and a higher laser fluence influencing the stoichiometry of the deposition.

In conclusion, although a low level of oxygen non-stoichiometry is not excluded, it would be insufficient at an oxygen pressure of 10^{-4} Torr to explain the differences between the samples *UC3* and *UC5*. Therefore, oxygen vacancies cannot alone be at the origin of the conduction.

III.4 Intermixing

The O-K EELS spectra, shown in Figure III.6, reveal modifications around the interface that cannot be assigned to oxygen vacancies. A shift of the peak C towards the lower energy loss overlapping the peak B is observed at the interface for both samples *UC3* and *UC5* compared to their bulk STO spectrum. This reveals that La atoms have diffused, at least, at 1 u.c. under the interface (within STO) and suggests A-site cation intermixing. Furthermore, presence of the pre-peak A in LAO film, related to the presence of Ti, reveals B-site cations diffusion. By following the variation of these peaks along EELS profiles across the interface (Figure III.7), we can estimate the extent of the intermixing.

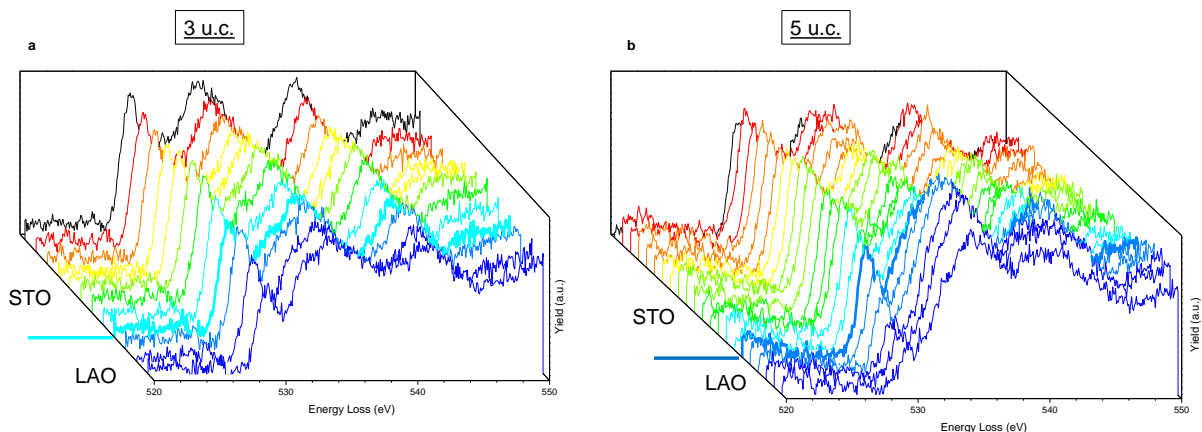


Figure III.7 | Spatial distribution of the EELS O-K absorption edges unit cell by unit cell. The spectrum measured at the interface is marked by a bold spectrum. **a**, EELS spectra collected from *UC3*. **b**, EELS spectra collected from *UC5*.

The pre-peak A is found in each unit cell of the film for both samples, meaning that Ti diffused up to the sample surface. Compared to the O-K edge of pure LaAlO_3 shown in Figure II.27, the C peak is shifted toward higher energies, indicating the presence of some Sr around O in the film. Moreover, the shift of the peak C also indicates that La is present into the substrate, as seen above. Hence, the analyses of EELS O-K absorption edges provided qualitative proof of A-site and B-site cations diffusions. We have seen in Chapter I (section I.5.3) that intermixing is able to contribute to the conduction of the LAO/STO heterostructure, hence it is crucial to get these chemical information

with high spatial resolution and accurate quantitative chemical analysis. We chose to investigate A-site cations intermixing by MEIS with a resolution below the cell dimension, while EELS was used to compare the diffusion length of A cations and B cations.

III.4.1 A-site cations intermixing

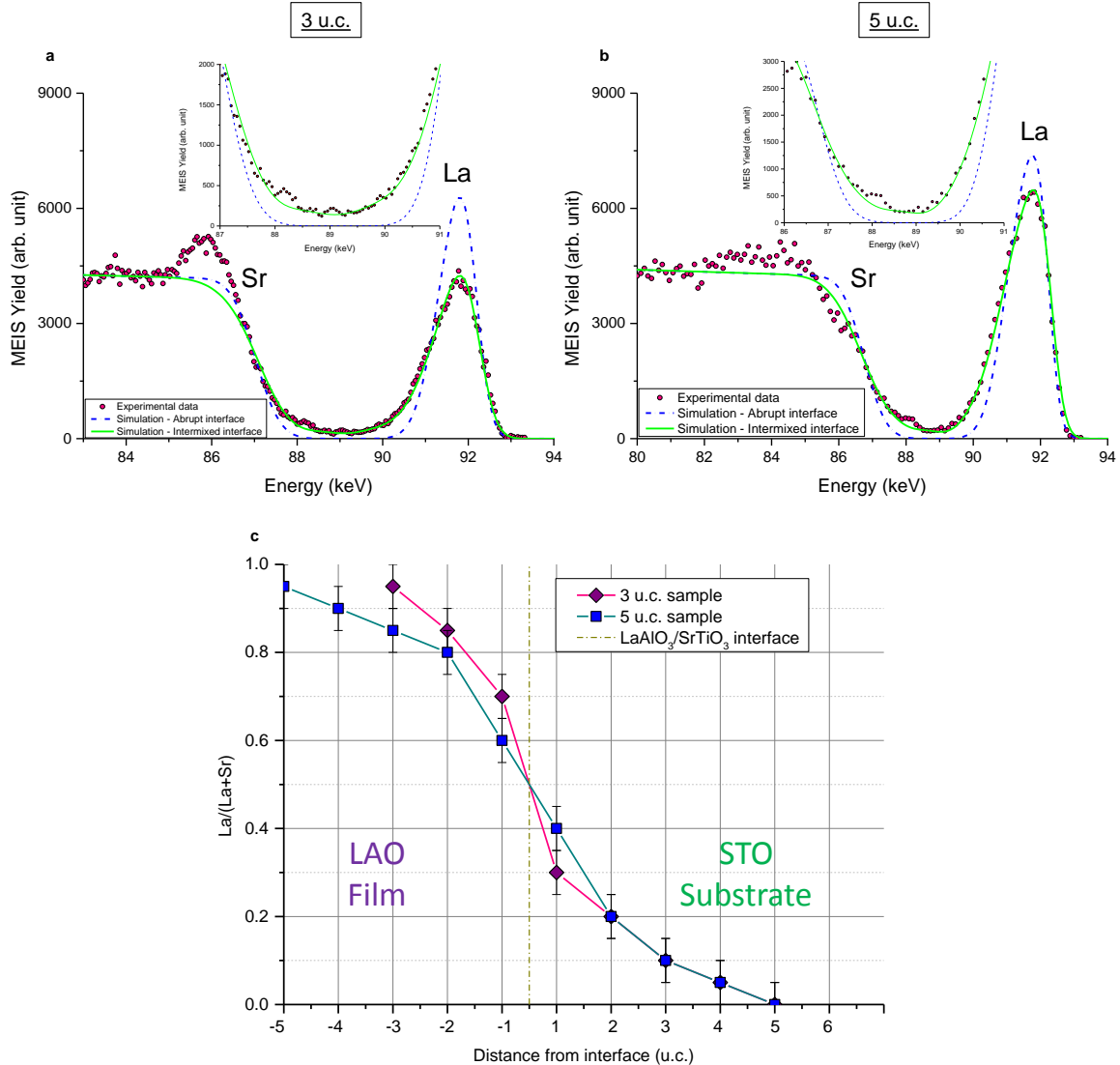


Figure III.8 | MEIS chemical profile of studied samples. Random MEIS experimental and simulated spectra of the (a) 3 u.c. sample with a backscattering angle of 115,4° (b) 5 u.c. sample with a backscattering angle of 114,5°. The experimental data are represented by red circles, the simulated spectra corresponding to the same system without intermixing by blue curve, and the simulated spectra fitting the experimental data by green curve. c, La/(La+Sr) profile throughout the first atomic layers. The x coordinates locate the cations by the number of unit cells to the interface (+ 1 = first u.c. in STO, - 1 = first u.c. in LAO...).

We have detailed in Chapter II (section II.5.3.1) the experimental method to extract the chemical profile from MEIS measurements in random mode. Here, investigations were led on the samples *UC3* and *UC5* to understand the role plays by intermixing on the electrical properties. First, the comparison between the experimental data (Red dots in Figure III.8a and Figure III.8b) and simulated

spectra for an abrupt interface (Blue curves in Figure III.8a and Figure III.8b) indicates clearly exchanges between film and substrate species. Fitting the experimental data gave rise to the variations of x ratio = $\text{La}/(\text{La} + \text{Sr})$ across the interface with an atomic resolution (Figure III.8c).

Strontium was found in each layer up to the surface for both films, confirming the results obtained from the EELS O-K absorption edges (Figure III.7). The film contains a cumulative amount of 0.9 (= 5 - (0.95+0.9+0.85+0.8+0.6)) Sr in the 5 u.c. sample (thus 4.1 La) and 0.5 (= 3 - (0.95+0.85+0.7)) Sr in the 3 u.c. one (thus 2.5 La). The La counter-diffusion depths were similar for the two samples, with 0.75 La for UC5 and 0.65 La for UC3, and down to 4/5 u.c. within the STO substrate. The substitution of La by Sr was slightly larger in the 5 u.c. film than in the 3 u.c. film at any depth, whereas within the substrate, only the first layer contained more La in the sample UC5 than in the sample UC3. The cumulative Sr content in the film was greater than the cumulative La content in the substrate for UC5, while the opposite was true for UC3. This suggests discrepancies in terms of cationic vacancies distribution.

The atomically-resolved MEIS depth profiles clearly demonstrated $\text{La} \leftrightarrow \text{Sr}$ intermixing. These exchanges of cations with different oxidation states can stabilize the interface and thus can lead to compensation of the dipole energy which otherwise would form at an ideal, abrupt interface [9,24–26]. Nevertheless, we show in Figure III.9 that the A-site cations intermixing is not sufficient to avoid the divergence of the electrostatic potential, even if we take into account an interfacial Ti oxidation state of +3.9 as measured in Figure III.4.

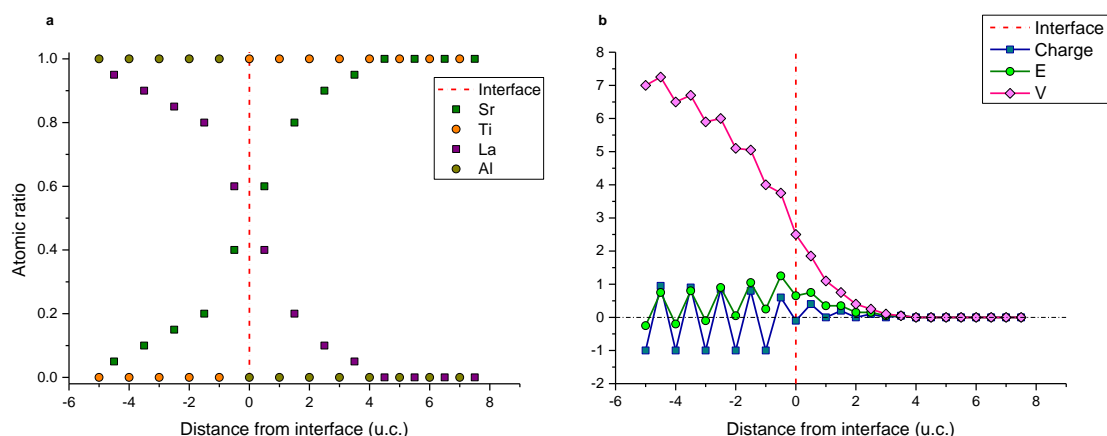


Figure III.9 | A-site cations intermixing consequences on the electrostatic potential in a purely ionic configuration. **a**, Atomic distribution determined from the Figure III.8c. **b**, Electrostatic potential V evolution in the interface region. The potential is diverging despite the $\text{La} \leftrightarrow \text{Sr}$ intermixing.

III.4.2 A-site versus B-site cations intermixing

The EELS investigations of the O-K edges have revealed intermixing of B cations. To compare A and B cations intermixing, we have followed the Ti-L_{2,3} and La-M_{4,5} edges in the interface region (Figure III.10). Unfortunately the K edge of aluminum (1560 eV) gave a too weak signal to be quantified and the position of the L_{2,3} edges of Sr (2007 eV, 1940 eV) was too far to allow quantification of La, Ti and Sr on the same spectrum. The quantification of the Ti to La ratio was difficult to discuss without the information on Sr and Al signals. Therefore our discussion is limited to the comparison of the Ti and

La diffusion lengths. A qualitative profile of Ti and La was obtained from the areas under their EELS signals (Figure III.10c and Figure III.10d).

As seen before, Ti diffused up to the film surface for both samples. Assuming a full occupancy of B-sites, Al would diffuse down to 3/4 u.c. into the substrate of the LAO(3 u.c.)/STO sample, and slightly deeper (4/5 u.c.) into the substrate of the LAO(5 u.c.)/STO sample. La atoms diffused down to about 5 u.c. within the substrate of the 3 u.c. sample whereas it was found deeper (6/7 u.c.) into the thicker sample STO. This would indicate an asymmetry in the intermixing depths on A- and B-sites cations. However, it should be noted here that the spatial resolution of these EELS measurements must be higher than one unit cell due to the enlarging of the probe width of the electron beam. It can be noticed that La cations are detected deeper by EELS (Figure III.10) than by MEIS (Figure III.8). This is explained by the straggling of He^+ particles that decreases the sensibility of this ion beam analysis with the depth of the analyzed region.

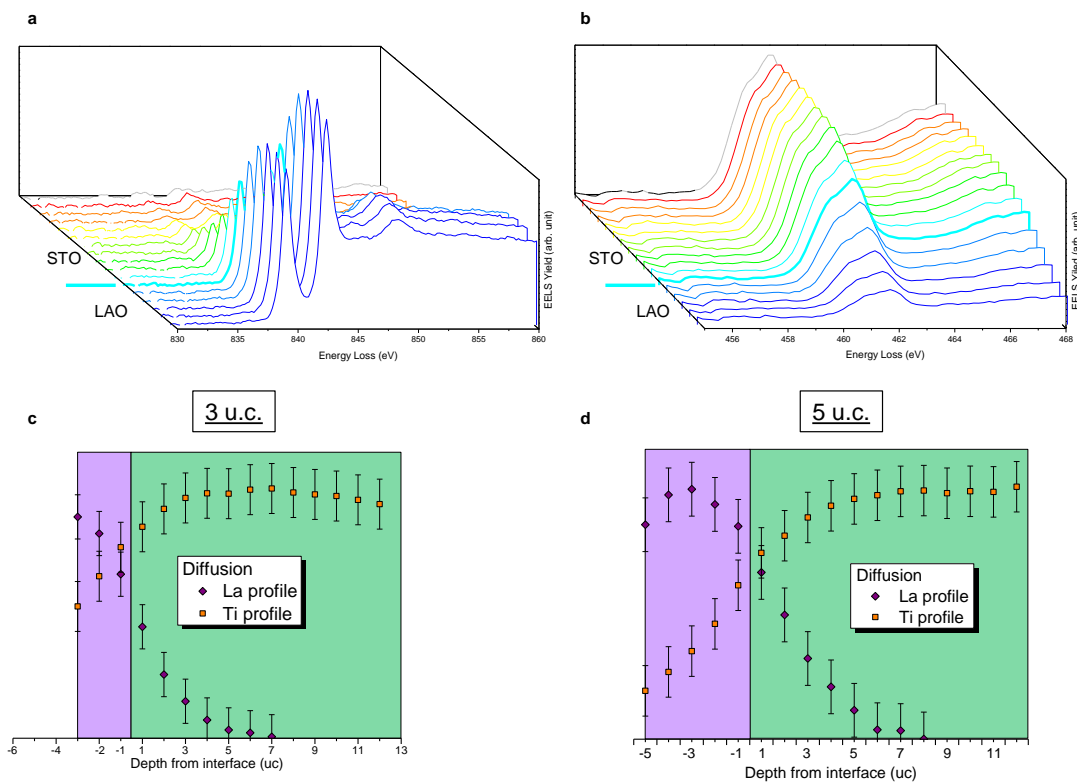


Figure III.10 | Cationic intermixing A-sites vs B-sites. **a-b**, Spatial distribution of the EELS **(a)** La- $M_{4,5}$ **(b)** Ti- $L_{2,3}$ absorption edges unit cell by unit cell within the sample UC_5 . The spectrum measured at the interface drawn in bold and cyan. For a same depth the two absorption edges were recorded on the same spectrum, with a dispersion of about 1 eV. **c-d**, Diffusion profiles of Ti and La from EELS analyses for the sample **(c)** UC_3 **(d)** UC_5 . The x coordinates locate the cations by the number of unit cells to the interface (+ 1 = first u.c. in STO, - 1 = first u.c. in LAO...).

The driving force for this B cation intermixing could be the reduction of the dipoles. First principles calculations carried out by Chambers *et al.* [9] indicate to a reduction or elimination of the electric field by $\text{Al} \leftrightarrow \text{Ti}$ intermixing. We have drawn on Figure III.11 the variation of the electrostatic potential assuming a purely ionic configuration and based on the intermixing and Ti valence

determined in our experimental MEIS and EELS data. Although a clear decreasing is observed compared to Figure III.9, due to the diffusion of B cations, the potential still diverges, suggesting an alternative mechanisms to compensate or screen the charge potential.

The donor doping of STO by La below the interface is one of the mechanisms proposed for the q-2D conduction. In our samples intermixing creates a $\text{La}_x\text{Sr}_{1-x}\text{Al}_y\text{Ti}_{1-y}\text{O}_3$ layer, where Al would act as an acceptor dopant in the substrate. Our results indicate that Al intermixes with Ti at shallower depths and lower ratio than La does with Sr, which is consistent with other investigations of the literature [24]. This shallower diffusion depth of B cations compared to A cations results in La_{Sr} donor dopants that are not fully compensated by Al_{Ti} acceptor dopants ($x > y$) and could provide charge carriers at the interface.

However one main finding undermines the scenario of a conducting $\text{La}_x\text{Sr}_{1-x}\text{TiO}_3$ layer. The difference in the values of $x = \text{La}/(\text{La}+\text{Sr})$ ratio just below the interface for 5 u.c ($x = 0.4 \pm 0.05$) and 3 u.c ($x = 0.3 \pm 0.05$) samples is not sufficient to explain the discrepancy in terms of electrical properties between these two samples which might be explained by differences in the ionization ratio of the donor centers or in the mobilities of the injected electrons.

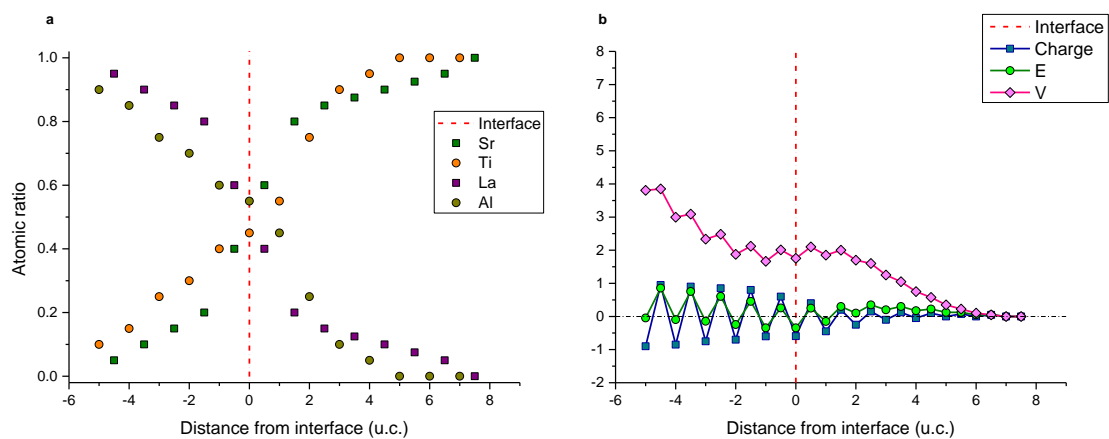


Figure III.11 | Influence of A-site and B-site cations intermixing on the electrostatic potential. a, A-site and B-site atomic distribution determined from the MEIS and EELS intermixing results. **b,** Electrostatic potential V evolution in the interface region. Compared to Figure III.9 the addition of B cation intermixing reduces the potential divergence, but cannot cancel it.

In addition, the compensation mechanism of the positive charges La_{Sr} is known to depend on the partial pressure of oxygen and growth temperature with a shift toward ionic compensation at higher p_{O_2} and lower T . Negatively charged strontium vacancies V_{Sr}'' are formed [27,28] that could be at the origin of the compensation of the positive remaining field at the interface. The consequences of these lattice defects on the heterostructure will be analyzed in a following section.

Cation intermixing, change in Ti valence or ionic vacancies will impact the interatomic distances around these defects. The structural distortions induced will be analyzed in the next section as they are expected to have a major effect on the transport properties [29–32].

III.5 Structural distortions

HAADF images in USTEM were first used to probe the position of A-site atoms. Figure III.12 shows a plot of the contrast on each pixel column, superposed to the image of a 10 u.c. system. The mean positions of the A atoms in a (001) plane was determined by the position of the extrema and the interplane distances were then deduced. This graph could suggest an elongation of the A-A distance around the interface, however the accuracy of this method was not adapted to our problematic. We were limited by the pixel size (0.0095 Å) but also by a possible thermal drift during the acquisition and noise of the image. Sang *et al.* [33] have demonstrated that precise atomic positions in perovskite can be determined using HAADF images. But the methodology, based on a computer analysis of a set of images is delicate. The following investigations have been achieved by MEIS.

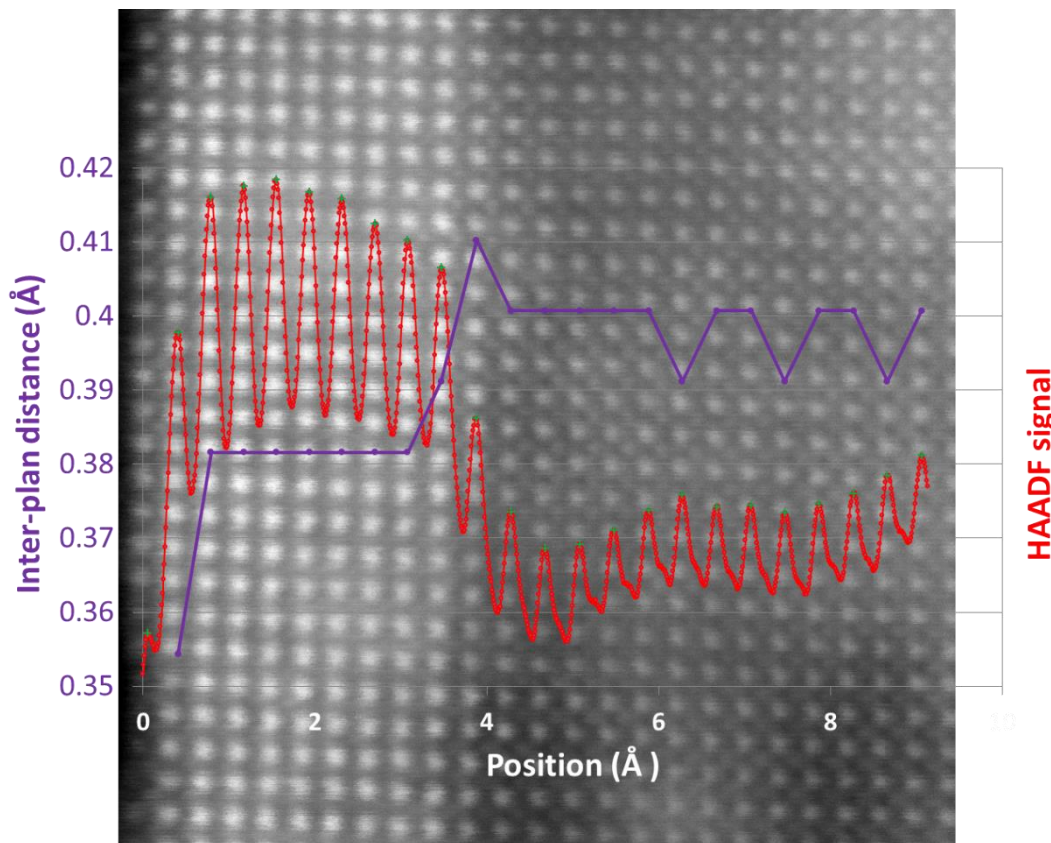


Figure III.12 | Evaluation of the c lattice variations in the [001] direction. HAADF image 10 u.c. sample. The red curve represents the HAADF signal averaged on vertical row of pixels. The purple curve represents the distance separating the maxima.

The distortions in LAO and STO structures we are looking for can consist in homothetic displacements of all the atoms of the cell due to the pseudomorphic film growth or/and in a buckling of AO or BO₂ layers due to some relaxation in the polar structure. We will first make the assumption that variations in Sr-Sr distances in the substrate or La-La ones in the film reflect the whole cell deformations. We will build strain profiles from the angular position of MEIS blocking dip for Sr and La. However these profiles will highlight a buckling of the A-O layers due to Sr ↔ La intermixing. The relative displacements of the atoms with respect to their neighbors will then be analyzed through the variations of the width of the blocking dipo.

III.5.1 Strain profiles

We have mentioned in Chapter II (section II.5.3.3) that the MEIS in blocking mode is particularly adapted for characterizing the strain within our structure. Figure III.13 presents (E, θ, N) maps for the samples *UC3* and *UC5*, taken in a scattering geometry that promoted blocking in the [101] direction. The He^+ energy range was selected to analyze both Sr and La scattering centers. A shadowing effect in the distribution of the scattered ions distribution is observed, characteristic of these “blocking dip” patterns.

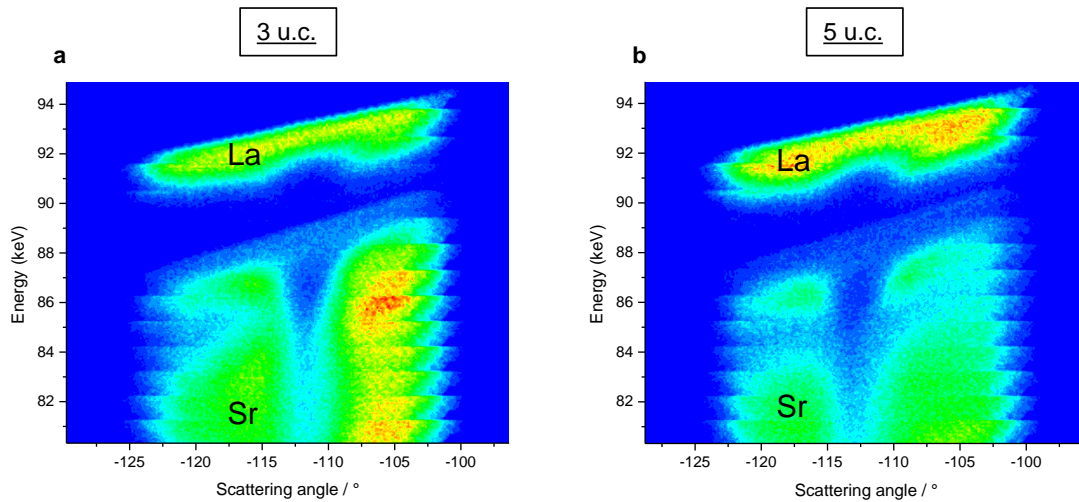


Figure III.13 | MEIS data in blocking mode. MEIS blocking map (E_1, θ_{Sc}, N) of the sample with a film thickness of (a) 3 u.c. (b) 5 u.c.

Following the methodology described in Chapter II (section II.5.3.3), two series of blocking dip profiles have been extracted from each map, corresponding respectively to the particles experiencing a second backscattering above the La and Sr first scattering centers. These profiles are displayed in Figure III.14. As a consequence of the $\text{La} \leftrightarrow \text{Sr}$ interdiffusion, He^+ particles backscattered by the La scattering centers are also found in the substrate and Sr scattering centers in the film. On each graph, the blocking dips associated with the scattering centers located in the film are plotted in purple, while those measured in the substrate are plotted in green. La blocking dip profiles in the sample *UC5* are displayed in Figure III.14b. We could extract profiles from this atom only for the first 7 u.c. that is to say only for the two first u.c. in the substrate, whereas MEIS random profiles showed a La diffusion down to 4 u.c. in STO. Indeed, the signal around the dips located deeper from the surface was too weak to be analyzed. This is due to the low concentration of La and to the higher signal-to-noise ratio in deeper regions. In the 3 u.c. sample, the first 7 u.c. analyzed could include the diffusion layer of 4 u.c. in the substrate.

In order to investigate the strain profiles of the two samples, we have followed the variations of the angular position of the blocking dip for each mono-layer. As explained in Chapter II (section II.5.3.3), the blocking angles at 13 u.c., for the sample *UC5*, and at 14 u.c., for the sample *UC3*, were taken as the reference, $\theta_{bk}(\text{ref})$, for an unstrained STO. They are indicated by the dashed vertical line on the graphs. We also consider the in-plane parameters fixed to those of unstrained cubic STO (0.3905 nm) (section II.5.3.3). One can see on Figure III.14a and Figure III.14b that the blocking dips from the La scattering centers drift towards the lower scattering angles (absolute value), suggesting that the corresponding unit cells are submitted to in-plane tensile strain with a decreasing out-of-plane lattice

parameter. Regarding the blocking dips generated by the Sr scattering centers, the structure seems to alternate between in-plane tensile and compressive strain, since their position drifts on both sides of the dashed line taken as reference.

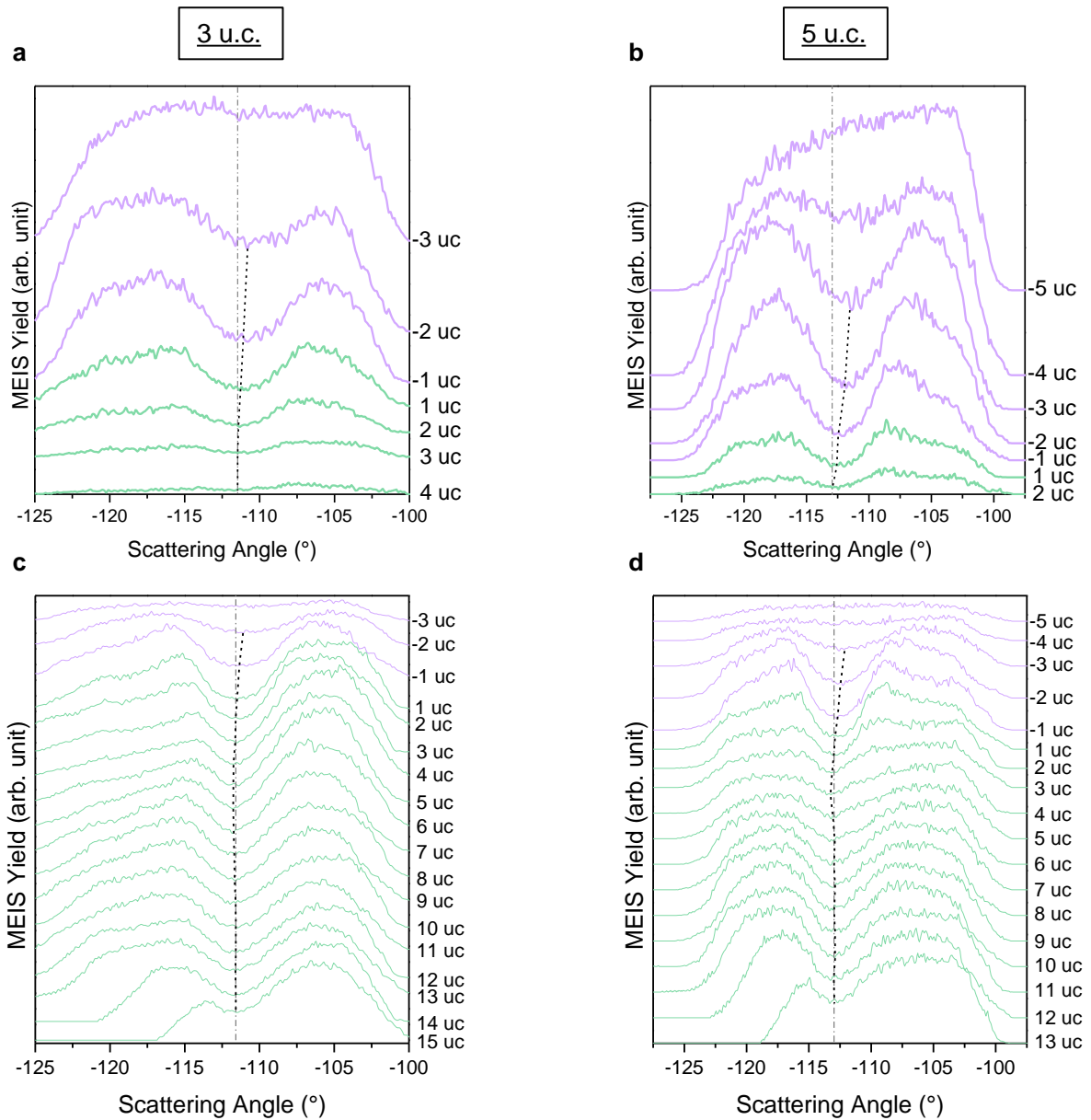


Figure III.14 | MEIS data in blocking mode. **a-b**, MEIS [101] La blocking dips of the sample **(a) UC3 (b) UC5**, as a function of depth corresponding to La atoms located in the film (purple curves) and in the substrate (green curves). **c-d**, MEIS [101] Sr blocking dips of the sample **(c) UC3 (d) UC5**, as a function of depth corresponding to Sr atoms located in the film (purple curves) and in the substrate (green curves). Dash-dotted lines are the position of the blocking dips for an unstrained cubic STO ($c/a = 1$). Dashed lines indicate the position of the blocking dips maxima for each unit cell. In the substrate, deviations of these positions from the dash-dotted line reveal structural distortions.

The quantification of the strain was then achieved. The angular position of the blocking dip was determined for each profile by fitting the dip regions with a parabola. The variations of θ_{bk} , with the depth analyzed, were then translated into variations of c/a ratio, according to the calculations

Chapter III | Origin(s) of the q-2DEG

described in Chapter II. The precision of this method can be estimated knowing that the pixel size of the map in the Y axis corresponded to about 32 pm in La and 29 pm in Sr. As the cell dimension is not a multiple of these values, and as we have segmented our graph by u.c. values, the maximum indetermination is 1 u.c.. The precision in angular position of the blocking dips was determined from the precision of the fit by the parabola, which is typically 0.1 °. This corresponds to about a precision of 0.0035 in the determination of c/a .

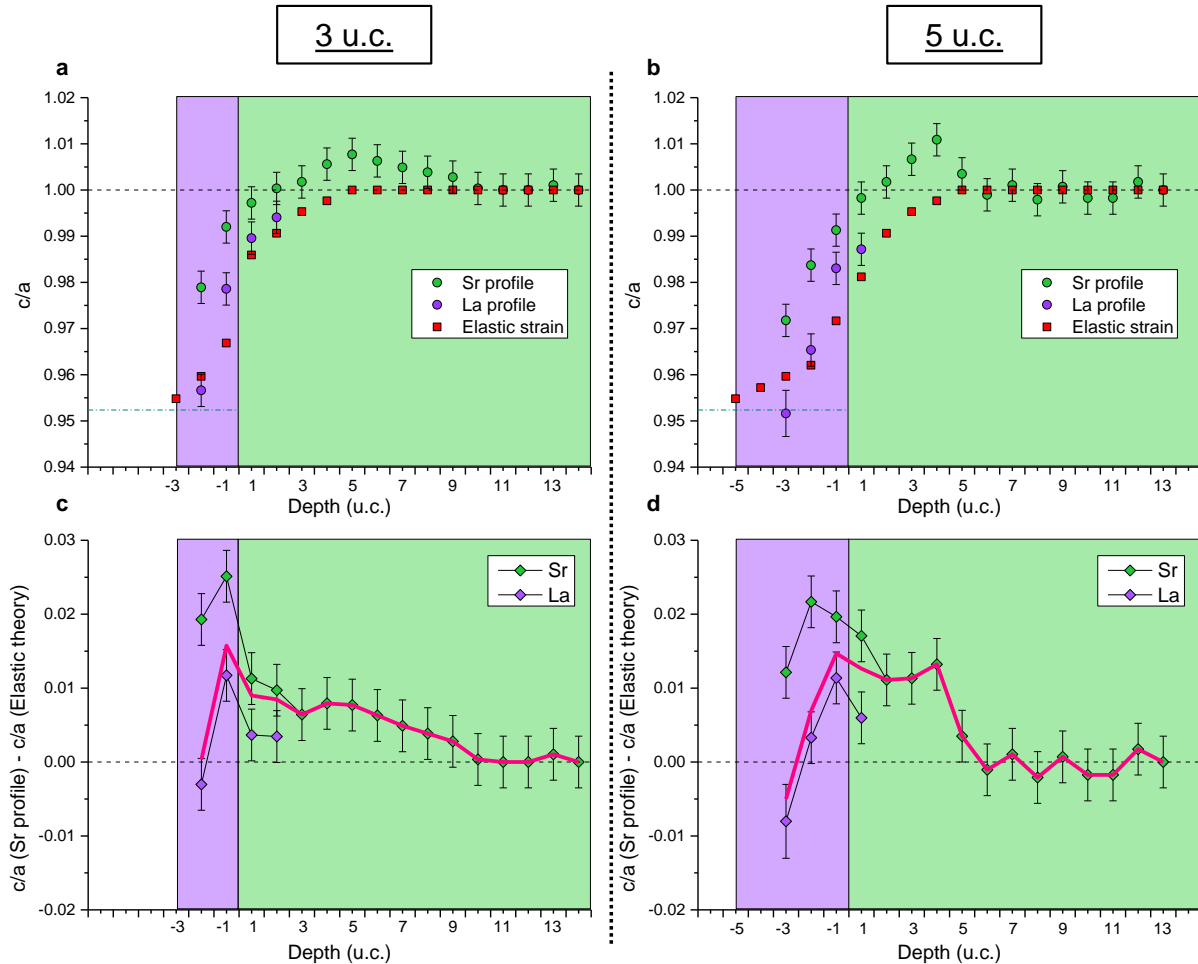


Figure III.15 | Profiles obtained from MEIS data in blocking mode. The x coordinates locate the cations by the number of unit cells to the interface (+ 1 = first u.c. in STO, - 1 = first u.c. in LAO...). Each data point indicates the c/a ratio calculated from this cation and the upper next A cation in [101]. **a–b**, Profiles of c/a for samples with film thicknesses of **(a)** 3 u.c. **(b)** 5 u.c. Purple circles represent the c/a values around La atoms. Green circles represent the c/a values around Sr atoms. Red squares represent the theoretical c/a values for intermixed heterostructure assuming a sole elastic epitaxial strain. The turquoise dash-dotted line indicates the theoretical $c/a = 0.952$ value for a fully epitaxial growth of LAO, ($a_{\text{STO}} = a_{\text{LAO}}$) and without intermixing. **c–d**, Difference between the c/a values measured experimentally - from Sr and La scattering centers - and those calculated from epitaxial strain (red squares) are plotted for the sample **(c)** UC3 **(d)** UC5. The pink curve represents the average of the Sr and La profiles weighted by their relative atomic ratio.

Figure III.15 presents the variation in c/a for the samples UC3 and UC5 calculated from θ_{bk} as a function of depth for La (purple dots) and Sr (green dots) scattering centers. For both samples, the

curves could be divided into three regions. In the deeper probed parts of the substrate the variations of c/a were negligible and these regions were supposed unstrained ($c/a = 1$). Then an intermediate region in the substrate was observed with $c/a > 1$ starting from 9 u.c. for the thinner film sample and from 5 u.c. for the thicker one and extending up to 2 u.c. below the interface. The maximum c/a was observed at depths of 5 u.c. and 4 u.c. into the substrate for the 3 u.c. and 5 u.c. films, respectively. Finally the region extending from 2 u.c. below the interface up to the film surface exhibited $c/a < 1$. The differences between the two samples laid mainly in the thicknesses of these regions as will be discussed later.

We note that for a given depth, the c/a ratios calculated from scattering on La and Sr do not match. For blocking in [101] direction, this indicates that the distance between two A-site cations located on the diagonal of the (010) face is altered by intermixing. In the film, the $Sr_{La}-La_{La}$ distance is longer than the $La_{La}-La_{La}$ one, whereas in the substrate the $La_{Sr}-Sr_{Sr}$ distance is shorter than the $Sr_{Sr}-Sr_{Sr}$ one. This blocking dip analysis brings an evidence of some distortions or buckling of the layer around the hosted cations. They could originate from differences in cation radii as well as electrical charges. In order to investigate further the nature of the strain, we have evaluated the contribution of epitaxial strain to the total strain in these hetero-structures. These epitaxial strains were calculated from a purely elastic model based on unstrained cell parameters deduced, in the intermixed region, from Vegard's law between STO and LAO, and represented by red squares in Figure III.15. The theoretical local epitaxial strain was calculated for the exact composition of each layer previously determined from the experimental MEIS chemical profiles. The cubic cell parameter a_0 of each fully relaxed $La_xSr_{1-x}Al_xTi_{1-x}O_3$ slices was calculated based on Vegard's law:

$$a_0(x) = (1 - x) \cdot a_{STO} + x \cdot a_{LAO}$$

The in-plane stress stretches the cubic cell into a quadratic cell with parameters $a_{//} = a_{STO}$ and $a_{\perp} = c$. The corresponding in-plane $\varepsilon_{//}$ and out-of-plane ε_{\perp} elastic strains are related through the equation below:

$$\frac{\varepsilon_{//}}{\varepsilon_{\perp}} = \frac{a_{STO} - a_0}{a_0} \cdot \frac{a_0}{c - a_0} = -\frac{(1 - \nu)}{2\nu}$$

With ν the Poisson ratio of $La_xSr_{1-x}Al_xTi_{1-x}O_3$ estimated from a mixing rule between $\nu_{LAO} = 0.24$ [2], and $\nu_{STO} = 0.23$ [34]. This equation can be reformulated into:

$$\frac{c}{a_{STO}} = -\frac{2\nu}{1 - \nu} + \frac{1 + \nu}{1 - \nu} \cdot \frac{a_0(x)}{a_{STO}}$$

The strength of this innovative approach is that the intermixing profiles, obtained from MEIS random mode on the exact same samples, were used for these elastic calculations. The depth variations of c/a , as predicted from epitaxial elastic strain and based on the chemical profile depicted in Figure III.8c are plotted in red squares in Figure III.15a and Figure III.15b. Then, the as-calculated ratios c/a_{STO} , due to the epitaxial strain, have been subtracted to the total c/a ratio determined from MEIS blocking mode maps (Figure III.15c and Figure III.15d).

The c/a ratio measured experimentally with MEIS blocking dips around the interface are clearly larger than the values predicted by purely elastic strains especially around the interface where a maximum is reached. Thus, epitaxial elastic strain cannot be the only factor that explains the strain level

measured. Nor can it explain the differences in the strain variations observed between the samples *UC3* and *UC5*. To enhance our comprehension of these results, we have investigated how this “strain” profiles could be coupled with the “buckling” profiles.

III.5.2 Buckling profiles

We detailed in Chapter II (section II.5.4) that the width of the blocking dips gives information on relative atomic displacements. The width of the blocking dips presented in Figure III.14 have been measured and plotted in Figure III.16. We have first considered the $^4\text{He}^+$ scattered by Sr in the deepest part of the substrate. They escaped the material with an energy of about 80.3 keV, and the corresponding blocking width was 4.1° . We now figure out which atoms fix the shadow cone, and thus the blocking dip width observed in Figure III.14. In the abacus of “Sr blocked by Sr” (Figure II.45a) the data point (80.3 keV, 4.1°) lies on a curve corresponding to a thermal vibration amplitude of 0.033 \AA . For the same thermal vibrations a blocking by O would produce a shadow cone of 3.97° (Figure II.45b). If now we put the data point (80.3 keV, 4.1°) on the graph “Sr blocked by O” (Figure II.45b), the thermal vibration is 0.038 \AA , which would induce a shadow cone from Sr of 4.15° . For this range of thermal vibration amplitude the widths of the blocking dips are only slightly larger when controlled by the second Sr neighbor of higher Z than by a first O neighbor of lower Z. We will consider Sr as controlling the dip width.

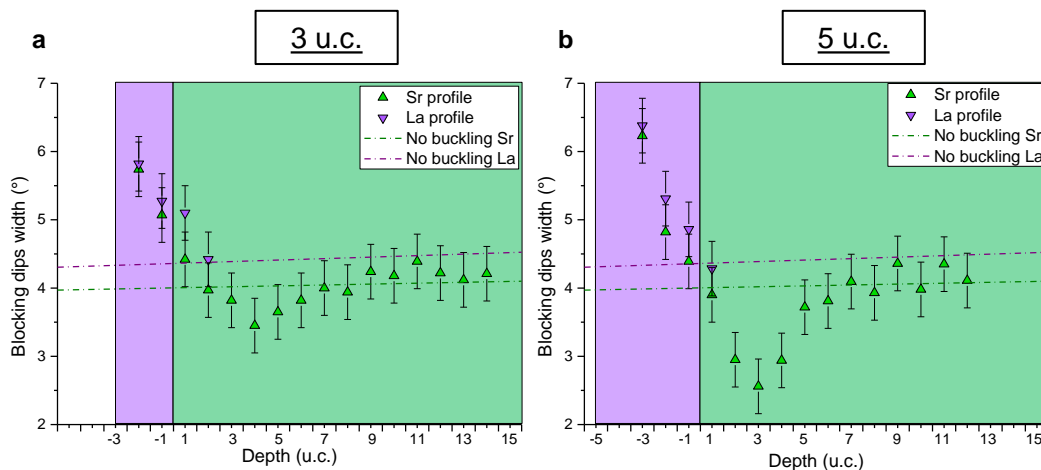


Figure III.16 | Width variations of the blocking dip as a function of depth. **a**, Experimental profile of the sample *UC3*. **b**, Experimental profile of the sample *UC5*. Green (Purple) triangles represent the width determined from the blocking dips generated by Sr (La). The green (purple) dash-dotted line represents the theoretical blocking width measured from Sr (La) atoms for a non-buckled structure, and calculated from Figure II.45.

Taking the thermal vibration just determined and the correspondence between depth in u.c. and energy for Sr scattering centers, we can calculate the dip width expected in a perfect STO substrate when moving toward the interface, for Sr blocking atoms. This width is plotted in Figure III.16 and compared to the experimental widths.

Interestingly, we observe strong similarities between the variations of the angular position (Figure III.15) and width (Figure III.16) of the blocking dips. Three areas are distinguished that have the same extend at ± 1 u.c. than those seen in the strain profiles. In the sample *UC5* the minimum width is

thinner and closer from the interface compared to the sample UC3. Equivalent trends were found when comparing the strain profiles of these two samples. All these similarities play in favor of strong links between the “strain” and the “buckling” profiles. We now analyze these curves regarding the crystal defects that could be found around the interface.

III.5.3 Origins of the strain and buckling

III.5.3.1 Deformation induced by Ti³⁺

The difference, between the c/a values measured experimentally and those calculated from epitaxial strain reached a maximum around the interface for the conducting and insulating samples (Figure III.15c and Figure III.15d). We have also seen that the Ti³⁺ concentration was the highest near the interface (Figure III.4). Since the d orbitals, empty for Ti⁴⁺, are occupied by one electron for Ti³⁺, the degeneracy of the t_{2g} energy levels (d_{xy} , d_{xz} , d_{yz} orbitals) must be lifted. There is a debate in the literature whether the degeneracy would be lifted by a contraction or an elongation of the cell (Figure I.4).

A first scenario would imply a pure Jahn-Teller effect that stabilizes the d_{xy} orbitals and induces a contraction of the TiO₆ octahedron [35]. The elongation of the cell observed does not exclude such a contraction of the octahedron through a buckling of Sr-O-Sr chains, where the oxygen anion planes depart from the cation ones, as was emphasized using first-principles calculations [36]. But the origin of the cell elongation must be found elsewhere.

A second scenario would favor a stabilization of the d_{xz} and d_{yz} orbitals through an elongation of the oxygen octahedra (pseudo Jahn-Teller effect) [24,30,37,38]. The in-plane compressive stresses imposed by the LAO film to the first STO cell(s) in addition to the larger size of Ti³⁺ could be ones of the causes driving this stabilization [24]. A modelling of the Ti 3d charge distribution below the interface by Okamoto *et al.* [39] shows long tails extending away from the interface which support an elongation of the cell. However, two main reasons encourage to find others explanation for this elongation than a pseudo Jahn-Teller effect. First, the very low concentration of Ti³⁺ in the interface region that we have found by EELS (Figure III.4). Secondly, the c/a profiles below the interface are significantly distinct in the samples UC3 and UC5, despite similar Ti oxidation state measured by EELS. Therefore, other additional origins for this cell distortion must be searched.

III.5.3.2 Compensation of the polar field by dipole formation: Ti off-centering

Ferroelectric-like distortions, with asymmetries in the TiO₆ octahedra, were also hypothesized to drive the interface electrical characteristics [38]. The HAADF image of a 10 u.c. sample (Figure III.17) shows Ti cations off-centered, moving towards the film surface in the first unit cells around the interface for the film and the substrate. We must add that the direction of displacement seen in the substrate is reversed to that expected for a positively charged LaO⁺/TiO₂⁰ interface. However, the intermixing has redistributed the charges (Figure III.11). At about 3 u.c. below the interface and deeper in the substrate, Ti is seen in the center of the A cations. In the thinner film samples, these Ti shifts were hardly seen. In conclusion, these ferroelectric-like distortions might contribute to the deformation around the interface but we believe that they cannot explain the distortions seen deeper in the substrate.

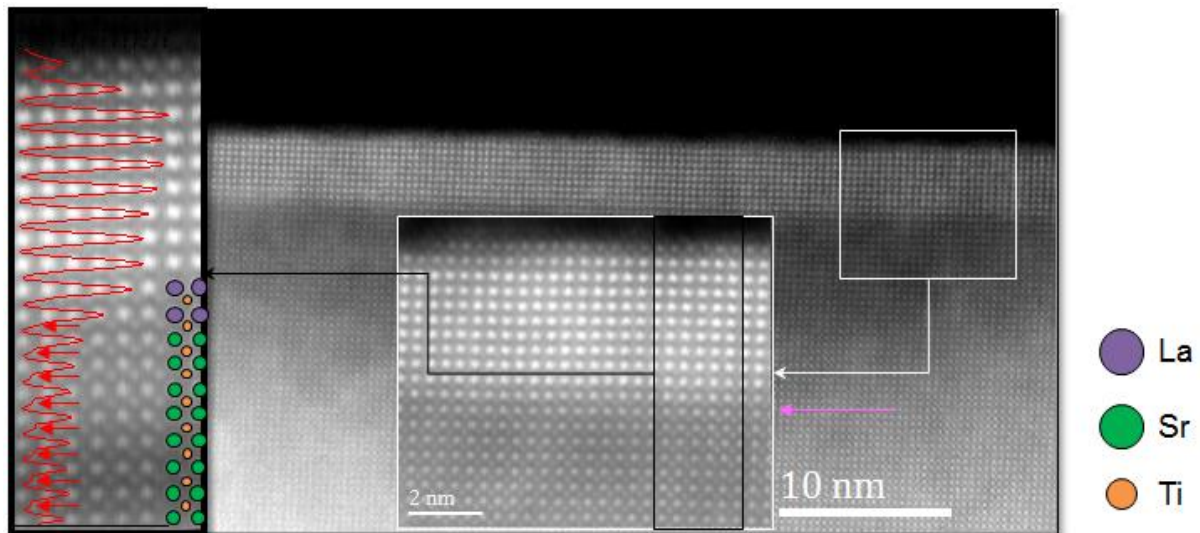


Figure III.17 | Representative HAADF images of 10 u.c.-thick LaAlO₃ films grown pseudomorphically on SrTiO₃. The interface is shown by a pink arrow. The left inset highlights the off-center displacement of Ti near the interface with an ADF profile where the Ti positions are marked with red arrows.

III.5.3.3 Compensation of the polar field by dipole formation: buckling of A-O and/or B-O layers

In the frame of our international project, modeling by first-principles calculations of the relaxed atomic position and of the layer-projected density of states has been carried out by Ittipon Fongkaew and Walter Lambrecht. Details can be found in [36]. The modelling was firstly done for an abrupt interface (without intermixing). The polar field is partially compensated by counter dipolar field induced by a buckling of the AO and BO₂ layers where anions and cations are no longer on the same planes. The layer projected densities of states show that, from 4 u.c., the valence band of the surface LAO crosses the conduction band of STO. A charge transfer can occur between the two bands that spreads over 5 layers in the substrates. A buckling of the layers is evidenced. The buckling of the LaO layers increases from the interface toward the surface, while the buckling of the AlO₂ layers decreases toward the surface. The charge transfer above the critical thickness does not reduce the buckling. To compare with our experimental results (Figure III.15), the c/a ratio profiles concerning the A-A and B-B distances have been plotted for a 3 u.c. and 5 u.c. film samples. The corresponding curves are shown in Figure III.18. It is interesting to see that the variation in the films shows the same trends as in our experimental “strain” profile. Buckling in the films is also supported by our “buckling” profiles that show widening of the blocking dips in this film region. This confirmed that the LAO film buckling is driven by polar distortion [19,40–42] but that it is not cancelled by charge transfer at the 5 u.c. interface contrary to what is expected from the polar catastrophe model. However, the strain levels in the substrate are not correctly described by the modeling. Swapping La-Sr atoms across the interface in the model to take into account intermixing did not decrease the discrepancies.

This first analysis shows that the deformation profiles in the substrates and the differences between the two samples can be explained neither by a change in Ti valence, nor by a relaxation of the atomic positions by a buckling. Intermixing is also rejected due to a similarity of the chemical profiles in the

two samples. In addition the diffusion length in the sample *UC3* is shorter than the extent of the in-plane compressive stresses. We have then considered the possible contribution of ionic vacancies. A main contribution of oxygen vacancies to the deformation is unlikely as they could not be detected by EELS at the partial pressure used to grow these samples. Moreover, an oxygen vacancy causes only a negligible volume change bulk STO and a weak contraction would be expected normal to the TiO_2 layer [43]. In LAO/STO systems, there is no sign of out-of-plane lattice parameter changes due to V_O'' [44–46]. Titanium vacancies, $V_{Ti}^{4'}$, will not be considered, owing to their high formation energies [43,47]. Strontium vacancies are our last candidates.

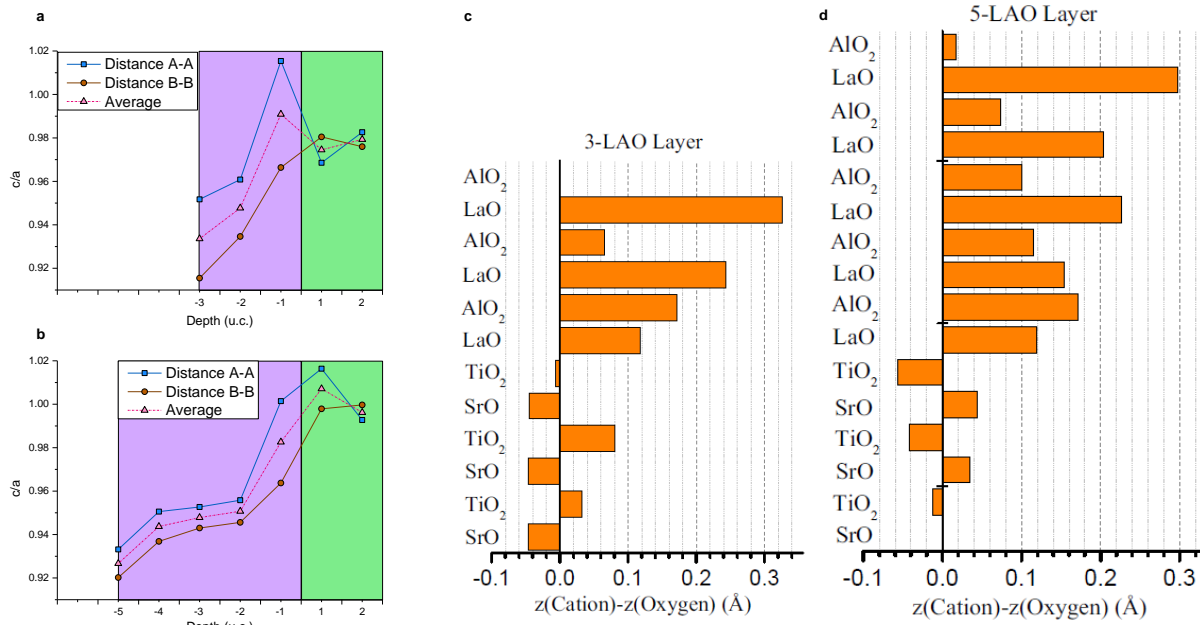


Figure III.18 | Modeling results. a-b, Calculated c/a from A-A and B-B distances in non-intermixed layers of (a) 3 u.c.-thick (b) 5 u.c.-thick LAO on a 5 layer STO calculated in a symmetric slab geometry. The A-A and B-B curves do not match, the structure is distorted. The buckling of the LaO layers increases from the interface toward the surface, while the buckling of the AlO_2 layers decreases toward the surface. Adapted from work carried out by I.Fongkaew and W.Lambrecht. c-d, Modeling of the buckling in the same with a film thickness of (c) 3 unit cells (d) 5 unit cells). From [36].

III.5.3.4 Formation of Strontium vacancies in the substrate and their impact on deformation

Strontium vacancies, V_{Sr}'' , could be formed by several reactions. The annealing of STO in oxidative atmosphere is reported to induce the formation of SrO islands at the surface and V_{Sr}'' below the surface [48] (Figure III.19d). Our substrates are submitted to an annealing process at 950°C for one hour in an oxygen-rich atmosphere after the etching that allows the TiO_2 termination. We have to say that we did not detect SrO domains or Ruddlesden-Popper phase in the thin foils we observed.

Strontium vacancies could also be formed in the sub-surface region during PLD by the energetic plume or by a defect equilibrium reaction induced by the $\text{Sr} \leftrightarrow \text{La}$ intermixing. At the oxygen partial pressure used, the La donors, or any electronic disequilibrium, are partially compensated by V_{Sr}'' (ionic compensation) [27,28,49] (Figure III.19), the film being a sink for the expelled Sr ions. Vonk *et al.* [22] found these defects in a thin region near the interface, which they also associated to the La-

doping. The lower level of electron compensation at such oxygen partial pressure could explain the high valence measured for Ti cations.

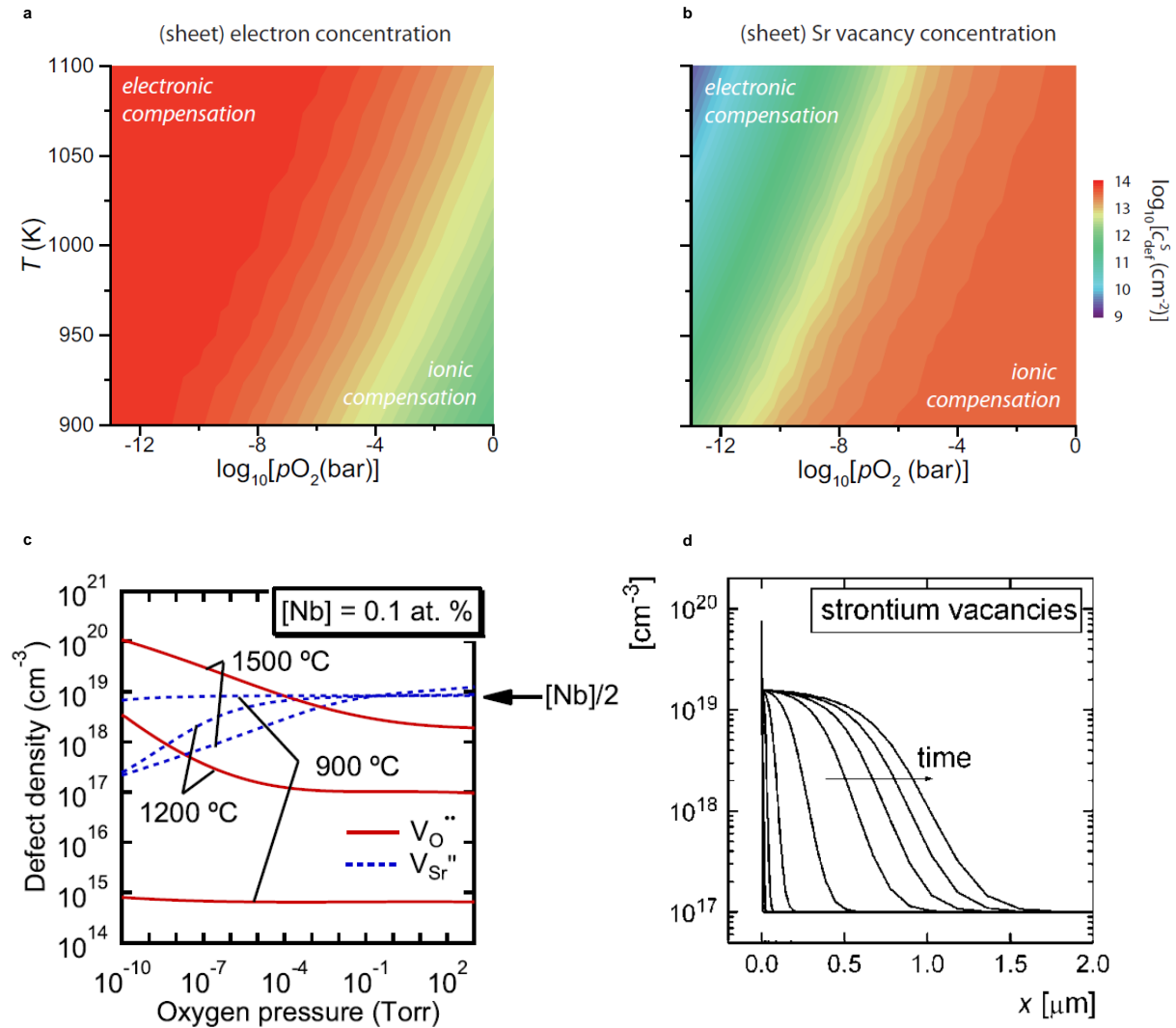


Figure III.19 | Influence of temperature and oxygen partial pressure on the compensation mechanism of the electronic disequilibrium. a-b, Compensation mechanisms of the interfacial charge. Calculations of (a) electron concentration (b) Sr vacancies concentration as a function of growth p_{O_2} and T . The concentration of electrons (Sr vacancies) increases at higher (lower) T and lower (higher) p_{O_2} . From [28]. c, Concentration of O and Sr vacancies calculated in a Nb-doped STO for various T as a function of p_{O_2} . From [49]. d, Concentration in strontium vacancies regarding the distance to the surface measured after annealing in oxidative atmosphere. From [48].

Modeling of atomic relaxation around strontium vacancies in bulk STO by Freedman *et al.* [43] shows an overall expansive strain. As in-plane parameters are more constrained, this may result in an expansion of the cell dimension in the growth direction [22,44]. Ohnishi *et al.* [44], as well as Wickelin *et al.* [50], varied the laser fluence during the homoepitaxial growth of STO, and demonstrate this c -lattice expansion in the film with the formation of Sr vacancies.

We can make the hypothesis that strontium vacancies are responsible for the increase of c/a seen in the substrate of our two samples. What could explain the thinner blocking dips observed in the

region of the substrate below the interface ? It cannot be attributed to buckling of the layers as we have seen that this should induce an opposite effect with a widening of the dips (Figure II.44). The removal of a strontium atom, without relaxing the atomic positions, does not modify significantly the dip width for the thermal vibration considered, as the closer anion give rise to an equivalent shadow cone (Figure II.45). In a relaxed structure, this oxygen anion should be repelled by the strontium vacancy toward the Sr scattering center. A widening of the dip would be expected. Strontium vacancies cannot explain the thinner dip width. A vacancy pair $V_{Sr}'' - V_O^\bullet$ could induce a net decrease of the width as shadow cone would be controlled by the second Sr in the [101] direction (fourth neighbor of the scattering center). But the low concentration in V_O^\bullet does not support this hypothesis. The strong decrease of the dip width can only be explained by a significant increase in the interatomic distance in [101] direction between the scattering and blocking atoms, as a consequence of the c-lattice expansion. This explains why the “strain” profiles and the “buckling” profiles show similar trends.

III.5.3.5 Distribution of the strontium vacancies in the 3 u.c. and 5 u.c. sample

If strontium vacancies are likely to be present in our substrates and to cause an expansion of the c parameter, we still have to explain the distinct strain profiles in the two samples Figure III.15c and Figure III.15d show that the areas under the curves of the non-elastic contributions of the strain in the substrate are similar for the two samples. However the region with $c/a > 1$ extends deeper in the substrate of the sample UC3 and the deformation is larger in the substrate of the sample UC5. This indicates a difference in the distributions of the Sr vacancies more than in their concentrations, consistently with the identical growth conditions used to synthesize both samples.

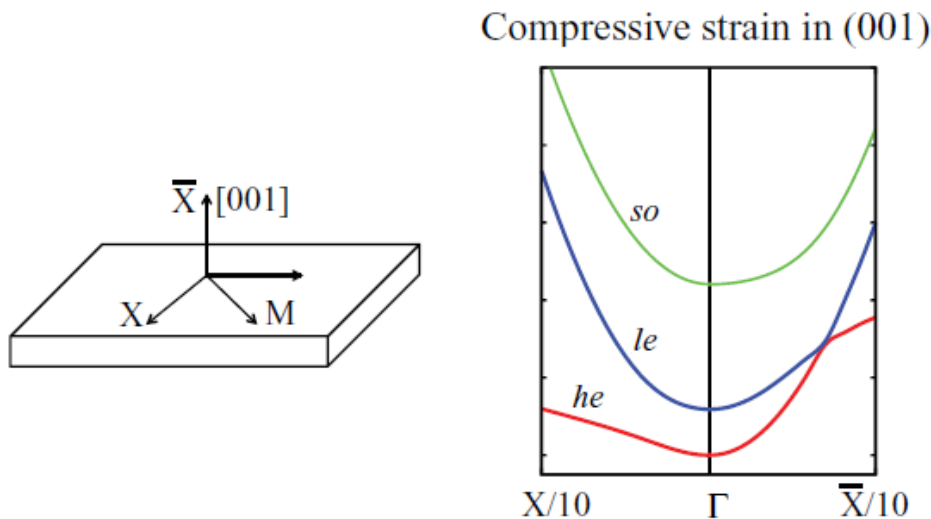


Figure III.20 | SrTiO₃ band structure close to the conduction band minimum at Γ under -1% compressive strain in the (001) plane. Adapted from [53]. The slope of the lowest conduction band indicates that the electron mass for in-plane transport is heavier than along the [001] direction.

The distinct distributions might be explained by a difference in the polar fields developed. The lower dipolar field in the thinner film must induce a weaker V_{Sr}'' attraction toward the interface than in the 5 u.c. sample, explaining the deeper region with $c/a > 1$ in the 3 u.c. assembly. The consequence of this in-plane compression on the conduction is a dilution of the 2D charge confinement along the c-axis [30,51–53] (Figure III.20). The mobile charges could be transferred deeper in the STO substrate

Chapter III | Origin(s) of the q-2DEG

of the sample *UC3* than the sample *UC5*. The existence of these defects does not play in favor of a high in-plane mobility, as they will act as scattering centers.

Interestingly Salvinelli *et al.* [54] has recently studied similar samples (varying only by their film thicknesses) resulting in differences in terms of Sr vacancies distribution within STO as a function of the LAO thickness. However, in contrast to our work, they found higher concentration and more diluted Sr vacancies in the thicker sample. They ascribed this behavior to either PLD growth, either the chemical treatment to obtain the preferential TiO₂-terminated substrate, or either the A-site intermixing. While the two former causes can hardly explain the differences seen for samples prepared in the same conditions, the latter remains consistent with their interdiffusion experimental results showing $(La + Sr) < 1$ for thicker film below the interface.

In conclusion, structural distortions occur in both samples despite their discrepancies in terms of electrical properties. The measured c/a ratios are larger than those predicted by epitaxial strains taking intermixing into account. This indicates that compressive electrostatic forces developed around the interface. These forces extended deeper into the substrate in the sample *UC3*, reducing the confinement and diluting the interfacial charge carrier. Several factors can contribute to the deformation such as a buckling of the layers or intermixing to counteract the dipolar field in the film, a (pseudo) Jahn-Teller effect by the change in titanium oxidation state, or the formation of strontium vacancies by ionic compensation or due to the process. Only the strontium vacancies could explain the differences seen in the strain profile in STO for the samples *UC3* and *UC5*. These distortions in STO are not at the origin of the charge transfer but seem to play a significant role on the electrical properties of our LAO/STO heterostructures, and notably on the carrier mobility [51,55] more than the carrier density.

III.6 Discussion

This chapter outlined the mechanisms known as possible trigger of the conduction at the LAO/STO hetero-interface. It was shown that none of them are self-sufficient to explain the electrical behavior of the samples *UC3* and *UC5*. We will propose a scenario gathering our experimental results.

Diverging potential ?

The growth of the LAO polar film on our TiO₂-terminated substrate induces the development of a polar field in the film. Contrary to the first model proposed by Ohtomo, the potential slope in the film can be reduced even below the critical thickness by two simultaneous mechanisms, intermixing and buckling:

- Ti \leftrightarrow Al intermixing forms Al_{Ti} (acceptor, below the interface) - Ti_{Al} (donor, in the film) antisite pairs. As the donor level is higher than the acceptor one, a transfer of electrons is possible from the film to the substrate first layers. It must be added that the donor defects cannot inject electrons to the conduction band and acceptor defects, holes in the valence band since their energy level is too deep in the band gap [56]. This electron transfer reduces the polar field but cannot make the interface conductive.

-In LaO and AlO₂ layers, the displacements of the cations toward the surface relative to the anions produce counter dipoles. Although we did not image oxygen atoms by HAADF, we associate

the displacement of Ti seen in the film in Figure III.17 to such a buckling. The first principle calculations of Figure III.18 also show a clear buckling in a 3 u.c. film that reduces the dipolar field.

In the 5 u.c. film, buckling and intermixing also counteract the dipolar field. We believe that the band bending produced by the resultant field ($E_{\text{Polar}} - E_{\text{Intermixing}} - E_{\text{Buckling}}$) is not high enough for a crossing of the conduction band of STO with the valance band of LAO, contrary to Ohtomo's model that did not consider buckling and intermixing. The mobile charges observed in the 5 u.c. do not originate from the valance band of LAO.

Source of charge carriers

Three principal sources of mobile carriers can be considered: oxygen vacancies in STO, La doping, charge transfer from the surface.

The oxygen vacancies were not clearly evidenced in the substrate by EELS measurements (Figure III.6). A reduction of the bulk STO as source of electrons is quite unlikely.

La doping can release charge carriers. The density of carrier measured by EELS is however significantly smaller than that of the donor dopant concentration. A partial charge carrier recombination in the acceptor and donor doped $\text{La}_x\text{Sr}_{1-x}\text{Al}_y\text{Ti}_{1-y}\text{O}_3$ layer is expected to reduce the net donor doping. A partial compensation of La_{Sr} by V_{Sr}'' is another mechanism that lowers the carrier concentration. Since the samples UC3 and UC5 enclose a similar doping level but have opposite electrical behavior, additional source of charge carriers, or differences in their mobilities should be considered.

Donor defects at the surface of a polar film, like oxygen vacancies or hydrogen adsorbed on surface oxygen, see their formation energy modified by the potential build-up. Oxygen vacancy formation on LAO surface should not be favored at the partial pressure used. However their energy formation is seen to decrease with the increase of film thickness and polarity. Yu *et al.*[56] have determined that $V_{\text{O}}^{\bullet\bullet}$ become stable from 4 u.c.. These donor defects at the LAO surface have a higher energy level than the STO conduction band. They can transfer electrons to the interface. The dipolar field can be cancelled for $\frac{1}{4} V_{\text{O}}^{\bullet\bullet}$ per LAO unit cell of the surface. Similar conclusions have been established for H^+ adsorbate by Fongkaew *et al.* [36].

Charge confinement

If the carrier origin is identified, the carrier densities are not explained at this point. This model of charge injection from the top film layer assumes their 2D confinement in the interface quantum well. The low carrier density measured by EELS, n_{EELS} , around the interface in the sample UC5 and the large carrier density obtained by Van der Paw measurements in Hall configuration, n_{H} , are not consistent with a strict 2D confinement of the charges. Can we now merge these two carrier densities into a common conduction mechanism? The Hall coefficient gives $n_{\text{H}} = 1.25 \cdot 10^{15} \text{ cm}^{-2}$. The upper limit given by the electronic reconstruction, that assumes 0.5 free electron per u.c., give a volume carrier density $n_{+3.5,3D} = (0.5 \text{ carrier})/a_{\text{STO}}^3 = 8.4 \cdot 10^{21} \text{ cm}^{-3}$. This would necessitate a layer of $n_{\text{H}}/n_{+3.5,3D} = 14.9 \text{ \AA}$, giving a spread of the carrier on about 4 u.c.. A conducting layer made of $\text{Ti}^{3.9+}$ (0.1 carrier/u.c., $n_{+3.9,3D} = 1.7 \times 10^{21} \text{ cm}^{-3}$) would be about 19 u.c. thick. If we take into account 3 layers of Ti valence +3.9 and others layers at +3.95, corresponding to the detection limit of our

Chapter III | Origin(s) of the q-2DEG

measurement, the conduction would spread over 32 u.c.. As aid in section III.2.2 the valence measurements by EELS is indicative, and we are only able to give a range of depth for carrier dilution which must be at least 10 u.c..

The driving force for this carrier dilution is hypothesized below with the introduction of structural distortions.

Structural distortions induced by ionic compensation mechanism

In the above sections, the polar field was reduced by buckling, and charge injection either from Ti_{Al} or by surface donor defects. The deformation profiles obtained in Figure III.15 show an elongation of the cell along the c-axis below the interface for the samples *UC3* and *UC5* that cannot be attributed only to Ti off-centering or Jahn-Teller-like effect. We have explained this deformation by strontium vacancies, formed either during the processing from the high energetic impingement of the incoming particles or by an ionic compensation of the doping in which the vacancies trapped two electrons. These vacancies can contribute to reduce the dipolar field. In the sample *UC5*, which develops higher polar field than the sample *UC3*, the strain level below the interface is higher. We can explain this by a higher vacancy concentration in this region. The presence of V_{Sr}'' has two consequences on the electron conductivity. Firstly on the charge carrier density: since the interfacial charge can be partially compensated by these charge defects, the density of carrier injected from the surface is lowered. Secondly on the charge carrier mobility: in-plane compression induces significantly higher electron mass for transport in the (001) planes than along [001] directions (Figure III.20) for which light masses are calculated [53]. On the contrary a 2D confinement of the charges would require a heavy mass along [001] and light mass on (001). We explain the dilution of the charge carriers in the substrate region by a thermally activated transport of the charge carrier in the direction of lighter masses, normal to (100).

From these experimental results we conclude that more than the carrier quantity, the carrier mobility must be the crucial parameter to explain the insulating/conducting transition. Interestingly, the literature confirms a link between structural distortions and the carrier mobility. Structural distortions were the only discriminating parameter between our samples. We have chosen to put forward the role of negatively-charged defects, the strontium vacancies, in these distortions.

This chapter was mainly devoted to samples with two film thicknesses grown in the same conditions. The above mentioned conclusions are meaningful for the set of growth parameters used. The modifications of the LAO/STO heterostructure behavior induced by variations in these growth conditions will be investigated in the next chapter.

Bibliography

- [1] H. Zaid, M. H. Berger, D. Jalabert, M. Walls, R. Akrobetu, I. Fongkaew, W. R. L. Lambrecht, N. J. Goble, X. P. A. Gao, et al., "Atomic-resolved depth profile of strain and cation intermixing around LaAlO₃/SrTiO₃ interfaces," *Sci. Rep.* **6**, 28118 (2016).
- [2] P. Bouvier and J. Kreisel, "Pressure-induced phase transition in LaAlO₃," *J. Phys. Condens. Matter* **14**, 3981 (2002).
- [3] M. Huijben, A. Brinkman, G. Koster, G. Rijnders, H. Hilgenkamp, and D. H. A. Blank, "Structure-Property Relation of SrTiO₃/LaAlO₃ Interfaces," *Adv. Mater.* **21**, 1665–1677 (2009).
- [4] A. S. Kalabukhov, Y. A. Boikov, I. T. Serenkov, V. I. Sakharov, V. N. Popok, R. Gunnarsson, J. Börjesson, N. Ljustina, E. Olsson, et al., "Cationic disorder and phase segregation in LaAlO₃/SrTiO₃ heterointerfaces evidenced by medium-energy ion spectroscopy," *Phys. Rev. Lett.* **103** (2009).
- [5] J. Mannhart and D. G. Schlom, "Oxide Interfaces--An Opportunity for Electronics," *Science* **327**, 1607–1611 (2010).
- [6] M. Breitschaft, V. Tinkl, N. Pavlenko, S. Paetel, C. Richter, J. R. Kirtley, Y. C. Liao, G. Hammerl, V. Eyert, et al., "Two-dimensional electron liquid state at LaAlO₃-SrTiO₃ interfaces," *Phys. Rev. B* **81**, 153414 (2010).
- [7] C. Cancellieri, N. Reyren, S. Gariglio, A. D. Caviglia, A. Fête, and J.-M. Triscone, "Influence of the growth conditions on the LaAlO₃/SrTiO₃ interface electronic properties," *EPL Europhys. Lett.* **91**, 17004 (2010).
- [8] G. Zhu, G. Radtke, and G. A. Botton, "Bonding and structure of a reconstructed (001) surface of SrTiO₃ from TEM," *Nature* **490**, 384–387 (2012).
- [9] S. A. Chambers, M. H. Engelhard, V. Shutthanandan, Z. Zhu, T. C. Droubay, L. Qiao, P. V. Sushko, T. Feng, H. D. Lee, et al., "Instability, Intermixing and Electronic Structure at the Epitaxial LaAlO₃/SrTiO₃(001) Heterojunction," *Surf. Sci. Rep.* **65**, 317–352 (2010).
- [10] J.-L. Maurice, G. Herranz, C. Colliex, I. Devos, C. Carrétéro, A. Barthélémy, K. Bouzehouane, S. Fusil, D. Imhoff, et al., "Electron energy loss spectroscopy determination of Ti oxidation state at the (001) LaAlO₃/SrTiO₃ interface as a function of LaAlO₃ growth conditions," *Eur. Lett* **82**, 17003 (2008).
- [11] J. Verbeeck, S. Bals, A. N. Kravtsova, D. Lamoen, M. Luysberg, M. Huijben, G. Rijnders, A. Brinkman, H. Hilgenkamp, et al., "Electronic reconstruction at n-type SrTiO₃/LaAlO₃ interfaces," *Phys. Rev. B* **81** (2010).
- [12] C. Cantoni, J. Gazquez, F. Miletto Granozio, M. P. Oxley, M. Varela, A. R. Lupini, S. J. Pennycook, C. Aruta, U. S. di Uccio, et al., "Electron Transfer and Ionic Displacements at the Origin of the 2D Electron Gas at the LAO/STO Interface: Direct Measurements with Atomic-Column Spatial Resolution," *Adv. Mater.* **24**, 3952–3957 (2012).

- [13] G. Drera, F. Banfi, F. F. Canova, P. Borghetti, L. Sangaletti, F. Bondino, E. Magnano, J. Huijben, M. Huijben, et al., “Spectroscopic evidence of in-gap states at the SrTiO₃/LaAlO₃ ultrathin interfaces,” *Appl. Phys. Lett.* **98**, 052907 (2011).
- [14] G. Drera, G. Salvinelli, A. Brinkman, M. Huijben, G. Koster, H. Hilgenkamp, G. Rijnders, D. Visentin, and L. Sangaletti, “Band offsets and density of Ti³⁺ states probed by x-ray photoemission on LaAlO₃/SrTiO₃ heterointerfaces and their LaAlO₃ and SrTiO₃ bulk precursors,” *Phys. Rev. B* **87**, 075435 (2013).
- [15] M. Sing, G. Berner, K. Goß, A. Müller, A. Ruff, A. Wetscherek, S. Thiel, J. Mannhart, S. A. Pauli, et al., “Profiling the Interface Electron Gas of LaAlO₃/SrTiO₃ Heterostructures with Hard X-Ray Photoelectron Spectroscopy,” *Phys. Rev. Lett.* **102**, 176805 (2009).
- [16] E. Slooten, Z. Zhong, H. J. A. Molegraaf, P. D. Eerkes, S. de Jong, F. Massee, E. van Heumen, M. K. Kruize, S. Wenderich, et al., “Hard x-ray photoemission and density functional theory study of the internal electric field in SrTiO₃/LaAlO₃ oxide heterostructures,” *Phys. Rev. B* **87**, 085128 (2013).
- [17] M. Takizawa, S. Tsuda, T. Susaki, H. Y. Hwang, and A. Fujimori, “Electronic charges and electric potential at LaAlO₃/SrTiO₃ interfaces studied by core-level photoemission spectroscopy,” *Phys. Rev. B* **84** (2011).
- [18] M. Basletic, J.-L. Maurice, C. Carrétéro, G. Herranz, O. Copie, M. Bibes, É. Jacquet, K. Bouzehouane, S. Fusil, et al., “Mapping the spatial distribution of charge carriers in LaAlO₃/SrTiO₃ heterostructures,” *Nat. Mater.* **7**, 621–625 (2008).
- [19] J. Zhou, T. C. Asmara, M. Yang, G. A. Sawatzky, Y. P. Feng, and A. Rusydi, “The interplay of electronic reconstructions, lattice distortions, and surface oxygen vacancies in insulator-metal transition of LaAlO₃/SrTiO₃,” *Phys Rev B* **92** (2015).
- [20] S. A. Chambers, “Understanding the mechanism of conductivity at the LaAlO₃/SrTiO₃(001) interface,” *Surf. Sci.* **605**, 1133–1140 (2011).
- [21] S. Gariglio, A. Fête, and J.-M. Triscone, “Electron confinement at the LaAlO₃/SrTiO₃ interface,” *J. Phys. Condens. Matter* **27**, 283201 (2015).
- [22] V. Vonk, J. Huijben, D. Kukuruznyak, A. Stierle, H. Hilgenkamp, A. Brinkman, and S. Harkema, “Polar-discontinuity-retaining A-site intermixing and vacancies at SrTiO₃/LaAlO₃ interfaces,” *Phys. Rev. B* **85** (2012).
- [23] Z. Q. Liu, L. Sun, Z. Huang, C. J. Li, S. W. Zeng, K. Han, W. M. Lü, T. Venkatesan, and Ariando, “Dominant role of oxygen vacancies in electrical properties of unannealed LaAlO₃/SrTiO₃ interfaces,” *J. Appl. Phys.* **115**, 054303 (2014).
- [24] P. R. Willmott, S. A. Pauli, R. Herger, C. M. Schlepütz, D. Martoccia, B. D. Patterson, B. Delley, R. Clarke, D. Kumah, et al., “Structural basis for the conducting interface between LaAlO₃ and SrTiO₃,” *Phys Rev Lett* **99**, 155502 (2007).
- [25] N. Nakagawa, H. Y. Hwang, and D. A. Muller, “Why some interfaces cannot be sharp,” *Nat. Mater* **5**, 204–209 (2006).

- [26] C. L. Jia, S. B. Mi, M. Faley, U. Poppe, J. Schubert, and K. Urban, "Oxygen octahedron reconstruction in the SrTiO₃/LaAlO₃ heterointerfaces investigated using aberration-corrected ultrahigh-resolution transmission electron microscopy," *Phys. Rev. B* **79** (2009).
- [27] U. Balachandran and N. G. Eror, "Electrical Conductivity in Lanthanum-Doped Strontium Titanate," *J. Electrochem. Soc.* **129**, 1021–1026 (1982).
- [28] F. Gunkel, R. Waser, A. H. H. Ramadan, R. A. De Souza, S. Hoffmann-Eifert, and R. Dittmann, "Space charges and defect concentration profiles at complex oxide interfaces," *Phys. Rev. B* **93**, 245431 (2016).
- [29] A. Annadi, A. Putra, Z. Q. Liu, X. Wang, K. Gopinadhan, Z. Huang, S. Dhar, T. Venkatesan, and Ariando, "Electronic correlation and strain effects at the interfaces between polar and nonpolar complex oxides," *Phys Rev B* **86**, 085450 (2012).
- [30] F. Schoofs, M. A. Carpenter, M. E. Vickers, M. Egilmez, T. Fix, J. E. Kleibeuker, J. L. MacManus-Driscoll, and M. G. Blamire, "Carrier density modulation by structural distortions at modified LaAlO₃/SrTiO₃ interfaces," *J. Phys. Condens. Matter Inst. Phys. J.* **25**, 175005 (2013).
- [31] H. W. Jang, D. A. Felker, C. W. Bark, Y. Wang, M. K. Niranjana, C. T. Nelson, Y. Zhang, D. Su, C. M. Folkman, et al., "Metallic and Insulating Oxide Interfaces Controlled by Electronic Correlations," *Science* **331**, 886–889 (2011).
- [32] F. J. Wong, S.-H. Baek, R. V. Chopdekar, V. V. Mehta, H.-W. Jang, C.-B. Eom, and Y. Suzuki, "Metallicity in LaTiO₃ thin films induced by lattice deformation," *Phys. Rev. B* **81**, 161101 (2010).
- [33] X. Sang, E. D. Grimley, C. Niu, D. L. Irving, and J. M. LeBeau, "Direct observation of charge mediated lattice distortions in complex oxide solid solutions," *Appl. Phys. Lett.* **106**, 061913 (2015).
- [34] M. D. Biegalski, D. D. Fong, J. A. Eastman, P. H. Fuoss, S. K. Streiffer, T. Heeg, J. Schubert, W. Tian, C. T. Nelson, et al., "Critical thickness of high structural quality SrTiO₃ films grown on orthorhombic (101) DyScO₃," *J. Appl. Phys.* **104**, 114109 (2008).
- [35] V. Vonk, M. Huijben, K. J. I. Driessen, P. Tinnemans, A. Brinkman, S. Harkema, and H. Graafsma, "Interface structure of SrTiO₃/LaAlO₃ at elevated temperatures studied in situ by synchrotron X rays," *Phys Rev B* **75**, 235417 (2007).
- [36] I. Fongkaew, S. Limpijumnong, and W. R. L. Lambrecht, "Effects of structural relaxation, interdiffusion, and surface termination on two-dimensional electron gas formation at the LaAlO₃/SrTiO₃ interface," *Phys. Rev. B* **92**, 155416 (2015).
- [37] J.-L. Maurice, "Electronic conductivity and structural distortion at the interface between insulators SrTiO₃ and LaAlO₃," *Phys Status Solidi A* **203**, 2209–2214 (2006).
- [38] U. Schwingenschlögl and C. Schuster, "Interface relaxation and electrostatic charge depletion in the oxide heterostructure LaAlO₃/SrTiO₃," *EPL Europhys. Lett.* **86**, 27005 (2009).
- [39] S. Okamoto, A. J. Millis, and N. A. Spaldin, "Lattice Relaxation in Oxide Heterostructures: LaTiO₃/SrTiO₃ Superlattices," *Phys. Rev. Lett.* **97**, 056802 (2006).

Chapter III | Origin(s) of the q-2DEG

- [40] R. Pentcheva and W. E. Pickett, "Avoiding the polarization catastrophe in LaAlO₃ overlayers on SrTiO₃ through polar distortion," *Phys. Rev. Lett.* **102**, 107602 (2009).
- [41] S. A. Pauli, S. J. Leake, B. Delley, M. Björck, C. W. Schneider, C. M. Schlepütz, D. Martoccia, S. Paetel, J. Mannhart, et al., "Evolution of the Interfacial Structure of LaAlO₃ on SrTiO₃," *Phys. Rev. Lett.* **106**, 036101 (2011).
- [42] T. C. Asmara, A. Annadi, I. Santoso, P. K. Gogoi, A. Kotlov, H. M. Omer, M. Motapothula, M. B. H. Breese, M. Rübhausen, et al., "Mechanisms of charge transfer and redistribution in LaAlO₃/SrTiO₃ revealed by high-energy optical conductivity," *Nat. Commun.* **5** (2014).
- [43] D. A. Freedman, D. Roundy, and T. A. Arias, "Elastic effects of vacancies in strontium titanate: Short- and long-range strain fields, elastic dipole tensors, and chemical strain," *Phys Rev B* **80**, 064108 (2009).
- [44] T. Ohnishi, K. Shibuya, T. Yamamoto, and M. Lippmaa, "Defects and transport in complex oxide thin films," *J. Appl. Phys.* **103**, 103703 (2008).
- [45] H. Guo, S. Dong, P. D. Rack, J. D. Budai, C. Beekman, Z. Gai, W. Siemons, C. M. Gonzalez, R. Timilsina, et al., "Strain Doping: Reversible Single-Axis Control of a Complex Oxide Lattice via Helium Implantation," *Phys. Rev. Lett.* **114**, 256801 (2015).
- [46] S. A. Chambers, "Epitaxial Growth and Properties of Doped Transition Metal and Complex Oxide Films," *Adv. Mater.* **22**, 219–248 (2010).
- [47] F. Gunkel, S. Wicklein, S. Hoffmann-Eifert, P. Meuffels, P. Brinks, M. Huijben, G. Rijnders, R. Waser, and R. Dittmann, "Transport limits in defect-engineered LaAlO₃/SrTiO₃ bilayers," *Nanoscale* **7**, 1013–1022 (2015).
- [48] R. Meyer, R. Waser, J. Helmbold, and G. Borchart, "Observation of Vacancy Defect Migration in the Cation Sublattice of Complex Oxides by ¹⁸O Tracer Experiments," *Phys. Rev. Lett.* **90**, 105901 (2003).
- [49] Y. Kozuka, Y. Hikita, C. Bell, and H. Y. Hwang, "Dramatic mobility enhancements in doped SrTiO₃ thin films by defect management," *Appl. Phys. Lett.* **97**, 012107 (2010).
- [50] S. Wicklein, A. Sambri, S. Amoruso, X. Wang, R. Bruzzese, A. Koehl, and R. Dittmann, "Pulsed laser ablation of complex oxides: The role of congruent ablation and preferential scattering for the film stoichiometry," *Appl. Phys. Lett.* **101**, 131601 (2012).
- [51] Z. Huang, K. Han, S. Zeng, M. Motapothula, A. Y. Borisevich, S. Ghosh, W. Lü, C. Li, W. Zhou, et al., "The Effect of Polar Fluctuation and Lattice Mismatch on Carrier Mobility at Oxide Interfaces," *Nano Lett.* **16**, 2307–2313 (2016).
- [52] C. W. Bark, D. A. Felker, Y. Wang, Y. Zhang, H. W. Jang, C. M. Folkman, J. W. Park, S. H. Baek, H. Zhou, et al., "Tailoring a two-dimensional electron gas at the LaAlO₃/SrTiO₃ (001) interface by epitaxial strain," *Proc. Natl. Acad. Sci.* **108**, 4720–4724 (2011).

- [53] A. Janotti, D. Steiauf, and C. G. Van de Walle, "Strain effects on the electronic structure of SrTiO₃ : Toward high electron mobilities," *Phys. Rev. B* **84**, 201304(R) (2011).
- [54] G. Salvinelli, G. Drera, A. Giampietri, and L. Sangaletti, "Layer-resolved cation diffusion and stoichiometry at the LaAlO₃/SrTiO₃ heterointerface probed by X-ray photoemission experiments and site occupancy modeling," *ACS Appl. Mater. Interfaces* **7**, 25648–25657 (2015).
- [55] C. Bell, S. Harashima, Y. Hikita, and H. Y. Hwang, "Thickness dependence of the mobility at the LaAlO₃/SrTiO₃ interface," *Appl. Phys. Lett.* **94**, 222111 (2009).
- [56] L. Yu and A. Zunger, "A polarity-induced defect mechanism for conductivity and magnetism at polar–nonpolar oxide interfaces," *Nat. Commun.* **5**, 5118 (2014).

Chapitre III – Résumé

Le chapitre III a pour objectif d'identifier le ou les mécanismes responsable des propriétés conductrices à l'interface de l'hétérostructure LAO/STO. On a commencé par constater la bonne qualité de dépôts, avec une croissance de film pseudomorphique sans défauts d'accommodation plastique, sur un échantillon avec un film d'épaisseur égale à 10 mailles élémentaires (uc) à l'aide d'analyses microscopique avec une résolution atomique. Puis, pour répondre à cette problématique, deux échantillons ont été étudiés, élaborés dans les mêmes conditions de croissance, avec des films d'épaisseurs distinctes, respectivement en-dessous (3 uc – nommé UC3) et au-dessus (5 uc – nommé UC5) de l'épaisseur critique. Dans un premier temps, les mesures des propriétés électriques ont confirmé respectivement le caractère isolant et conducteur de l'échantillon UC3 et UC5, plaçant bien l'épaisseur critique du film pour laquelle la conduction apparaît entre ces deux valeurs. La suite du chapitre est consacrée à isoler chaque mécanisme, proposé dans la littérature comme élément potentiellement déclencheur de la conduction à l'interface LaO/TiO₂, et à comprendre leur influence sur les propriétés des hétérostructures étudiées dans cette thèse.

Tout d'abord, nous nous sommes concentrés sur le modèle de catastrophe polaire, qui prédit un transfert d'un demi-électron à l'interface venant occuper les niveaux 3d du Ti. Les mesures EELS à l'interface du seuil d'absorption Ti-L_{2,3} n'ont pas permis d'atteindre la valence théorique de +3.5 pour l'échantillon conducteur UC5, mais plutôt un état d'oxydation de Ti^{3.9(+/-0.05)}. Une valence similaire est mesurée pour l'échantillon isolant UC3. De plus, si on considère que les porteurs de charges viennent exclusivement de Ti³⁺, la densité théorique des électrons à l'interface de UC5 ($6.6 \times 10^{13} \pm 3.28 \times 10^{13} \text{ cm}^{-2}$) est nettement inférieure aux mesures expérimentales ($n > 1.2 \times 10^{15} \text{ cm}^{-2}$), ce qui rend caduc le caractère strictement bidimensionnel de la conduction, attendu dans le modèle de catastrophe polaire. Cette hypothèse a été renforcée par les mesures EELS de la valence du Ti dans les premières couches atomiques autour de l'interface, qui ne nous ont pas permis d'atteindre la densité de porteurs mesurée. Ainsi, le modèle de catastrophe polaire ne peut être utilisé comme argument exclusif permettant de comprendre l'apparition de la conduction dans les hétérostructures LAO/STO.

De même, les mesures EELS du seuil de l'oxygène n'ont pas permis de détecter la présence de lacunes d'oxygènes, connues pour apporter deux électrons par défaut, ni à l'interface ni dans le substrat STO d'aucun des échantillons. Ce résultat est cohérent avec la faible contribution de Ti³⁺ mesurée. En conclusion, bien qu'une faible concentration de ces défauts n'est pas totalement exclue, elle ne serait pas suffisante pour expliquer les différentes propriétés électriques mesurées dans les échantillons UC3 et UC5.

Les mesures EELS du seuil O-K ont mis en évidence un mécanisme également suspecté d'être à l'origine de la conduction, l'interdiffusion. Afin d'obtenir des informations quantitatives sur l'ampleur de ce phénomène, nous avons menés des investigations à l'aide d'une technique permettant d'obtenir le profil chimique avec une résolution atomique, le MEIS en mode Random. Les résultats sur l'interdiffusion des cations A ($\text{La} \leftrightarrow \text{Sr}$) ont montré une très faible différence en termes d'échange cationique entre l'échantillon isolant (UC3) et conducteur (UC5). Alors que les atomes de Sr diffusent jusqu'en surface des deux films, la longueur de diffusion des atomes de La dans le substrat est égale entre les deux échantillons. La différence se manifeste par une concentration de La légèrement plus grande dans la couche sous l'interface de l'échantillon conducteur. De plus, les analyses EELS supplémentaires sur les seuils $\text{La-M}_{4,5}$ et $\text{Ti-L}_{2,3}$ ont montré une dissymétrie entre les l'interdiffusion des cations A et B, caractérisée par une longueur de diffusion plus faible de cations B. Ce résultat permet d'envisager un dopage de La_{Sr} apportant des porteurs à l'interface. Toutefois, le niveau de dopage est insuffisant pour expliquer la conduction dans l'échantillon UC5, tout comme l'interdiffusion est insuffisante pour totalement lever la divergence du potentiel électrostatique dans le film. Ainsi, ce mécanisme ne peut pas prétendre à gouverner seul les propriétés électriques de l'hétérostructure LAO/STO.

Le dernier mécanisme que nous avons abordé dans ce chapitre, et non des moindres, représente les distorsions structurales. Les nombreux phénomènes se déroulant suite à la croissance du film sur le substrat, engendrent inévitablement des déformations au sein de la structure du système, qui influent sur le comportement électrique de celui-ci. Nous avons quantifié ces déformations locales par MEIS en mode Blocking. La position angulaire des « blocking dips » maille par maille nous permet de remonter à la variation de la position des premiers atomes rétrodiffusant les particules incidentes. Les profils de déformations, caractérisant les variations c/a , ont ainsi été extraits avec une précision atomique. En soustrayant la contribution de la déformation épitaxiale, obtenue à l'aide de la loi de Vegard en la corrélant avec les profils chimiques expérimentaux, le profil de contrainte reste non nul, avec une large partie en compression, ce qui indique des contributions supplémentaires à la déformation. La corrélation de ces profils avec ceux de flambage, obtenus en mesurant la largeur angulaire à mi-hauteur des « blocking dips » suggère des sources communes de déformation. Ainsi, l'objectif ici est de comprendre l'origine de cette expansion (dans la direction [001]) de la maille qui s'étend en profondeur dans l'échantillon isolant, alors qu'elle est plus importante à l'interface de l'échantillon conducteur. La nature de ces distorsions structurales a été divisée en quatre contributions principales. Tout d'abord, le remplissage de la couche 3d du Ti par un électron aboutit à une seconde levée de dégénérescence énergétique des niveaux e_g et t_{2g} . Cette différenciation énergétique est accompagnée par une déformation de la maille, via une contraction des octaèdres d'oxygène, c'est l'effet Jahn-Teller (ou une élongation dans le cas d'un effet pseudo Jahn-Teller). Or, les résultats expérimentaux ont montré une faible contribution de Ti^{3+} à l'interface. Donc, si l'effet Jahn-Teller semble participer à l'expansion de la maille, il n'est pas suffisant pour expliquer son ampleur. De plus, les différences observées dans les profils de déformation à l'interface entre l'échantillon isolant et conducteur, malgré un état d'oxydation similaire, de même que la faible distribution en profondeur de Ti^{3+} , nous incitent à identifier d'autres causes. Les distorsions ferroélectriques représentent également un candidat à cette compression puisque des images STEM-HAADF, avec une résolution atomique, à l'interface d'un échantillon avec un film plus épais ont révélé un décalage des atomes de Ti par rapport au centre de la maille. Cependant, ces décalages ont été constatés dans la région de l'interface, c'est-à-dire bien moins étendus que le profil de

déformation. Ainsi, des alternatives doivent une nouvelle fois être apportées pour comprendre le comportement structural de nos échantillons. Outre la formation de dipôles via le flambage des couches atomiques, pour contrer le champ polaire se créant dans le film (démonstré par modélisation par W.Lambrecht de CWRU), ou les distorsions liées aux échanges cationiques qui ne permettent pas une nouvelle fois de décrire convenablement les profils de déformations expérimentaux des deux échantillons, nous avons menés des investigations sur la présence de lacunes cationiques. En effet, plusieurs articles avancent que dans les conditions de croissance de nos échantillons UC3 et UC5, la compensation du déséquilibre électronique se fait partiellement par la formation de lacunes de Sr. Or ces défauts engendrent une expansion de la maille, ce qui pourrait expliquer cette large compression à l'interface et dans le substrat. Quant à l'extension plus profonde de la déformation dans l'échantillon isolant, elle s'explique par une distribution plus étendue des lacunes cationiques. En effet, le potentiel électrostatique étant moins important dans le film, la compensation des charges nécessaire est moindre, ce qui résulte en un plus faible pouvoir d'attraction des lacunes à l'interface. Ainsi, des distorsions structurales ont été trouvées dans l'échantillon isolant et conducteur. C'est le seul mécanisme discriminant, parmi l'ensemble de l'étude réalisée. Bien que la nature de ces distorsions ne permettent pas d'expliquer une augmentation de la densité de porteurs de charges, elle joue un rôle prépondérant sur les propriétés électriques des hétérostructures LAO/STO, et notamment sur la mobilité des porteurs.

Nous avons alors proposé un modèle expliquant les comportements électriques distincts des échantillons UC3 et UC5, malgré les valences de titane proches sous l'interface. Les porteurs de charges dans UC3 proviendraient d'un transfert de charge entre Ti_{Al} de surface vers Al_{Ti} sous l'interface. Mais les niveaux d'énergie des électrons correspondants sont trop profonds dans la bande interdite pour être mobiles. Dans UC5, le potentiel électrique en surface de film abaisse l'énergie de formation de défauts donneurs tels que des lacunes d'oxygènes ou des atomes d'hydrogènes adsorbés. La création de ces défauts, qui n'était pas favorisée dans UC3, devient possible à la surface de UC5. Les niveaux donneurs, plus hauts que le bas de la bande de conduction du STO permettent le transfert d'électrons mobiles sous l'interface. Les contraintes de compression dans le plan (001) mesurées sous l'interface augmentent la masse effective des électrons dans le plan et la diminuent dans la direction perpendiculaire. Ceci participe à la dilution des porteurs de charges observée.

Chapter IV

Dependence of the $\text{LaAlO}_3/\text{SrTiO}_3$ electrical properties to growth conditions

Effect	Samples batch	Sample Extended Name	Sample Shorter Name	Thickness (u.c.)	p_{O_2} (Torr)	Laser Fluence (J/cm^2)	Plume angle	Temperature ($^\circ\text{C}$)
Film thickness	TEM + MEIS	(1) UC3P4#2T7	UC3	3	10^{-4}	1.2	#2	750
		(2) UC5P4#2T7	UC5	5	10^{-4}	1.2	#2	750
		(3) UC10P4#2T7	UC10	10	10^{-4}	1.2	#2	750
p_{O_2}	TEM	(3) UC10P4#2T7	UC10P4	10	10^{-4}	1.2	#2	750
		(4) UC10P5#2T7	UC10P5	10	10^{-5}	1.2	#2	750
		(5) UC10P6#2T7	UC10P6	10	10^{-6}	1.2	#2	750
	MEIS	(2) UC5P4#2T7	UC5P4	5	10^{-4}	1.2	#2	750
		(6) UC5P5#2T7	UC5P5	5	10^{-5}	1.2	#2	750
		(3) UC10P4#2T7	UC10#2	10 (3)	10^{-4}	1.2	#2	750
Deposition Angle (+ Laser Fluence)	TEM	(7) UC10P4#4T7	UC10#4	10	10^{-4}	2.0	#4	750
		(1) UC3P4#2T7	UC3#2	3	10^{-4}	1.2	#2	750
	MEIS	(8) UC5P4#4T7	UC5#4	5 (3)	10^{-4}	2.0	#4	750
		(1) UC3P4#2T7	UC3T7	3	10^{-4}	1.2	#2	750
T $^\circ\text{C}$	TEM	(2) UC5P4#2T7	UC5T7	5	10^{-4}	1.2	#2	750
		(3) UC10P4#2T7	UC10T7	10	10^{-4}	1.2	#2	750
		(9) UC10P4#2T5	UC10T5	10	10^{-4}	1.2	#2	550

Table IV.1 | Growth parameters of the samples studied in this chapter. Nine samples have been selected to vary four parameters. The samples are listed by their full names UCwPx#yTz, where w refers to the number of unit cells, x the oxygen partial pressure in the PLD chamber, y the position with respect to the plume, and z the temperature. The table is divided in four subgroups where only one parameter is varied at a time, except for the deposition angle where the laser fluence also changes. In these subgroups the sample names are simplified. Some samples can be found in different subgroups with same extended names but distinct shorter names.

Chapter IV | Dependence to growth conditions

Chapter II gave a literature overview of the critical role played by the growth conditions on the behavior of the LAO/STO heterostructures. In Chapter III, the growth conditions were fixed except the growth duration. We analyzed the chemical and structural differences of two samples with film thicknesses one unit cell below and above the reported threshold thickness for the insulating/conducting transition. In Chapter IV, we will vary the process parameters one by one to determine their impact on the different conduction mechanisms highlighted in the previous chapters. First the film thickness will be increased to 10 u.c. while keeping the other parameters constant. Then, the effect of the oxygen pressure during the PLD growth, the plume angle (i.e. the substrate position within the PLD chamber), and the temperature of the deposition will be discussed. The nine main samples investigated in this chapter, with their respective PLD growth parameters, are summarized in Table IV.1 above. The samples name has been shortened in the text according to the specific parameters varying in each section, for ease of reading.

IV.1 Film thickness effect

In Ohtomo & Wang's model [1], the polar divergence is supposed to be cancelled by the transfer of half an electron from the film surface to the interface once the LAO film thickness reaches 4 u.c.. Additional LAO layers are not supposed to bring supplementary charge carriers to the interface. In this section we will compare a 10 u.c.-thick film sample (*UC10P4#2T7*, or **UC10**) to the 5 u.c. (*UC5P4#2T7*, or **UC5**) and 3 u.c. (*UC3P4#2T7*, or **UC3**) samples described in the last chapter, all obtained in the same conditions ($p_{O_2} = 10^{-4}$ Torr, Fluence = 1.2 J/cm², position = #2, Temperature = 750°C). As mentioned previously, the pseudomorphic growth of the 10 u.c. sample was established by the analysis of its electron diffraction patterns and HAADF images (Figure III.1 and Figure III.2).

IV.1.1 Electrical Measurements

Hall Effect measurements, carried out by N.Goble in the frame of our international project, revealed significant discrepancies between the two conductive samples (Figure IV.1). The charge carrier density decreased by more than one order of magnitude for the thicker film sample. To lesser extent, the mobility was also decreased. This brings additional evidences of that Ohtomo & Wang's model is quite simplistic.

These results are in agreement with Bell *et al.* [2] experiments showing a systematic thickness dependence of the conduction above 4 u.c., with weaker mobility, weaker carrier density and higher resistance for thicker LAO films. The mobility of a 5 u.c.-thick and 25 u.c.-thick samples were separated by two orders of magnitude but no clear explanations could be provided.

In order to understand this film thickness effect, we will investigate in the next section each mechanism known as possible provider of carriers or influencing the properties of the LAO/STO heterostructure.

Sample	Film thickness	Sheet resistance (RT)	Carrier density (RT)	Carrier mobility (RT)
UC3	3 u.c.	$> 10^8 \Omega/\square$	X	X
UC5	5 u.c.	$\sim 2 \times 10^3 \Omega/\square$	$\sim 1.2 \times 10^{15} \text{ cm}^{-2}$	$\sim 2.2 \text{ cm}^2/\text{Vs}$
UC10	10 u.c.	$\sim 8 \times 10^4 \Omega/\square$	$\sim 6.5 \times 10^{13} \text{ cm}^{-2}$	$\sim 1.3 \text{ cm}^2/\text{Vs}$

Table IV.2 | Electrical measurements for samples of increasing thicknesses.

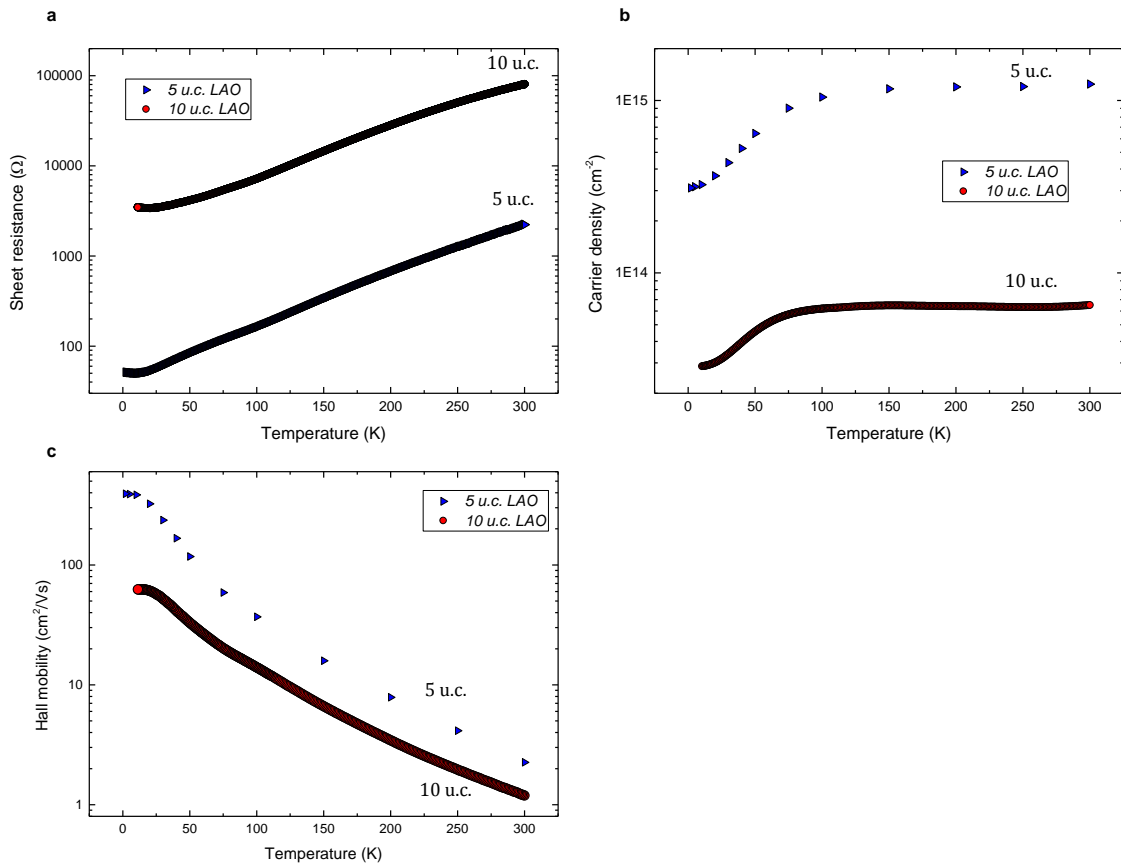


Figure IV.1 | Transport properties of the samples UC5 and UC10. Evolution of (a) sheet resistance, (b) carrier density, (c) Hall mobility, as a function of temperature. The sample UC5 exhibits higher transport properties than UC10.

IV.1.2 Ti^{3+} Contribution

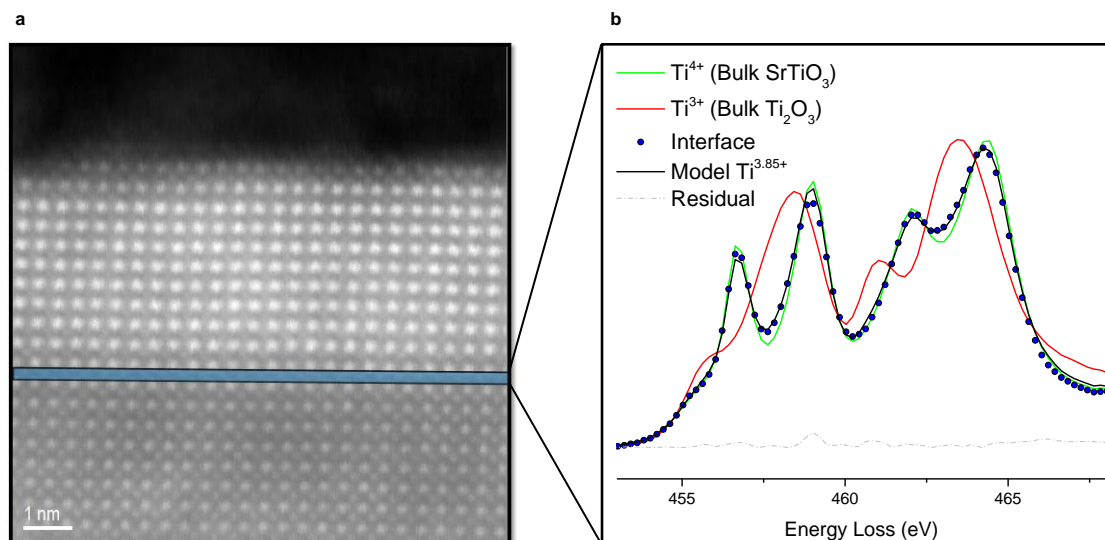


Figure IV.2 | Ti-L_{2,3} edge EELS taken at the UC10 interface. a, HAADF image of the region of interest selected in the corresponding spectrum image to record the Ti EELS spectrum at the interface. b, EELS spectrum of the interface (dots) modeled (black line) with the two parent spectra for Ti^{4+} (green curve), Ti^{3+} (red curve). A valence of +3.85 is deduced. The color code is available in Figure III.4.

Chapter IV | Dependence to growth conditions

We have estimated the Ti valence at the sample *UC10* from its EELS Ti-L_{2,3} absorption edges. Using the methodology previously described (Figure II.25), a Ti oxidation state of $Ti^{3.85+ (\pm 0.05)}$ is derived (Figure IV.2), leading to a maximum theoretical density of free charge carriers of 9.84×10^{13} ($\pm 3.28 \times 10^{13}$) cm^{-2} . This carrier density is once again weaker than the value predicted by the polar catastrophe (3.3×10^{14} cm^{-2}). Adding the carriers coming from 1 u.c. above to 5 u.c. below the interface (Figure IV.3) leads to a value of 3.41×10^{14} ($\pm 3.28 \times 10^{13}$) cm^{-2} , very close to this theoretical values. This confirms the dilution of the carriers.

The carrier density obtained from EELS on the 10 u.c.-thick sample is higher than that obtained by the same methodology on the 5 u.c. (Figure III.4d). Therefore, in agreement with published results using core-level photoemission spectroscopy [3], we have found that the Ti^{3+} contribution increases with the film thickness (Table IV.3). This contradicts the polar catastrophe model. Nonetheless, the carrier density obtained from EELS is higher than the value of 6.5×10^{13} cm^{-2} deduced from Hall measurements (Figure IV.1). This indicates that a significant part of these charge carriers must be localized and cannot participate to the conduction. The next sections will analyze the chemical and structural differences in the 5 and 10 u.c. sample to understand why the carrier injection increases with the film thickness whilst the carrier mobility decreases.

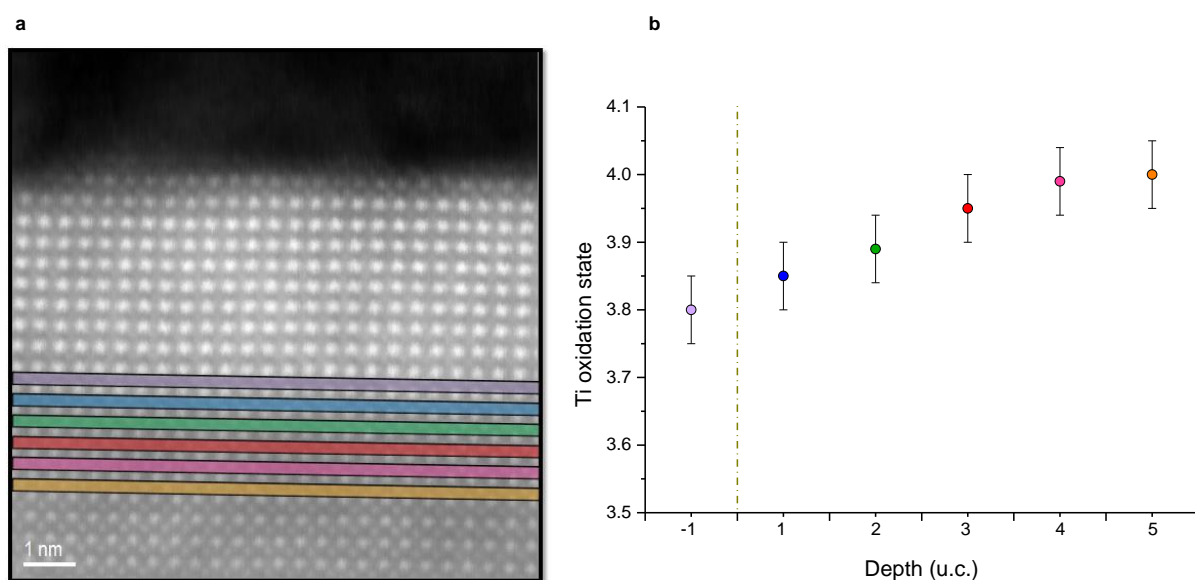


Figure IV.3 | Evolution of the Ti oxidation state throughout the sample *UC10*. **a**, HAADF image of the region of interest probed to measure the Ti EELS spectrum through the sample. Each region of interest is represented by one colored strip. **b**, Ti valence profile unit cell by unit cell determined by a linear combinations of Ti^{4+} and Ti^{3+} recorded on the same spectrometer.

Sample	Film thickness	Ti valence (interface)
<i>UC3</i>	3 u.c.	$Ti^{3.9+ (\pm 0.05)}$
<i>UC5</i>	5 u.c.	$Ti^{3.9+ (\pm 0.05)}$
<i>UC10</i>	10 u.c.	$Ti^{3.85+ (\pm 0.05)}$

Table IV.3 | Ti oxidation state at the interface for samples of increasing thicknesses.

IV.1.3 Oxygen vacancies

Figure IV.4 displays in green triangles the O-K spectrum corresponding to the deepest part of STO in the thin foil. No clear signature of oxygen vacancies was found in the sample *UC10* (Figure IV.4b) or *UC5* (Figure III.6d) as expected for bulk STO at this oxygen pressure. The red circle spectrum recorded at the LaO/TiO₂ interface shows a small decrease of the peak A (referenced in Figure II.27), and a widening of the peak C shifting toward the A peak. This reveals a reduction of the Ti oxidation state and/or intermixing. The decrease of the A peak is however less pronounced than in the 5 u.c. sample (Figure IV.4d). No features characteristic of oxygen vacancies can be recognized around the interface. The concentration of oxygen vacancies does not increase with the duration of the deposition in the PLD chamber at such O₂ partial pressure. The higher density of electrons at the interface of the sample *UC10* does not originate from oxygen vacancies.

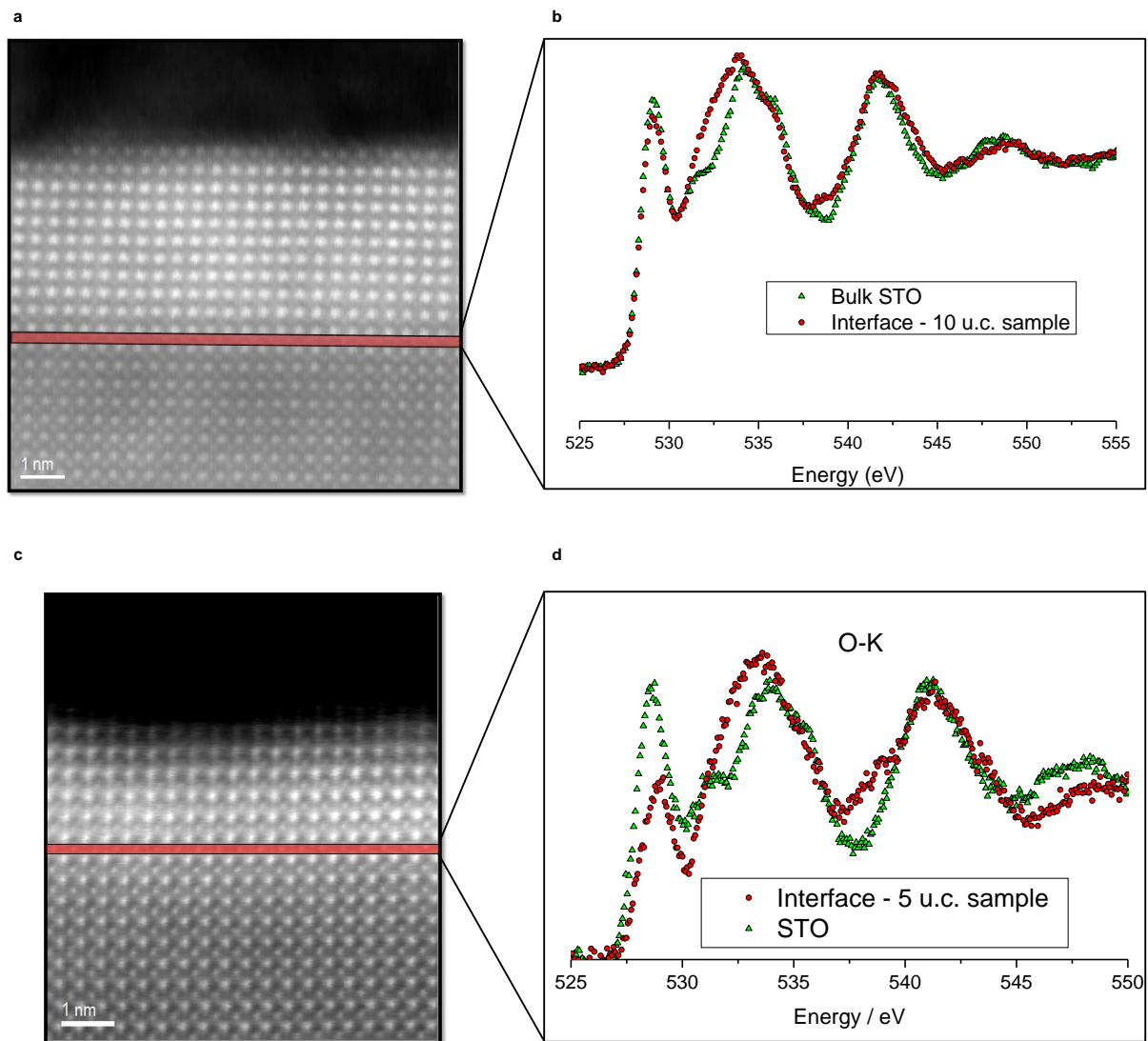


Figure IV.4 | Experimental EELS fine structure of the O-K absorption edge across samples with increasing thicknesses. a-c, HAADF image of the region of interest probed to measure the O-K EELS spectrum at the interface of (a) *UC10* (c) *UC5*. b-d, EELS spectrum at the interface (red dots) and within the STO bulk (green triangles) of the sample (b) *UC10* (d) *UC5*.

Sample	Film thickness	$V_{\text{O}}^{\ddot{}}$ in STO bulk	$V_{\text{O}}^{\ddot{}}$ at interface
UC3	3 u.c.	< detection limit	< detection limit
UC5	5 u.c.	< detection limit	< detection limit
UC10	10 u.c.	< detection limit	< detection limit

Table IV.4 | Oxygen vacancies for samples of increasing film thicknesses.

IV.1.4 Intermixing

The variations of the EELS O-K pre-peak, unit cell by unit cell (Figure IV.5a) was used to determine the extension of titanium within the LAO film, and qualitative diffusion profiles for Ti and La were derived from the area under Ti-L_{2,3} and La-M_{4,5} post edges at each unit cell (Figure IV.5b). The O EELS pre-peak remains clearly visible up to 5/6 u.c. within the LAO film of the sample *UC10*, which is confirmed by the Ti profile. Assuming a full occupancy of B-sites, Al would diffuse down to 3/4 u.c. into the substrate to compensate the decrease of the Ti signal (Figure IV.5b). Concerning A-site cations, La atoms diffused down to about 4/5 u.c. within the substrate.

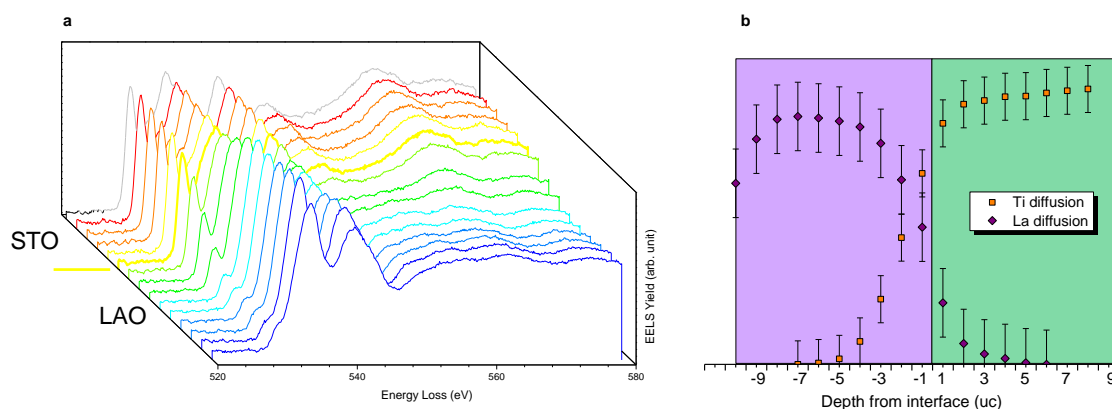


Figure IV.5 | Intermixing profile of the sample *UC10*. **a**, Spatial distribution of the EELS O-K absorption edges unit cell by unit cell. The spectrum measured at the interface is marked in bold yellow spectrum. **b**, Diffusion profiles of Ti and La from EELS analyses. The x coordinates locate the cations by the number of unit cells to the interface (+ 1 = first u.c. in STO, - 1 = first u.c. in LAO...). The decreasing of La profiles close to the film surface must be due to the reduction of the TEM sample thickness.

Figure IV.6 displays the MEIS spectra of the 10 u.c. sample in random mode for a scattering angle of 126.5°. This sample was the first one that was analyzed by MEIS during this thesis. The interface was located deeper from the surface compared those of the 3 and 5 u.c. samples. The accuracy of the measurements was lowered by the straggling of He⁺ when probing deeper parts. Moreover in this first analysis, the sample orientation was not optimized to fully avoid channeling. We still plot the La/(La+Sr) profile obtained from the simulation of the spectrum in Figure IV.6b with a higher error bar. La is seen down to 4 u.c. in the substrate, likewise Sr is found up to 4 u.c. within the film.

Ti atoms spread to similar extent between the sample *UC5* and *UC10*, according to the EELS results. Moreover, La atoms were found at similar depth, and with the same concentration, into the substrate of the two conductive samples, according to the MEIS results. However, Sr diffused less deeply within the film of the sample *UC10*, and to a lower amount. The trend of higher diffusion lengths for thicker films seen for the 3 u.c. and 5 u.c. is not valid for this 10 u.c.-thick film.

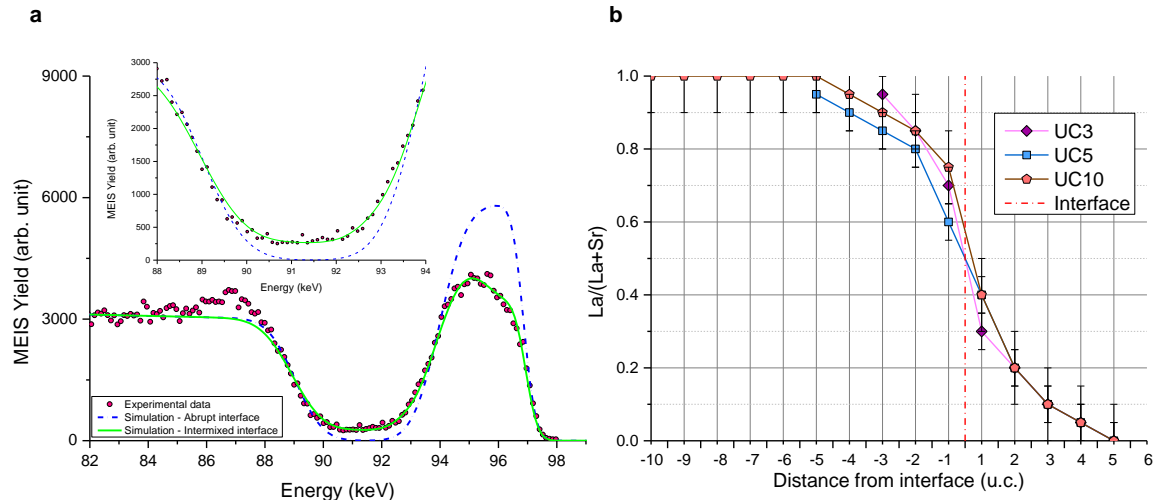


Figure IV.6 | MEIS chemical profile of the sample UC10. **a**, Random MEIS experimental and simulated spectra with a backscattering angle of 126.5° . The experimental data are represented by red circles, the simulated spectra corresponding to the same system without intermixing by blue curve, and the simulated spectra fitting the experimental data by green curve. **b**, La/(La+Sr) profile throughout the first atomic layers obtained from the MEIS chemical measurements and comparing the samples UC3 (purple diamond) UC5 (blue square) and UC10 (red pentagon). The x coordinates locate the cations by the number of unit cells to the interface (+ 1 = first u.c. in STO, - 1 = first u.c. in LAO...).

Sample	Film thickness	La diffusion (EELS)	Ti diffusion (EELS)	Al diffusion (EELS)	La diffusion (MEIS)	Sr diffusion (MEIS)
UC3	3 u.c.	5 u.c.	3 u.c.	3/4 u.c.	4/5 u.c.	3 u.c.
UC5	5 u.c.	6/7 u.c.	5 u.c.	4/5 u.c.	4/5 u.c.	5 u.c.
UC10	10 u.c.	4/5 u.c.	5/6 u.c.	3/4 u.c.	4/5 u.c.	4/5 u.c.

Table IV.5 | Intermixing for samples of increasing film thicknesses.

IV.1.5 Thickness effect: Discussion

The experimental EELS and MEIS profiles across the 10 u.c.-thick film interface combined with the measured Ti valence were used to draw a theoretical electrostatic potential for this sample (Figure IV.7). The larger number of polar unit cells deposited increased significantly the electrostatic potential. The valence band of LAO is expected to cross the conduction band of STO. However the Ti valence decreased only slightly compared to the 5 u.c. system. The transfer of electrons from the film surface to the interface by band bending was not significantly favored indicating that the polar field was weaker than what is predicted. As for the samples UC3 and UC5, buckling is expected to have produced a counter dipole.

The small increase in the density of carriers compared to the 5 u.c sample cannot not be explained by a higher concentration of La on Sr sites since intermixing at interface is close in the two configurations. The electrons are more likely provided by donor defects at the film surface. Amongst these defects, oxygen vacancies have a formation energy that decreases when the film thickness increases, as described in the discussion of Chapter III. The contribution of these defects to the electron reconstruction is enhanced in the 10 u.c. film compared to the thinner 5 u.c. one. Owing to

the lack of reference spectra for oxygen-deficient LAO, the oxygen vacancies could not be asserted by the EELS measurements of the O-K absorption edge at the surface of the sample *UC10*.

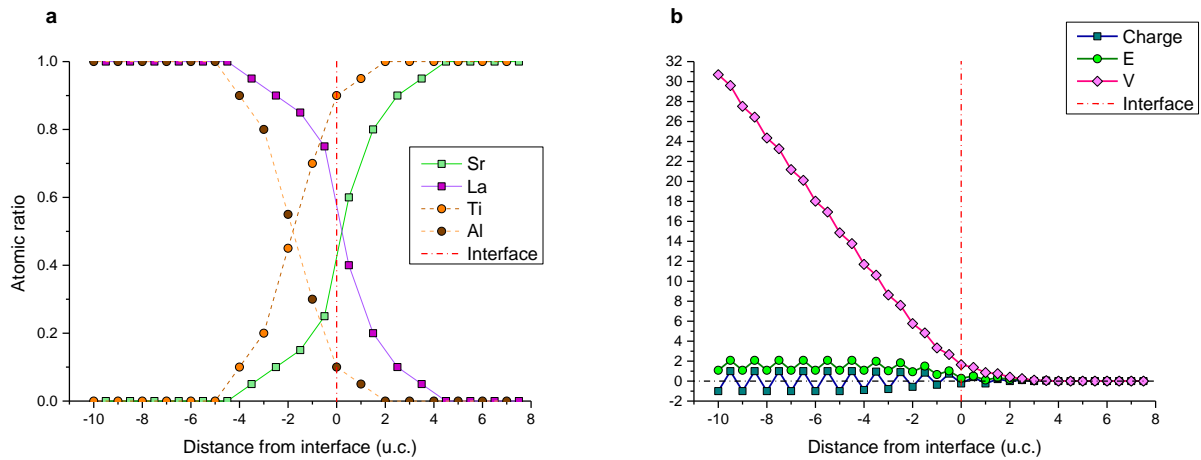


Figure IV.7 | Theoretical electrostatic potential exhibited by *UC10* according to the EELS and MEIS experimental results. **a**, Atomic distribution determined from Figure IV.5b and Figure IV.6b. **b**, Electrostatic potential V evolution throughout the sample. The potential divergence is more pronounced in this system than for an abrupt interface. In order to limit this divergence and to bring nearer the potential V to 0, we need to provide acceptor dopants.

The lower conductivity of the thicker film/substrate assembly despite a smaller valence of their Ti reveals a lower mobility of the electrons transferred. Huang *et al.* [4] explained the suppression of carrier mobility they observed for thicker samples by defects introduced to relax the stress. The strain analysis we have carried out by MEIS in blocking mode for thinner samples was not achieved for this 10 u.c.-thick film, as its reliability would have been reduced by the stronger straggling in the deeper interface region. Without experimental evidences of the deformation, some insight can be given from the HRTEM observation of the film/substrate interface. Despite a higher elastic energy stored in this thicker film, no relaxation by misfit dislocations occurred that could explain the lower mobility. The elastic strains are similar. The discrepancy between the theoretical electrostatic potential calculated (Figure IV.7b) and the observed charge carrier density indicates that the polar field was partially cancelled by other mechanisms than the electron reconstruction. Structural distortions inducing counter dipoles in the film have been mentioned. In addition strontium vacancies in the sub-interface region of the substrate are expected since they are favored to compensate the electronic disequilibrium at such growth conditions [5]. They could be responsible for a lower charge mobility and conductivity measured.

With these growth conditions, structural distortions seem to be the main mechanism controlling the conduction of the LAO/STO heterostructure above the critical thickness. Hence, in this configuration, film thicknesses just above the conduction threshold must be favored to optimize the performances of the heterostructure.

IV.2 Effect of Oxygen Partial Pressure during film growth

The strong p_{O_2} dependence of the heterostructures behavior has been emphasized in Chapter II. In this section we will investigate the influence of this growth parameter with five samples, separated into two categories. The first set consists in three samples with 10 u.c.-thick films deposited at 10^{-4} Torr (*UC10P4#2T7*, or ***UC10P4***), 10^{-5} Torr (*UC10P5#2T7*, or ***UC10P5***), 10^{-6} Torr (*UC10P6#2T7*, or ***UC10P6***) and prepared for TEM analyses, while the second set comprises two thinner samples (i.e. 5 u.c.) deposited at 10^{-4} Torr (*UC5P4#2T7*, or ***UC5P4***), 10^{-5} Torr (*UC5P5#2T7*, or ***UC5P5***), and devoted to MEIS investigations.

IV.2.1 Film growth

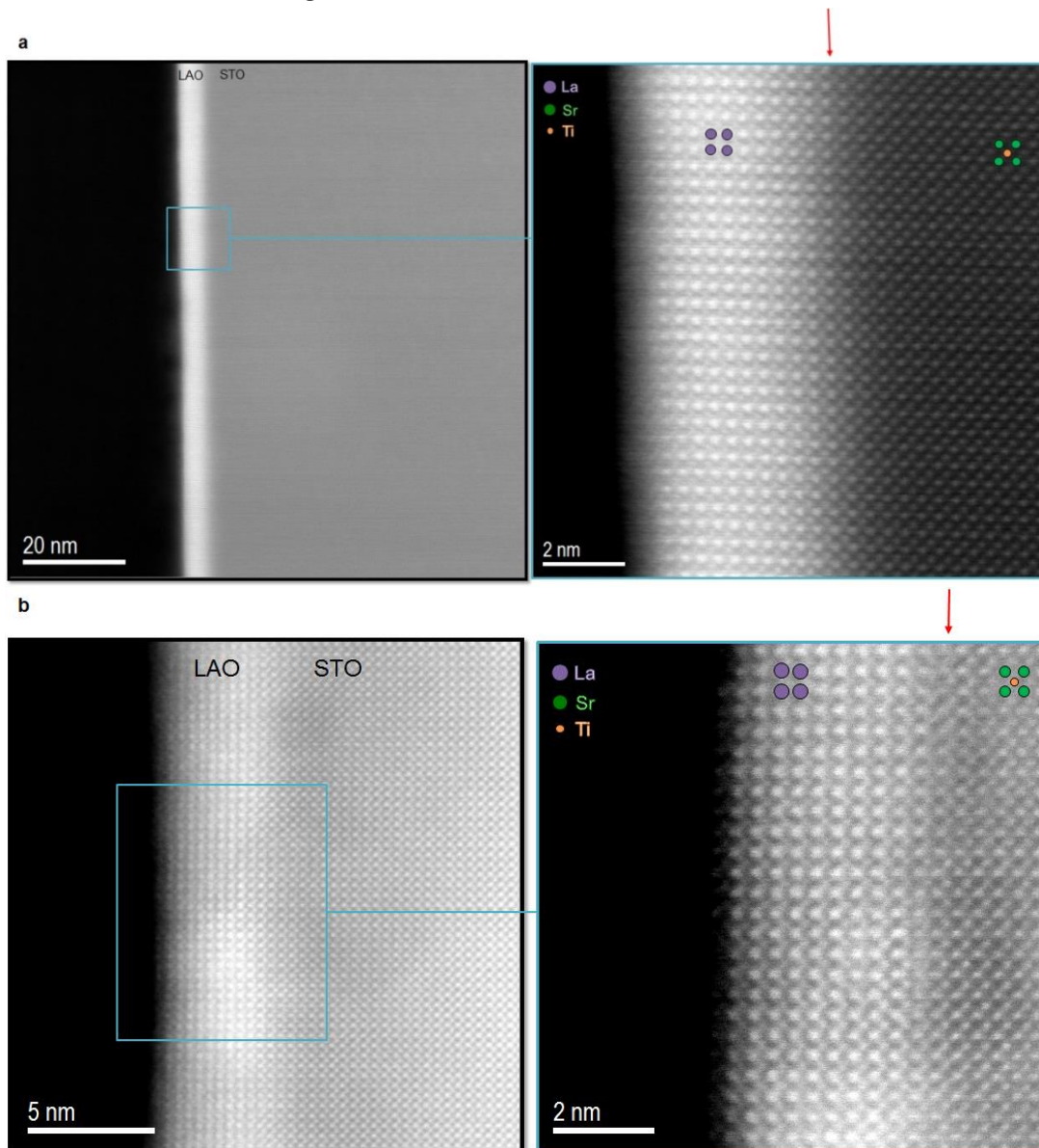


Figure IV.8 | Representative HAADF images of LaAlO_3 films grown pseudomorphically on SrTiO_3 under lower oxygen partial pressure. The interface is shown by a red arrow, La (Sr) {Ti} atoms are illustrated by purple (green) {orange} circles. No misfit dislocations could be detected at LAO/STO interfaces along the entire distance observed via Nion UltraSTEM. **a**, USTEM pictures representing the sample *UC10P5*. **b**, USTEM pictures representing the sample *UC10P6*.

Chapter IV | Dependence to growth conditions

The films with a thickness of 10 u.c. deposited at 10^{-5} (*UC10P5*) and 10^{-6} Torr (*UC10P6*) exhibit pseudomorphic growths with in-plane lattice parameters of the film fitting the substrate ones (Figure IV.8), similarly to what was previously described for the sample *UC10P4* (Figure III.1 and Figure III.2). No defects have been detected on the USTEM Nion pictures, and the film thicknesses reach the 10 u.c. targeted by our collaborators. The lowering of the oxygen pressure did not alter the quality of the epitaxial growth.

IV.2.2 Electrical Measurements

Figure IV.9 presents the electrical properties of the three 10 u.c.-thick film/substrate assemblies grown at decreasing oxygen partial pressure.

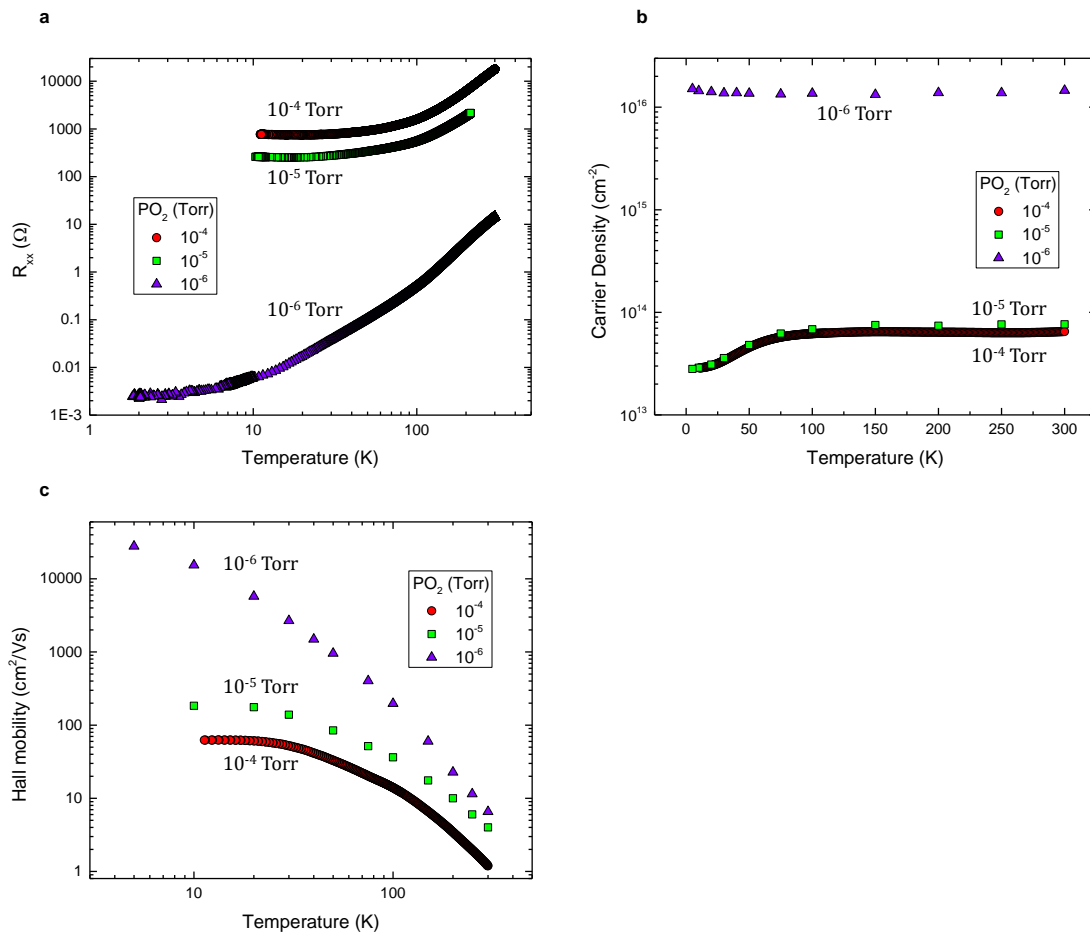


Figure IV.9 | Transport properties of the samples *UC10P4*, *UC10P5* and *UC10P6*. Evolution of (a) sheet resistance, (b) carrier density, (c) Hall mobility, as a function of temperature. The lower is the oxygen pressure, the higher are the carrier density and mobility. Transport properties are improved by decreasing the oxygen pressure during the growth of the films. This decrease in the sheet resistance and increase of carrier density is even more pronounced going from 10^{-5} to 10^{-6} Torr.

Sample	Oxygen growth pressure	Sheet resistance (RT)	Carrier density (RT)	Carrier mobility (RT)
<i>UC10P4</i>	10^{-4} Torr	$\sim 8 \times 10^4 \Omega/\square$	$\sim 6.5 \times 10^{13} \text{ cm}^{-2}$	$\sim 1.3 \text{ cm}^2/\text{Vs}$
<i>UC10P5</i>	10^{-5} Torr	$\sim 2 \times 10^3 \Omega/\square$	$\sim 7.9 \times 10^{13} \text{ cm}^{-2}$	$\sim 4 \text{ cm}^2/\text{Vs}$
<i>UC10P6</i>	10^{-6} Torr	$\sim 15 \Omega/\square$	$\sim 1.5 \times 10^{16} \text{ cm}^{-2}$	$\sim 6.9 \text{ cm}^2/\text{Vs}$

Table IV.6 | Electrical measurements for samples varying by their oxygen growth pressures.

IV.2.3 Ti^{3+} Contribution

The EELS $Ti-L_{2,3}$ absorption edges recorded at the interface of the two samples (i.e. *UC10P5* and *UC10P6*) are displayed in Figure IV.10, while the EELS measurements of the sample *UC10P4* was already presented in Figure IV.2. To fit the spectra, the reference Ti^{4+} spectrum was obtained from deep part of STO of *UC10P4*, since STO in the sample *UC10P5* or *UC10P6* could have been partially reduced during the film growth at lower oxygen growth pressure.

Owing to differences in the thicknesses of the TEM thin foils for the reference spectra and the spectra to be fitted [6,7], the L_2 and L_3 post edges could not be fitted together. We first chose to fit the L_3 post edges to minimize issues due to plural scatterings (Figure IV.10b and Figure IV.10e). It can be seen that the t_{2g} peak of the L_3 post edge could hardly be fitted properly (Figure IV.10b). We have then considered that the L_2 post edge was more discriminating to evaluate the Ti^{3+} contribution on the experimental EELS spectra (Figure IV.10c and Figure IV.10f).

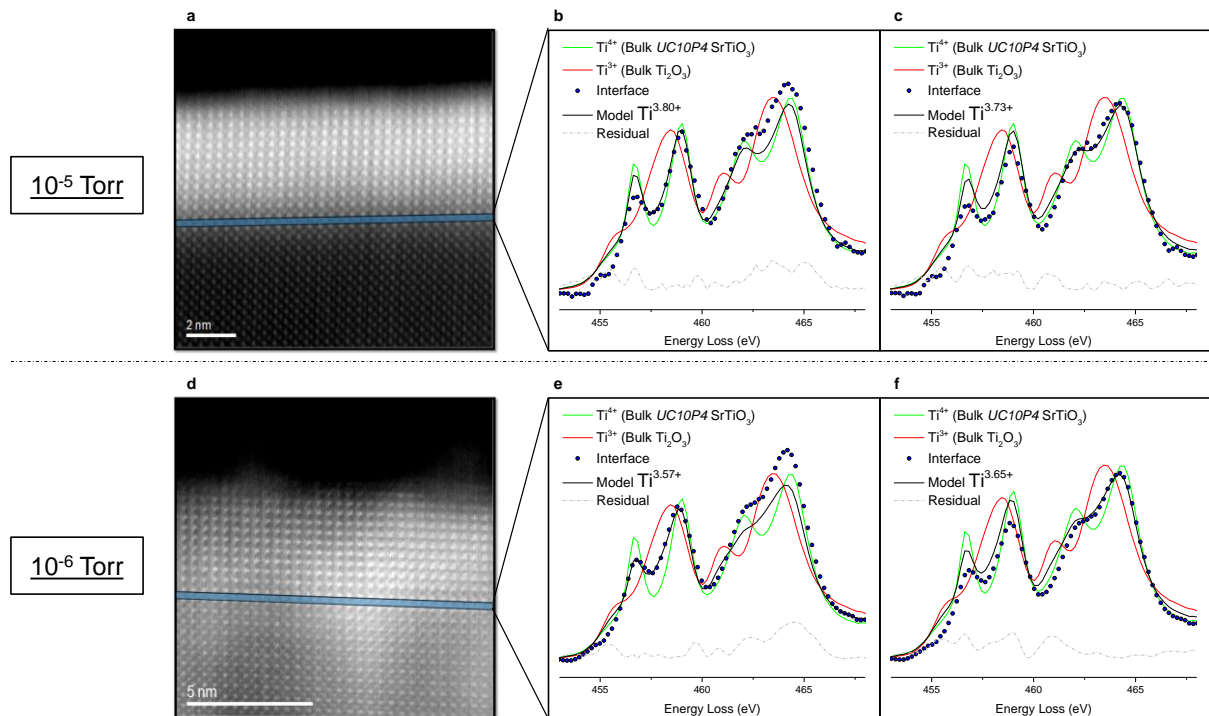


Figure IV.10 | $Ti-L_{2,3}$ edge EELS taken at the $LaAlO_3/SrTiO_3$ interface under lower oxygen partial pressure. a-d, HAADF image of the region of interest probed to measure the Ti EELS spectrum at the interface of (a) *UC10P5* (d) *UC10P6*. **b-c**, EELS spectrum at the interface of the sample *UC10P5* fitted on the (b) L_3 (c) L_2 peak. **e-f**, EELS spectrum at the interface of the sample *UC10P6* fitted on the (e) L_3 (f) L_2 peak. The color code is given in Figure III.4.

With this fitting protocol, the Ti oxidation state at the interface was evaluated and the data obtained are summarized in Table IV.7. Hence, whatever the post edges favored for fitting the experimental EELS spectrum, the Ti oxidation state is clearly reduced at lower oxygen pressure. Hall Effect measurements gave a lower charge carrier density for the sample *UC10P5* compared to what is measured from EELS. The carriers must be localized as it was proposed for the sample deposited at higher pressure (i.e. *UC10P4*). The opposite is seen for *UC10P6* with electrical measurements

Chapter IV | Dependence to growth conditions

indicating a carrier density two orders of magnitude higher than what is calculated with EELS at the interface. This would imply a 3D conduction in STO.

Sample	Oxygen pressure	Ti valence interface (EELS Ti-L ₃)	Ti valence interface (EELS Ti-L ₂)	Carrier density (EELS Ti-L ₃) (+/- 3.28x10 ¹³) cm ⁻²	Carrier density (EELS Ti-L ₂) (+/- 3.28x10 ¹³) cm ⁻²
UC10P4	10 ⁻⁴ Torr	Ti ^{3.85+} (+/-0.05)		6.6x10 ¹³ cm ⁻²	
UC10P5	10 ⁻⁵ Torr	Ti ^{3.80+} (+/-0.05)	Ti ^{3.73+} (+/-0.05)	1.31x10 ¹⁴ cm ⁻²	1.77x10 ¹⁴ cm ⁻²
UC10P6	10 ⁻⁶ Torr	Ti ^{3.57+} (+/-0.05)	Ti ^{3.65+} (+/-0.05)	2.82x10 ¹⁴ cm ⁻²	2.30x10 ¹⁴ cm ⁻²

Table IV.7 | Ti oxidation state for samples varying by their oxygen growth pressures.

IV.2.4 Oxygen vacancies

We will first analyze the consequence of a lower oxygen partial pressure on the oxygen stoichiometry within the substrate. Fingerprints of oxygen vacancies are clearly visible in the sample *UC10P6* grown at the lowest oxygen pressure (Figure IV.11a). Most of the features detailed by Muller *et al.* [8] for a SrTiO_{3-δ} (with δ ≈ 0.13) are recognized: the B peak is higher and broader compared to that of the A peak and the valley between the peaks C and D is shallower. Concerning the sample *UC10P5*, only a slight broadening of the B peak is noticed compared to *UC10P4*. It was reported by Gariglio *et al.* [9] that the oxygen partial pressure of about 10⁻⁵ Torr represents a limit for promoting these intrinsic defects.

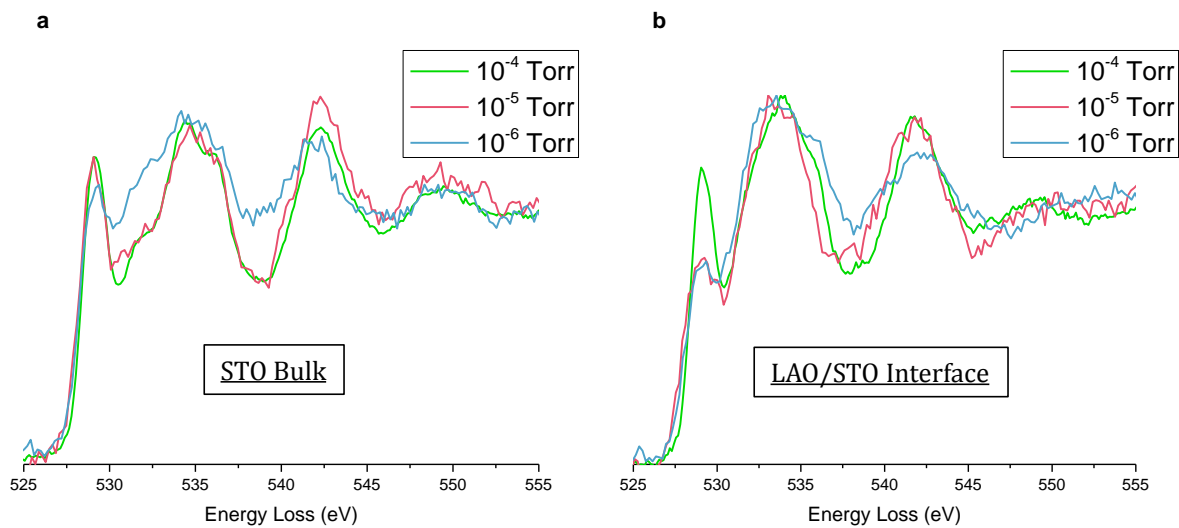


Figure IV.11 | Experimental EELS fine structure of the O-K absorption edge across the samples varying by their oxygen growth pressure. a, O-K EELS spectra within the STO bulk. The green (red) {blue} spectrum corresponds to the sample *UC10P4* (*UC10P5*) {*UC10P6*}. **b,** O-K EELS spectra at the interface. The green (red) {blue} spectrum corresponds to the sample *UC10P4* (*UC10P5*) {*UC10P6*}.

The O-K absorption edges at the LaO/TiO₂ interface of the three samples differing by their p_{O_2} are shown in Figure IV.11b. The main changes are seen on the peak A which decreases significantly for *UC10P5* and *UC10P6*, as well as on the peak C that shifts towards the lower energies. We will see later that intermixing is mainly responsible for these modifications. However a contribution of Ti³⁺ is not excluded for *UC10P6*. A shallower valley between the C and D peaks is noticed for *UC10P6* interface than for the two others at the interface. But, compared to the *UC10P6* substrate this valley is deeper. Knowing that both intermixing and oxygen vacancies compete to lift the valley, and that

intermixing will be revealed, this deeper valley attests a lower concentration of $V_{\text{O}}^{\bullet\bullet}$ at *UC10P6* interface. Concerning the sample *UC10P5*, the shallower valley at the interface compared to the bulk cannot be assigned specifically to $V_{\text{O}}^{\bullet\bullet}$ or intermixing.

Finally, we have measured the EELS O-K spectra at the top film surface of each sample (Figure IV.12). We observe significant differences between the three EELS spectra. The valleys between the two first O-K peaks are less marked for samples grown at lower O pressure. The environment of surface O anions is strongly modified by the growth pressure. To our knowledge, no O-K EELS spectra are referenced for $\text{LaAlO}_{3-\delta}$. If oxygen vacancies are likely to contribute to the observed changes, the local crystal disorder at the film surface observed on the thin foils may be also responsible for O-K post edge modifications.

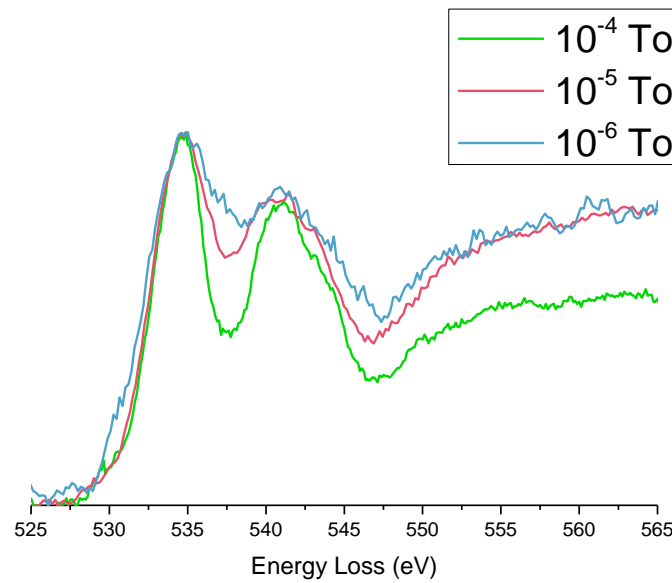


Figure IV.12 | Experimental EELS fine structure of the O-K absorption edge within the LAO film of the samples varying by their oxygen growth pressure.

Sample	Oxygen pressure	$V_{\text{O}}^{\bullet\bullet}$ in STO bulk	$V_{\text{O}}^{\bullet\bullet}$ at interface	$V_{\text{O}}^{\bullet\bullet}$ at film surface
<i>UC10P4</i>	10^{-4} Torr.	< detection limit	< detection limit	< detection limit
<i>UC10P5</i>	10^{-5} Torr.	< detection limit	< detection limit	Low concentration
<i>UC10P6</i>	10^{-6} Torr.	High concentration	Medium concentration	High concentration

Table IV.8 | Oxygen vacancies for samples varying by their oxygen growth pressures. Each column is independent and the qualitative from one column cannot be compared with the others.

IV.2.5 Intermixing

IV.2.5.1 EELS investigations

The diffusion length of Ti in the film and La in the substrate for *UC10P5* and *UC10P6* investigated using the O-K, Ti-L_{2,3} and La-M_{4,5} absorption edges (Figure IV.13) are summarized in Table IV.9. The lowering of the oxygen partial pressure has favored the cationic exchanges. Interestingly, the

Chapter IV | Dependence to growth conditions

extension of the A-sites cations is, if not similar, very close to the diffusion length of B-sites cations, as it was found in the 10 u.c. sample grown at the highest O pressure (i.e. *UC10P4*). At most, the A cations would diffuse one unit cell deeper, which would minimize the impact of the donor doping.

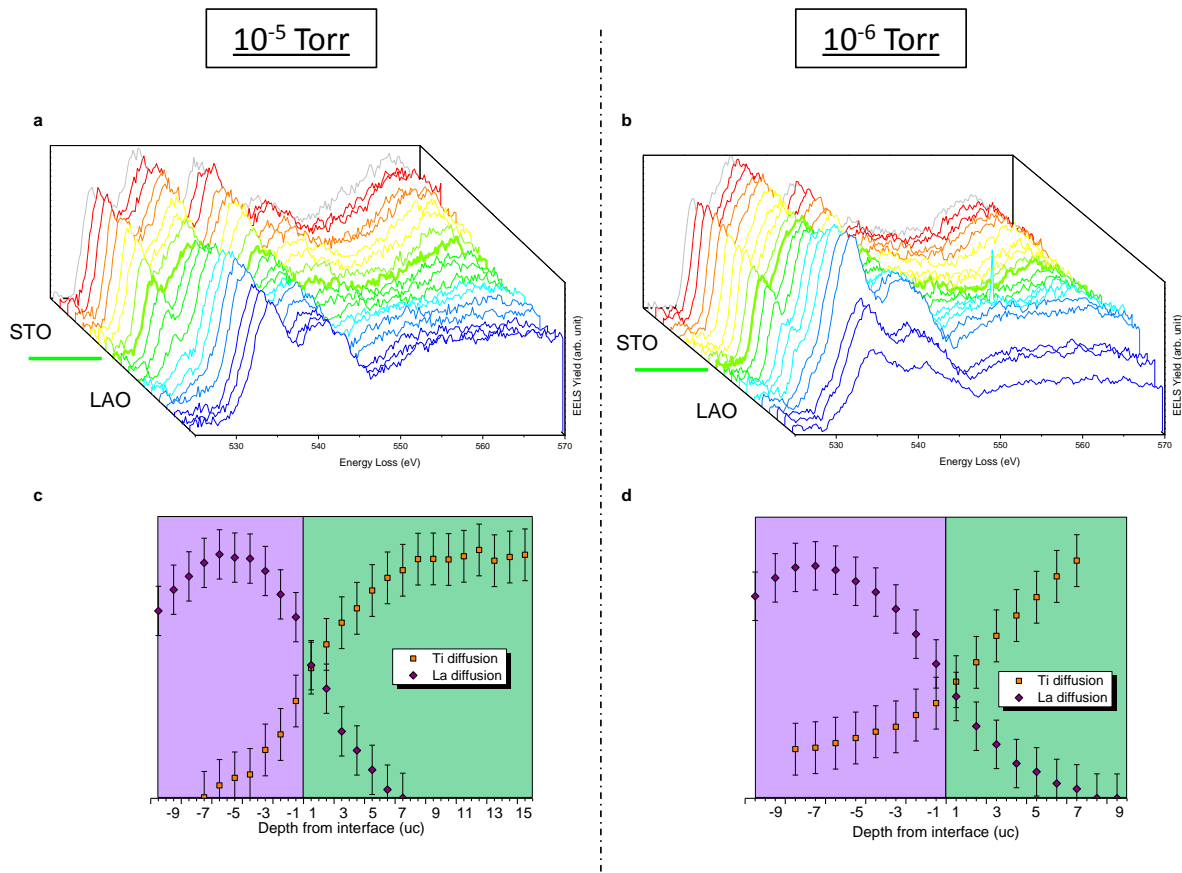


Figure IV.13 | Intermixing profiles of the samples *UC10P5* and *UC10P6* through EELS measurements. a-b, Spatial distribution of the EELS O-K absorption edges unit cell by unit cell within the sample (a) *UC10P5* (b) *UC10P6*. The spectrum measured at the interface is marked by in bold green. c-d, Diffusion profiles of Ti and La from EELS analyses within the sample (c) *UC10P5* (d) *UC10P6*. The x coordinates locate the cations by the number of unit cells to the interface (+ 1 = first u.c. in STO, - 1 = first u.c. in LAO...). The decreasing of La profiles close to the film surface must be due to a reduction of the thickness at the edge of the thin foil.

IV.2.5.2 MEIS investigations

A quantification of the La \leftrightarrow Sr intermixing at lower partial pressure of oxygen has been achieved from MEIS spectrum recorded in random mode on a thinner sample (5 u.c.) grown at 10⁻⁵ Torr (i.e. *UC5P5*). Figure IV.14a presents the experimental MEIS spectrum with red dots. The blue curve displays the simulated spectrum for an abrupt interface that clearly does not fit the experimental curve.

The ratio $x = \text{La}/(\text{La} + \text{Sr})$ allowing the best fit of the experimental spectrum is plotted with green circles in Figure IV.14b, and put into perspective with the results obtained earlier for the sample *UC5P4* drawn with blue squares. In the substrate, the diffusion length of La is 3 u.c. deeper than for *UC5P4* (i.e. 7 u.c. vs 4 u.c.) and the La concentration is higher at any depth. The cumulative number of La atoms in a 1 u.c. width column inside the substrate reaches 2.1 in *UC5P5* against 0.75 for

UC5P4. Strontium was detected up to the film surface of the sample *UC5P5* with a cumulative concentration of about one atom in a pile up of 5 u.c. which is larger than value of 0.9 Sr measured for the sample *UC5P4*. The profile of Figure IV.14b is not symmetric with respect to the interface plane : in a column of 1 u.c. width the cumulative La number inside the substrate (2.1 La) is larger than Sr in the film (1 Sr), suggesting more strontium vacancies in the substrate of *UC5P5* available to welcome La atoms. This activated diffusion can also be at the origin of the higher La concentration 1 u.c. above the interface in the sample grown at lower O pressure.

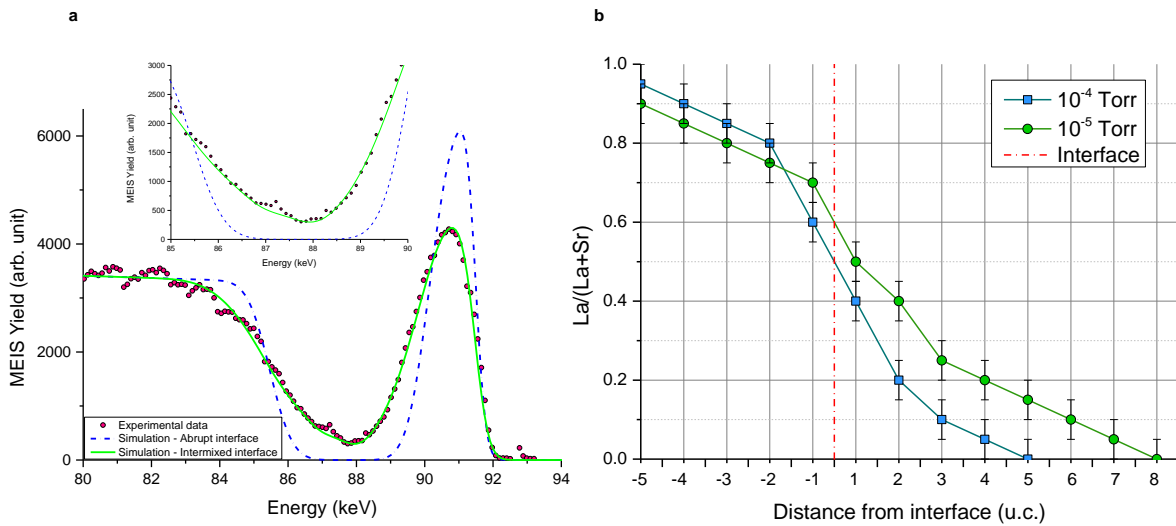


Figure IV.14 | MEIS chemical profile of the sample *UC5P5* grown at 10^{-5} Torr. **a**, Random MEIS experimental and simulated spectra with a backscattering angle of $124,9^\circ$. The experimental data are represented by red circles, the simulated spectra corresponding to the same system without intermixing by blue curve, and the simulated spectra fitting the experimental data by green curve. **b**, La/(La+Sr) profile throughout the first atomic layers obtained from the MEIS chemical measurements and comparing the samples *UC5P4* (blue square) and *UC5P5* (green circle). The x coordinates locate the cations by the number of unit cells to the interface (+ 1 = first u.c. in STO, - 1 = first u.c. in LAO...).

Sample	Oxygen pressure	La diffusion (EELS)	Ti diffusion (EELS)	La diffusion (MEIS)	Sr diffusion (MEIS)
<i>UC10P4</i>	10^{-4} Torr	5/6 u.c.	5/6 u.c.	n.a.	n.a.
<i>UC10P5</i>	10^{-5} Torr	7 u.c.	7 u.c.	n.a.	n.a.
<i>UC10P6</i>	10^{-6} Torr	8/9 u.c.	8/9 u.c.	n.a.	n.a.
<i>UC5P4</i>	10^{-4} Torr	6/7 u.c.	5 u.c.	4/5 u.c.	5 u.c.
<i>UC5P5</i>	10^{-5} Torr	n.a.	n.a.	7/8 u.c.	5 u.c.

Table IV.9 | Intermixing for samples varying by their oxygen growth pressures.

IV.2.6 Structural distortions

IV.2.6.1 Strain Profiles

The MEIS technique in blocking mode was also used on the sample *UC5P5* in order to investigate the structural distortions dependence on the growth oxygen pressure. The sample was oriented to promote blocking of the He^+ particles in their way out in the [101] direction. The analyzer was tuned

Chapter IV | Dependence to growth conditions

to measure only the energy of the particles scattered by La and Sr. Figure IV.15 exhibits the corresponding blocking dip patterns from which the c/a profile was derived.

The MEIS blocking curves could be plotted down to a depth of 13 u.c. (5 u.c. film + 8 u.c. substrate) within the sample *UC5P5* for Sr scattering centers and only down to 7 u.c. for La scattering centers. The lower concentration of La added to a higher signal-to-noise ratio in deeper layers strongly reduced the measurement accuracy of the maximum blocking (minimum of intensity) positions.

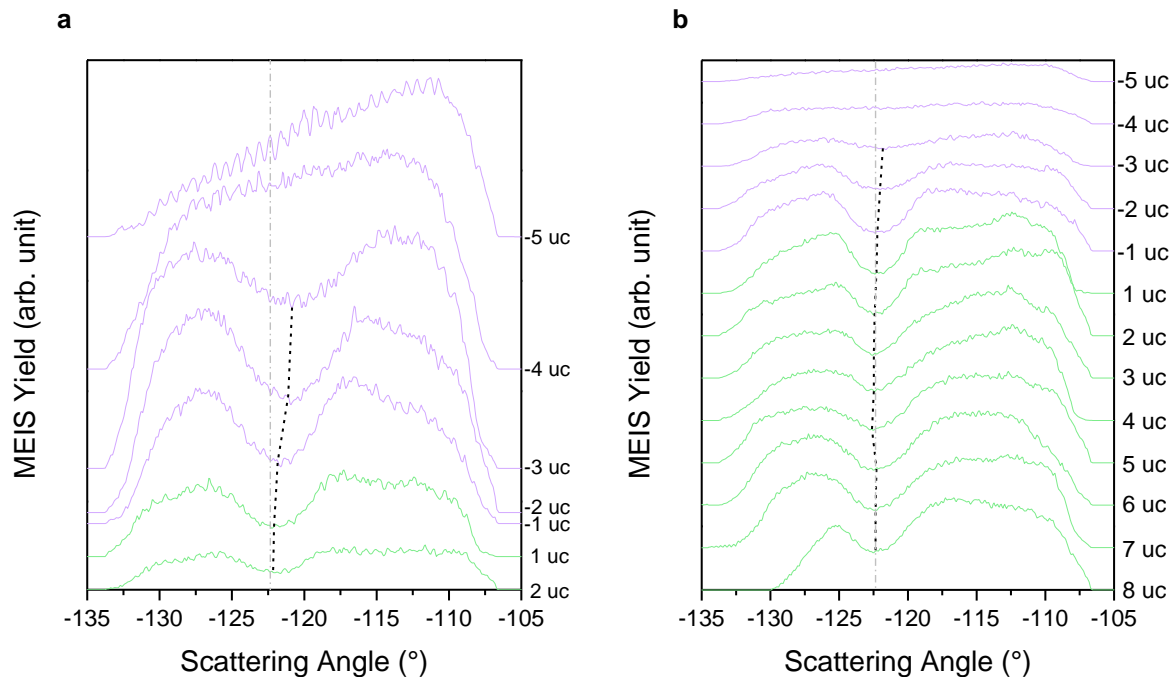


Figure IV.15| MEIS data in blocking mode obtained for the sample *UC5P5*. **a**, MEIS [101] blocking dips as a function of depth corresponding to La scattering centers located in the film (purple curves) and in the substrate (green curves). **b**, MEIS [101] blocking dips as a function of depth corresponding to Sr scattering centers located in the film (purple curves) and in the substrate (green curves). Dash-dotted grey lines are the position of the blocking dips for an unstrained cubic STO ($c/a = 1$). Dashed black lines indicate the position of the blocking dips maxima for each unit cell. In the substrate, deviations of these positions from the dash-dotted line reveal structural distortions.

The blocking angle of the deepest probed layer, 8 u.c. below the interface, was taken as the reference blocking angle for a cubic cell ($c/a=1$). One could object that the substrate might not be cubic at this depth as it corresponds to the first u.c. with no La detected (Figure IV.14b). The energy range chosen for this experiment did not permit to probe deeper parts of the substrate that would have been more appropriate for an unstrained reference. We will make the assumption that the low concentration of La in the upper layer affects only weakly the mean A-A distance at this depth. We also remember that the the substrate of *UC5P5* encloses a low concentration of oxygen vacancies that could impact the c/a ratio. However we have seen earlier that the deformation induced by oxygen vacancies can be neglected [10–14]. Therefore we can take the reference blocking angle at 8 u.c. keeping in mind that a small vertical translation of the curve is not excluded.

The c/a strain profile of the sample *UC5P5* is plotted in Figure IV.16a, and can be divided in three regions as it was done for the samples *UC3* and *UC5P4* in the previous chapter. An unstrained region

($c/a \approx 1$) seen from the deepest probed region to 6 u.c. below the interface. Then in-plane compressive strains ($c/a > 1$) develop over a length of 4 u.c., with a maximum at 5 u.c. under the interface.

The theoretical epitaxial strain is calculated from an elastic model taking into account the intermixing profile of Figure IV.14b for determining the unstrained cell dimensions, as was detailed in Chapter III (section III.5.1). The corresponding data are plotted with red squares in Figure IV.16a. Once again, the c/a measured experimentally are larger than those induced by epitaxial strain, revealing others contributions to the structural distortions, and specifically to the expansion of the cell. Figure IV.16c transcribed the differences between these two components of the strain.

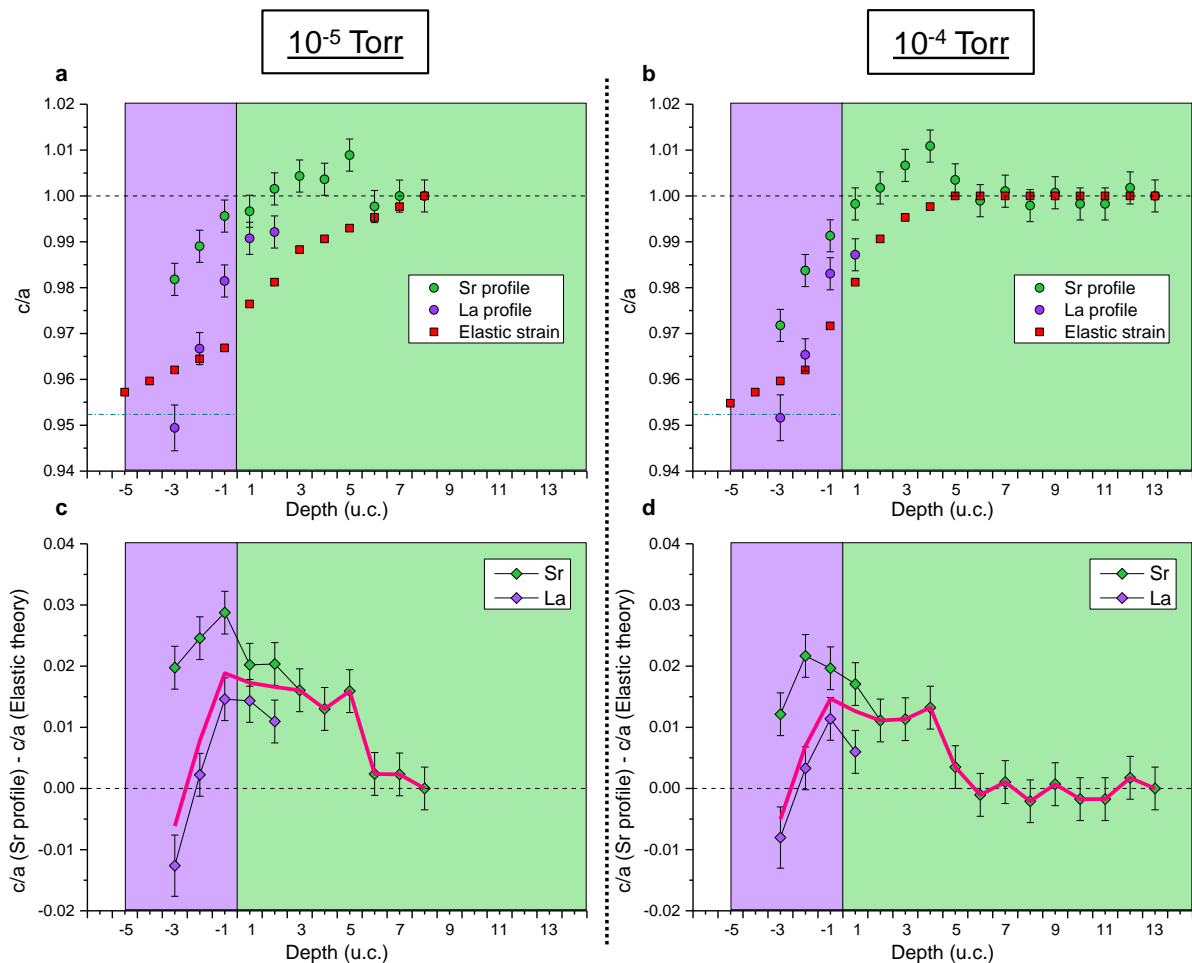


Figure IV.16 | MEIS strain profiles for samples varying by their oxygen growth pressure. The x coordinates locate the cations by the number of unit cells to the interface (+ 1 = first u.c. in STO, - 1 = first u.c. in LAO...). Each data point indicates the distance separating this cation to the A cation located in the above cell. **a–b**, Profiles of c/a for samples grown at **(a)** 10^{-5} Torr **(b)** 10^{-4} Torr. The color code is available in Figure III.15. **c–d**, Difference between the c/a values measured experimentally - from He^+ scattered on Sr and La atoms - and those calculated from epitaxial strain are plotted for the sample **(c)** UC5P5 **(d)** UC5P4. The pink curve represents the weighted average of the profiles. Figure IV.16b and Figure IV.16d duplicate Figure III.15b and III.15d for an easier comparison between UC5P5 and UC5P4.

Chapter IV | Dependence to growth conditions

Interestingly, the strain profile of the sample *UC5P5* is quite similar to that of *UC5P4* grown at 10^{-4} Torr (Figure IV.16b), in term of localisation of the three regions previously described. However, the strain levels are higher at lower partial pressure with an area under the curve twice that found for *UC5P4*.

IV.2.6.2 Buckling profiles

The angular FWHM of the blocking dips experimentally extracted were measured for each unit cell of the sample *UC5P5* (Figure IV.17a) as an indicator of the buckling occurring within the structure (widening of the shadow cone) or to in-plane compression (thinning of the shadow cone). The blocking width for non-buckled STO was assumed to be the same as the one determined for the sample *UC5P4* (Figure IV.17b) (thermal vibrations are equal and buckling from V_O^{\bullet} is neglected). Three areas are once again distinguishable with no variation of the blocking width into the STO deep substrate, followed by a thinning of the blocking dip with a minimum width at 3 u.c. under the interface, and finally the blocking dip becomes wider in the film up to the sample surface. The region with thinner blocking dips is shallower in *UC5P5* (down to 3/4 u.c.) than in *UC5P4* (down to 6/7 u.c.), and the thinning in this region is also less marked for *UC5P5*. This seems in contradiction with the higher strain level measured for *UC5P5* that should accentuate the thinning of the shadow cones. We interpret this relative widening of the cones in this strained region by the higher concentration of La which increases the probability of particles scattered by Sr to be blocked by La atoms. The shadow cone produced by La is intrinsically wider (Figure II.45c) and the buckling around hosted atoms also contributes to this widening.

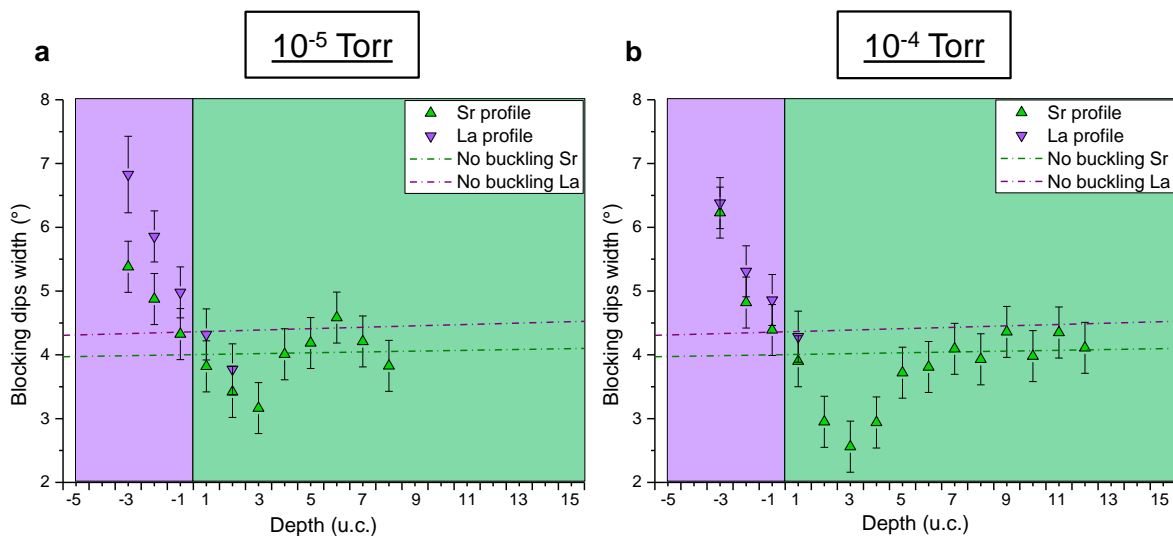


Figure IV.17 | Width variations of the blocking dips as a function of depth. **a**, Experimental profile of the sample *UC5P5*. **b**, Experimental profile of the sample *UC5P4*. The color code is available in Figure III.16.

IV.2.6.3 Ferroelectric-like distortions

The ferroelectric-like distortions also play a role in the expansion of the c-lattice. It was clearly evidenced for the sample *UC10P6* grown at 10^{-6} Torr (Figure IV.18). The Ti atoms are pushed toward the film surface in a region extending at least 3 u.c below and above the interface (Figure IV.18b). Unfortunately, the quality of the HAADF pictures taken for the sample *UC10P5* grown at 10^{-5} Torr did not permit to follow the displacements of Ti atoms.

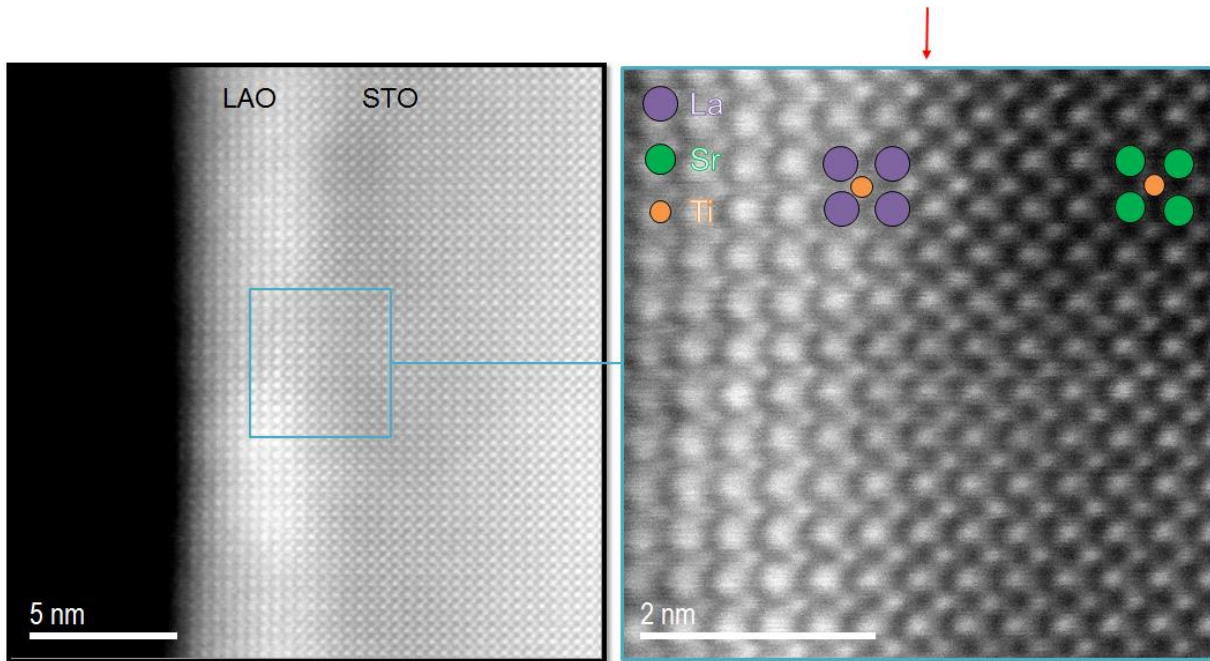


Figure IV.18 | Representative HAADF images of the sample UC10P6 grown at 10^{-6} Torr. The interface is shown by a red arrow. La (Sr) {Ti} atoms were represented by purple (green) {orange} circles. The off-center displacement of Ti near the interface is clearly seen and the effect seems to be stronger compared to the sample deposited at higher O pressure.

IV.2.7 Oxygen Partial Pressure effect: Discussion

The combination of these experimental results shows that a detectable amount of oxygen vacancies are inserted within the heterostructures from an oxygen partial pressure threshold of 10^{-5} Torr. These extrinsic defects govern the conduction only at 10^{-6} Torr where a transition from a 2D to a 3D conduction mechanism occurs together with a dramatic increase in the electrical conductivity. This is consistent with the literature where the electrical properties have been reported to be significantly enhanced at lower O partial pressure [9,15–17]. It must be noted that the electrons injected in the bulk, by the UC10P6 STO reduction, do not seem to cancel the dipolar field developed in the film. A positive charge, shifted below the interface by the intermixing, remains that repels Ti cations of the sub-interface region towards the film surface (Figure IV.18) and the oxygen vacancies towards the bulk. The concentration of oxygen vacancies close to the interface is also reduced by a charge defect equilibrium associated to the La doping in this region [18]. This explains the lower oxygen vacancies seen close to the interface of the sample UC10P6 (Figure IV.11b).

At 10^{-5} Torr, the conduction cannot be explained by a sole charge injection through bulk oxygen vacancies. Two sources of donor doping exist as those identified in the sample grown at 10^{-4} Torr: the oxygen vacancies in the top film layers and the La diffusion in the sub-interface layers. Both are promoted at this lower partial pressure of oxygen. The A and B cations intermixing is larger and more extended for samples grown at lower p_{O_2} , consistently with the literature [19–21]. At this point, the net charge resulting from this donor-acceptor doping is not determined. The signature of O-K at the film surface testify a modification of the O environment induced at least partially by a higher concentration of $V_O^{\bullet\bullet}$ at lower p_{O_2} , increasing the charge transferred to the interface. This explains the lower valence of Ti measured by EELS. However the valence predicted by the polar catastrophe

model is not reached. A mixed compensation of the interfacial charge by electrons and strontium vacancy is again expected at $p_{O_2} = 10^{-5}$ Torr [5] (Figure III.19a and Figure III.19b). The higher electrostatic deformation of the lattice in *UC5P5* compared to *UC5P4* (Figure IV.16c and Figure IV.16d) is attributed partially to a higher concentration of V_{Sr}'' . We can make the assumption that the charge to compensate was increased by a higher donor doping than in *UC5P4*. In addition, the stronger ferroelectric-like distortions and Jahn-Teller (or pseudo-) effect contribute to this higher deformation of the lattice. The in-plane compressive strain developed reduces the mobility of the charge carriers and their density by a transfer to deeper regions. As for *UC5P4*, this dilution can explain the difference between the carrier densities measured by EELS and Hall Effect.

IV.3 Deposition angle effect

Among the numerous process parameters impacting the film growth, the position of the STO substrate on the sample holder regarding the plasma plume is barely considered in the literature. The first indication of a possible major contribution was given by Warusawithana *et al.* [22]. They evidenced that, for films grown by MBE, the variation of the angle between the LAO source and the substrate results in variations of film stoichiometry and interface conductivity (see section I.5.5). In order to investigate the role of the plume angle in the interface behavior, we have analyzed two sets of samples varying by their positions on the substrate as illustrated in Figure II.14a where the positions #2 and #4 correspond to low and high angles respectively. Films of thicknesses of 5 u.c. (*UC5P4#4T7*, or **UC5#4**, at position **#4**) and 10 u.c. (*UC10P4#4T7*, or **UC10#4**, at position **#4**) have been grown at these positions, as summarized in Table IV.1. To keep deposition rate per pulse number constant between the low and high angle conditions, the laser fluence for the high angle plume deposition has been increased to 2 J.cm^{-2} . Therefore, according to the literature exposed in Chapter II (see section II.3.1), the film stoichiometry should be affected by such modification, and more precisely the films should be Al-richer.

IV.3.1 Film growth

The first evidence of the influence of the deposition angle is the quality of the growth. The HAADF picture of the sample *UC10#4* (Figure IV.19) does not exhibit a clear interface between the LAO film and the STO substrate. The HAADF signal from the sample surface to the STO does not display the clear step expected from the La/Sr chemical contrast (Figure IV.19b). The precise localization of the interface is thus not possible through this method.

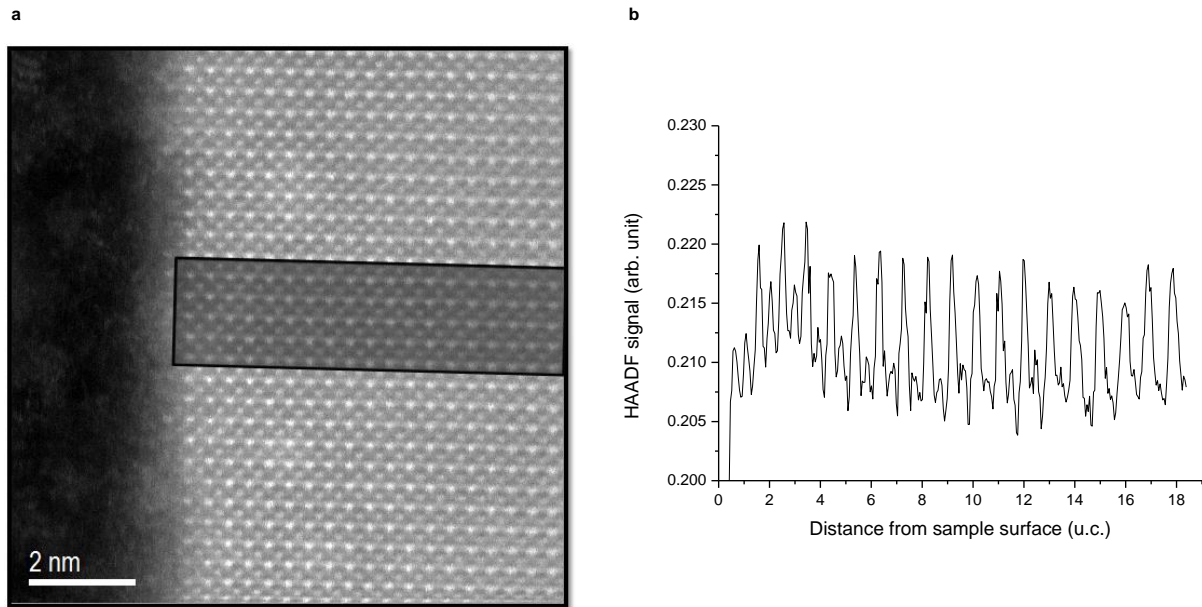


Figure IV.19 | Film growth quality of the sample UC10#4. **a**, Representative HAADF image of LaAlO_3 films grown pseudomorphically on SrTiO_3 . No misfit dislocations could be detected at LAO/STO interfaces along the entire distance observed via Nion UltraSTEM. However, no clear interface between LAO and STO could be detected. **b**, Intensity profile of the image averaged over the area defined by the black rectangle in **a**. No clear differences in the intensity could be measured throughout the sample.

The position of the interface has been estimated using EELS spectrum images on Sr- $L_{2,3}$, Ti- $L_{2,3}$ and La- $M_{4,5}$ absorption edges (Figure IV.21). The overlaps between La and Ti (Figure IV.21c), as well as between La and Sr (Figure IV.21f), were seen at approximately 2/3 u.c. from the crystallized sample surface. We made the assumption that this position corresponded to the interface depth.

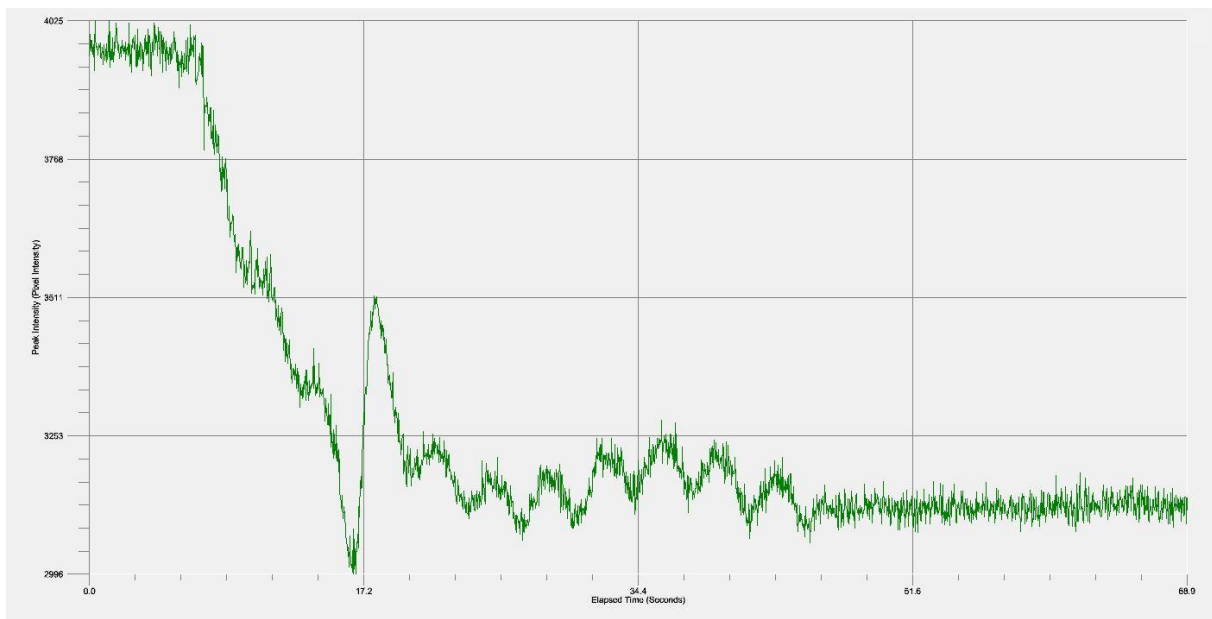


Figure IV.20 | RHEED signal intensities recorded during the growth of the sample UC10#4. From R. Akrobetu work.

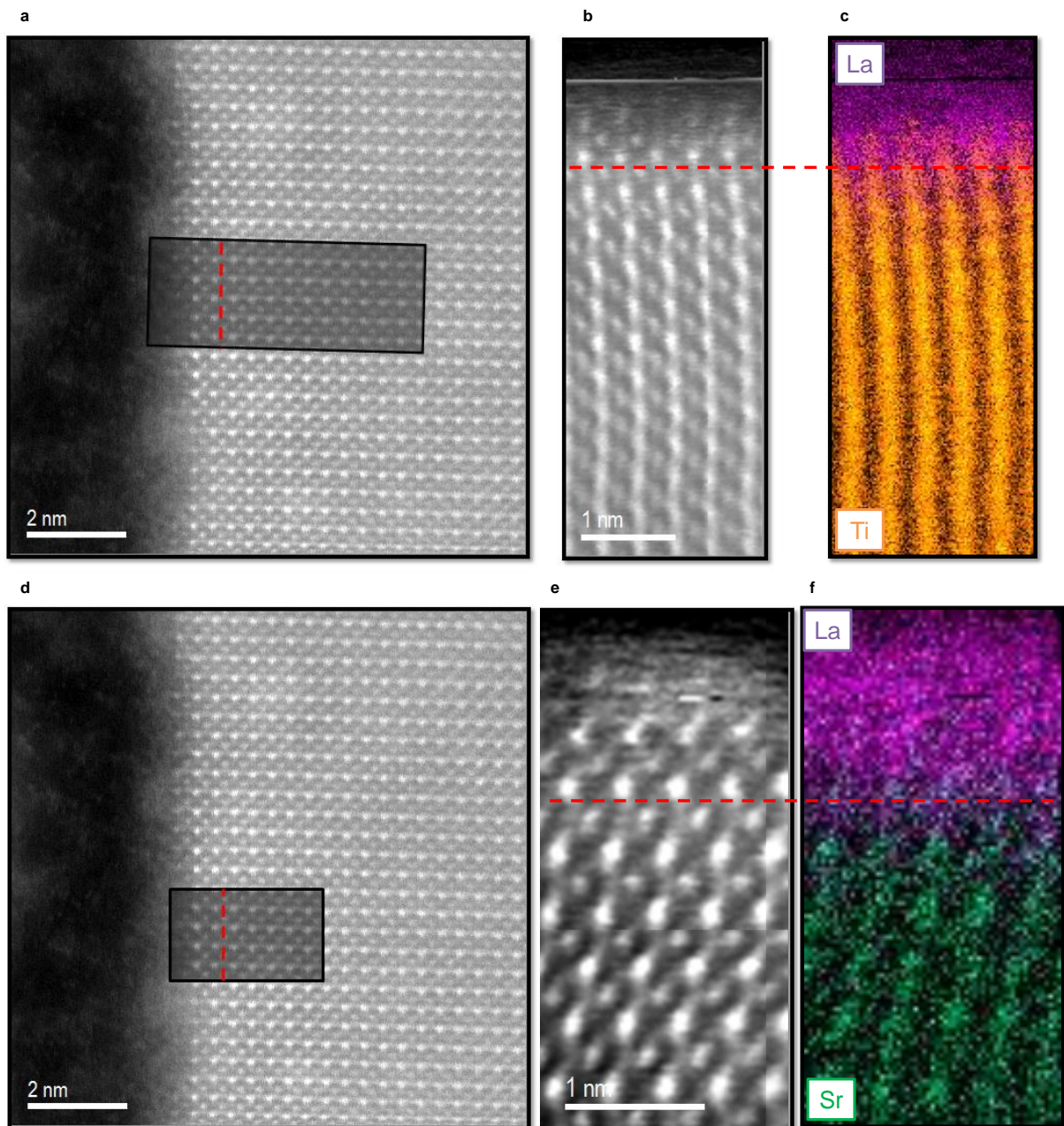


Figure IV.21 | Estimation of the position of the sample UC10#4 interface. The red dashed dotted line represents the position of the interface deduced from the spectrum images. **a**, Representative HAADF image of the sample top surface. The black rectangle represents the area probed by EELS and displayed in **b**. **c**, Superposition of La- $M_{4,5}$ (purple) and Ti- $L_{2,3}$ (orange) spectrum images. **d**, Representative HAADF image of the sample top surface in a distinct area regarding **a**. The black rectangle represents the area probed by EELS displayed in **e**. **f**, Superposition of La- $M_{4,5}$ (purple) and Sr- $L_{2,3}$ (green) spectrum images.

This results in a film thickness of two or three unit cells whereas the modulations of the RHEED signal intensity indicated 10 distinct oscillations (Figure IV.20). This discrepancy will be discussed in the following sections. Despite this strong alteration of the growth quality, the first layers deposited grew pseudomorphically on the STO substrate and no interface dislocations could be detected.

IV.3.2 Ti³⁺ Contribution

Figure IV.22 displays EELS Ti-L_{2,3} absorption edges around the interface as localized in the previous section and the deduced Ti oxidation states. The lower valence was found within the film at 1 u.c. above the presumed interface with a value of +3.82(+/-0.05) (Figure IV.22b). At the interface it reached only +3.95(+/-0.05) (Figure IV.22c). If Ti³⁺ were formed they did not extent deeper into the substrate since the valence of Ti was found equal to +3.98(+/-0.05) two unit cells under the interface (Figure IV.22d).

Sample	Sample position	Ti valence (interface)
<i>UC10#2</i>	#2	Ti ^{3.85+} (+/-0.05)
<i>UC10#4</i>	#4	Ti ^{3.95+} (+/-0.05)

Table IV.10 | Ti oxidation state for the samples varying by their positions on the sample holder

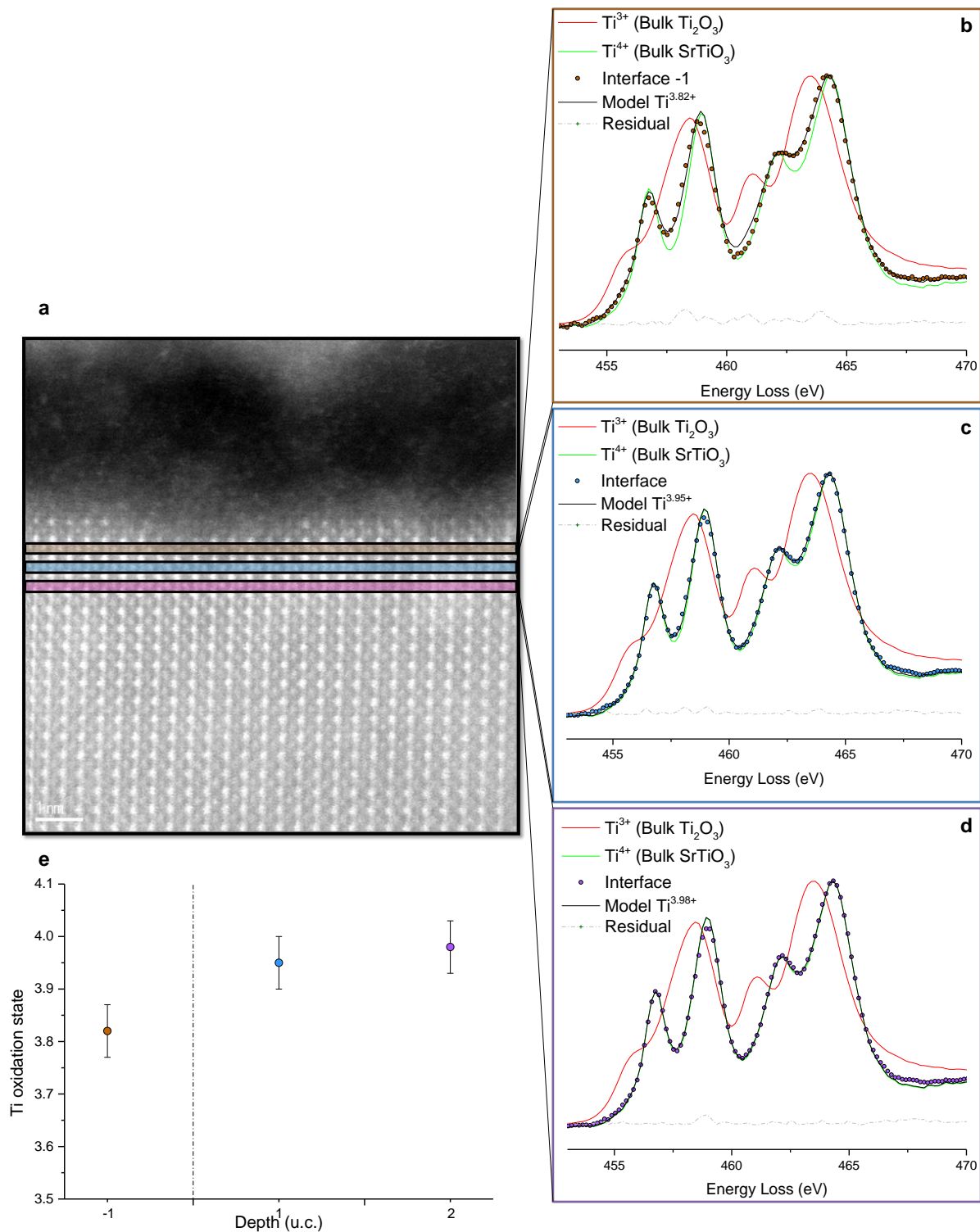


Figure IV.22 | Ti-L_{2,3} edge EELS taken around the LaAlO₃/SrTiO₃ interface of the sample UC10#4. a, HAADF image of the region of interest probed to measure the Ti EELS spectrum through the sample. Each region of interest is represented by one colored rectangle. **b-d**, EELS spectrum at **(b)** 1 u.c. above the interface **(c)** the interface **(d)** 1 u.c. under the interface. The **(b)** brown **(c)** blue **(d)** purple dots spectra correspond to the experimental EELS measurement at **(b)** 1 u.c. above the interface **(c)** the interface **(d)** 1 u.c. under the interface. The color code is available in Figure III.4. **e**, Ti valence profile unit cell by unit cell.

IV.3.3 Oxygen vacancies

Figure IV.23a presents the EELS O-K absorption edges in the deep substrate of the samples *UC10#4* and *UC10#2* grown at the same oxygen partial pressure. The spectra are similar, hence the change in plume angle did not affect the oxygen stoichiometry of the substrate, as expected. However, significant changes are noticed at the interface (Figure IV.23b). First, the small decreasing of the peak A could be induced by a small reduction of Ti^{4+} at the interface or to $Ti \leftrightarrow Al$ intermixing. The peak C is at the same position as in the O-K EELS spectra of the bulk, suggesting a weak $Sr \leftrightarrow La$ intermixing. The increasing of the peak B and of the valley between the peaks C and D, suggests the presence of V_{O}^{\bullet} at the interface of the sample *UC10#4*.

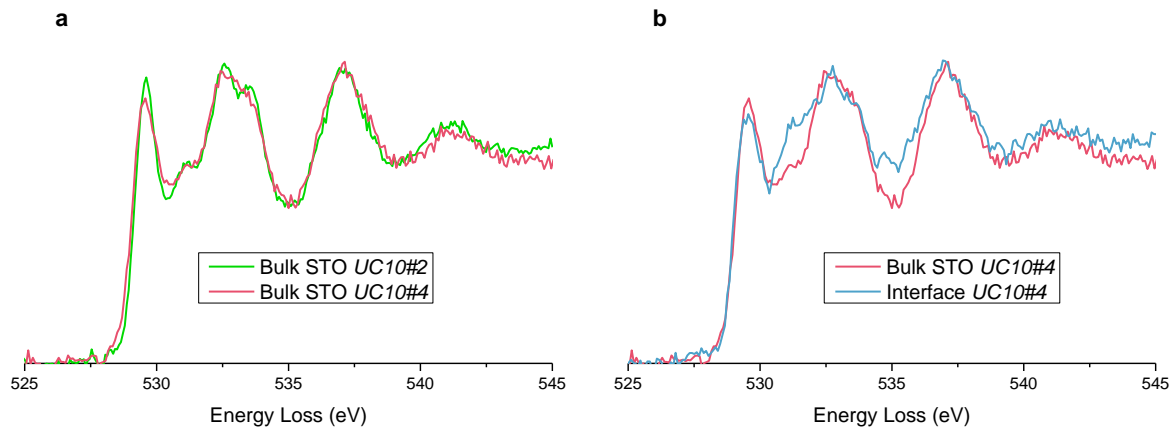


Figure IV.23 | Experimental EELS fine structure of the O-K absorption edge across the sample *UC10#4*. **a**, Comparison between the O-K EELS spectra within the STO bulk of *UC10#2* (Green curve) and *UC10#4* (Red curve). Similar spectra are observed meaning that V_{O}^{\bullet} concentration in both samples is below the detection limit. **b**, O-K EELS spectra within the STO bulk (Red curve) and at the interface (Blue curve). The post edge oscillations of the interface spectrum reveal the presence of oxygen vacancies.

Sample	Sample position	V_{O}^{\bullet} in STO bulk	V_{O}^{\bullet} at interface
<i>UC10#2</i>	#2	< detection limit	< detection limit
<i>UC10#4</i>	#4	< detection limit	✓

Table IV.11 | Oxygen vacancies for the samples varying by their positions on the sample holder.

IV.3.4 Intermixing

Owing to the difficulties met in the previous section to localize the interface by HAADF and EELS, we chose to quantify the intermixing at high plume angle only by MEIS. A sample with a theoretical film thickness of 5 u.c. deposited at the position #4, *UC5#4*, was selected to record spectra in random mode. A representative spectrum is shown in Figure IV.24a. Its simulation could not be achieved with 5 unit cells layers (Purple dash dotted curve in Figure IV.24a). As for the sample *UC10#4*, this shows a discrepancy with the 5 oscillations of the corresponding RHEED data. The best fit was obtained with 3 layers of film deposited (Blue dash dotted curve in Figure IV.24a), and a diffuse interface (Green curve in Figure IV.24a). The cumulative of La content within the whole heterostructure is 2.95 +/- 0.05 which corresponds to the deposition of 3 u.c. of LAO. Compared to a 3 u.c. film grown in position #2 (*UC3#2*), the diffusion of Sr in the film is similar. Strontium reaches the film surface and a

Chapter IV | Dependence to growth conditions

one u.c. width column of the film encloses 0.5 Sr. In the substrate, the diffusion profiles are not identical. La concentration and diffusion length in STO are lower at higher plume angle (Figure IV.24b).

The cumulative amount of La atoms in a column with a width of one u.c. in the substrate is 0.45 +/- 0.05 La, while 0.65 +/- 0.05 La was found inside the substrate of *UC3#2*.

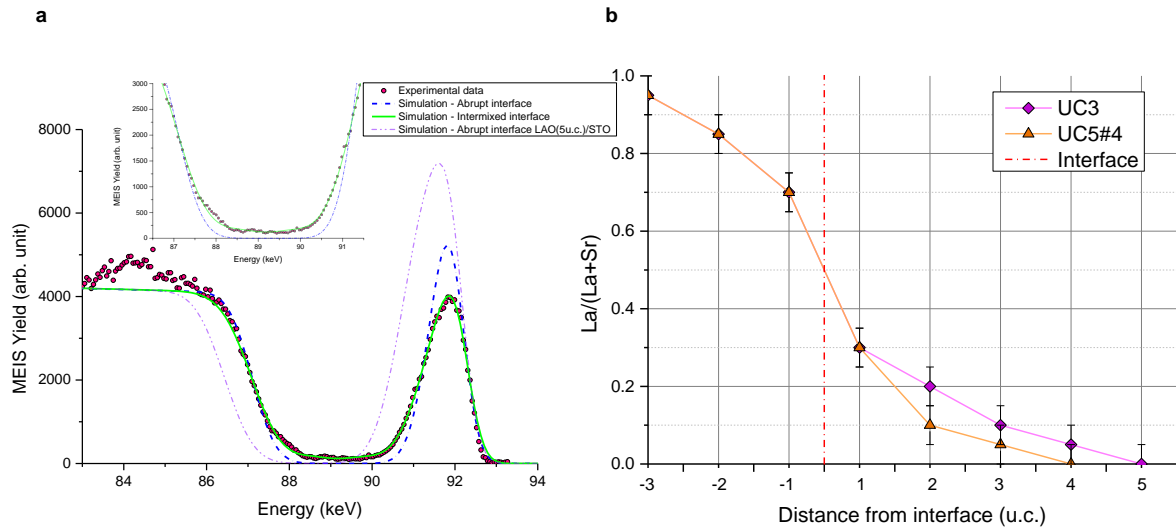


Figure IV.24 | MEIS chemical profile of the sample *UC5#4*. **a**, Random MEIS experimental and simulated spectra with a backscattering angle of 116,5°. The experimental data are represented by red circles, the simulated spectra corresponding to the LAO(2.5 u.c.)/STO system without intermixing by blue curve, and the simulated spectra fitting the experimental data by green curve. The transparent purple curve represents a simulated structure with a film thickness of 5 u.c.. **b**, La/(La+Sr) profile throughout the first atomic layers obtained from the MEIS chemical measurements and comparing the samples *UC3#2* (purple diamond) and *UC5#4* (orange triangle). The x coordinates locate the cations by the number of unit cells to the interface (+ 1 = first u.c. in STO, - 1 = first u.c. in LAO...).

Sample	Sample position	La diffusion in the substrate (MEIS)	Sr diffusion in the film (MEIS)
<i>UC3#2</i>	#2	4/5 u.c.	3 u.c.
<i>UC5#4</i>	#4	3/4 u.c.	3 u.c.

Table IV.12 | Intermixing for samples varying by their positions on the sample holder.

IV.3.5 Structural distortions

Strain Profiles

Figure IV.25 presents the blocking dips patterns of La and Sr scattering centers obtained from the sample *UC5#4*. The sample was probed down to 18 u.c. from the top surface and the corresponding maximum blocking angle was taken as the reference for a cubic STO. The *c/a* variations deduced are shown in Figure IV.26a and compared with the strain profiles obtained for the sample *UC3#2* (Figure IV.26b). As it was established in all the previous samples, the three regions with *c/a* = 1, *c/a* > 1, and *c/a* < 1 are observable. While the *c/a* > 1 area starts at the same depth (i.e. 9 u.c. from the interface) between the samples *UC5#4* and *UC3#2*, the *c/a* < 1 region starts 2 u.c. before, at 3 u.c. below the

interface versus 1 u.c. for *UC3#2*. Hence, the $c/a < 1$ region is more extended (i.e. 5 u.c. up to the film surface) in the sample *UC5#4*.

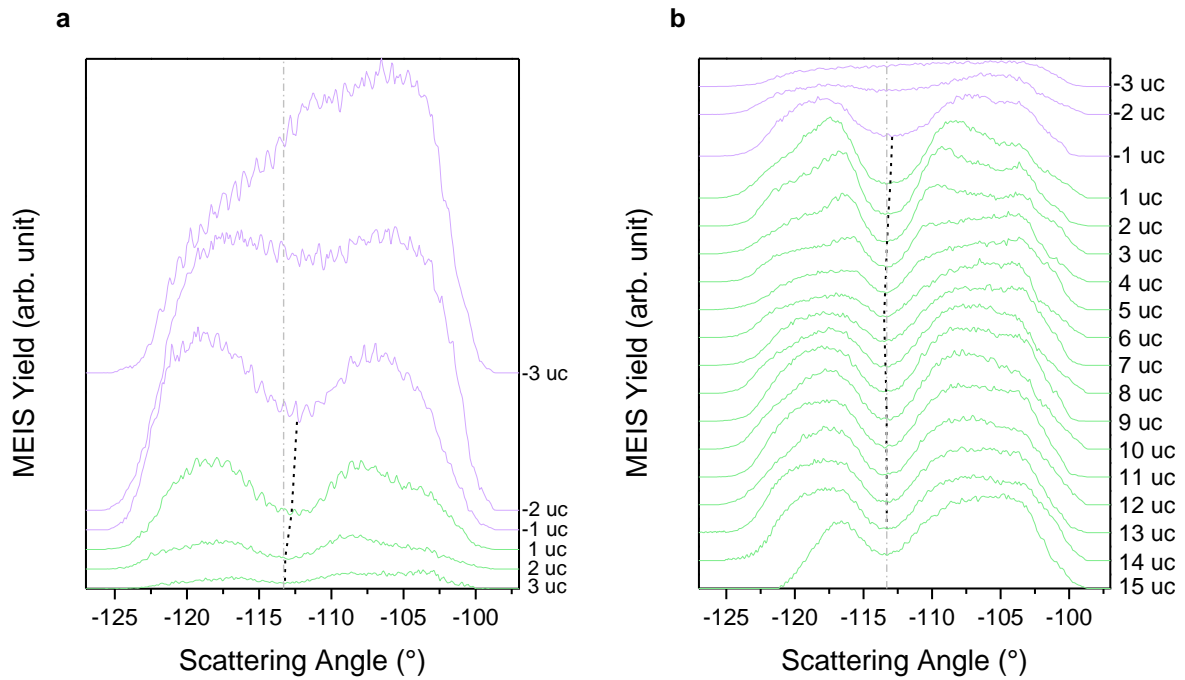


Figure IV.25 | MEIS data in blocking mode obtained for the sample *UC5#4*. **a**, MEIS [101] blocking dips as a function of depth corresponding to La atoms located in the film (purple curves) and in the substrate (green curves). **b**, MEIS [101] blocking dips as a function of depth corresponding to Sr atoms located in the film (purple curves) and in the substrate (green curves). Dash-dotted grey lines are the position of the blocking dips for an unstrained cubic STO ($c/a = 1$). Dashed black lines indicate the position of the blocking dips maxima for each unit cell. In the substrate, deviations of these positions from the dash-dotted line reveal structural distortions.

In order to identify the origins of the strain, the theoretical epitaxial strain, based on the MEIS chemical profile experimentally determined (Figure IV.24b), was calculated and plotted by red squares in Figure IV.26a. The difference between the theoretical and the experimental strain from the sample *UC5#4* is shown in Figure IV.26c. Once again, the epitaxial strain is not sufficient to describe the structural distortions measured in the sample *UC5#4*. In the substrate we observe positive values indicating c -lattice expansion in the [001] direction, as it was the case for all samples studied so far. However, for the first time a decrease of this expansion is noticed in the substrate region from 2 u.c. to 5 u.c. below the interface, where the non-elastic contribution of the strain almost vanishes.

Owing to symmetry between the angular position and width profiles established with all the previous samples, buckling profiles were not considered as they did not improve the understanding of the conduction mechanism.

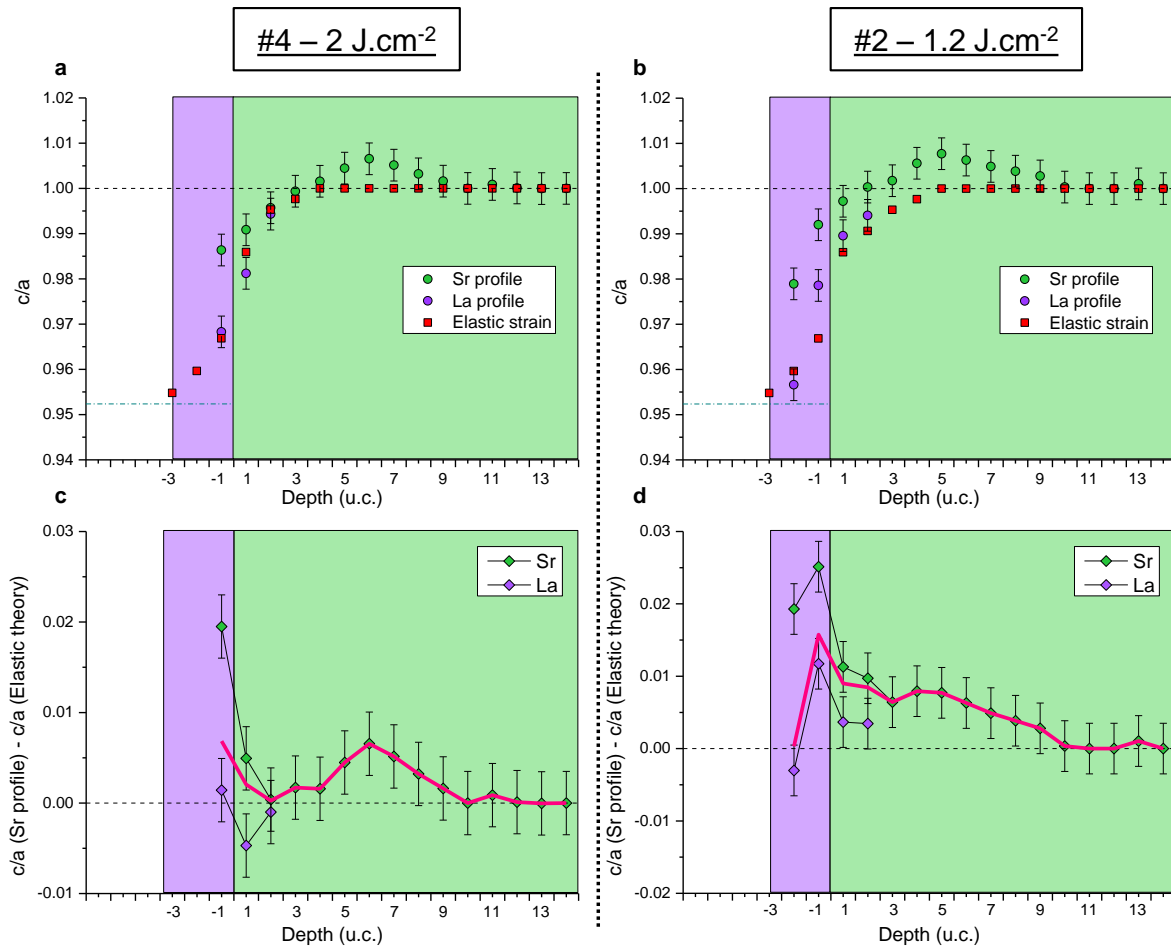


Figure IV.26 | MEIS strain profiles for samples varying by their substrate position relatively to the plasma plume. The x coordinates locate the cations by the number of unit cells to the interface (+ 1 = first u.c. in STO, - 1 = first u.c. in LAO...). Each data point indicates the distance separating this cation to the A cation located in the above cell. **a-b**, Profiles of c/a for samples grown at position **(a)** #4 – UC5#4 **(b)** – #2 – UC3#2. The color code is available in Figure III.15. **c-d**, Difference between the c/a values measured experimentally - from He^+ scattered from Sr and La atoms - and those calculated from epitaxial strain are plotted for the sample **(c)** UC5#4 **(d)** UC3#2. The pink curve represents the weighted average of the profiles. Figure IV.26b and Figure IV.26d, and Figure III.15a and Figure III.15c are the exact same ones, they were plotted here for clarity.

IV.3.6 Deposition Angle: Discussion

The films of the samples UC5#4 and UC10#4 have been deposited from species coming from the edge of the plume that were ablated by a higher laser fluence. From the thickness of 5 u.c. or 10 u.c. that were aimed, only 3 u.c. were deposited. The hypothesis of an amorphous upper layer is rejected for UC5#4, since the MEIS random spectrum, which should not be sensitive to the crystal order, does not indicate a thicker film. For UC10#4, the HAADF images of Figure IV.19 exhibits a film thickness of maximum 1.5 nm, that cannot correspond to an equivalent of 10 u.c. deposited. We explain this discrepancy by two factors: the increase of the fluence which is known to produce a stronger ablation of the B (Al) cations [10,23,24] and the deviation from stoichiometry in the plume edges. With these conditions of growth, we made the assumption that the species coming from the edges of the plume were highly richer in aluminum and that the growth rate was reduced.

This growth of an Al-rich film explains the lower diffusion length of La when compared with a 3 u.c.-thick film (*UC3#2*) grown from the center of the plume (Figure IV.24b). In the literature, the La non-stoichiometry of the film is charged balanced either by positively-charged oxygen vacancies [25,26], or by Al antisites formation [22]. The fingerprint of the oxygen vacancies can be seen at the interface, rather than within the STO bulk (Figure IV.23), suggesting that the former mechanism is favored to compensate the La non-stoichiometry.

The similitude in the strain profiles of *UC5#4* and *UC3#2* in the region going from 4 u.c. to 13 u.c. inside the substrate is understood as reflecting a similar strontium vacancy distribution in these 3 u.c. films (Figure IV.26c). The difference in the two profiles below the interface (1 u.c. to 3 u.c. region), with a deformation close to the elastic one for *UC5#4* is explained by the presence of oxygen vacancies in the interface region of *UC5#4*. Schottky pairs $V_{Sr}'' - V_O^{\bullet\bullet}$ can be formed, such defects are reported to produce a weak contraction of the lattice [14].

Compared to *UC3#2*, the Ti valence of this “3 u.c.” sample (*UC10#4*), close to +4, is higher. In *UC3#2*, charge transfer between Ti_{Al} (film) \leftrightarrow Al_{Ti} (interface) contributed to the decrease of the Ti valence. In this La-poor film, we believe that, rather than the Al_{La} defects proposed by Warusawithana *et al.* [22], Sr_{La} defects are formed. Ti_{Al} donor defects of the film cancel partially the charge of these Sr_{La} acceptor defects, and do not contribute to the lowering of the Ti valence.

Hall Effect measurements were not carried out on these specimens. We infer from the thickness of the film below the critical one, the low Ti valence, the small amount of La_{Sr} donor dopants, and from the strain profile distributed deep into the substrate, that the samples *UC10#4* and *UC5#4* are insulating.

A La/Al ratio lower than 0.97 was considered by Warusawithana *et al.* [22] as the composition threshold for conduction above the critical thickness. We expected to investigate a 10 u.c. La-poor film. Due to the thinner film deposited we were not able to confirm or disconfirm this composition threshold.

IV.4 Temperature effect

The last growth condition effect was investigated in this thesis is the temperature. One sample with a theoretical film thickness of 10 u.c. deposited at 10^{-4} Torr was grown at 550°C and called ***UC10T5*** (*UC10P4#2T5*), that will be compared with samples with film grown at 750°C.

IV.4.1 Film growth

Unfortunately, probable issues with the RHEED system made the monitoring of the growth quite complex for this sample. Figure IV.27 represents the STEM-HAADF picture of the sample *UC10T5*. The quality of the film growth was degraded. The growth started pseudomorphically, with no interface dislocations, but the structure became amorphous in the upper part of the film. According to Fête *et al.* [27], decreasing the growth temperature from 950°C to 650°C does not alter the crystallinity of the film. Bark *et al.* [28] displayed even a fully crystallized LAO film of 12 u.c. grown at 550°C. Conversely, films grown at room temperature by Liu *et al.* [29] were amorphous with one or two well oriented layers at the interface. The amorphous part of our film cannot be attributed to the FIB preparation of this TEM cut, since previous samples we prepared by FIB following the same

procedure did not exhibit such features. A PLD growth temperature lower than 550°C is suspected to have induced this poor crystallinity of the film.

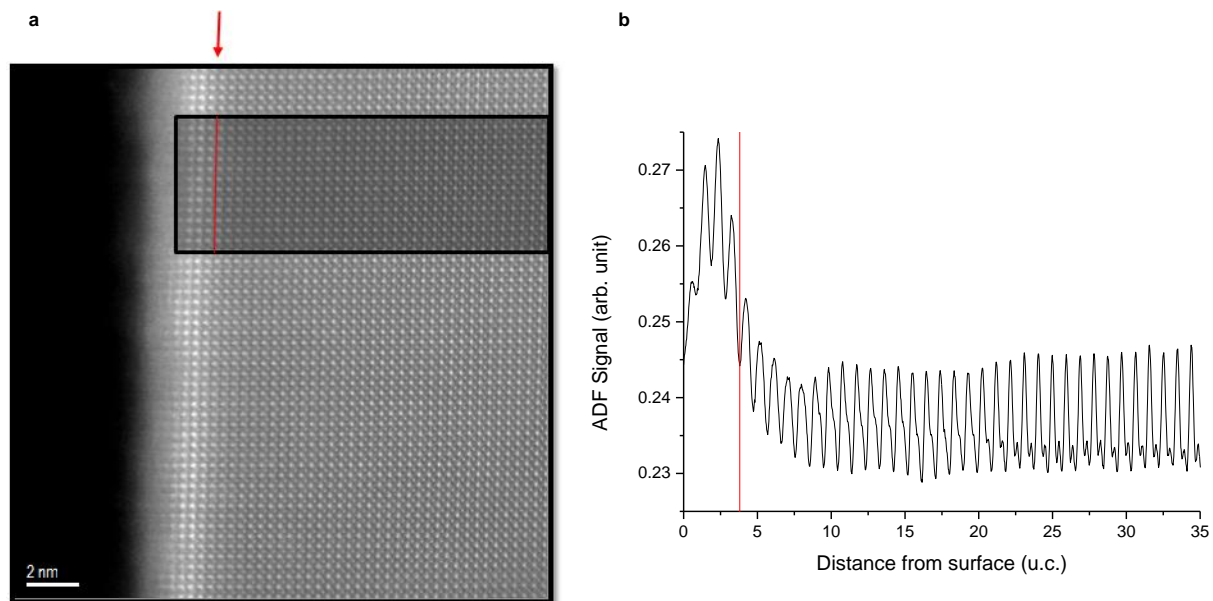


Figure IV.27 | Film growth quality of the sample UC10T5. **a**, Representative HAADF image of LaAlO₃ films grown pseudomorphically on SrTiO₃. No misfit dislocations could be detected at LAO/STO interfaces along the entire distance observed via Nion UltraSTEM. However, the top surface of the film is subjected to partial amorphization. The analysis of the intensity profile led to the localization of the LAO/STO interface noted by a red arrow. **b**, Intensity profile of the image averaged over the area defined by the black rectangle in **a**. The variations of the intensity permitted to estimate the position of the interface, marked with a red line.

In order to situate the interface, an intensity profile from the surface to the bulk is plotted (Figure IV.27b) that averages about 13 lateral unit cells. The interface is fixed at half height of the slope between the film and the substrate and marked with a red line (Figure IV.27). A film thickness of 3 u.c. to 4 u.c. is deduced if we only consider the crystallized part, but taking into account the amorphous part we can estimate that an equivalent thickness of 7/8 u.c. of LAO on the STO substrate was deposited. Due to the ambiguity in the determination of the film thickness, we will compare the film characteristics with those of UC3T7, UC5T7 and UC10T7.

IV.4.2 Ti³⁺ Contribution

The oxidation state of Ti at the interface, measured on the EELS Ti-L_{2,3} absorption edges (Figure IV.28), was equal to about +3.89 (+/- 0.05), that is higher than what was found at the interface of the sample UC10T7 but equivalent as that of UC3T7 and UC5T7 (Table IV.13).

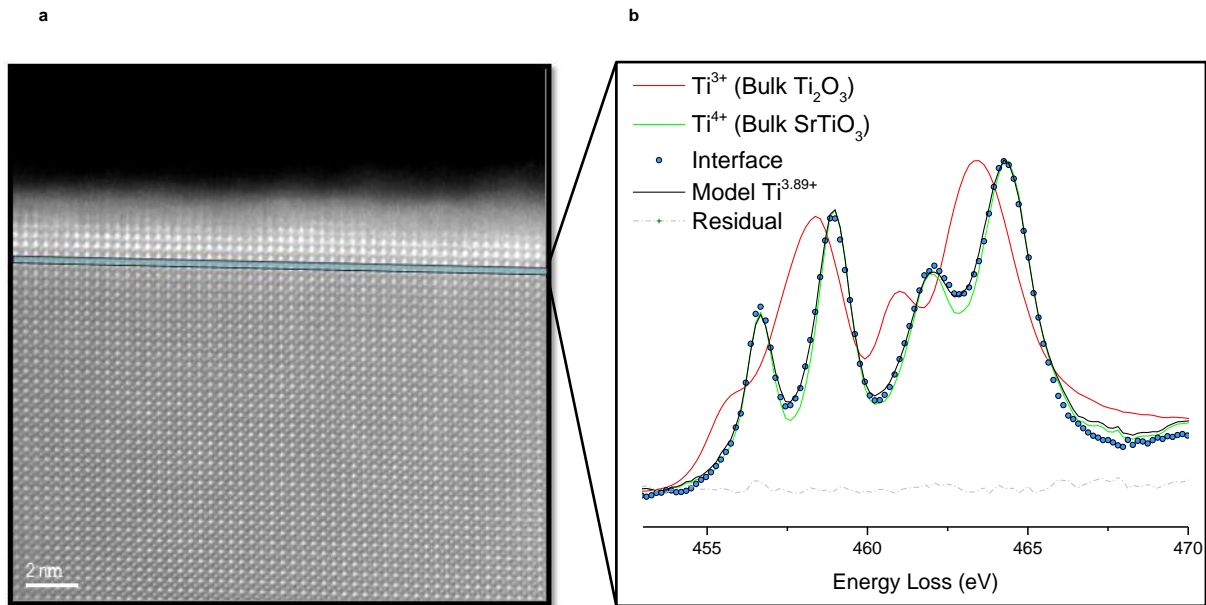


Figure IV.28 | Ti-L_{2,3} edge EELS taken at the LaAlO₃/SrTiO₃ interface of the sample UC10T5. a, HAADF image of the region of the interface probed to measure the Ti EELS spectrum. The blue rectangle represents the area used to measure the Ti-L_{2,3} absorption edge. **b,** EELS spectrum of Ti measured at the interface. The color code is available in Figure III.4.

Sample	Growth Temperature	Film thickness	Ti valence (interface)
UC3T7	750°C	3 u.c.	Ti ^{3.92+} (+/-0.05)
UC5T7	750°C	5 u.c.	Ti ^{3.91+} (+/-0.05)
UC10T7	750°C	10 u.c.	Ti ^{3.85+} (+/-0.05)
UC10T5	< 550°C	?	Ti ^{3.89+} (+/-0.05)

Table IV.13 | Ti oxidation state for samples varying by the temperature used during the film deposition.

IV.4.3 Oxygen vacancies

Figure IV.29 shows the EELS O-K absorption edges at the interface and within the STO bulk of the sample UC10T5.

Figure IV.29a compares the EELS O-K spectra from the STO bulk of the samples UC10T7 and UC10T5. The shape of these spectra exhibits strong similarities, revealing that no oxygen vacancies were provided by decreasing the growth temperature. The interpretation of the interface spectrum (Figure IV.29b) is slightly more delicate. The slight shift of the peak C towards the lower energies, as well as its broadening, indicates cationic exchanges between La and Sr cations at the interface of the sample UC10T5, as it was mentioned in Chapter II (section II.4.3.2). In addition, we can distinguish a slight rise of the peak B, suggesting that a small amount of oxygen vacancies cannot be totally excluded. However, the gap between the peaks C and D remains the same; if oxygen vacancies are present the concentration is weak.

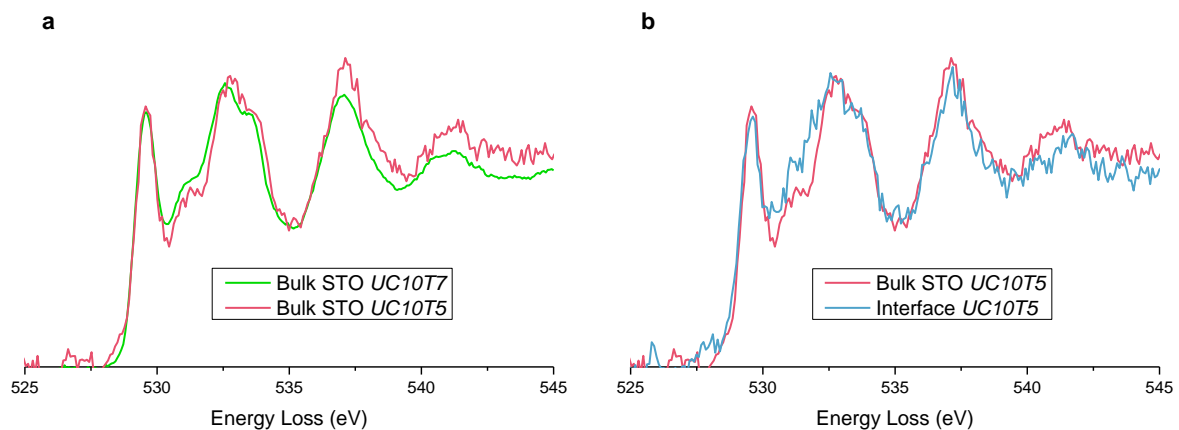


Figure IV.29 | Experimental EELS fine structure of the O-K absorption edge across the sample UC10T5. **a**, O-K EELS spectra within the STO bulk for UC10T7 (Green curve) and UC10T5 (Red curve). Similar spectra are observed, no signature of extrinsic defects are detected. **b**, O-K EELS spectra of the sample UC10T5 within the STO bulk (Red curve) and at the interface (Blue curve). The shape of the peak corresponding to the interface reveals mainly cationic exchanges, but a small amount of oxygen vacancies is not totally excluded.

Sample	Growth Temperature	Film thickness	$V_{\ddot{O}}$ in STO bulk	$V_{\ddot{O}}$ at interface
UC3T7	750°C	3 u.c.	< detection limit	< detection limit
UC5T7	750°C	5 u.c.	< detection limit	< detection limit
UC10T7	750°C	10 u.c.	< detection limit	< detection limit
UC10T5	< 550°C	?	< detection limit	< detection limit

Table IV.14 | Oxygen vacancies for samples varying by the temperature used during the film deposition.

IV.4.4 Intermixing

The O-K absorption edge at the interface of the sample UC10T5 highlighted cationic exchanges between the film and the substrate. Owing to the amorphous part of the film, the O-K pre-peak in the crystalline part was probed only up to 5 u.c. above the interface (Figure IV.30a). This strong indicator of Ti presence inside the film was found up to this last O-K spectrum, revealing Ti diffusion at least up to 4/5 u.c. within the film. This was confirmed by the Ti profile obtained from the area under the Ti-L_{2,3} EELS spectra (Figure IV.30b). The Ti signal did not vanish at 4 u.c. from the interface. The diffusion length must thus be longer than 4 u.c. but could not be more precisely measured.

The diffusion of La cations clearly extended down to 2/3 u.c. within the STO substrate. The Ti concentration in the substrate started to decrease 2/3 u.c. below the interface, to be replaced by Al if we consider that all the B-sites are occupied within STO. Hence the Al and La diffusion lengths in the substrate were similar, but shorter than in samples deposited at higher temperature. This can be explained by the mobility of the ionic species which is reduced at lower temperature [5]. In addition the ionic compensation of the interfacial charge is favored [5] at lower growth temperature, implying higher concentration of cationic defects (Figure III.19) to compensate the polar field. These results provide a first explanation to the weaker Ti³⁺ contribution at the interface of the sample UC10T5.

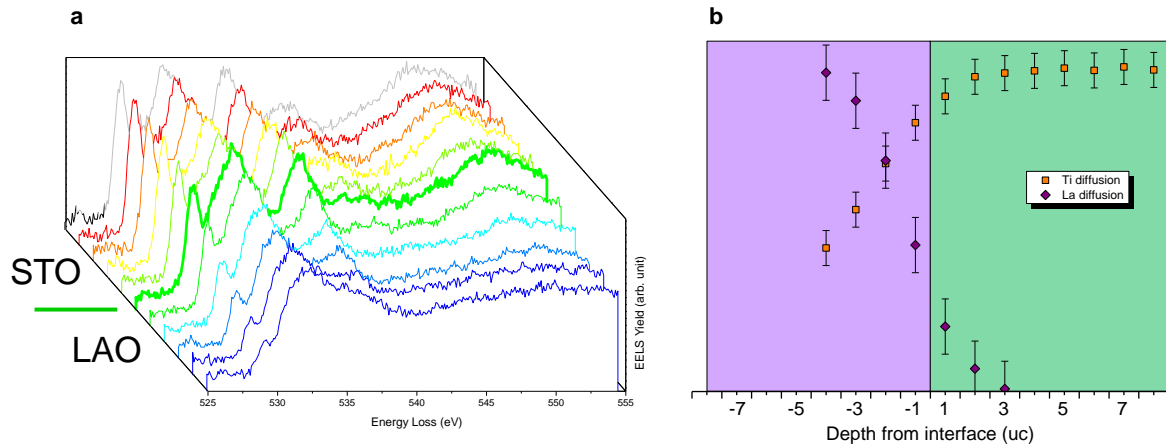


Figure IV.30 | Intermixing profile of the sample UC10T5 through EELS measurements. a, Spatial distribution of the EELS O-K absorption edges unit cell by unit cell. The spectrum measured at the interface is marked by a bold spectrum. **b**, Diffusion profiles of Ti and La from EELS analyses.

Sample	Growth temperature	Film thickness	La diffusion (EELS)	Ti diffusion (EELS)
UC3T7	750°C	3 u.c.	5 u.c.	3 u.c.
UC5T7	750°C	5 u.c.	6/7 u.c.	5 u.c.
UC10T7	750°C	10 u.c.	5/6 u.c.	5/6 u.c.
UC10T5	< 550°C	?	2/3 u.c.	4/5 u.c.

Table IV.15 | Intermixing for samples varying by the temperature used during the film deposition.

IV.4.5 Structural distortions

The thickness of the film associated to the disordered top region did not encourage to perform structural distortions investigations by MEIS. Regarding ferroelectric distortions, the HAADF images of the sample UC10T5 interface shows no clear off-centering of Ti (Figure IV.31) and the low concentration of Ti³⁺ at the interface plays in favor of a weak Jahn-Teller contribution to the deformation.

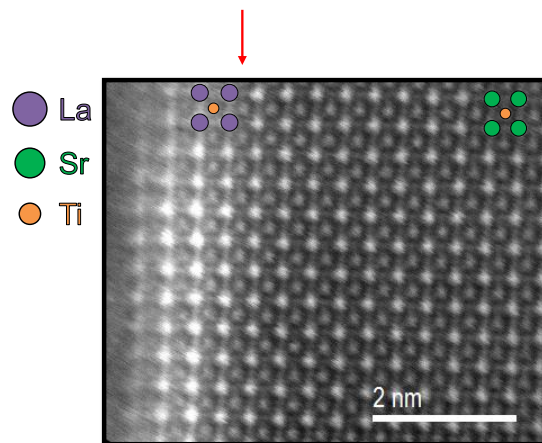


Figure IV.31 | Representative HAADF images of the sample UC10T5 grown at 550°C. The interface is shown by a red arrow. La (Sr) {Ti} atoms were represented by purple (green) {orange} circles. The off-center displacement of Ti near the interface is not obvious. We have thus considered that this TEM cut did not exhibit ferroelectric-like distortions.

IV.4.6 Temperature effect: Discussion

The aim of this section was to investigate the role of growth temperature in the conduction mechanisms of our LAO/STO interface, all other growth parameters being constant, and keeping a 10 u.c. crystallized polar film. However we have seen that the growth conditions were questionable since the top layer of the film was amorphous while examples from the literature show films of high crystallinity at the same growth temperature. We are suspecting a temperature of growth lower than 550°C. Interestingly this growth temperature would be also below the cubic/rhombohedral transition of LAO (540°C).

We chose not to discard this sample, but to evaluate the possibility of conduction in such a film structure, knowing that Liu *et al.* reported conducting (amorphous LAO)/STO interfaces for LAO films grown at room temperature at 10^{-4} Torr [29,30]. For these authors, electrons at the interface were donated by oxygen vacancies created in the top region of STO during the deposition.

The comparison of *UC1075* with our other samples grown in the same conditions at 750°C is not straightforward since we do not know the extent of the built-in potential in *UC1075*. If it is restricted to the 3 crystallized u.c., we should compare it to the sample *UC377*, which has a film below the critical thickness. But it is not excluded that the transition region to the amorphous structure exhibits a weak polarity that makes the comparison with the 5 u.c.-thick film sample more realistic.

A lower growth temperature is expected to reduce the electron compensation and to shift the mix ionic-electronic compensation (V_{Sr}'' , e') toward strontium vacancies [5] as shown in Figure III.19a and Figure III.19b. Since the valence of the sample *UC577* is similar, despite a higher V_{Sr}'' concentration, to that of *UC1075* we assumed that the charge to compensate was higher than for the sample *UC577*. Contrary to Liu's conclusions for their amorphous film, the injection of charges carrier in our mixed crystalline/amorphous film is induced by the film polarity more than by oxygen vacancies formed at the interface, since their signature is very weak (Figure IV.29).

In this context we can analyze the effect of a lower temperature on the conduction behavior. The diffusion rate is lower reducing the donor doping of STO by La (Figure IV.30). The ionic compensation of the positive charge is favored, increasing the concentration of Sr vacancies. The density of carrier is lower for the same film thickness and with lower mobility due to higher structural deformation expected from the increased concentration of Sr vacancies. Vonk *et al.* [31] also indicate higher deformations at a growth temperature of 200°C compared to 850°C but they attribute it to a stronger buckling driven by a Jahn-Teller effect. The high valence in *UC1075*, added to the absence of visible Ti shift (Figure IV.31) does not play in favor of this conclusion for our system.

If a decrease of temperature could be seen firstly as a way to favor electron reconstruction from the surface at the expense of donor doping by intermixing, it can be seen that the scenario is more complex. The enhanced ionic compensation reduces both electron density and mobility. A lower interface conductivity is expected compared to films of same thicknesses grown at higher temperature.

IV.5 Discussion

All along Chapter IV, we have investigated the effects of growth duration, oxygen partial pressure, plume angle and temperature on the mechanisms identified at the origin of the electrical properties of the LAO/STO heterostructures. A complex link between the process parameters and systems behavior is evidenced. For each parameter, a triggering mechanism is favored regarding the other ones. While the structural distortions limit the behavior of thicker films, the oxygen vacancies dominate the conduction in sample grown at lower oxygen pressure. The film stoichiometry is crucial, that must be carefully controlled with the deposition angle. Finally, the temperature plays a significant role in the mobility of species, and the density of cationic vacancies seems to be the restricting factor. Even if we did not have the chance to analyze the influence of other growth conditions, such as the laser fluence as a unique contributing factor or the target-to-substrate distance, this chapter gives an overview of the strong link existing between the process and the properties, through the studies of the interface structures. This experimental work provides clarifications about the wide discrepancies observed in terms of electrical properties in the literature.

Therefore, in order to optimize the electrical behavior of the LAO/STO heterostructures, several conditions should be reached. According to our experimental investigations, the optimized sample should be deposited:

- With a film thickness just above the critical threshold of 4 u.c. to minimize the structural distortions seen in the substrate covered by thicker films.
- At the lowest growth oxygen pressure above the 3D/2D transition (i.e. around 10^{-5} Torr) to favor oxygen vacancies formation at the film surface and donor dopants below the interface, and to favor electronic compensation.
- At the highest growth temperature to favor electronic compensation and to reduce the distortions within the structure.
- In front of the plasma plume to avoid the deviations from the stoichiometric composition.

Bibliography

- [1] A. Ohtomo and H. Y. Hwang, "A high-mobility electron gas at the LaAlO₃/SrTiO₃ heterointerface," *Nature* **427**, 423–426 (2004).
- [2] C. Bell, S. Harashima, Y. Hikita, and H. Y. Hwang, "Thickness dependence of the mobility at the LaAlO₃/SrTiO₃ interface," *Appl. Phys. Lett.* **94**, 222111 (2009).
- [3] M. Takizawa, S. Tsuda, T. Susaki, H. Y. Hwang, and A. Fujimori, "Electronic charges and electric potential at LaAlO₃/SrTiO₃ interfaces studied by core-level photoemission spectroscopy," *Phys. Rev. B* **84** (2011).
- [4] Z. Huang, K. Han, S. Zeng, M. Motapothula, A. Y. Borisevich, S. Ghosh, W. Lü, C. Li, W. Zhou, et al., "The Effect of Polar Fluctuation and Lattice Mismatch on Carrier Mobility at Oxide Interfaces," *Nano Lett.* **16**, 2307–2313 (2016).
- [5] F. Gunkel, R. Waser, A. H. H. Ramadan, R. A. De Souza, S. Hoffmann-Eifert, and R. Dittmann, "Space charges and defect concentration profiles at complex oxide interfaces," *Phys. Rev. B* **93**, 245431 (2016).
- [6] G. Zhu, G. Radtke, and G. A. Botton, "Bonding and structure of a reconstructed (001) surface of SrTiO₃ from TEM," *Nature* **490**, 384–387 (2012).
- [7] L. F. Kourkoutis, H. L. Xin, T. Higuchi, Y. Hotta, J. H. Lee, Y. Hikita, D. G. Schlom, H. Y. Hwang, and D. A. Muller, "Atomic-resolution spectroscopic imaging of oxide interfaces," *Philos. Mag.* **90**, 4731–4749 (2010).
- [8] D. A. Muller, N. Nakagawa, A. Ohtomo, J. L. Grazul, and H. Y. Hwang, "Atomic-scale imaging of nanoengineered oxygen vacancy profiles in SrTiO₃," *Nature* **430**, 657–661 (2004).
- [9] S. Gariglio, A. Fête, and J.-M. Triscone, "Electron confinement at the LaAlO₃/SrTiO₃ interface," *J. Phys. Condens. Matter* **27**, 283201 (2015).
- [10] T. Ohnishi, K. Shibuya, T. Yamamoto, and M. Lippmaa, "Defects and transport in complex oxide thin films," *J. Appl. Phys.* **103**, 103703 (2008).
- [11] H. Guo, S. Dong, P. D. Rack, J. D. Budai, C. Beekman, Z. Gai, W. Siemons, C. M. Gonzalez, R. Timilsina, et al., "Strain Doping: Reversible Single-Axis Control of a Complex Oxide Lattice via Helium Implantation," *Phys. Rev. Lett.* **114**, 256801 (2015).
- [12] S. A. Chambers, M. H. Engelhard, V. Shutthanandan, Z. Zhu, T. C. Droubay, L. Qiao, P. V. Sushko, T. Feng, H. D. Lee, et al., "Instability, Intermixing and Electronic Structure at the Epitaxial LaAlO₃/SrTiO₃(001) Heterojunction," *Surf. Sci. Rep.* **65**, 317–352 (2010).
- [13] M. Golalikhani, Q. Y. Lei, G. Chen, J. E. Spanier, H. Ghassemi, C. L. Johnson, M. L. Taheri, and X. X. Xi, "Stoichiometry of LaAlO₃ films grown on SrTiO₃ by pulsed laser deposition," *J. Appl. Phys.* **114**, 27008 (2013).

- [14] D. A. Freedman, D. Roundy, and T. A. Arias, "Elastic effects of vacancies in strontium titanate: Short- and long-range strain fields, elastic dipole tensors, and chemical strain," *Phys Rev B* **80**, 64108 (2009).
- [15] M. Basletic, J.-L. Maurice, C. Carrétéro, G. Herranz, O. Copie, M. Bibes, É. Jacquet, K. Bouzehouane, S. Fusil, et al., "Mapping the spatial distribution of charge carriers in LaAlO₃/SrTiO₃ heterostructures," *Nat. Mater.* **7**, 621–625 (2008).
- [16] C. Cancellieri, N. Reyren, S. Gariglio, A. D. Caviglia, A. Fête, and J.-M. Triscone, "Influence of the growth conditions on the LaAlO₃/SrTiO₃ interface electronic properties," *EPL Europhys. Lett.* **91**, 17004 (2010).
- [17] G. Herranz, M. Basletić, M. Bibes, C. Carrétéro, E. Tafra, E. Jacquet, K. Bouzehouane, C. Deranlot, A. Hamzić, et al., "High mobility in LaAlO₃/SrTiO₃ heterostructures: origin, dimensionality, and perspectives," *Phys. Rev. Lett.* **98**, 216803 (2007).
- [18] Y. Kozuka, Y. Hikita, C. Bell, and H. Y. Hwang, "Dramatic mobility enhancements in doped SrTiO₃ thin films by defect management," *Appl. Phys. Lett.* **97**, 12107 (2010).
- [19] A. Kalabukhov, Y. A. Boikov, I. T. Serenkov, V. I. Sakharov, J. Börjesson, N. Ljustina, E. Olsson, D. Winkler, and T. Claeson, "Improved cationic stoichiometry and insulating behavior at the interface of LaAlO₃/SrTiO₃ formed at high oxygen pressure during pulsed-laser deposition," *EPL Europhys. Lett.* **93**, 37001 (2011).
- [20] J.-L. Maurice, G. Herranz, C. Colliex, I. Devos, C. Carrétéro, A. Barthélémy, K. Bouzehouane, S. Fusil, D. Imhoff, et al., "Electron energy loss spectroscopy determination of Ti oxidation state at the (001) LaAlO₃/SrTiO₃ interface as a function of LaAlO₃ growth conditions," *Eur. Lett* **82**, 17003 (2008).
- [21] G. Salvinelli, G. Drera, A. Giampietri, and L. Sangaletti, "Layer-resolved cation diffusion and stoichiometry at the LaAlO₃/SrTiO₃ heterointerface probed by X-ray photoemission experiments and site occupancy modeling," *ACS Appl. Mater. Interfaces* **7**, 25648–25657 (2015).
- [22] M. P. Warusawithana, C. Richter, J. A. Mundy, P. Roy, J. Ludwig, S. Paetel, T. Heeg, A. A. Pawlicki, L. F. Kourkoutis, et al., "LaAlO₃ stoichiometry is key to electron liquid formation at LaAlO₃/SrTiO₃ interfaces," *Nat. Commun.* **4** (2013).
- [23] S. Wicklein, A. Sambri, S. Amoruso, X. Wang, R. Bruzzese, A. Koehl, and R. Dittmann, "Pulsed laser ablation of complex oxides: The role of congruent ablation and preferential scattering for the film stoichiometry," *Appl. Phys. Lett.* **101**, 131601 (2012).
- [24] E. Breckenfeld, N. Bronn, J. Karthik, A. R. Damodaran, S. Lee, N. Mason, and L. W. Martin, "Effect of Growth Induced (Non)Stoichiometry on Interfacial Conductance in LaAlO₃/SrTiO₃," *Phys. Rev. Lett.* **110**, 196804 (2013).
- [25] H. K. Sato, C. Bell, Y. Hikita, and H. Y. Hwang, "Stoichiometry control of the electronic properties of the LaAlO₃/SrTiO₃ heterointerface," *Appl. Phys. Lett.* **102**, 251602 (2013).

- [26] E. Breckenfeld, N. Bronn, N. Mason, and L. W. Martin, "Tunability of conduction at the LaAlO₃/SrTiO₃ heterointerface: Thickness and compositional studies," *Appl. Phys. Lett.* **105**, 121610 (2014).
- [27] A. Fête, C. Cancellieri, D. Li, D. Stornaiuolo, A. D. Caviglia, S. Gariglio, and J.-M. Triscone, "Growth-induced electron mobility enhancement at the LaAlO₃/SrTiO₃ interface," *Appl. Phys. Lett.* **106**, 51604 (2015).
- [28] C. W. Bark, D. A. Felker, Y. Wang, Y. Zhang, H. W. Jang, C. M. Folkman, J. W. Park, S. H. Baek, H. Zhou, et al., "Tailoring a two-dimensional electron gas at the LaAlO₃/SrTiO₃ (001) interface by epitaxial strain," *Proc. Natl. Acad. Sci.* **108**, 4720–4724 (2011).
- [29] Z. Q. Liu, C. J. Li, W. M. Lu, X. H. Huang, Z. Huang, S. W. Zeng, X. P. Qiu, L. S. Huang, A. Annadi, et al., "Origin of the Two-Dimensional Electron Gas at LaAlO₃/SrTiO₃ Interfaces: The Role of Oxygen Vacancies and Electronic Reconstruction," *Phys. Rev. X* **3**, 1010–1010 (2013).
- [30] Z. Q. Liu, L. Sun, Z. Huang, C. J. Li, S. W. Zeng, K. Han, W. M. Lü, T. Venkatesan, and Ariando, "Dominant role of oxygen vacancies in electrical properties of unannealed LaAlO₃/SrTiO₃ interfaces," *J. Appl. Phys.* **115**, 54303 (2014).
- [31] V. Vonk, M. Huijben, K. J. I. Driessen, P. Tinnemans, A. Brinkman, S. Harkema, and H. Graafsma, "Interface structure of SrTiO₃/LaAlO₃ at elevated temperatures studied in situ by synchrotron X rays," *Phys Rev B* **75**, 235417 (2007).

Chapitre IV – Résumé

Le dernier chapitre de cette thèse s'articule autour de l'influence des paramètres de croissance sur les mécanismes identifiés comme responsable de la conduction à l'interface des hétérostructures LAO/STO, et donc sur ses propriétés. En effet, la variation des conditions de croissance est à l'origine de la grande disparité des propriétés publiées dans la littérature. Ainsi, nous avons menés des investigations sur quatre paramètres importants que sont l'épaisseur du film, la pression partielle d'oxygène, l'angle de dépôt entre la plume et le substrat, et enfin la température lors du dépôt.

L'épaisseur du film est un facteur essentiel du comportement électrique des hétérostructures LAO/STO. Tout d'abord, une épaisseur critique de film LAO égale à 4 uc (dans des conditions de dépôt standards) est nécessaire pour induire des propriétés conductrices au matériau. Au-dessus de cette épaisseur critique, le système sera également soumis à l'influence de l'épaisseur du film déposée. Notamment, l'hétérostructure aura de moins bonnes performances électriques (densité et mobilité des porteurs mesurées par effet Hall plus faibles) lorsque le film sera plus épais. Toutefois une concentration plus importante de porteurs a été mesurée à l'interface du film plus épais. L'origine de ces porteurs ne peut pas être les défauts extrinsèques, puisque les mesures EELS sur le spectre de l'oxygène n'ont pas permis de détecter la présence de lacunes d'oxygènes à l'interface et dans le substrat STO. Le dopage par La est également exclu car on a mesuré un échange cationique légèrement plus faible à mesure que l'épaisseur du film augmente. Cette différence entre la quantité de porteurs, définie par EELS, et les mesures électriques s'explique par une baisse de la mobilité de ces porteurs. Ce phénomène est attribué aux distorsions structurales qui augmentent avec l'épaisseur du film. Le potentiel électrostatique dans le film grandit avec le film, ce qui nécessite une compensation plus importante, notamment par une déformation de la maille cristalline (flambage, lacunes cationiques, etc.). Ainsi, dans ces conditions de croissance particulières, les distorsions structurales semblent jouer le rôle prépondérant sur les propriétés électriques. On en a conclu que pour optimiser le fonctionnement de ces systèmes, l'épaisseur du film devait être minimisée pour améliorer la conduction, tout en restant au-dessus de l'épaisseur critique de 4 uc.

Lors de la croissance du film LAO sur le substrat STO, la pression partielle d'oxygène joue un rôle déterminant. En effet, les propriétés électriques sont grandement augmentées lorsque p_{O_2} est diminuée pendant le dépôt. La densité de porteurs augmentent considérablement, ce qui est cohérent avec les mesures EELS effectuées sur le seuil d'absorption Ti-L_{2,3} à l'interface, où la contribution de Ti³⁺ y est très importante à basse pression. D'ailleurs, une dilution des porteurs en profondeur a été constatée dans l'échantillon élaboré à 10⁻⁶ Torr, suggérant une conduction tridimensionnelle. Une des sources principales de ces électrons dans ces conditions est liée à la

Chapter IV | Dependence to growth conditions

quantité relative de lacunes d'oxygènes que nous avons détecté par EELS à partir de 10^{-5} Torr, à la fois dans le substrat STO, et à l'interface, mais également à la surface du film. Plus la pression d'O lors de la croissance est faible, et plus la quantité de défauts extrinsèques mesurée est importante. Le mécanisme d'interdiffusion a quant à lui été étudié à la fois par EELS et par MEIS en mode Random. Les résultats ont systématiquement montré que les cations diffusent plus en profondeur et en plus grande quantité dans les échantillons déposés à plus basse p_{O_2} . La longueur de diffusion des cations A et B sont néanmoins similaires, ce qui peut limiter la contribution du dopage par les donneurs La^{3+} , bien que ces derniers soient plus facilement ionisés. Toutefois, une plus grande contribution de Ti^{3+} à l'interface, ainsi qu'un échange cationique favorisée, aboutissent à des déformations plus importantes de la maille. L'analyse MEIS en mode Blocking nous renseigne sur l'effet de la pression partielle d'oxygène sur le comportement structural à une échelle atomique. Les données expérimentales mettent en avant une amplification des distorsions structurales à plus basse pression d'O. Ceci est cohérent avec l'ensemble des résultats expérimentaux obtenus. En d'autres termes à basse pression d'O, d'une part la forte contribution de Ti^{3+} autour de l'interface s'accompagne d'un effet Jahn-Teller (ou pseudo-) d'autant plus important, d'autre part la déformation épitaxiale est également exacerbée suite à une interdiffusion plus grande, enfin le mécanisme de compensation ionique du déséquilibre électronique est favorisée. Ce dernier s'accompagne d'une concentration plus importante en lacunes de strontium à basse pression d'O, et donc d'une expansion plus grande de la maille. Cette plus grande déformation réduit la mobilité des porteurs, or on a pu constater une meilleure conduction des échantillons élaborés à basse pression. Ainsi, on conclut qu'à basse pression partielle d'oxygène, les mécanismes dominants les propriétés électroniques des hétérostructures LAO/STO sont représentés par les lacunes d'oxygènes et l'interdiffusion.

La position du substrat vis-à-vis de la plume a un impact considérable sur la croissance du film LAO. La plume ayant une composition inhomogène, suivant l'angle de déposition, la composition du film et les propriétés de l'hétérostructure seront profondément modifiées. D'autant plus que la fluence du laser a été adaptée à la position de l'échantillon par rapport à la plume, afin de garder un taux de dépôt similaire entre tous les échantillons étudiés dans cette thèse. Ainsi, la densité énergétique du laser a été augmentée pour les échantillons positionnés en bord de plume. La combinaison de ces deux paramètres a abouti à des dépôts ni homogène, ni stœchiométrique, avec une épaisseur de film LAO plus faible que ce qui était prévu initialement. La déficience en La lors de la croissance du film permet notamment de comprendre la quantité de lacunes d'oxygènes détectée par EELS à l'interface de l'échantillon élaboré à l'extrémité de la plume, contrairement à l'hétérostructure dont le substrat se situait au centre de celle-ci. Ce résultat justifie le faible apport électronique à l'interface mesuré par EELS, de même que des échanges cationiques en moins grande quantité et moins en profondeur, particulièrement la diffusion de La. Finalement, l'étude structurale de l'échantillon élaboré en bordure de plume a montré une déformation plus faible, avec une contribution non-élastique presque nulle à l'interface, à cause notamment de la combinaison des lacunes d'oxygènes et de strontium ($V_{Sr}'' - V_O'$). Afin d'optimiser les propriétés des hétérostructures LAO/STO, il est donc primordial de placer le substrat au centre de la plume lors du dépôt.

Finalement, nous avons analysé l'effet de la température utilisée lors de la croissance du film, réalisée à plus basse température. Bien qu'une amorphisation partielle du film ait été constatée, due probablement à une maîtrise relative du paramètre thermique lors du dépôt, nous avons comparé

les résultats de cette hétérostructure avec l'ensemble des échantillons déjà caractérisés. Ainsi, la valence de Ti à l'interface est plus grande dans l'échantillon élaboré à basse température si on le compare à celui ayant une épaisseur de film de dix mailles élémentaires déposé à 10^{-4} Torr. Ce phénomène peut s'expliquer par une compensation ionique favorisée à basse température, comparé à la compensation électronique. Par contre, elle est similaire à ce qui a été mesuré à l'interface des échantillons dont l'épaisseur est égale à trois et cinq mailles élémentaires (à 10^{-4} Torr). Dans ce cas, la charge à compenser serait plus importante. En effet, si à plus basse température on retrouve un état d'oxydation similaire à l'interface alors que la formation de lacunes de strontium est privilégiée, c'est que le potentiel divergeant est plus important. Alors qu'à 750°C , et à 10^{-4} Torr, aucun défaut extrinsèque n'ait été détecté, à plus basse température une faible concentration ne peut être totalement exclue à l'interface. Les mesures EELS des seuils d'absorption O-K, Ti-L_{2,3}, et La-M_{4,5} ont permis d'évaluer l'extension de l'interdiffusion cationique au sein de la structure à basse température. Ces analyses révèlent que la diffusion des cations A est moins étendue lorsque l'échantillon est élaboré à basse température. Une première explication réside, une nouvelle fois, dans la formation de lacunes de Sr. En effet, la densité de ces lacunes réduit la force motrice de l'échange cationique. Ainsi, le dopage donneur est réduit à basse température. De plus, une concentration plus importante de ces lacunes cationique étant favorisée à basse température, les distorsions structurales sont censées être plus grandes, diminuant la mobilité des porteurs, ce qui a pour conséquence une hétérostructure aux propriétés électriques réduites. Ainsi, les propriétés conductrices seront nettement améliorées à haute température de croissance.

Conclusion & Outlook

In the frame of this international collaboration, LaAlO₃/SrTiO₃ heterostructures have been processed, their structure analyzed and their electrical behavior determined. This thesis was devoted to the characterization of these hetero-interfaces built between a polar and a non-polar perovskites. Their structure is far from the ideal picture proposed in the first articles following Ohtomo's historical publication. If the pseudomorphic growth was established for all the samples by the absence of interfacial dislocations, many other defects have been found around the interface. Oxygen and cation vacancies, cation intermixing, cell deformation and buckling are the main defects evidenced. They have been systematically characterized using five imaging and analytical tools. The following table summarizes the dedicated tools chosen for each of the structural features investigated.

	SAD via TEM	STEM-HAADF	STEM-EELS	MEIS Random	MEIS Blocking
Epitaxy	×	×			
Ti valence			×		
Oxygen vacancies			×		
Cation intermixing		×	×	×	
Strain (V''_{Sr})		×			×
Atomic displacement		×			×

× principal technique, × secondary technique

Table V.1 | Tools used to lead the experimental investigations in this thesis.

When this collaboration was launched, no consensus was reached among the scientific community about the origins of the transport measurements and three main conduction mechanisms at room temperature were put forward: the polar catastrophe, intrinsic doping by oxygen vacancies and La doped-SrTiO₃. We have demonstrated that none of them separately could trigger a 2D conduction.

- The polar catastrophe has been rapidly ruled out. The polar field developed in the film is partially counteracted from the very first LAO unit cells deposited. A buckling of the layers and an electron transfer from the film to the interface by intermixed B cations ($Ti_{Al}^{film} \rightarrow$

Conclusion & Outlook

Al_{Ti}^{int}) reduce the potential slope and do not allow the crossing of the LAO valence band and STO conduction band.

- A 3D conduction by a reduction of the STO substrate is unavoidable at low partial pressure of oxygen. The transition from a 3D to a quasi 2D conduction was seen to occur between $p_{O_2} = 10^{-6}$ Torr and 10^{-5} Torr. In the quasi 2D regime the role of oxygen vacancies is indirect, they are not detected (or at a very low level) at the interfaces.
- Intermixing has been established for all samples grown at 750°C, whether conducting or insulating. The diffusion of La donor and Al acceptor cations into the STO substrate partially annihilates the source of free carriers. The differences in the A and B cations diffusion length, for the samples *UC3* and *UC5* (10^{-4} Torr, #2), could bring some net donor doping. But the insulating state in *UC3*, indicates that the charges were not transferred to the conduction band. They could have been compensated by strontium vacancies.

In addition, many articles mentioned an elongation of the *c* parameter of STO below the interface, explained by a Jahn-Teller type of effect on $Ti^{3+}O_6$ octahedra. We have confirmed an elongation of the STO cells but the low concentration of Ti^{3+} around the interface pushed us to find another origin for this deformation.

The growing LaO^+/AlO_2^- layers on TiO_2^0 surface store a dipolar energy and create a positively charged interface. From the defect population we have highlighted, a model of compensation for the dipolar field and interfacial charge is proposed, involving the interplay of several mechanisms:

- #1 The relaxation of the ionic layers that buckle to produce counter-dipoles with oxygen anions moving toward the interface and cations toward the film surface.
- #2 The presence of negatively charged strontium vacancies at the interface. The film can act as sink for the expelled strontium atoms. These vacancies might also result from the plume impingement or substrate preparation.
- #3 The interdiffusion of B cations and the electron transfer to the interface: $Ti_{Al}^{film} \rightarrow Al_{Ti}^{int}$. These electrons are trapped and do not participate to the conduction.
- #4 The formation of donor defects at the film surface such as surface oxygen vacancies or surface hydrogen. Their energy formation is reduced with the potential build-up. Their energy level allows electron transfers to the STO conduction band.

When the first unit cells are deposited, the mechanism #4 is not activated, the interface is insulating. This was the case for the 3 u.c. sample *UC3P4#2T7* (Figure V.2a). From a critical thickness, the surface potential allows the formation of donor defects at the surface. The interfacial charge can be partially compensated with mobile electrons, the interface is conducting. This was the case for the 5 u.c. sample, *UC5P4#2T7* (Figure V.2a). The conduction threshold is in between 3 and 5 u.c.

The electron transfer by mechanism #3 or #4 only partially compensates the positive charge. A mix ionic (V_{Sr}'' , #2), electronic (#3, #4) compensation takes place at $p_{O_2} = 10^{-5}$ Torr and 10^{-4} Torr. The strontium vacancies are responsible for an elongation of the *c* parameter in the substrate below the interface. The in-plane compressive strain reduces the in-plane transport properties and does not allow a strict 2D confinement of the charges, they are diluted over several unit cells below the interface.

The process parameters have a strong influence on the respective weights of these four mechanisms:

- Increasing the film thickness (Figure V.2a), at 750°C 10⁻⁴ Torr, rises the V_{Sr}'' concentration below the interface and the deformation of the cells. The out-of-plane mobility is increased at the expense of the in-plane one. The 2D confinement is hindered, charges are more diluted (Figure V.2a). A thickness just above the conduction threshold must be preferred.
- Decreasing the oxygen partial pressure (Figure V.2b) increases the oxygen vacancy concentration at the film surface. At $p_{O_2} = 10^{-5}$ Torr, the carrier density is increased, more from a film transfer than from a doping of the substrate by V_O'' . Intermixing is also favored, with a mix compensation of the La_{Sr} . The strain level below the interface is increased. At $p_{O_2} = 10^{-6}$ Torr, charge injection from bulk oxygen vacancies dominates and the conduction is three dimensional, with lower V_O'' concentration at the interface than in the bulk STO.
- Deposition from the edge of the plume (Figure V.2c) forms an Al-rich film and reduces A cation intermixing. La vacancies are partially charged balanced by oxygen vacancies. The formation of $V_{Sr}'' - V_O''$ pairs lowers the strain below the interface. Part of the La vacancies of the film could be filled by Sr, these acceptor defects being annihilated by Ti_{Al} . The behavior of Al-rich film above the critical thickness could not be analyzed.
- Decreasing the deposition temperature (Figure V.2d) reduces intermixing and shifts the compensation of positive interfacial charge toward V_{Sr}'' formation rather than electron transfer. The heterostructure is expected to develop a lower conductivity.

The following table summarizes the effect of the growth conditions on the defects and mechanisms presented in this thesis:

Growth conditions	Ti ³⁺ concentration (interface)	V_O'' (interface)	V_O'' (bulk)	Intermixing	Strain	Electronic compensation	Ionic compensation (V_{Sr}'')	Electrical properties
Thickness ↗ (> 4 u.c.)	↗	X	X	≈	↗	↗	↗	↘
p_{O_2} ↘: 10 ⁻⁵ Torr	↗	?	?	↗	↗	↗	↘	↗
p_{O_2} ↘: 10 ⁻⁶ Torr	↗	↗	↗	↗	↗	↗	↘	↗ 3D
Deposition angle Plume edge	↘	↗	X	↘	↘	?	?	?
Temperature ↘	↘	X	X	↘	↗	↘	↗	↘

Table V.2 | Effects of the growth parameters on the mechanisms analyzed experimentally in this thesis.

The prediction of the properties of the LAO/STO heterostructure is only possible if defect distributions can be controlled by the process and if the synergy of their actions on charge carrier is understood. We have seen the detrimental influence of in-plane compressive strain, which must be reduced to favor 2D confinement of the charges. Compressive strains were mainly brought by ionic compensation. A growth at lower p_{O_2} would favor electronic compensation. Knowing that a 3D conduction must be avoided for electronic applications, the 3D/2D conduction threshold must be searched more accurately to deposit the LAO films just above this threshold. However such low p_{O_2} will induce stronger intermixing and bring additional undesirable distortions. This illustrates the

Conclusion & Outlook

strong interdependency of the mechanism and the difficulty of the optimization of the transport properties.

This model must be undoubtedly refined, some information are missing that would have enriched the discussion and reinforced our understanding of this system.

- The quantification of aluminum diffusion was not achieved. The concentration of Al_{Tl} acceptor dopants in the substrate and the La/Al ratio in the film are not known and were hypothesized.
- We could not image the oxygen atoms by HAADF, their position is not known, the effect of strain on the tilt of octahedra was not addressed.
- A better knowledge of the surface structure of the film is required, as the surface defects are seen to control the electron transfer. Transmission electron microscopy is not well adapted for such investigation due to the possible artefacts introduced on the film surface during thin foil preparation.
- A secondary maximum of the in-plane compressive strain is observed within the STO substrate for the samples *UC3P4*, *UC5P4* and *UC5P5* (Figure V.1). Although this increase is within the error bar, its systematic occurrence must be questioned. Another contribution to the compressive strain might need to be searched.

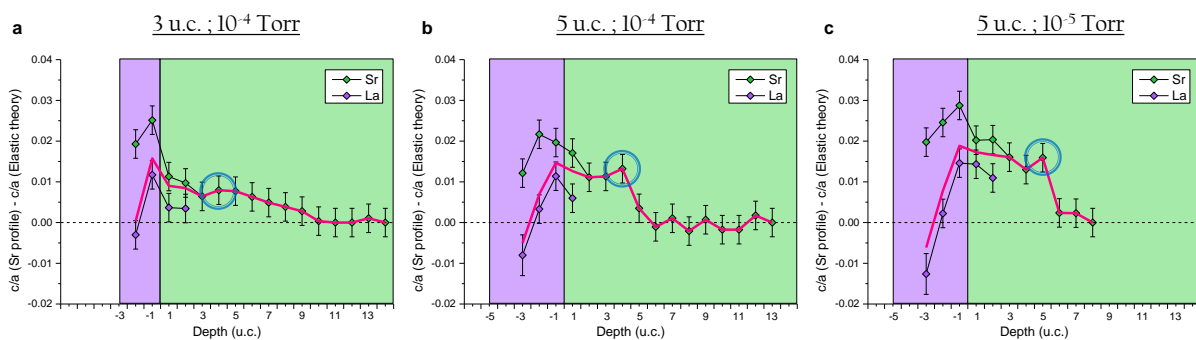


Figure V.1 | MEIS strain profiles for samples presented in this thesis. A secondary maximum systematically occurs within the bulk, suggesting a possible additional contribution to the compressive strain.

The growth conditions have been varied one by one. It would be interesting to investigate their combine effects. For example since the critical thickness is linked to the formation of surface $V_{\text{O}}^{\bullet\bullet}$, is this critical thickness lowered at lower p_{O_2} ? We have shown that the control of the interface strain is a key factor to tune the conduction properties. The growth of a LAO/STO double film on a non-polar perovskite substrate to favor an in-plane tensile strain in the STO film should be considered. In addition the carrier density, still low in comparison to classical semiconductors, could be increased by an extrinsic doping of the LAO film.

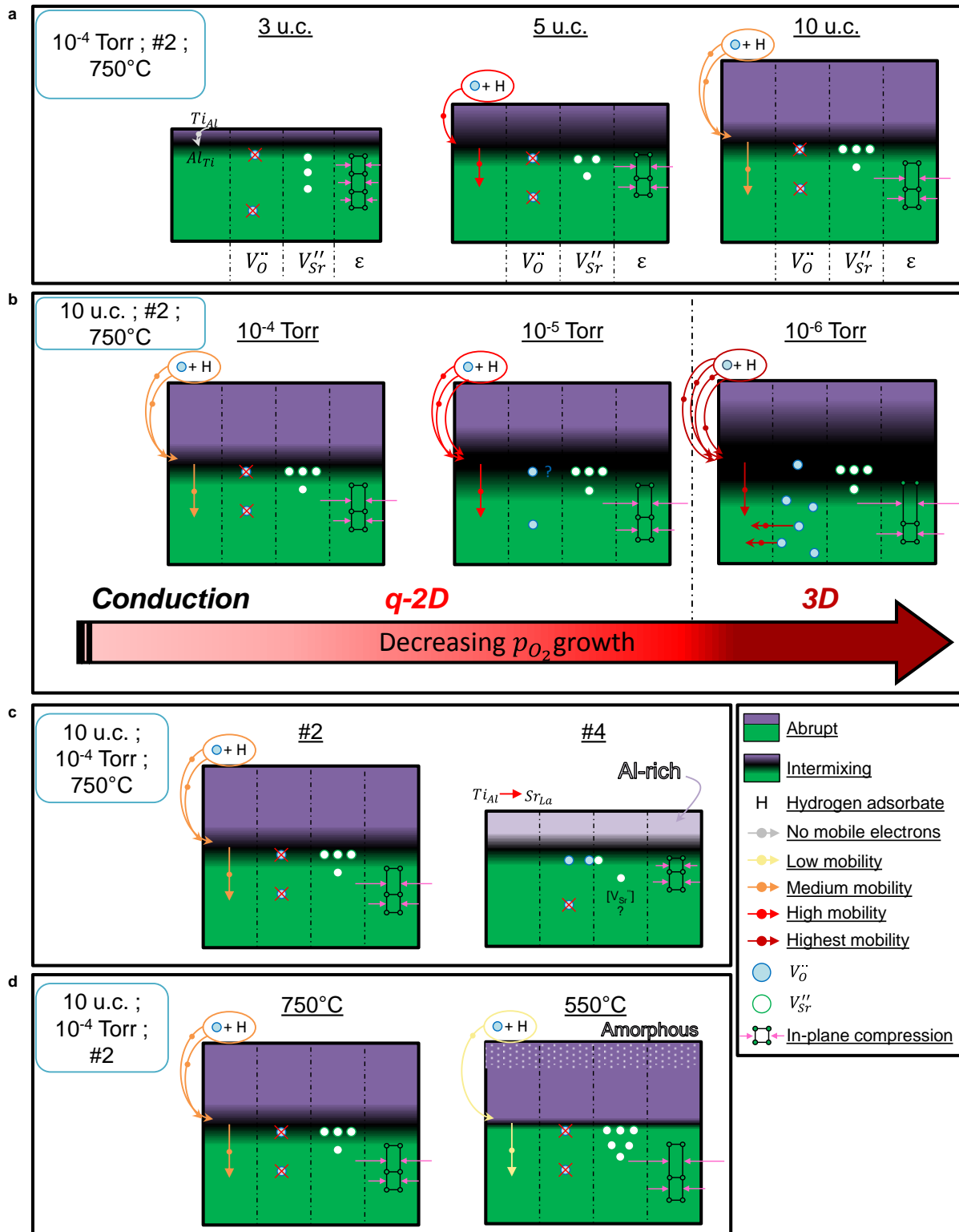


Figure V.2 | Summary of the thesis results. Schematic diagram concerning the samples varying from each other by the (a) film thickness (b) growth oxygen partial pressure (c) deposition angle (d) growth temperature.

...

Résumé

De nombreuses propriétés étonnantes ont été récemment découvertes à l'interface de deux perovskites isolantes l'une polaire l'autre non polaire. La discontinuité de charge à l'interface $\text{LaAlO}_3/\text{SrTiO}_3$ engendre un gaz d'électron quasi-bidimensionnel qui confère un caractère métallique à cette interface. Les mécanismes locaux et la quantification des propriétés ne font pas consensus car l'interdépendance de facteurs structuraux, chimiques et électroniques complexifie la résolution du problème posé. Une catastrophe polaire, des distorsions structurales, des lacunes d'oxygène, une interdiffusion cationique et une non-stœchiométrie du film ont été séparément avancées pour expliquer cette conduction. Dans le cadre d'un programme international, nous avons reçu des hétéro-interfaces conductrices et isolantes élaborées par ablation laser pulsé (PLD). L'origine des porteurs de charge a été recherchée par une approche globale liant procédé, structure et propriétés électriques (mesurées dans le consortium). Nous avons systématiquement analysé les interfaces en combinant imagerie à haute résolution (STEM-HAADF) et spectroscopies électroniques (EELS) et ioniques (MEIS). Une non planéité des couches atomiques, une interdiffusion cationique et un transfert d'électrons permettent de réduire la divergence de potentiel, la catastrophe polaire n'a donc pas lieu. La formation de défauts donneurs à la surface du film devient favorable au-delà d'une épaisseur critique. Les électrons sont transférés à l'interface dans la bande de conduction du STO. Nous avons mis en évidence un mécanisme de compensation concurrentiel de la charge interfaciale par des lacunes de strontium chargées négativement, qui mettent le substrat en compression plane et s'opposent au confinement 2D électrons. La variation des paramètres procédés, tels que la durée du dépôt, la pression partielle en oxygène, la température et la stœchiométrie de la plume déplace l'équilibre des différents mécanismes mis en évidence. Ce travail démontre la relation complexe liant procédé, propriétés électriques et distribution des défauts autour de ces interfaces singulières.

Mots Clés

Pérovskites, interfaces polaires/non-polaires, gaz d'électrons bidimensionnel, microscopie électronique en transmission, microélectronique tout oxyde

Abstract

Novel behavior at the interface between two insulating polar/non polar perovskites has been recently discovered. The polarization discontinuity at $\text{LaAlO}_3/\text{SrTiO}_3$ drives the formation of quasi two dimensional electron gas. Both the local mechanism and quantification of such behavior remain unclear due to interplay of structural, chemical and electronic factors. Several mechanisms have been proposed, such as the polar catastrophe, structural distortions, oxygen vacancies, cationic intermixing at the interface and film non-stoichiometry. In the frame of an international project conductive and insulating heterostructures have been synthesized by Pulsed-Laser Deposition. In this thesis, we have developed a comprehensive approach to investigate the origin of the charge carriers. The interfaces have been systematically analyzed by combining high resolution imaging (STEM-HAADF) to atomic resolved electron (EELS) and ion (MEIS) spectroscopies. The observed and quantified parameters have been related to the electrical properties of the interfaces measured in the consortium. Buckling of the atomic layers, intermixing and electron transfer reduce the polar divergence. This rules out the polar catastrophe scenario. The formation of donor defects at the film surface is favored above a critical film thickness. Electrons are transferred to interface in the STO conduction band. A competing compensation mechanism of the positive interfacial charge by negatively charged strontium vacancies has been demonstrated that generates an in-plane compression of the STO, unfavorable for a strict 2D confinement of the charges. Varying the process parameters such as growth duration, oxygen partial pressure, temperature, and plume stoichiometry, shifts the equilibrium of the different mechanisms highlighted. This thesis emphasizes the complex relations between the process and the properties through the defects distribution around these singular interfaces.

Keywords

Perovskites, polar/non polar interfaces, two-dimensional electron gas, transmission electron microscopy, all oxide microelectronic